



Universiteit
Leiden
The Netherlands

Clues from stellar catastrophes

Rimoldi, A.J.

Citation

Rimoldi, A. J. (2016, March 29). *Clues from stellar catastrophes*. Retrieved from <https://hdl.handle.net/1887/38640>

Version: Not Applicable (or Unknown)

License: [Leiden University Non-exclusive license](#)

Downloaded from: <https://hdl.handle.net/1887/38640>

Note: To cite this publication please use the final published version (if applicable).

Cover Page



Universiteit Leiden



The handle <http://hdl.handle.net/1887/38640> holds various files of this Leiden University dissertation

Author: Rimoldi, Alexander

Title: Clues from stellar catastrophes

Issue Date: 2016-03-29

Clues from Stellar Catastrophes

Proefschrift

ter verkrijging van
de graad van Doctor aan de Universiteit Leiden,
op gezag van Rector Magnificus prof. mr. C. J. J. M. Stolker,
volgens besluit van het College voor Promoties
te verdedigen op dinsdag 29 maart 2016
klokke 13:45 uur

door

Alexander Rimoldi

geboren te Auckland, Nieuw-Zeeland
in 1981

Promotiecommissie

Promotores: Prof. dr. S. F. Portegies Zwart (Universiteit Leiden)
Dr. E. M. Rossi (Universiteit Leiden)

Overige leden: Prof. M. Campanelli (University of Rochester)
Prof. T. Piran (Racah Institute of Physics)
Prof. dr. H. J. A. Röttgering (Universiteit Leiden)
Prof. dr. J. Schaye (Universiteit Leiden)
Dr. J. Vink (Universiteit van Amsterdam)

ISBN: 978-94-028-0108-8

Cover design: Dylan Horrocks

The back cover shows the motion of gas seen from inside an exploding star, from the simulations of Chapter 4.

To my parents

*The world is so full of a number of things,
I'm sure we should all be as happy as kings.*
— 'Happy Thought', Robert Louis Stevenson

Contents

1	Introduction	1
1.1	Overview	1
1.2	Astrophysical phenomena in this thesis	2
1.2.1	Supernovae and supernova remnants	2
1.2.2	Supermassive black hole environments	4
1.2.3	Two tales of two stars: supernovae in binary systems	6
1.2.4	Two tales of two stars: stellar collisions and blue stragglers	7
1.3	Methods used in this thesis	9
1.3.1	A new numerical shock solver	9
1.3.2	AMUSE	9
1.3.3	Smoothed-particle hydrodynamics	10
1.3.4	Stellar structure and merger modelling	10
1.3.5	Monte Carlo and MCMC methods	11
1.4	Content of this thesis	12
1.5	Outlook	14
2	The fate of SNRs near quiescent SMBHs	17
2.1	Introduction	18
2.2	Gaseous environments of quiescent nuclei	20
2.3	Evolution of remnants around quiescent black holes: analytic foundations	21
2.3.1	End of the ejecta-dominated stage	23
2.3.2	Deceleration in the adiabatic stage	24
2.3.3	Intermediate-asymptotic transition	26
2.3.4	Transition to the radiative stage	26

2.4	Evolution of remnants around quiescent black holes: numerical treatment	27
2.4.1	General prescription	28
2.4.2	Comparison with analytic solutions for single power-law profiles	30
2.4.3	Caveats and limitations of the model	31
2.5	Galactic nuclei model	32
2.5.1	Characteristic radii	33
2.5.2	Gas models	34
2.5.3	Massive star distributions	36
2.6	Results	36
2.6.1	Deceleration lengths	37
2.6.2	Morphological evolution	40
2.6.3	Adiabatic SNR lifetimes	43
2.7	Discussion and conclusions	47
	Appendix 2.A: Integrals of density in the ejecta-dominated stage . .	49
	Appendix 2.B: Numerical treatment of shock self-interactions . . .	54
3	The contribution of SNRs to X-ray emission near quiescent SMBHs	57
3.1	Introduction	58
3.2	Galactic nuclear environments	60
3.2.1	Galactic Centre observations	60
3.2.2	Quiescent galactic nuclei as autarkic systems	61
3.3	SNR dynamical evolution	63
3.3.1	X-ray emitting lifetime	64
3.4	Number of adiabatic remnants in a snapshot observation . . .	64
3.5	X-ray luminosity from SNRs in the sphere of influence	68
3.5.1	SNR spectral properties	68
3.5.2	SNR X-ray luminosity	71
3.5.3	Detectability	76
3.6	The sphere of influence SFR	78
3.7	Discussion and conclusions	79
4	Simulations of stripped core-collapse supernovae in close binaries	83
4.1	Introduction	84
4.2	Method	87
4.2.1	Stellar models	87
4.2.2	Hydrodynamical model set-up	88

4.2.3	Simulation of the supernova explosion	90
4.2.4	Measured parameters	91
4.2.5	Convergence test	92
4.3	Results	94
4.3.1	Shock breakout	95
4.3.2	Impact and mass loss from the companion	96
4.3.3	Momentum transfer and the velocity of the companion	99
4.3.4	Properties of the larger-scale SNR	104
4.3.5	Post-impact state of the companion	106
4.4	Discussion and conclusions	108
5	A method to infer globular cluster evolution from observations of blue stragglers	113
5.1	Introduction	114
5.2	Method	115
5.2.1	BSS models	115
5.2.2	Grid approach	117
5.2.3	MCMC approach	119
5.3	Results	121
5.3.1	Grid results	121
5.3.2	MCMC results	123
5.3.3	An independent estimate of the core-collapse time . .	125
5.4	Discussion and conclusions	127
	Thesis summary	131
	Nederlandse samenvatting	135
	Bibliography	140
	Curriculum Vitae	157
	List of publications	159
	Acknowledgements	161

1 Introduction

1.1 Overview

Much of astronomy plays out over timescales much longer than a human lifetime. From the gravitational dances of galaxies to the nuclear furnaces powering the stars within them, we typically see these processes as if frozen at a moment in time. Large ensembles of observations, along with the fortune of being able to view into the past with greater distances, are often needed to piece together a picture of the evolution of these phenomena. However, in certain cases, we are lucky enough to observe full astrophysical events unfolding before us—or, at least, study their consequences. These short-timescale processes, often involving high-energy astrophysics, form the basis of much of the work in this thesis. In particular, we focus on catastrophic events involving stars, and what these events can tell us about the environments in which they occur.

We begin by covering the main astrophysical phenomena examined here. The first topic is a common theme through most of the following chapters—and one of the most rapid events to occur in astronomy—the supernova explosion at the end of a massive star’s life (Section 1.2.1). In the first two of the following chapters, we are interested in studying the consequences of supernovae near supermassive black holes like the one in the center of our Milky Way Galaxy. We aim to use this as a tool to infer properties of otherwise obscure galactic centres. We therefore focus briefly on our understanding of the environment of these black holes (Section 1.2.2). In the subsequent chapter, we shift focus to the effect of a supernova on an even more immediate surrounding, a stellar companion (Section 1.2.3). The final chapter considers interactions between two stars not during an explosion but during a collision. By looking at the end product of these collisions, observed as ‘blue straggler’ stars, we may be able to infer properties of the stars that collided and of the parent cluster. Therefore, for the final subject, we present a brief overview of blue stragglers (Section 1.2.4).

In order to investigate this variety of problems, we create or employ a number of different techniques. These methods are needed as the problems do not lend themselves to tractable analytic solutions. Therefore, after reviewing the astrophysical topics in this thesis, we continue this introduction by covering the main methods used (Section 1.3). We then provide an overview of the content of each of the following chap-

ters, emphasizing the novel contributions of the thesis to these topics (Section 1.4). Finally, we conclude with an outlook, where we consider how future work, based on the results of this thesis, can continue to contribute to the problems we have addressed here (Section 1.5).

1.2 Astrophysical phenomena in this thesis

1.2.1 Supernovae and supernova remnants

Lying behind much of the work in this thesis are the predictions from a pillar of modern astronomy, the theory of stellar evolution. The changes in the structure of a star over its lifetime are now very well understood, and they are largely determined by a single parameter: its mass. Although the Sun is more massive than about 9 out of every 10 stars, its mass is still low enough that the end of its life will be a relatively gentle display, finally forming a planetary nebula containing a white dwarf remnant. For stars with initial masses greater than about 8 times the mass of the Sun ($8 M_{\odot}$), the (electron degeneracy) pressure that supports a white dwarf is eventually exceeded in the core.

The pressure in the core of a massive star is overcome by the inward force of gravity once the series of fusing elements reaches iron, with catastrophic consequences. On the timescale of about a second, the core of the star collapses into either a neutron star or, with a sufficiently large amount of mass, a black hole. The collapse of the core ends abruptly (the equation of state of the proto-neutron star is very stiff, meaning that its surface has little ‘give’ against the remaining in-falling matter), and the resulting ‘bounce’ at core-collapse drives a very strong shock outward through the remaining layers of the star. The energy from the resulting supernova explosion synthesises a large number of new elements—a primary source of the elements heavier than iron in the universe—and drives out the rest of the stellar material as supernova ejecta. The supernova ejecta trail the shock that has broken out through the surface of the star and into the interstellar medium (ISM). The cinder left behind from the core of the star, whether a neutron star or black hole, is referred to as a stellar remnant; the expanding shell of ejecta, as well as the ISM swept up by the shock, is referred to as a supernova remnant (SNR).

SNRs can usually be distinguished from the ISM for $\gtrsim 10^6$ years (Padmanabhan 2001). The evolution of radius and velocity for an SNR in a typical ISM is shown in Figure 1.1 (note that higher densities of gas near SMBHs will generally shorten the characteristic scales compared to the ‘canonical’ ones shown here). The initial stage of the SNR is referred to as the ejecta-dominated or free-expansion stage, where little of the ISM has been swept up by the shock and the SNR expands at roughly the initial velocity, determined by the kinetic energy imparted to the mass of the ejecta (blue in Figure 1.1). Once the mass swept up from the ISM is roughly equal to the mass of the ejecta, by momentum conservation the deceleration of the SNR becomes appre-

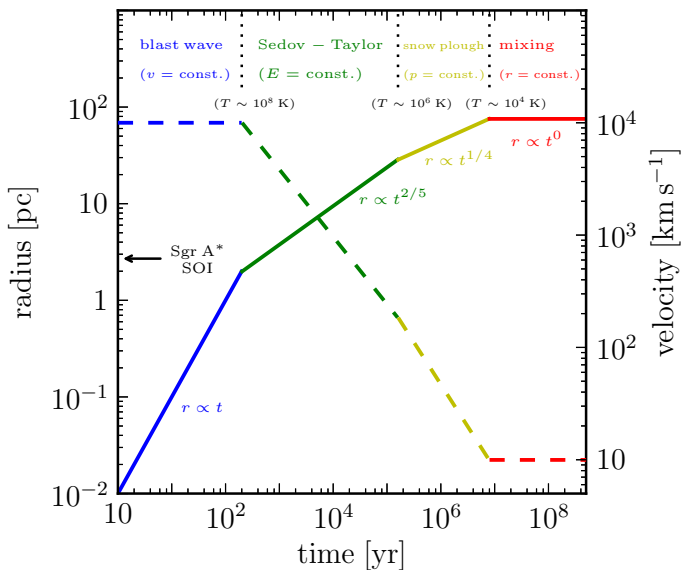


Figure 1.1: The stages of evolution of a supernova remnant for an energy of 10^{51} erg, an ejecta mass of $1 M_{\odot}$ for a typical ISM ambient density of $n_{\text{H}} \sim 1 \text{ cm}^{-3}$. Temperatures, T , are given at each of the timescales of the transitions. The solid line shows the evolution of the radius, while the dashed line shows the evolution of the velocity. (More realistically, the evolution is ‘intermediate-asymptotic’, transitioning between these limiting functions.) The scale of the sphere of influence of the Milky Way supermassive black hole, Sgr A*, is indicated with an arrow. [After Padmanabhan, 2001, Figure 4.6]

cial, and it has entered the next stage of adiabatic expansion (green in Figure 1.1). Particularly for a uniform ISM, where the expansion is spherically symmetric, this is also known as the Sedov–Taylor stage, and during this time the loss of energy interior to the SNR is minimal. Eventually the SNR decelerates to the point where the temperature behind the shock, which is proportional to the square of the shock velocity, is low enough for line emission to generate a more rapid loss of energy (yellow in Figure 1.1). The SNR has reached the radiative stage of evolution, and once the energy density behind the shock is sufficiently low, the expansion of the SNR is no longer pressure-driven but momentum-driven. Eventually the SNR slows to the sound speed of the ISM and mixes with the ambient medium (red in Figure 1.1).

For a strong shock originating from a point explosion in an ambient medium, it is possible to derive the velocity, and radius from the explosion, along the shock front as a function of time, during the adiabatic expansion of the SNR (the second, green, stage in Figure 1.1). This theory was first developed by Taylor (1950) and Sedov (1959) for investigations of (nuclear) explosions in a uniform ambient medium of gas. Soon after, Kompaneets (1960) developed a solution for shocks in the non-uniform (exponentially stratified) density of the Earth’s atmosphere. Subsequent solutions were developed for

other types of density profiles, such as for explosions offset from the center of power-law functions of radius (Korycansky 1992).

The theory elaborated by Kompaneets is generally applicable to different ambient density profiles, and is based upon a few assumptions. The first is that the post-shock pressure, P' , inside the SNR volume, V , is uniform and equal to some fraction, λ , of the mean energy density: $P' = (\gamma - 1)\lambda E/V$, for a given adiabatic exponent, γ . The second assumption is that the direction of the shock velocity is normal to the curve defining the shock front at a given moment. The third is that the magnitude of the shock velocity, v_s , is found by equating P' to the ram pressure of the ambient medium, ρv_s^2 . Like the Sedov–Taylor case, the solutions for the shock evolution in simple functions of density are self-similar, where the scaling depends on the energy of the explosion and the value of the ambient density.

We use the Kompaneets approximation to construct a numerical method of solving the decelerating shock front evolution in more general ambient media in the first of the following chapters. Instead, when studying supernovae in close binary systems, the initial free-expanding regime is the only relevant one, as the binary separation is much less than the radius at which the SNR reaches the stage of appreciable deceleration.

During the earliest evolution of the SNR (the first two stages of Figure 1.1), the temperature is high enough that much of the emission from the SNR is in the form of X-rays from bremsstrahlung (‘breaking radiation’ from the electromagnetic deflections of electrons). It is these early stages that are of particular interest in the first two chapters of this thesis, as we are interested in characterising the X-ray emission from SNRs for the time-scales that they survive near supermassive black holes.

1.2.2 Supermassive black hole environments

Black holes are found with masses spanning many orders of magnitude and in a wide range of environments. Following a supernova explosion in the most massive stars, the core of the star collapses into a stellar-mass black hole of several M_\odot . Their much larger cousins, supermassive black holes (SMBHs, which can be as massive as $10^{10} M_\odot$), are found in the centres of nearly all massive galaxies (Ferrarese and Ford 2005; Marleau et al. 2013). The origin and growth of supermassive black holes is an active and debated topic in astronomy. Instead, for this work, we are interested in the immediate environment of supermassive black holes like the one in the centre of the Milky Way, known as Sagittarius A* (abbreviated as Sgr A*). The ‘central engine’ of Sgr A*, like almost all SMBHs in the present-day (*i.e.* local) universe, is categorised as ‘quiescent’; that is, the emission of radiation from the vicinity of the SMBH is very low compared with much more active galactic nuclei (AGN).

Light emitted from near the SMBH comes from the accretion flow, and the radiated energy is supplied by the gravitational potential energy liberated by this in-falling matter. The measure of luminosity of the SMBH is typically given in units of the Ed-

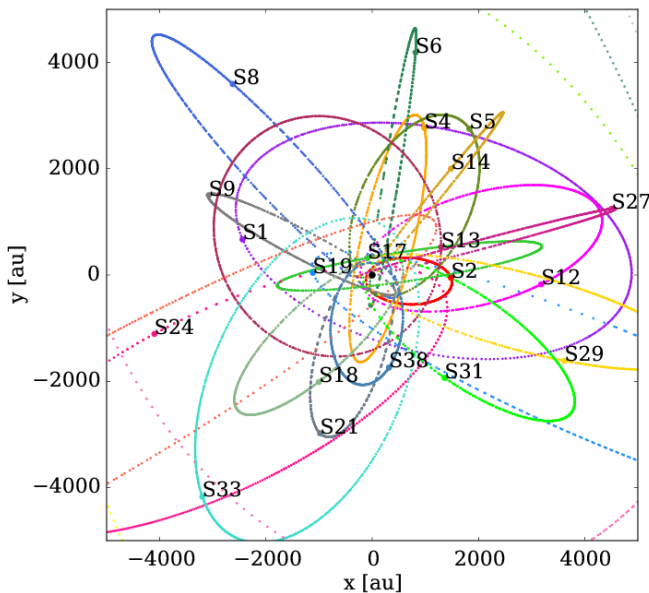


Figure 1.2: Orbits of the S-stars around the supermassive black hole (SMBH) Sgr A*. The orbits are integrated using `ph4` in the Astrophysical Multipurpose Software Environment (AMUSE), with observed orbital parameters from Gillessen et al. [2009]. The black point is the SMBH of Sgr A*. [From Lützgendorf et al., 2015]

dington luminosity, L_{Edd} , which is an upper limit at which the force on matter from the radiation pressure of the accretion flow equally opposes the central force of gravity. Due to the immense amount of potential energy released as radiation, accretion flows can be some of the most luminous objects in the universe. Quiescent SMBHs like Sgr A*, however, emit at many orders of magnitude less than the Eddington luminosity.

It is difficult to observe quiescent SMBHs, including Sgr A*, in bands such as the optical due to the large amount of obscuring matter—and, therefore, extinction—in the direction of the galactic nucleus. Instead, searches for these SMBHs have often employed instruments such as the *Chandra* X-ray telescope, as X-rays from the accretion flow penetrate the surrounding material more readily (Baganoff et al. 2003; Wang et al. 2013). A deeper understanding of these obscured environments can shed light on the evolutionary histories of these nuclei (such as the link between the AGN of the earlier Universe and their comparatively inactive present-day forms), as well as help to constrain or rule out different accretion flow models.

The low luminosity of quiescent SMBHs has been explained with radiatively-inefficient accretion flows (RIAFs), such as the ‘standard’ RIAF model, known as the advection-dominated accretion flow (ADAF; Narayan et al. 1995; Narayan and Yi 1995). In an ADAF, much of the energy is contained within the ions of the plasma in the accretion flow—whereas it is the electrons that emit most of the radiation. The exchange of energy between the ions and electrons is inefficient, and therefore much of the energy is carried (advected) into the SMBH before it can be radiated, explaining the very sub-Eddington luminosity. ADAFs are geometrically thick, and their properties can therefore be well approximated by power-law functions of radius

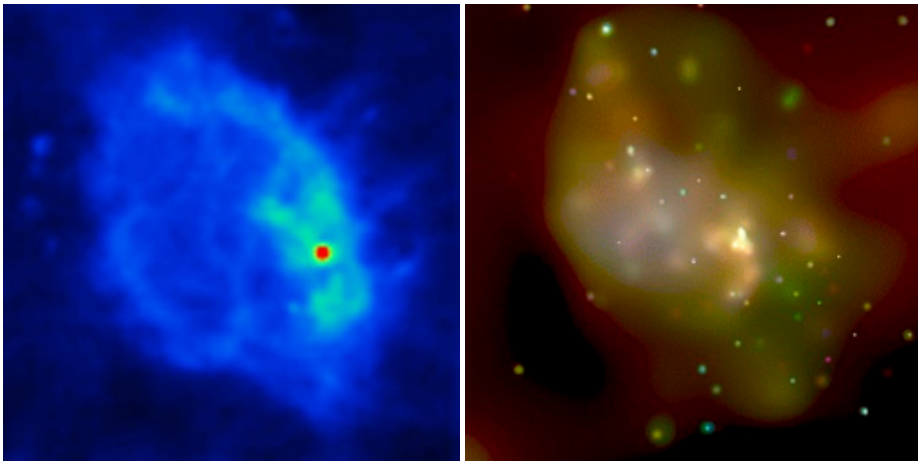


Figure 1.3: The Sgr A East supernova remnant at the centre of the Galaxy. Left: 20 centimetre continuum image from the Very Large Array (VLA); Sgr A* appears as a red point [University of Illinois/NCSA/R. Plante/K. Y. Lo/R. M. Crutcher]. Right: X-ray image from *Chandra*; Sgr A* is located near the bright white points. [ASA/MIT/F. Baganoff et al.]

from the SMBH. The exact form of the power-law dependences depend on the type of accretion model, and in this thesis we investigate a range of models and their effects on our predictions. We will use the radial properties of these models, in particular the density, as the background environment into which a supernova will explode.

Young, massive stars are often seen close to quiescent SMBHs, including Sgr A*, suggesting that ongoing star formation in such regions is common. The proximity of Sgr A* allows us to distinguish a group of massive stars as close as milliparsecs (thousands of au) from the black hole, known as the S-stars (Figure 1.2). Further out, to a distance of half a parsec, are hundreds of massive stars that appear to lie in a rough disc-like structure (Bartko et al. 2009). With this many massive stars, we expect that core-collapse supernovae near SMBHs like Sgr A* should be a frequent occurrence. Indeed, we do see evidence for at least one SNR near Sgr A*, known as Sgr A East (Maeda et al. 2002), which in fact seems to be engulfing the SMBH (Figure 1.3). The winds from the stars near the SMBH provide the material for the accretion flow for the black hole, which is the ambient medium into which any supernovae will explode.

1.2.3 Two tales of two stars: supernovae in binary systems

The majority of massive stars have a binary companion (Sana et al. 2012), and for core-collapse supernovae we therefore expect the presence of a companion star to be an important consideration. Core-collapse supernovae in giant stars typically produce supernovae classed as Type II (containing hydrogen lines). However, for closer binaries, much of the envelope of the exploding (primary) star can be stripped either by

stellar winds or by interactions with the close binary companion. The loss of the hydrogen envelope from the primary means that these stripped core-collapse supernovae tend to show little or no hydrogen, and are therefore classed as Type Ib (containing helium lines) or Type Ic (containing no helium lines). The mass of the ejecta in these supernovae is small (and may be almost non-existent in the case of ultra-stripped Type Ic supernovae), and therefore so is the total mass of the exploding star.

If there is negligible effect of the supernova impact on the companion star, the binary system is unbound if the mass lost in the supernova ejecta is more than half of the total mass of the system (Hills 1983). However, the analysis is complicated if the impact of the supernova ejecta cannot be ignored, which is the case at small orbital separations. The impact of the shell on the companion strips material from the outer layers of the star; additional material is subsequently lost due to ablation from shock heating. The impact also imparts additional momentum to the companion star.

The combined effects of mass lost and momentum gain—in particular, the directions in which material is lost (for example, we see a clear burst of material out the far side of the star due to shock convergence)—determine the final velocity of the companion. These effects were treated analytically by Tauris and Takens (1998) using impact predictions from Wheeler et al. (1975) and early, lower resolution simulations of the impact by Fryxell and Arnett (1981). We approach this problem with higher resolution simulations beginning from shortly after core bounce in the supernova progenitor to study the effects of the supernova on the companion star. Of particular importance to the theory developed in Tauris and Takens (1998) is the total amount of mass stripped from the companion star and the additional velocity imparted to the companion by the impact, and so we investigate these effects in our simulations.

1.2.4 Two tales of two stars: stellar collisions and blue stragglers

Star clusters are broadly grouped into two types: ‘open’ clusters, which contain hundreds or thousands of stars and have recently formed in the galactic disc, and ‘globular’ clusters, which are much older, dense hives of tens of thousands (up to millions) of stars found in galactic halos. Observations of globular clusters indicate that the majority of the stars share a common origin at the formation of the cluster, where the clusters often are almost as old as the Universe itself.

Over time, mass segregation causes more massive stars to sink towards the centre of globular clusters. In principle, this process causes an instability during which the core undergoes a runaway increase in density known as ‘core collapse’,¹ were it not for the dynamical heating from binaries in the core, whose supply of energy can prevent the collapse from continuing. Some globular clusters show evidence of a ‘cusp’ in surface brightness towards the centre, suggesting core collapse has occurred, whereas

¹Not to be confused with the same term referring to the process during a supernova

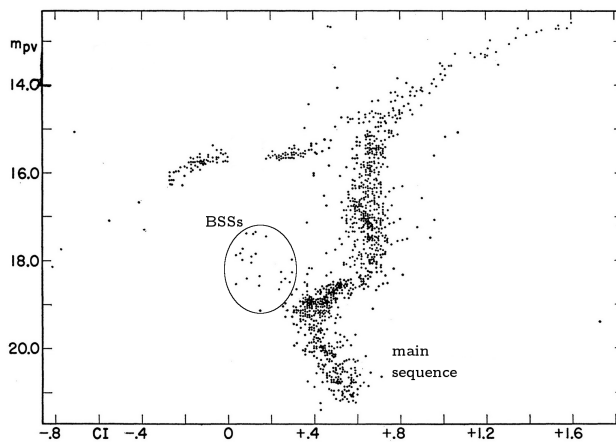


Figure 1.4: The first blue straggler stars (BSSs) discovered, found by Sandage in the globular cluster M3. [Adapted from Sandage, 1953]

others show a ‘core’ (flatter) distribution in brightness, suggesting they have not undergone core collapse.

Plotting the positions of the stars on a Hertzsprung-Russell (HR), or colour-magnitude, diagram shows that almost all the stars in globular clusters can be fit with an isochrone (a line of constant-age stellar models) through the ridge-line of the diagram. The position of the main-sequence turn-off of the isochrone gives an indication of the age of the cluster. However, a small number of globular cluster stars sit in the ‘blue’ region near the main sequence, above the turn-off (Figure 1.4).

Since they were found in M3 by Sandage (1953), these ‘blue straggler’ stars (BSSs) have posed a puzzle regarding their origin, and they have been discovered in other environments such as open clusters (Ahumada and Lapasset 2007) and the Milky Way bulge (Clarkson et al. 2011). Stars in these positions of the HR diagram should have left the main sequence and crossed the Hertzsprung gap had they formed at the same time as the rest of the stars in the cluster. BSSs therefore appear much younger than the rest of the cluster—yet these environments are nearly devoid of the gas required to build new stars. Instead, the two main channels proposed for the formation of BSSs are either the collision of two stars or the transfer of mass from one star to another in a binary system. The collision mechanism is expected to be more likely in the centre of globular clusters, where the stellar density is higher—particularly if the globular cluster has undergone core collapse.

Observations of globular clusters, such as the cluster Hodge 11 examined in this thesis, have placed the innermost BSSs and outermost BSSs at slightly offset positions on the HR diagram. This has been proposed as indicating different processes of BSS formation (for example, Li et al. 2013). Assuming a given BSS was formed from a collision, simulations of this process can be used to estimate a most likely collision

time. Doing this for a sample of the BSSs in the cluster allows us to test for consistency with a burst of formation that peaks at the cluster core collapse time. If the BSSs are collisional products, it is in principle possible to use this method to constrain the core collapse time of the cluster.

1.3 Methods used in this thesis

This thesis employs a variety of techniques to solve problems that are otherwise very complex or infeasible to solve analytically. Chapters 2 and 3 use the theory of shock front evolution (the Kompaneets approximation) to construct a more versatile numerical technique for solving the shock problem. The following, final two chapters employ codes within the Astrophysical Multipurpose Software Environment (AMUSE). Chapter 4 uses a smoothed-particle hydrodynamics code to model the problem of a supernova in a binary star system. Chapter 5 uses a combination of codes running with AMUSE to construct BSS models along with a code that performs a Markov Chain Monte Carlo study. We provide more detail in this section on all of these numerical techniques.

1.3.1 A new numerical shock solver

As we are interested in problems with density profiles that are no longer described by simple functions, analytic solutions to the differential equations for shock evolution using the Kompaneets approximation quickly become intractable. We therefore use this theoretical basis (outlined in Section 1.2.1) to develop a code that numerically solves for the evolution of shock fronts in any axisymmetric configuration of densities. The code uses the assumptions in the Kompaneets approximation by breaking the shock down into individual elements that are evolved along ‘flowlines’ in the gas, normal to the shock front. In particular, we will apply this code to explosions offset from a varying power-law gradient (and also with discontinuity resembling a torus with different density), all of which preserve the axisymmetry of the problem. Maintaining axisymmetry means the problem can be solved in two dimensions, as the properties of the shock (such as its total volume) can be found by rotation about the symmetry axis. This in turn entails rapid solutions for the shock evolution, allowing us to investigate a large sample of the parameter space of interest.

1.3.2 AMUSE

For the remaining problems investigated in this thesis, we employ a number of codes developed by the astrophysics community. Unifying these codes is the framework of AMUSE which is under active development in Leiden by a team lead by Simon Portegies Zwart. AMUSE provides an interface to codes covering a range of domains such as stellar evolution, hydrodynamics, gravitational (N -body) dynamics and radiative

transfer (often with multiple choices of codes for each domain). This enables complex astrophysical problems to be tackled by coupling codes across multiple domains, and allows ease of use of the codes with a unified python interface, which naturally handles units and physical constants. With AMUSE the final two chapters employ several codes, which we now turn to in more detail.

1.3.3 Smoothed-particle hydrodynamics

Distinct from grid-based hydrodynamics codes, which are typically Eulerian in construction (tracing a fluid by spatial coordinates), smoothed-particle hydrodynamics (SPH) codes are a particle-based Lagrangian formulation (tracing a fluid by mass). The fluid in SPH is broken down into (usually equal-mass) mass elements, each of which is assigned a ‘smoothing length’, h (where h is often determined by fixing the number of neighbour particles within h from a given particle). This gives the characteristic scale of the smoothing kernel.²

The smoothing kernel is used to calculate properties of the fluid, such as the density, pressure and pressure gradient, weighted across neighbouring particles by the kernel. The compact support of the kernel means that calculations are only performed on the N_{nb} neighbours within its support (an $\mathcal{O}(N_{\text{nb}}N) \sim \mathcal{O}(N)$ calculation) and not the whole particle set (which would be an $\mathcal{O}(N^2)$ calculation). Including self-gravity of the gas with direct N -body calculations would worsen the computation to $\mathcal{O}(N^2)$; instead, codes such as GADGET-2 (Springel 2005b) use a tree-based gravity calculation, which is dependent on the opening angle of the tree, but can improve the computational time to $\mathcal{O}(N \log N)$.

We use smoothed-particle hydrodynamics to investigate the effects of supernova on a close binary companion. As our problem involves the advection of gas in a vacuum (the stars in an orbit) as well as expansion of gas over a large range of radii (the supernova shell), this is naturally handled by the Lagrangian nature of SPH, without the restriction of bounding boxes common to grid codes.

1.3.4 Stellar structure and merger modelling

The coupled, non-linear differential equations of stellar structure do not have analytic solutions. As they must be solved numerically, a large number of stellar structure solvers have been developed over the past half-century. For our work, we use the stellar structure and evolution code MESA (Paxton et al. 2011). This solves the stellar structure equations under the conditions of local hydrostatic equilibrium using the Henyey method (Henyey et al. 1964), which assigns a one-dimensional Lagrangian mesh to

²In codes such as GADGET-2, which is used in this work, the kernels are cubic splines, although some recent codes have employed other kernels whose Fourier transforms do not go negative, which fixes a relatively benign ‘pairing instability’ seen with kernels like the cubic spline (Dehnen and Aly 2012).

the stellar interior. As opposed to finding structure solutions by iteratively performing explicit integrations from (for example) the stellar surface to the interior, the Henyey method performs iterative implicit integrations of the structure equations together with the equations of energy transport. The time evolution of the star is determined by nuclear reaction networks that change, at each time step, the composition (as well as, crucially, the opacity of the stellar material) and therefore the structure of the star. Stellar evolution models from MESA are used in the penultimate and final chapters of this thesis.

Stellar interactions can complicate the evolutionary picture considerably, and one of the most extreme interactions possible is the collision between two stars. One can simulate this process fully using hydrodynamical models of the stars, for example using the SPH technique described in the previous subsection. However, this process is computationally very expensive if many types of collisions need to be investigated. A general technique to calculate the structure of two merging stars has been developed by Gaburov et al. (2008) based on a technique first applied to low-mass stars by Lombardi et al. (1996). This implementation, in the form of the code Make-Me-A-Massive-Star (MMAMS), is motivated by Archimedes' principle for the buoyancy of fluid elements during a merger. The buoyancy of an element can be calculated from the entropy and composition of the fluid. The algorithm therefore uses a 'buoyancy' variable derived from the local specific entropy (which is conserved in adiabatic processes) to sort the fluid elements for the final stellar structure. This method has been validated against high-resolution hydrodynamic (SPH) simulations, and is much faster (converging in minutes) than the equivalent hydrodynamic simulations (which may take days to complete). We use both MESA and MMAMS in the current work to investigate the possible collisional origin of BSSs in a globular cluster in the final chapter.

1.3.5 Monte Carlo and MCMC methods

For calculations that are too difficult or complex for derivation from first principles, or to even fully simulate numerically, the Monte Carlo (MC) approach often offers a solution. Particularly useful for problems requiring statistical estimates, the MC method involves random sampling of input parameters to make estimates of the distribution of output parameters. One of the first MC computations to be performed was on an analogue computer designed by Enrico Fermi (the FERMIAC) to model neutron transport as a random process (Figure 1.5; Metropolis 1987).

Extending Monte Carlo techniques is the concept of a Markov Chain. This is a set of random variables that, at any given moment, has a transition probability to a future state that is independent of the past state of the chain—in a simplified sense, a Markov Chain is 'memoryless'. Markov Chain Monte Carlo (MCMC) methods are useful in sampling multidimensional distributions via random walks, which enable an estimation of (in a Bayesian picture) the posterior probability distribution. Over time, the density of the chain in the parameter space obtained by applying an MCMC

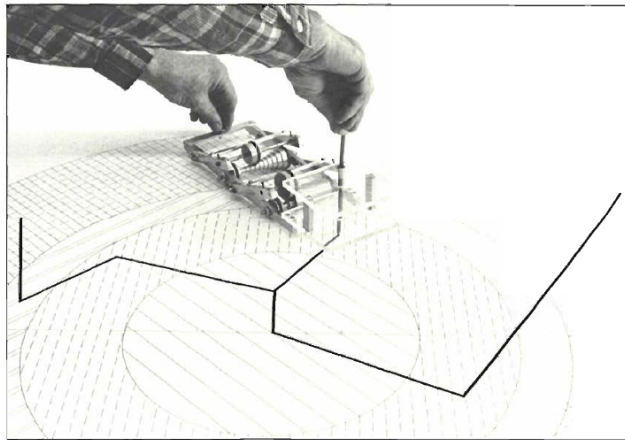


Figure 1.5: The FERMIAC analogue computer (the ‘Monte Carlo trolley’) in action. The paths of neutrons through a material were drawn on paper representations of different materials, where the drums on the trolley were set based on Monte Carlo choices of direction and distance traversed by fast or slow neutrons. [From Metropolis, 1987]

algorithm will represent the density of the posterior distribution.

One of the most common and intuitive MCMC algorithms, Metropolis–Hastings (Metropolis et al. 1953; Hastings 1970), evolves the chain from a given state by proposing a set of new values for the variables, and determining the resulting new posterior probability. If the new posterior is higher, the chain accepts the proposed values and transitions to the new state. If it is lower, the probability of the chain transitioning to the proposed position is proportional to the ratio of the new posterior to the current one (if the proposed step results in a low value, the chain is more likely to stay in its current position). In the code used in the last chapter, `emcee` (Foreman–Mackey et al. 2013), the Goodman–Weare algorithm (Goodman and Weare 2010) uses an ensemble of walkers in parameter space to construct the chain, where proposed values are made from linear extensions of the line connecting a given walker to another randomly selected walker.

For low-dimensional problems, MCMC methods can be compared with results from other optimisation methods such as χ^2 minimisation. We do such a comparison, with results from a grid of initial conditions, in the final chapter.

1.4 Content of this thesis

Much of the work in this thesis uses high-energy stellar phenomena as a tool to understand the nature, origin or evolution of their environments. The questions addressed inform the theory of supernova evolution, the nature of the environments near super-massive black holes and thus their influence on the galactic environment, as well as

the dynamical history of globular clusters. In addition to addressing these theoretical matters, much of this work is also devoted to making predictions and interpretations of data from current and next-generation observatories. Outlined below is the content of each of the following chapters.

In **Chapter 2**, we use the theory of the Kompaneets approximation for strong shocks in non-uniform media to create a novel code that solves the evolution of a shock in arbitrary axisymmetric density profiles. This shock solver was developed in particular to investigate SNR shock evolution near quiescent supermassive black holes, but the technique is general enough to be useful for a variety of astrophysical problems. In this chapter, we outline the theory behind this code, and provide examples of its use in predicting the lifetime of SNRs near quiescent supermassive black holes as well as the morphology of these SNRs over time.

We apply the above code in more detail to models of quiescent galactic nuclei in **Chapter 3**, where we outline ‘autarkic’ or self-similar dependences of properties of the gas and stellar population on the SMBH mass. We additionally add a dense molecular torus, as observed in our own galaxy, to the density profiles to investigate the effect of its presence. We estimate the total number of core-collapse SNRs surviving around SMBHs based on the lifetimes found from our code, for supernovae exploding in the sphere of influence of a large range of SMBH masses. We predict the temperature evolution, as well as the total emission in hard and soft X-ray bands, from core-collapse supernovae that exploded in the sphere of influence of such SMBHs. We compare with other sources of X-ray emission and estimate the detectability of this contribution and potential for contamination in searches of quiescent SMBHs. We also comment on the implications for inferring the star-formation rate from the X-ray emission of the SNR component.

In **Chapter 4**, we model for the first time the explosion of a stripped core-collapse supernova from the moments after core bounce using stellar structure models of the progenitor and companion stars. The simulations are performed in AMUSE using the smoothed-particle hydrodynamics code GADGET-2. We use our simulations to estimate the amount of mass stripped from the companion star and the velocity imparted to the companion by the ejecta impact. These results can be used to calibrate theoretical predictions of the final binary parameters—or the runaway velocities of stars that originate from binaries disrupted by the supernova. These predictions are also important in understanding the potential for binary-disrupted runaway stars to contaminate the low-velocity population of hypervelocity stars (stars unbound from the galaxy).

The work in **Chapter 5** employs the codes MESA and MMAMS in AMUSE to produce BSSs formed from the collision of two stars born at the formation of the globular cluster Hodge 11. We generate a grid of these models over the two initial masses and collision time, and convert the final BSS model to magnitudes in the *Hubble Space Telescope* (HST) bands used to observe Hodge 11 by integrating the best-fit synthetic spectra from the BaSeL database. We additionally use the MCMC code emcee with our stellar modelling to estimate the initial conditions, starting from the observed HST

magnitudes. We show general agreement between the two approaches, and comment on the implications of the collision times found for the BSSs. This correspondence of the MCMC code with the grid approach also suggests it can be used for higher-dimensional parameter searches for similar problems. By predicting the collision time of BSS progenitors, we can use the method developed here to predict the core-collapse time of the globular cluster, and therefore shed light on the evolutionary history of globular clusters.

1.5 Outlook

The ideas and tools presented here can be extended in a number of ways to continue addressing the questions outlined in Section 1.4.

In Chapter 2, we develop a numerical solver for shock fronts in order to predict the fate of SNRs from supernovae that explode near quiescent SMBHs. Although created to answer this specific question, this code was constructed in a manner to allow it to be as generally applicable as possible, and can therefore be used with any axisymmetric density profile. This lends itself to use for other problems involving shocks in the ISM. A natural development would be to extend the code to three dimensions; although this would be more computationally expensive, it would remove any constraints on the form of the ambient medium.

In Chapter 3, we make predictions of the X-ray emission from young core-collapse SNRs near quiescent SMBHs. These predictions suggest this emission is right at the cusp of detectability in many cases given current instruments. However, it is clear that this X-ray component should be considered as a possible contaminant in future X-ray searches for quiescent SMBHs. Next-generation X-ray telescopes such as ATHENA, with higher sensitivity, will help to constrain these predictions, and our work can then be used to infer in more detail the nature of SMBH environments. We show that, if SNRs can be observed near other quiescent SMBHs, their presence can also be used to give an indirect measurement of the local star-formation rate. Furthermore, in the Milky Way, a clear application of our code would be a more comprehensive investigation of the possible origins and age of the Sgr A East SNR.

In Chapter 4, we predict the effects on a companion star to a Type Ibc supernova. The flexibility of AMUSE allows us to easily modify this code to answer a number of other questions. Most immediately, different types of progenitors (such as ultra-stripped primaries) or companions (sub-solar or giants) are readily added with different stellar evolution models. It is also possible to easily incorporate other components to this model to study the effects of a supernova on them, such as circumbinary planets. The predictions from this work can be used to better determine the properties of runaway stars from supernova-disrupted binaries that may appear in searches for hypervelocity stars, such as with the recently launched *Gaia* mission.

In Chapter 5, we propose a method for estimating the collision time of stars that form BSSs in globular clusters, and apply this to observations of Hodge 11 in the

Large Magellanic Cloud. Our work shows that this method can be a powerful tool in inferring the dynamical history of clusters, such as the core-collapse time. This method may also be applied to other environments where BSSs are observed, such as in the galactic centre, to shed light on the formation history of the stellar component. The confirmation of effectiveness of the MCMC approach indicates it can be used for similar questions involving a larger number of free parameters, such as the merger of stars with different metallicities or birth ages, or multiple stellar collisions.

2 The fate of supernova remnants near quiescent supermassive black holes

A. Rimoldi, E. M. Rossi, T. Piran, S. F. Portegies Zwart
Monthly Notices of the Royal Astronomical Society, 447, 1 (2015)

There is mounting observational evidence that most galactic nuclei host both supermassive black holes (SMBHs) and young populations of stars. With an abundance of massive stars, core-collapse supernovae are expected in SMBH spheres of influence. We develop a novel numerical method, based on the Kompaneets approximation, to trace supernova remnant (SNR) evolution in these hostile environments, where radial gas gradients and SMBH tides are present. We trace the adiabatic evolution of the SNR shock until 50% of the remnant is either in the radiative phase or is slowed down below the SMBH Keplerian velocity and is sheared apart. In this way, we obtain shapes and lifetimes of SNRs as a function of the explosion distance from the SMBH, the gas density profile and the SMBH mass. As an application, we focus here exclusively on quiescent SMBHs, because their light may not hamper detections of SNRs and because we can take advantage of the unsurpassed detailed observations of our Galactic Centre. Assuming that properties such as gas and stellar content scale appropriately with the SMBH mass, we study SNR evolution around other quiescent SMBHs. We find that, for SMBH masses over $\sim 10^7 M_{\odot}$, tidal disruption of SNRs can occur at less than 10^4 yr, leading to a shortened X-ray emitting adiabatic phase, and to no radiative phase. On the other hand, only modest disruption is expected in our Galactic Centre for SNRs in their X-ray stage. This is in accordance with estimates of the lifetime of the Sgr A East SNR, which leads us to expect one supernova per 10^4 yr in the sphere of influence of Sgr A*.

2.1 Introduction

There is compelling evidence for a supermassive black hole (SMBH) with a mass of $4.3 \times 10^6 M_{\odot}$ in the nucleus of the Milky Way, associated with the Sgr A* radio source. The strongest evidence comes from the analysis of orbits of the so-called ‘S-stars’ very near this compact object, such as that of the star S2 with a period of only 16 yr and pericentre of $\sim 10^2$ au (Schödel et al. 2002, 2003; Ghez et al. 2003; Eisenhauer et al. 2005; Ghez et al. 2008; Gillessen et al. 2009).

Most other massive galaxies contain SMBHs (Marleau et al. 2013), some with masses as high as $10^{10} M_{\odot}$ (McConnell et al. 2011). The observed fraction of active nuclei is no more than a few per cent at low redshifts (Schawinski et al. 2010), and most galactic nuclei house very sub-Eddington SMBHs, like Sgr A* (Melia and Falcke 2001; Alexander 2005; Genzel et al. 2010). These SMBHs are believed to be surrounded by radiatively inefficient accretion flows (RIAFs), where only a small fraction of the accretion energy is carried away by radiation (Ichimaru 1977; Rees et al. 1982; Narayan and Yi 1994).

In addition to the ubiquity of SMBHs, young stellar populations and appreciable star formation rates are common in many quiescent galactic nuclei (Sarzi et al. 2005; Walcher et al. 2006; Schruba et al. 2011; Kennicutt and Evans 2012; Neumayer and Walcher 2012).¹ This is seen most clearly in the abundance of early-type stars in the central parsec of the Milky Way (see Do et al. 2013b,a; Lu et al. 2013, for some recent reviews). Moreover, it appears that star formation in the Galactic Centre region has been a persistent process that has increased over the past 10^8 yr (Figer et al. 2004; Figer 2009; Pfuhl et al. 2011). Over that time, an estimated $\gtrsim 3 \times 10^5 M_{\odot}$ of stars have formed within 2.5 pc of the SMBH (Blum et al. 2003; Pfuhl et al. 2011).

Continuous star formation in galactic nuclei will regularly replenish the supply of massive stars in these regions. This naturally leads to the expectation of frequent core-collapse supernovae in such environments. As an example, Zubovas et al. (2013) show that, per $10^6 M_{\odot}$ of stellar mass formed in the Galactic Centre, approximately one supernova per 10^4 yr is expected for the past 10^8 yr.

Only one supernova remnant (SNR) candidate has been identified close to the SMBH sphere of influence (SOI): an elongated shell known as Sgr A East, at the end of its adiabatic phase. It has an estimated age of about 10^4 yr and appears to be engulfing Sgr A* with a mean radius of approximately 5 pc (Maeda et al. 2002; Herrnstein and Ho 2005; Lee et al. 2006; Tsuboi et al. 2009). In addition, there are a couple of observations that indirectly point towards supernovae in the SOI. The first is CXOGC J174545.5–285829 (‘The Cannonball’), suspected to be a runaway neutron star associated with the same supernova explosion as Sgr A East (Park et al. 2005; Nynka et al. 2013; Zhao et al. 2013). The second is the recently discovered magnetar SGR J1745–2900, estimated to be within 2 pc of Sgr A* (Degenaar et al. 2013; Kennea

¹Evidence for recent star formation has also been seen around active galactic nuclei (AGN; for example, Davies et al. 2007). However, active nuclei are not the subject of this study.

et al. 2013; Rea et al. 2013).

Any supernova exploding in the SOI of a quiescent SMBH will expand into a gaseous environment constituted mainly by the SMBH accretion flow, whose gas is supplied by the winds from massive stars. The density distribution within the flow is therefore set by both the number and distribution of young stars and the hydrodynamical properties of a radiatively inefficient accretion regime. This interplay gives an overall density distribution that is a broken power law, for which the break occurs where the number density of stellar wind sources drops off. For the Galactic Centre, this corresponds to ~ 0.4 pc (for example, Quataert 2004).

In such environments, we expect SNRs to evolve differently from those in the typically flat interstellar medium, away from the SMBH. The density gradients have the potential to distort SNRs and decelerate them significantly. Once the expansion velocity falls below the SMBH velocity field, the remnant will be tidally sheared and eventually torn apart. This can substantially shorten an SNR lifetime compared to that in a constant-density interstellar environment. In turn, this can reduce the expected number of observed SNRs in galactic nuclei.

Since quiescent accretion flows are fed by stellar winds, which can be also partially recycled to form new stars together with the gas released by supernova explosions, the scenario we consider is of a self-regulating environment, where young stars and gas (or, in other words, star formation and accretion on to the SMBH) are intimately related. This holds until a violent event—for example, a merger—drives abundant stars and gas from larger scales to the galactic nucleus. Observations and modelling of our Galactic Centre support this picture. In particular, winds from massive stars are sufficient to account for the observed accretion luminosity and external gas feeding is not required (e.g. Quataert 2004; Cuadra et al. 2006) or observed. Furthermore, there is strong evidence for the recent star formation occurring in situ (Paumard et al. 2006).

In this chapter, we determine the morphology and X-ray lifetimes of SNRs, which, in turn, can be used to constrain the environment of SMBHs. We develop a numerical method to trace SNR evolution and determine their X-ray lifetime. The influence of the SMBH on SNRs will be considered first indirectly, through its influence on the gaseous environment, and then directly, through its tidal shear of the ejecta.

The chapter is organized as follows. Section 2.2 introduces the gaseous environments found around quiescent SMBHs. Section 2.3 uses analytic methods to qualitatively trace SNR evolution. Section 2.4 describes our numerical method, which allows us to follow the evolution of an SNR in an arbitrary axially symmetric gas distribution. We then specialize it to a quiescent SMBH environment. Section 2.5 outlines the galactic models used for the environments of the supernova simulations. Section 2.6 presents our results for SNR shapes and lifetimes. Our concluding remarks are found in Section 2.7.

2.2 Gaseous environments of quiescent nuclei

In this section, we outline the expected gas distributions near the SMBH in quiescent galactic nuclei. These gas distributions will be used as the environment for the SNR model explicated in Sections 2.3 and 2.4. We will then proceed to scale the general environment discussed here for the Galactic Centre to other SMBHs in Section 2.5.

Quiescent SMBHs are surrounded by RIAFs, which are the environments in which the SNR will evolve. RIAFs are relatively thick, for which the scale-height, H , is comparable to the radial distance, R , from the SMBH ($H/R \approx 1$). The mechanisms of energy transport within the flow vary depending on the model, and these variations affect the power-law gradient in density near the SMBH. Advection-dominated accretion flow (ADAF) models assume that much of the energy is contained in the ionic component of a two-temperature plasma. As the ions are much less efficient radiators than electrons, energy is advected into the SMBH by the ions before it can be lost via radiation (Narayan et al. 1995; Narayan and Yi 1995). Additionally, convection-dominated accretion flow (CDAF) models rely on the transport of energy outward via convective motions in the gas (Quataert and Gruzinov 2000; Ball et al. 2001). Finally, the adiabatic inflow–outflow model (ADIOS; Blandford and Begelman 1999, 2004; Begelman 2012) accounts for winds from the flow that expel hot gas before it is accreted.

For the region near the SMBH, predicted exponents, ω_{in} , of the power law in gas density, ρ , lie in the range of $\omega_{\text{in}} = 1/2$ to $3/2$. The lower and upper limits of ω_{in} are derived from the predictions of the CDAF/ADIOS and ADAF models, respectively. A drop-off in stellar number density at a radius $R = R_{\text{b}}$ from the SMBH would cause a break in the mass density, ρ , at the same radius, since it is the winds from these stars that feed the accretion flow.

The best example of a RIAF is that surrounding Sgr A*. It has been extensively studied theoretically and observationally and will constitute our prototype. A density distribution from the one-dimensional analytic model of wind sources has approximately a broken power-law shape with $\omega_{\text{in}} = 1$ inside the density break and $\omega_{\text{out}} = 3$ outside (Quataert 2004). Simulations of stellar wind accretion show comparable density profiles (Cuadra et al. 2006). Furthermore, the value of $\omega_{\text{in}} = 1$ is consistent with GRMHD accretion simulations (for example, McKinney et al. 2012). Recent observations using long integrations in X-ray suggest that a gradient of $\omega_{\text{in}} \approx 1/2$ may provide a better fit to the inner accretion flow of Sgr A* (Wang et al. 2013).

We can therefore, generally describe the ambient medium of a quiescent SOI with a broken power law for the density of the form:

$$\rho(R) = \begin{cases} \rho_0 \left(\frac{R}{R_0}\right)^{-\omega_{\text{in}}} & R \leq R_{\text{b}} \\ \rho_{\text{b}} \left(\frac{R}{R_{\text{b}}}\right)^{-\omega_{\text{out}}} & R > R_{\text{b}}, \end{cases} \quad (2.1)$$

for $\omega_{\text{in}} \in \{1/2, 1, 3/2\}$, $\omega_{\text{out}} = 3$, using a reference point for the density at $R = R_0$ away from the SMBH.

The strongest observational constraint on the density around Sgr A* is given by *Chandra* X-ray measurements at the scale of the Bondi radius ($R_0 \approx 0.04$ pc) of $n_0 \approx 130 \text{ cm}^{-3}$ ($\rho_0 \approx 2.2 \times 10^{-22} \text{ g cm}^{-3}$; Baganoff et al. 2003). The accretion rate closer to the SMBH can be further constrained by Faraday rotation measurements, though the relative error is large (Marrone et al. 2007). Indeed, we find that fixing the density at 0.04 pc and varying ω_{in} between 1/2 and 3/2 produces a range of densities at small radii that fall within the uncertainty in the density inferred from Faraday rotation. The radius for the break in stellar number density and gas density in the Milky Way is taken to be $R_b = 0.4$ pc.

2.3 Evolution of remnants around quiescent black holes: analytic foundations

Here, we outline the physics describing the early stages of SNR evolution that are of interest in this work. The theory described in this section will be used as the foundation of a general numerical method to solve the problem, outlined in Section 2.4. At this point, we do not directly take into account the gravitational force of the SMBH, but instead just the gaseous environment. The gravity of the SMBH can be ignored when the expansion velocity of the SNR is much larger than the Keplerian velocity around the SMBH. For example, around Sgr A*, at a velocity of 10^4 km s^{-1} gravity can be ignored for radii larger than $\sim 10^{-4}$ pc. The gravitational field of the SMBH will be accounted for later, when we consider tidal effects on the expanding remnant, which are important only once the remnant has slowed down significantly.

A supernova explosion drives a strong shock into the surrounding gas at approximately the radial velocity of the ejected debris. Typically, it is assumed that a significant amount of the ejecta is contained within a shell just behind the shock front (for example, Koo and McKee 1990). As it expands, the shock sweeps up further mass from the surrounding medium. By momentum conservation, the combined mass of the fraction of ejecta behind the shock front (M_{ej}) plus the swept-up gas (M_{s}) must decelerate. The deceleration is considered to be appreciable when the swept-up mass becomes comparable to that of the debris, and therefore this ejecta-dominated phase holds for $M_{\text{s}} \ll M_{\text{ej}}$.

The subsequent adiabatic expansion of the shock front is modelled with the assumption that losses of energy internal to the remnant are negligible. For this decelerating regime, the Rankine–Hugoniot strong-shock jump conditions can yield exact similarity (length scale-independent) solutions for the kinematics of the shock front. The evolution is determined by its energy, E , and the ambient density, ρ (McKee and Truelove 1995). In all of this work, we use a canonical value of 10^{51} erg for the explosion energy. In a uniform ambient medium, the adiabatic stage is classically

modelled using the spherically symmetric Sedov–Taylor solution (Taylor 1950; Sedov 1959). This has self-similar forms for the spherical radius and speed of the SNR of $R' \propto (E/\rho)^{1/5} t^{2/5}$ and $v \propto (E/\rho)^{1/5} t^{-3/5}$, respectively, where R' is measured from the explosion site.

Following the initial work by Sedov and Taylor, Kompaneets (1960) developed a non-linear equation from the jump conditions that allows self-similar solutions for the shock front evolution in certain density stratifications. The original work by Kompaneets considered an atmosphere with exponential stratification, but many other solutions have since been obtained (see the review by Bisnovaty-Kogan and Silich 1995, as well as Bannikova et al. 2012 and the references therein). Of particular relevance to the gas distributions in galactic nuclei, Korycansky (1992)—hereafter, K92—showed that, with a specific coordinate transformation, a circular solution to the Kompaneets equation can be obtained for explosions offset from the origin of a power-law density profile, $R^{-\omega}$ (for $\omega \neq 2$).

The early ejecta-dominated and late adiabatic stages are well characterized by the purely analytic solutions for each stage. In between, the solution asymptotically transitions between these two limits (this is known as ‘intermediate-asymptotic’ behaviour; Truelove and McKee 1999).² The late evolution of the remnant, the radiative stage, occurs when the temperature behind the shock drops to the point at which there is an appreciable number of bound electrons. Consequently, line cooling becomes effective, the radiative loss of energy is no longer negligible, and the speed of the shock will drop at a faster rate. For SNRs in a constant density of $n \approx 1 \text{ cm}^{-3}$, the radiative phase begins at approximately $3 \times 10^4 \text{ yr}$ (Blondin et al. 1998). We do not model the remnant during this phase, but we will estimate the onset of the transition to the radiative stage.

In the present work, we model SNRs over the first two (ejecta-dominated and adiabatically expanding) stages of evolution in a range of galactic nuclear environments. The evolution begins with a spherically expanding shock, and therefore we do not consider any intrinsic asymmetries in the supernova explosion itself. Collectively, any possible intrinsic asymmetries in SNRs are not expected to be in a preferential direction, and so they should not bias the generalized results presented here.

The overall geometry of this analysis is laid out in Fig. 2.1, which indicates the main coordinates, distance scales and density distributions. The explosion point is at a distance $R = a$, measured from the SMBH (the origin of our coordinate system). The shock front extends to radial distances R' , measured from the explosion point. Each point along the shock is at an angle ψ , measured from the axis of symmetry about the explosion point. The initial angle made with the axis of symmetry of each point on the shock, at $t \rightarrow 0$, is denoted ψ_0 .

²For an illustration of this transition, see fig. 2 of Truelove and McKee (1999).

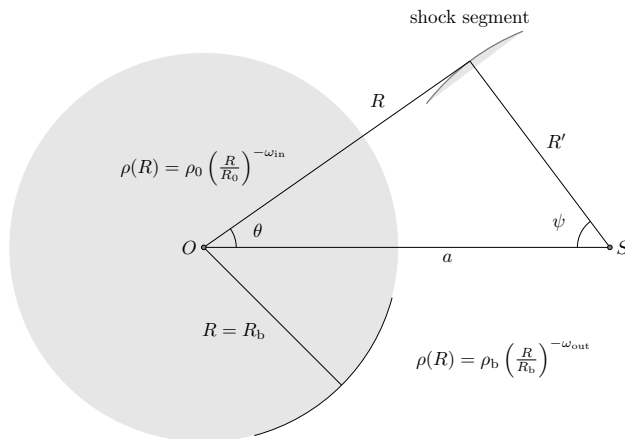


Figure 2.1: Basic geometry of the problem. The supernova occurs at a point S , a distance $R = a$ away from the SMBH, which is located at the origin, O . The shock front extends to distances measured radially from the explosion point S by the coordinate R' . The angle made by a point on the shock, measured from the $\theta = 0$ axis about the explosion point, is denoted ψ . Each point on the shock has an initial angle $\psi(t \rightarrow 0) \equiv \psi_0$. The entire density distribution $\rho(R)$ can be characterized by: the choice of the inner gradient ω_{in} (defining the density within the shaded circle), the outer gradient ω_{out} , the reference density ρ_0 (at a reference radius R_0), and a break at R_b between the gradients ω_{in} and ω_{out} .

2.3.1 End of the ejecta-dominated stage

In order to estimate where the shock front kinematics appreciably deviate from the ejecta-dominated solution, we integrate the background density field along spherical volume elements swept out by the expanding remnant. This provides an estimate of the mass swept up from the environment, M_s . The ejecta-dominated solution is taken to end when M_s is equal to some specified portion of the ejecta mass, M_{ej} . We use a canonical value of $1M_{\odot}$ for this fraction of ejecta mass. The distance from the explosion point (along the coordinate R') at which this occurs is denoted the ‘deceleration length’, L , here (it also known as the ‘Sedov Length’ in the standard treatment of SNRs in a uniform ρ).

Since our density profiles are not uniform, different directions of expanding ejecta will sweep up mass at different rates. In general, we must consider a solution for L that depends on ψ_0 , the initial angle of each surface element of the shock with respect to the axis of symmetry (see Fig. 2.1). We therefore determine the value of $L(\psi_0)$ corresponding to small surface elements of the shock front. When the explosion occurs close to the SMBH, the solution is expected to converge to that of an integral over a sphere, due to the spherical symmetry of the background density.³ Therefore, as a

³The three-dimensional volume integrals (of an offset sphere) over a singular density converge for the shallow power laws used here: $1/2 \leq \omega_{\text{in}} \leq 3/2$ for $\rho \propto R^{-\omega_{\text{in}}}$.

reference, we also find the radius L of the sphere whose volume encloses $M_s \approx M_{\text{ej}}$.

The explosion occurs at a distance $R = a$ from the origin. For a single power-law stratification, we use the explosion point for the reference density, $\rho_0 = \rho(a) \equiv \rho_a$, such that

$$\rho(R) = \rho_a \left(\frac{R}{a} \right)^{-\omega}. \quad (2.2)$$

We consider a small surface element of the SNR at an angle ψ_0 over an infinitesimal solid angle. In a single power-law stratification with the form of equation (2.2), the length $L(\psi_0)$ can be estimated from the mass integrated through R' at a given angle ψ_0 :

$$\rho_a a^\omega \int_0^{L(\psi_0)} R^{-\omega} R'^2 dR' = M_{\text{ej}}. \quad (2.3)$$

Note that we are integrating over the coordinate R' that extends radially from the explosion point, but that the density varies radially with the coordinate R as measured from the SMBH. For integrals over a broken power-law density, the density break adds complications to the integrals analogous to equation (2.3). The solutions are discussed further in Appendix 2.A.

These methods for estimating the deceleration length provide a means for testing the level of asymmetry and distance scales in the ejecta-dominated stage of evolution, and will be further discussed in Section 2.6.1, where we show results.

2.3.2 Deceleration in the adiabatic stage

We use the Kompaneets (1960) approximation alongside the coordinate transformation identified by K92 to follow the adiabatic deceleration of the shock front in a single power-law density profile. The assumptions and main equations of this prescription will also be used in our full numerical treatment for arbitrary density profiles (Section 2.4). We shall give here the analytic solutions for $\omega = 1$ and 3. These solutions will be used to validate our numerical treatment (Section 2.4). They also give an indication of the shock behaviour in a broken power-law density profile, when it expands fully interior or fully exterior to the density break.

The Kompaneets approximation involves setting the post-shock⁴ pressure, P' , to be uniform throughout the shock volume and equal to (some fraction, λ , of) the mean interior energy density. For an arbitrary volume V ,

$$P' = \frac{(\gamma - 1) \lambda E}{V}, \quad (2.4)$$

wherein the Kompaneets approximation proper is to take λ to be constant. The ratio of specific heats is taken to be $\gamma = 5/3$ both internal and external to the shock.

⁴For thermodynamic variables, we use primes ($'$) to indicate the post-shock values (the values behind the shock front).

Two additional assumptions in the treatment are that the directions of the local velocity vectors along the shock front are normal to the shock front, and that the magnitude of the velocity is determined by taking the post-shock pressure to be equal to that of the ram pressure of the environment (ρv_s^2 , where ρ is the density of the unshocked gas) at that point (K92):

$$v_s(R, t) = \sqrt{\frac{(\gamma^2 - 1) \lambda E}{2\rho(R) V(t)}}. \quad (2.5)$$

Following the coordinate transformation of K92, the ‘time’ is parametrized by y (which actually has a dimension of length) via

$$dy = \sqrt{\frac{(\gamma^2 - 1) \lambda E}{2\rho_0 V(y)}} dt, \quad (2.6)$$

as well as the dimensionless parameter $x = |2 - \omega| y / (2a) \equiv y/y_c$. The parameter x is, therefore, equal to y scaled with respect to a critical value y_c , which is when the shock either reaches the origin ($\omega = 1$) or ‘blows out’ to infinity ($\omega = 3$). Therefore, x (like y) can be considered to represent the ‘time’ in this transformation. The constant $\lambda \approx 1$ is given by the difference in pressure behind the shock front relative to the average pressure internal to the remnant, and in a power-law profile is (Shapiro 1979)

$$\lambda = \frac{(17 - 4\omega) / 9}{1 - (9 - 2\omega)^{-(17-4\omega)/12-3\omega}}. \quad (2.7)$$

In an ambient density with a single power-law form of equation (2.2), the K92 transformation gives a self-similar solution to the Kompaneets equation (see equations⁵ 10 and 11 of K92) for an explosion at $R = a$ (see Fig. 2.1):

$$\left(\frac{R}{a}\right)^{2\alpha} - 2\left(\frac{R}{a}\right)^\alpha \cos(\alpha\theta) - x^2 + 1 = 0, \quad (2.8)$$

for the polar coordinates R and θ , where $\alpha \equiv (2 - \omega) / 2$. This can be identified as a circular solution for a given x in the two variables $(R/a)^\alpha$ and $\alpha\theta$. Analytic solutions for the volume, time and velocity in $\omega = 1$ and 3 densities are presented in Appendix 2.A.

The equations describing the shock front can alternatively be parametrized by ψ_0 , the initial angle of a point on the shock with respect to the axis of symmetry. The subsequent equations of motion for a given ψ_0 describe the paths of flowlines in the shock in terms of the polar coordinates measured from the SMBH (K92):

$$R = a (1 + 2x \cos \psi_0 + x^2)^{1/(2\alpha)}, \quad (2.9)$$

$$\theta = \frac{1}{|\alpha|} \arctan\left(\frac{x \sin \psi_0}{1 + x \cos \psi_0}\right). \quad (2.10)$$

⁵Note that there are two sign errors in the exponents of equation 11 in K92.

This flowline-based treatment is a useful context for the numerical approach to the shock evolution presented in Section 2.4.1, and these equations will be used to compare with the numerical results.

2.3.3 Intermediate-asymptotic transition

The Kompaneets solution for the velocity diverges for $x \rightarrow 0$, given that the volume $V(x) \rightarrow 0$. In this limit, the energy density and, therefore, also the velocity, tend to infinity. The solution is, however, not intended to describe the initial evolutionary stage of the remnant. In order for the numerical treatment to correctly follow the SNR evolution, we must account for the initial coasting stage. A full analytic joining of the intermediate-asymptotic solutions between the ejecta-dominated and adiabatic stages is complex, even for an $\omega = 0$ ambient medium (see, for example, Truelove and McKee 1999).

As a model for this intermediate behaviour, we employ an effective density (mass) term to the solution that gives a transition between the expected solutions. The density of the medium is modified to:

$$\rho_{\text{eff}} \equiv \rho(R) + \frac{M_{\text{ej}}}{V}, \quad (2.11)$$

where the additional effective term counters the divergent behaviour of the velocity at small volumes. This has the desired property that when the volume is large $\rho \rightarrow \rho(R)$ in the standard Kompaneets approximation, while at small volumes the second term dominates to provide the initial coasting phase of the remnant. With this effective mass term, the SNR leaves the ejecta-dominated phase around the point at which the mass swept up from the environment is comparable to the initial mass behind the shock.

2.3.4 Transition to the radiative stage

As the shock slows, the late evolution of a typical SNR is marked by an increase in radiative losses. Although we will not model this stage, we intend to check the time-scales over which SNRs will reach this stage in quiescent nuclei (if they survive sufficiently long).

Typically, cooling functions show a marked increase in thermal radiation once the gas temperature drops to $\sim 10^6$ K (for example, Schure et al. 2009). This occurs due to the formation of a sufficient number of electrons bound to ions to allow for effective line cooling. Once regions of gas behind the shock drop to this temperature, the deceleration of the SNR becomes more pronounced. By calculating the temperature behind the shock we can determine the time at which parts of the remnant begin to cool more effectively.

It is possible to determine the temperature of the shocked gas via the ideal gas law,

$$P' = \frac{k_B \rho' T'}{m_u \mu} \quad (2.12)$$

(where, again, we denote post-shock values with primes, k_B is Boltzmann's constant, m_u is the atomic mass unit and μ is the mean molecular mass), as well as the jump conditions for the (post-shock) density and pressure,

$$\rho' = \rho \frac{\gamma + 1}{\gamma - 1} \quad \text{and} \quad P' = \frac{2\rho v_s^2}{\gamma + 1}. \quad (2.13)$$

For $\gamma = 5/3$,

$$T' = \frac{2(\gamma - 1)m_u \mu}{(\gamma + 1)^2 k_B} v_s^2 = \frac{3m_u \mu}{16k_B} v_s^2, \quad (2.14)$$

and the post-shock temperature is found to be $T' \approx 10^6$ K for $v_s \approx 300$ km s⁻¹. Therefore, if we monitor each point along the shock for the time at which the velocity drops below this value, we may estimate the time at which radiative processes become significant.

As the cooling function is also dependent on ρ , for a given temperature the rate of cooling is also expected to be amplified in regions of post-shock material with higher density. However, by the time that SNRs are radiative, they have survived the expansion past the SMBH and entered into the more uniform density beyond the SOI, such that the ambient density is similar across all points of the shock. At this stage, the SNRs are reasonably symmetric around the SMBH and the velocity is similar across all of the shock front, so that most of the SNR reaches the radiative stage at similar times. If the SNR survives expansion past the SMBH, this late evolution is largely uninfluenced by the details of any early interactions near the SMBH.⁶

2.4 Evolution of remnants around quiescent black holes: numerical treatment

Purely analytic solutions for the shock front evolution via the Kompaneets equation are not feasible for many density configurations. Therefore, we developed a numerical method that solves for the evolution of a shock front using the physical assumptions of the Kompaneets approximation described in Section 2.3.

The primary assumptions that must be encompassed by the method culminate in constraints on the velocity. Namely, the direction of the velocity of any point must be perpendicular to the shock front, and the magnitude of the velocity must be determined by the energy density behind the shock and local ambient density as prescribed in equation (2.5).

⁶For a detailed consideration of the radiative transition in power-law media, see Petruk (2005).

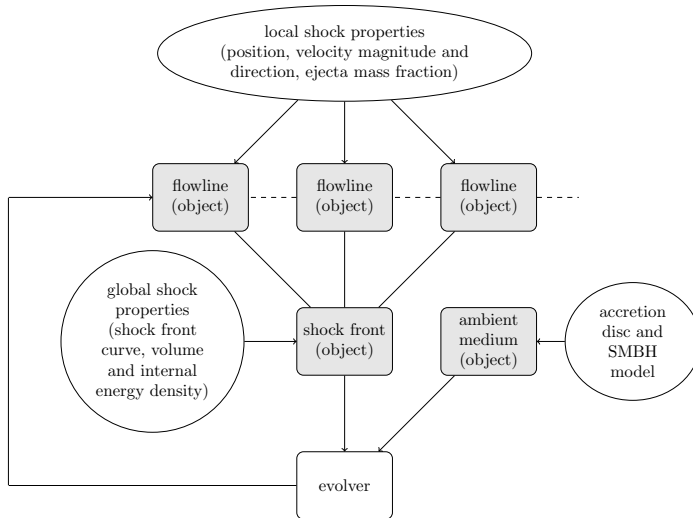


Figure 2.2: The basic numerical scheme, as described in Section 2.4.1. Shaded boxes show the basic types of objects in the numerical construction. The choice of the number of flowlines determines the resolution, and only a few are shown here schematically. The flowlines track local physical properties of the shock (velocity and ejecta mass fraction). Collectively, they define the location of the shock front, with global physical properties such as its energy density, determined by the volume. Along with the environment (most importantly, the background mass density), the global shock properties determine the evolution of all the individual flowlines in the subsequent time step.

2.4.1 General prescription

The numerical treatment follows an approach by which the shock is described by the evolution of flowlines through the background gas. The flowlines are the paths followed by tracer ‘particles’ (points) distributed along the shock front, analogous to the analytic treatment with the ψ_0 parameter of equations (2.9) and (2.10).

Fig. 2.2 shows a schematic of the approach. The initial (spherical) state of the shock is broken down into flowlines characterized by their angle ψ_0 . During the evolution, the number of flowlines is dynamic. To keep a reasonable resolution of the shock front, new flowlines can be inserted, with mean properties of adjacent flowlines, if the distance between two points on the shock is over a defined threshold. For our simulations, a threshold of the order of 0.05 pc has proven sufficient to describe a smooth shock front evolution on Milky Way-like scales. Flowlines may also be deleted in regions where parts of the shock front are colliding. The background gas prescribes the evolution of the shock, but the behaviour of the post-shock gas is not tracked, and thus the background gas can be treated as being independent of the shock.

The kinematics of the shock front are determined by the velocity vectors at each flowline. To determine the magnitude of the velocity, we use the jump conditions across the shock, and for those we need the energy density within the shocked volume

(which is assumed to be a constant within this volume) as well as the local mass density in the environment (see equations 2.5 and 2.11.⁷ This stage of evolution is adiabatic, and so given an initial explosion energy we therefore calculate the energy density using the instantaneous volume enveloped by the shock front.

In an axisymmetric arrangement of gas density and explosion point, calculation of the volume is simplified by the geometrical symmetry; it is determined by a solid of rotation of the area of a two-dimensional slice about this axis. Any arbitrary ordered set of points (x_i, y_i) can specify the location of the shock front. Given these two-dimensional coordinates, the volume, by the second theorem of Pappus, is equal to the product of the area of the non-intersecting polygon defined by these coordinates and the distance travelled by its centroid under rotation about the symmetry axis (Kern and Bland 1948). Using the fact that the components of the centroid, $C = (C_x, C_y)$, of a polygon are given by

$$C_\xi = \frac{1}{6A} \sum_{i=1}^{n-1} (\xi_i + \xi_{i+1}) (x_i y_{i+1} - x_{i+1} y_i) \quad (2.15)$$

for $\xi \in \{x, y\}$, the volume of the SNR can be determined from

$$V = \frac{\pi}{3} \sum_{i=1}^{n-1} (y_i + y_{i+1}) (x_i y_{i+1} - x_{i+1} y_i). \quad (2.16)$$

With the magnitude of the velocity known, each point on the shock evolves by determining the unit vector for the velocity that is perpendicular to its neighbouring points. The position is then linearly translated over a small time step using the velocity vector.

We assign an ejecta mass element to each flowline. Fig. 2.3 shows a schematic of this implementation. Due to rotational symmetry, each point on the shock at $t \rightarrow 0$ represents a ring segment of the SNR in three dimensions. We assign a thickness to each of these ring segments based on the spacing between the flowlines in the initial spherical state. The fraction of ejecta mass represented by the flowline is then the ratio of the area of this zone of the sphere to the total surface area of the sphere.

Due to asymmetry in the background density and the presence of a strong density contrast near the origin, segments of the shock may collide with one another. This shock front self-interaction can lead to collisions in which kinetic energy is converted into internal energy. Since it cannot be easily radiated away, we expect a transient acceleration outward of the heated gas, after which the fluid will return to the dynamics imposed by the global expansion. The numerical treatment of these self-interactions is outlined in Appendix 2.B. This treatment results in the deletion of some flowlines, accounting for the modification of the flow in this region.

⁷For simplicity, the ratio $\lambda \approx 1$ of the post-shock pressure to mean interior energy density is set to be exactly unity in equation (2.5). As the shock velocity is proportional to $\sqrt{\lambda}$, the effect of this is small compared to other limitations inherent in the Kompaneets approximation discussed in Section 2.4.3.

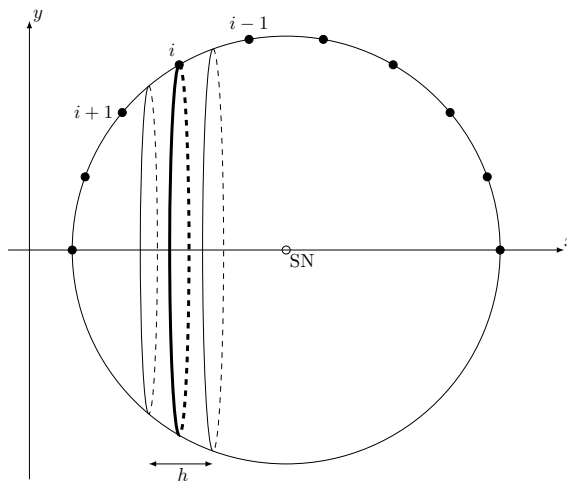


Figure 2.3: A schematic of the initial, spherical state of the SNR, with initial positions for the flowlines (filled circles) around the point of explosion (open circle labelled ‘SN’). Flowlines in the positive- y portion of the x - y plane define a three-dimensional shock front by rotation about the axis of symmetry. Rotating each flowline about this axis produces a ring (shown for the i^{th} flowline as a thick line). The midpoints between the i^{th} flowline and its neighbours define the limits of the zone of the sphere assigned to that flowline (thin lines). For a sphere of radius R' , the area of this zone is proportional to the height of the zone, h , since its surface area is $2\pi R'h$. The fraction of total ejecta mass assigned to the flowline is then the ratio of this area to the total area of the sphere.

2.4.2 Comparison with analytic solutions for single power-law profiles

Fig. 2.4 shows the morphology of an SNR, running into a circum-SMBH environment with density power-law gradient $\omega = 1$ (left-hand panel) and $\omega = 3$ (right-hand panel). There, we compare the analytic prescription described in Section 2.3.2 and Appendix 2.A with our numerical method. The numerical solutions are found to match the analytic form very well. There is very slight deviation between the two methods, more noticeably in the $\omega = 3$ case, which is due to the fact that the numerical method requires a small spherical initial step. The analytic solution is closer to a sphere at small times in the $\omega = 1$ solution so there is almost no discernible discrepancy.

Fig. 2.5 shows a comparison between our numerical (solid lines) and the analytic (dashed lines, arbitrary scaling) results in a broken power-law medium with $\omega_{\text{in}} = 1$ and $\omega_{\text{out}} = 3$. This figure shows the distance and velocity evolution of selected sample points on the shock front. We follow the portion of the shock that propagates towards the SMBH (blue lines), away from the SMBH (red lines) and at an initial angle of $\psi_0 = \pi/2$ (green line). The numerical radius and velocity are seen to transition from the coasting (radius $R' \propto t$, velocity $v = \text{const.}$) phase to forms similar to those seen in the pure Kompaneets solutions.

As expected, the evolution of the trailing part of the shock, as it gets closer to

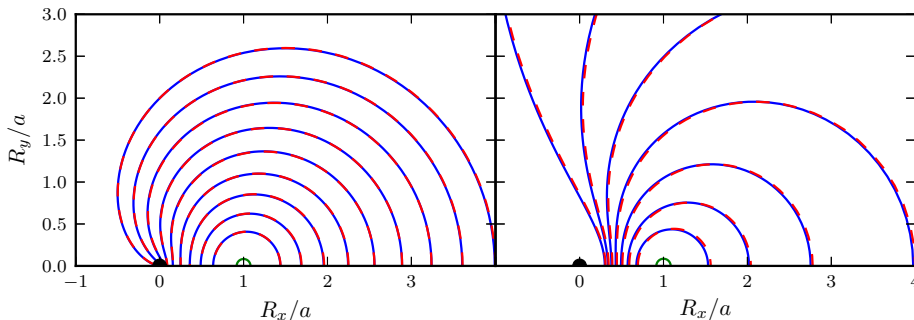


Figure 2.4: Numerical results (blue) compared with analytic solutions (red, dashed) for the locations of the shock front in density profiles with $\omega = 1$ (left-hand panel) and $\omega = 3$ (right-hand panel). The initial (spherical) state for the numerical solutions is shown in green. Units are given as ratios of distance (R_x, R_y) to explosion distance a from the density singularity at $(0, 0)$ (the SMBH in our model). The results can be written in parametric form in terms of x , which increases with time t up to a critical value of $x = 1$; see Section 2.3.2 as well as the expressions for $t(x)$ in Appendix 2.A. The solutions for $\omega = 1$ are found up to $x = 1$, while for $\omega = 3$ they are given up to $x = 0.8$ due to the divergence of solutions as $x \rightarrow 1$ in this latter case. The trailing part of the shock (the part directly towards the SMBH) for $\omega = 1$ solution reaches $R_x/a = 0$ at $x = 1$, while leading point (directly away from the SMBH) reaches $R_x/a = 4$. The trailing part of the $\omega = 3$ solution asymptotically approaches a distance of $R_x/a = 1/4$ as $x \rightarrow 1$, while in the same limit the leading part of the shock follows $R_x/a \rightarrow \infty$.

the SMBH, approaches the analytic solution for a pure $\omega = 1$ medium. Likewise, the leading part of the shock asymptotes to the pure $\omega = 3$ analytic solution, as it expands away from the SMBH. The green line shows how the evolution of a flow-line that emerges at 90° from the $\theta = 0$ axis has, instead, an intermediate behaviour, which is influenced by the overall broken power-law density. The figure also shows for reference the Sedov–Taylor solution (black dashed line, Taylor 1950; Sedov 1959) for an explosion in a uniform ambient medium ($R' \propto t^{2/5}$ and $v \propto t^{-3/5}$).

2.4.3 Caveats and limitations of the model

For more complex background density configurations, such as one with many large density contrasts that trigger self-interactions and turbulence, one may consider a treatment of self-interacting shocks that is more in-depth and sophisticated than that presented in Appendix 2.B. The increase in velocity of any small self-intersecting region is expected to be a brief transient phenomenon; therefore, we do not presently apply any boost in velocity when merging flowlines, instead only accounting for the net direction of the flow that results from two colliding parts of the shock. The reason is that, in all our simulations, the portion of the shock front which undertakes self-interaction is limited, and therefore the treatment of these regions have a small effect on the overall volume evolution. Obviously, if one considers a more complex

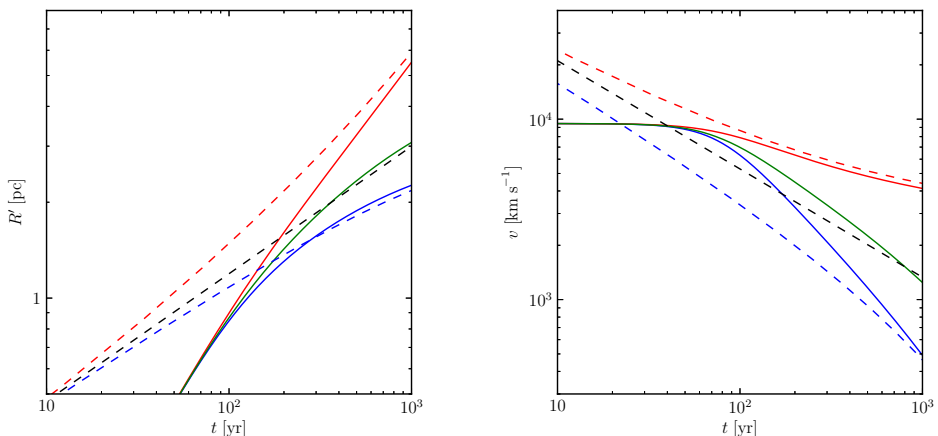


Figure 2.5: Example of radius and velocity evolution for a remnant in a broken-power-law medium (solid lines). The explosion occurs at 3 pc (near the density break between $\omega_{\text{in}} = 1$ and $\omega_{\text{out}} = 3$) around a $5 \times 10^8 M_{\odot}$ SMBH using the scaling described in Section 2.5. Solid lines are plotted from snapshots of the evolution of the remnant in the numerical treatment, where blue (lowermost) curves are for the trailing flowline (towards the SMBH) and red (uppermost) curves are for the leading one (away from the SMBH). The green curve shows the behaviour of a flowline in the numerical treatment that emerges at 90° from the $\theta = 0$ axis ($\psi_0 = \pi/2$). Some analytic results (with arbitrary scaling) are given as dashed lines for comparison. Black is the form of the Sedov-Taylor (uniform medium, $\omega = 0$) solutions. The red dashed curve shows the solution for the point on the shock travelling directly away from the SMBH for a shock in a purely $\omega = 3$ medium. The blue dashed curve shows the solution for the point on the shock travelling directly towards the SMBH in a purely $\omega = 1$ medium.

geometry where self-interaction dominates the evolving volume, full hydrodynamical simulations are the only reliable tool of investigation.

The Kompaneets approximation itself has some drawbacks, in that it generally predicts too large a velocity, and therefore size, for the shock once it accelerates (Koo and McKee 1990; Matzner and McKee 1999). In the context of the present problem, this is more pronounced in the outer density region with a steeper, R^{-3} , gradient. If much of the shock is in the R^{-3} region, the overestimation of velocities and sizes will therefore be greater.

2.5 Galactic nuclei model

In our quiescent SOIs, with no appreciable inflow of gaseous material from further out, the gas density distribution is that of an RIAF. The distribution of early-type stars (the only population of interest here) is dictated only by local and current conditions, not bearing imprints of the long term history of the assembly of the nucleus. These facts will allow us to rescale features of our Galactic Centre (observationally constrained because of its proximity) to quiescent nuclei with different SMBH masses.

2.5.1 Characteristic radii

We consider SN explosions within the SOI of an SMBH. Their fate can be influenced by both the SMBH gravity and its gaseous environment. Correspondingly, there are characteristic radii in the nucleus associated with these properties. The first is that of the SOI: the range out to which the gravity of the SMBH dominates over that of the gravitational potential of the bulge. Following the definition of Peebles (1972), we use

$$R_{\text{SOI}} \equiv \frac{GM_{\bullet}}{\sigma^2}, \quad (2.17)$$

for a black hole of mass M_{\bullet} , where σ is the velocity dispersion of stars about the SMBH. We use this parameter not only to define the outer edge for the range of explosion distances considered, but also to rescale Milky Way properties to galactic nuclei with different M_{\bullet} . To obtain an expression for the SOI which depends only on M_{\bullet} , we use the well-known (M_{\bullet} - σ) relation between black hole mass and velocity dispersion (Ferrarese and Merritt 2000; Gebhardt et al. 2000). Using the observationally determined Gebhardt et al. (2000) result,⁸ $M_{\bullet} = 1.2 \times 10^8 \left[\sigma / (200 \text{ km s}^{-1}) \right]^{15/4} M_{\odot}$, we obtain

$$R_{\text{SOI}} \approx 2.7 \left(\frac{M_{\bullet}}{4.3 \times 10^6 M_{\odot}} \right)^{7/15} \text{ pc}, \quad (2.18)$$

where here, and hereafter, we rescale equations for the Galactic Centre black hole mass. For what follows, a useful parameter to rescale the Milky Way properties is the ratio $\zeta \propto M_{\bullet}^{7/15}$, between the R_{SOI} of a generic M_{\bullet} and that of Sgr A*.

The closer a supernova explodes to the SMBH, the stronger the tidal forces, which may become high enough to disturb and eventually disrupt the remnant in a dynamical time. This happens when the velocity of the shock front becomes comparable to the Keplerian velocity, v_{K} , associated to the SMBH gravity field. We do not model distortions due to tidal effects but we account for the tidal disruption of the remnant when we quantify its ‘lifetime’ (see Section 2.6.3). To this end we test for whether $v_{\text{s}} < v_{\text{K}}$ to detect parts of the shock that have decelerated enough to be sheared by the SMBH. We therefore introduce another characteristic radius—the innermost radius for the existence of SNRs, R_{sh} , which is limited by SMBH shearing. This minimal shearing

⁸Recent studies imply that the M_{\bullet} - σ relation is steeper than this, and σ may have an exponent closer to 5 (for example, Morabito and Dai 2012). Although there is still some ambiguity in the value of this exponent, we tested the effect of a very steep relationship $M_{\bullet} = 1.2 \times 10^8 (\sigma / (200 \text{ km s}^{-1}))^{5.3} M_{\odot}$ motivated by Morabito and Dai (2012). Even with this large exponent, we find that our main results, the time-scales in Section 2.6.3, are generally only increased by a factor of 2 (while the scaling of radii by the spheres of influence also increases by at most a factor of 2). As the overall consequence is small, we do not present additional results for a steeper M_{\bullet} - σ relation in this work.

radius is the point at which v_K is comparable to the initial SNR ejecta velocity, v_{init} :

$$\begin{aligned}
 R_{\text{sh}} &\equiv \frac{GM_{\bullet}}{v_{\text{init}}^2} \\
 &= 1.9 \times 10^{-4} \left(\frac{M_{\bullet}}{4.3 \times 10^6 M_{\odot}} \right) \left(\frac{v_{\text{init}}}{10^4 \text{ km s}^{-1}} \right)^{-2} \text{ pc} \\
 &= 900 \left(\frac{v_{\text{init}}}{10^4 \text{ km s}^{-1}} \right)^{-2} R_g,
 \end{aligned} \tag{2.19}$$

where R_g is the gravitational radius of the SMBH.

Supernovae that occur within R_{sh} are completely sheared, as the velocity of the ejecta in all directions is less than the Keplerian velocity around the SMBH. Note, however, that SNRs can be sheared also at larger radii as the ejecta slows down, and may reach the local Keplerian velocity at a radius larger than R_{sh} . Comparing the shock velocity to the Keplerian velocity is effectively equivalent to comparing the ram pressure with the ambient baryonic pressure, P_{gas} , since $v_K \approx c_s \propto \sqrt{P_{\text{gas}}/\rho}$ (where c_s is the sound speed in the external medium). Additionally, we note that for the same reason we can ignore the shearing of remnants during the initial explosion for $a > R_{\text{sh}}$, we can also neglect the (Keplerian) orbital motion of the progenitor stars.

Finally, for the gas models, the reference radius for the density, R_0 , and the location of the break in the gas density power law R_b (as explained in Fig. 2.1) are scaled in our model by the SOI, such that $R_0 \equiv \zeta R_{0,\text{MW}}$ and $R_b \equiv \zeta R_{b,\text{MW}}$.

2.5.2 Gas models

As mentioned previously, we expect that quiescent SMBHs are surrounded by RI-AFs, similar to that which is suggested in the Galactic Centre. This implies that all flows have similar density gradients, which is set by the physical processes which characterize this accretion regime. Additionally, their accretion rate must be modest and, in particular, lower than the critical value for advection-dominated accretion of $\dot{M}_{\text{crit}} = \alpha^2 \dot{M}_{\text{Edd}}$, or

$$\dot{M}_{\text{crit}} = 9 \times 10^{-3} \left(\frac{M_{\bullet}}{4.3 \times 10^6 M_{\odot}} \right) M_{\odot} \text{ yr}^{-1}, \tag{2.20}$$

where \dot{M}_{Edd} is the Eddington rate, $\alpha = 0.3$ (Narayan and Yi 1995) and we assume a 10% radiation efficiency for \dot{M}_{Edd} . At a reference distance of $R_{0,\text{MW}} \approx 0.04$ pc, the accretion rate is estimated from observations and simulations to be around $\dot{M} \approx 10^{-5} M_{\odot} \text{ yr}^{-1}$ (Cuadra et al. 2006; Yuan 2007). Therefore, Sgr A* is accreting at $\sim 10^{-3}$ of its critical rate.

We extend properties of the Sgr A* accretion flow to other quiescent nuclei as follows. The primary material for accretion in quiescent nuclei originates from the winds from massive stars in the SOI. Since the total mass of stars in the SOI scales

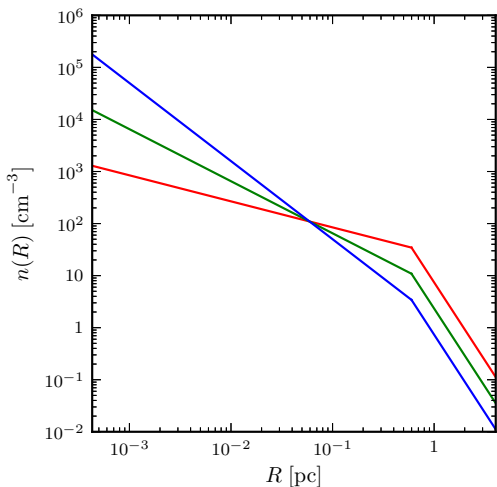


Figure 2.6: Example of a gas density model used for a galaxy with a $10^7 M_\odot$ SMBH, showing the number density, n , as a function of radius, R , from the SMBH. The shallowest inner gradient (red line) corresponds to $\omega_{\text{in}} = 1/2$, the middle (green line) to $\omega_{\text{in}} = 1$ and the steepest (blue line) to $\omega_{\text{in}} = 3/2$. All models have a gradient outside the break of $\omega_{\text{out}} = 3$. The density is scaled using a reference point R_0 , seen as the point of convergence of all the inner density gradients (in this case, $R_0 = 0.06$ pc). A break in the density distribution is located at a constant $R = R_b$ for all choices of the density gradient (in this case, $R_b = 0.6$ pc). The left-hand and right-hand limits of the horizontal axis are determined by the shearing radius (equation 2.19) and SOI (equation 2.17), respectively.

with M_\bullet , then so too will the number of massive stars and, therefore, the accreted mass: $\dot{M} \propto M_\bullet$. As above, $\dot{M}_{\text{crit}} \propto M_\bullet$, as well, and therefore the ratio $\dot{M}/\dot{M}_{\text{crit}}$ is constant over M_\bullet . In other words, for our physically motivated picture of ‘quiescent’ nuclei, the SMBH is accreting at the same fraction of Eddington as Sgr A* ($\dot{M} \approx 10^{-5} \dot{M}_{\text{Edd}}$).⁹

Given this accretion rate of $\dot{M}/\dot{M}_{\text{crit}} \approx 10^{-3}$, we can estimate the density at R_0 for nuclei with a different M_\bullet . To do so we use the continuity equation for the flow,

$$\dot{M} \approx 4\pi R_0^2 \rho(R_0) v_K(R_0), \quad (2.21)$$

where the scale height $H \approx R$ and the radial velocity $v_R \approx v_K$.

The reference density for our general galactic nuclei models is therefore

$$n_0 = n(R_0) \approx 130 \left(\frac{M_\bullet}{4.3 \times 10^6 M_\odot} \right)^{1/2} \zeta^{-3/2} \text{ cm}^{-3}. \quad (2.22)$$

An example of our density model for $M_\bullet = 10^7 M_\odot$ and three different inner gradients is given in Fig. 2.6, where the effect on the density profiles of fixing the scaling reference point at R_0 is evident.

⁹It is possible for SMBHs to be accreting at different fractions $\dot{M}/\dot{M}_{\text{crit}} < 1$ and still be termed ‘quiescent’ in the conventional sense. However, the accretion rate given here is the most physically motivated value based on scaling of quantities by M_\bullet , and deviations from this value are beyond the scope of this work.

2.5.3 Massive star distributions

Given a physical number density $n_*(R)$ of stars at a distance R from the centre of mass, the projection on to the celestial sphere gives, as a function of the projected radius R_{pr} , a surface density of stars $\Sigma_*(R_{\text{pr}})$. Observationally, the latter quantity is typically given. Assuming a spherically symmetric spatial distribution, it is possible to reverse the projection to infer the spherical number density,

$$n_*(R) = \frac{-1}{\pi} \int_R^\infty \frac{d\Sigma_*(R_{\text{pr}})}{dR_{\text{pr}}} \frac{dR_{\text{pr}}}{\sqrt{R_{\text{pr}}^2 - R^2}}, \quad (2.23)$$

provided that the physical number density $n_*(R)$ falls off at large R at a rate greater than R^{-1} . For power-law distributions, this gives a correspondence of the observed radial dependence, $R_{\text{pr}}^{-\Gamma}$, to the physical dependence, $R^{-\gamma}$, via the relationship $\gamma \sim \Gamma + 1$.

For the Milky Way, there is evidence for two different power-law distributions in the old and young stellar populations of the Galactic Centre. A particular curiosity is an apparent depletion of late-type (K, M) giants in the inner 0.5 pc (Do et al. 2009). This leads to a much shallower (possibly inverted) inner power-law for the late-type distribution compared to that of the early-type (O, B) stars. Recent analyses estimate the radial dependence of the early-type stars in the Milky Way nuclear star cluster to be approximately R_{pr}^{-1} inside the power-law break and $R_{\text{pr}}^{-3.5}$ outside (Buchholz et al. 2009; Do et al. 2013b), corresponding to values of γ of 2 and 4.5, respectively.

In the nuclei of different galaxy types, variations in the stellar distributions for longer-lived stars are possible due to differing nuclear assembly histories. However, in our picture of a self-regulating SOI, the young star distributions are taken to be the same across the range of M_\bullet , where the most recent star formation in this region is indifferent to the history of the nucleus. Therefore, for our galactic nuclei model, we use the same values for γ as those given above for the early-type stars around Sgr A*. As before, we scale the break in the stellar number density by the SOI of the SMBH, which defines the transition radius between the two values of γ .

2.6 Results

We proceed to describe our main results, based on the method outlined in the previous sections. In Section 2.6.1, we examine the effect of black hole mass and gas density profile on the deceleration length using the prescriptions of Section 2.3.1. Then, using the numerical method of Section 2.4, the overall SNR morphology is presented in Section 2.6.2. Finally, in Section 2.6.3, we investigate the X-ray emitting lifetimes based on shearing of the SNR ejecta by the SMBH. We then use this last result to predict the mean SNR lifetimes expected within the SMBH spheres of influence for different M_\bullet .

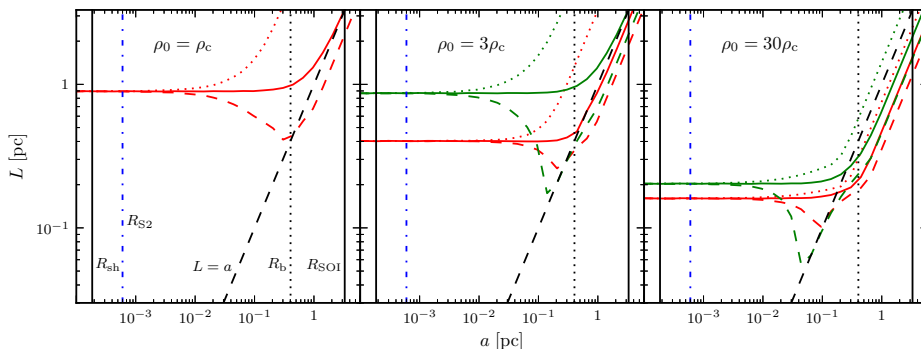


Figure 2.7: Deceleration lengths, L , as a function of explosion distance from the SMBH, a , for a Milky Way model ($M_{\bullet} = 4.3 \times 10^6 M_{\odot}$) with density scalings of the canonical density 130 cm^{-3} of 1, 3 and 30 times (left to right). Red lines show the $\omega_{\text{in}} = 1/2$ model and green lines show the $\omega_{\text{in}} = 1$ model. The solid curves are the average deceleration lengths derived by integrating the mass over a sphere, as discussed in Section 2.3.1. The dotted and dashed curves are integrals away from and towards the origin, respectively. The shearing radius (2×10^{-4} pc) and the SOI for Sgr A* are marked by R_{sh} and R_{SOI} , respectively. The vertical dotted black line is the location of the break in density, outside of which $\omega_{\text{out}} = 3$. The diagonal dashed black line shows $L = a$, which represents the distance to the SMBH. The blue dot-dashed line shows the pericentre distance of the star S2. The curves for $\omega_{\text{in}} = 1$ are not plotted in the left-hand panel since most of the points lie outside of the SOI axis bounds.

2.6.1 Deceleration lengths

The SNR begins to appreciably decelerate once the swept up mass becomes comparable to the ejecta mass. This end of the ejecta-dominated stage can be characterized by a deceleration length from the explosion point, L , determined by the density integrals of Section 2.3.1, which varies with direction. This deceleration length depends on the gas density and on the radial density profile. These depend respectively on the SMBH accretion rate and accretion mode (for example, CDAF versus ADAF).

Considering the values of L in various environments, we obtain an indication of the length- and time-scales over which SNRs will end their ejecta-dominated stage and start decelerating. As a reference for the crossing time-scale of a nucleus, recall that an SNR that does not appreciably decelerate from its initial $\sim 10^4 \text{ km s}^{-1}$ would reach a radius of 1 pc in approximately 100 yr. An investigation of L in different directions indicates which SNRs will decelerate within this time-scale. It also provides a test for the level of asymmetry of the SNR during this stage of evolution. We will later proceed to model SNRs through the decelerating stage.

Figs 2.7 and 2.8 depict two curves describing the deceleration length, L , approximately towards and away from the SMBH. The angle ψ_0 approximately towards the SMBH is taken to be $10^{-3} \pi$, such that the integrated path through the density runs very close to the SMBH, but does not pass through the singularity at the origin. The difference between these two curves provides a measure of the asymmetry of the rem-

nant at the end of the ejecta-dominated stage. For comparison, in Fig. 2.7, a third curve (solid line) is shown that describes an average deceleration length derived by an integral over a sphere.

We first consider a model of the background gas in the Milky Way. Fig. 2.7 shows L for three different density values: the observationally motivated ‘canonical’ density $\rho_0 = \rho_c$ (in number density, $n_c \approx 130 \text{ cm}^{-3}$, left-hand panel), and 3 (central panel) and 30 (right panel) times that value. We consider values other than the canonical density, as, even in quiescent nuclei such as the Galactic Centre, there is the possibility for variation in the overall density of the accretion flow. For example, denser accretion flows can result from sudden accretion episodes from tidally disrupted stars or clouds,¹⁰ or they can be associated with more intense star formation activity in the nucleus. Scaling the density also shows the effect of under- or misestimating the gas density from the X-ray emission.

As expected with increasing density, there is an overall trend towards lower values of L/a . There is also a trend towards more symmetric remnants with increasing density, since in general the ratio L/a is reduced for higher densities.

The investigation of different density profiles (see Fig. 2.6) leads us to conclude that CDAF/ADIOS model, preferred by Galactic Centre observations (Wang et al. 2013), gives, quite generally, shorter deceleration lengths (red lines in Figures 2.6 and 2.7). The flatter CDAF/ADIOS profile (smaller ω_{in}) is denser in most of the SOI of the black hole, therefore reducing L/a .

For the canonical value of density in the Milky Way (left panel of Fig. 2.7), the deceleration lengths are $L \gtrsim 1 \text{ pc}$. Considering the CDAF model, we remark that, for the canonical density, the majority of the SNRs would decelerate beyond the SMBH location. Ejecta from a star such as S2 (marked with a blue dot–dashed line in Fig. 2.7) is expected to evolve more symmetrically than that from a star further out, in the stellar disc(s) ($\sim R_b$). Already with a factor of few enhancement in density, SNRs in and beyond the stellar disc would decelerate appreciably before they reach Sgr A* (see central panel).

Fig. 2.8 shows deceleration lengths for each of $\omega_{\text{in}} \in \{1/2, 1, 3/2\}$ for galactic nuclei with SMBH masses of $10^7 M_\odot$ (red), $10^8 M_\odot$ (green) and $10^9 M_\odot$ (blue). Hereafter, we scale the explosion distance by the location of the break in gas density, R_b , as it is the value of a at which a change in behaviour of SNRs is expected. Accretion rates (and thus gas density normalization) and characteristic radii are rescaled as explained in Section 2.5, and all increase with black hole mass.

For $M_\bullet \lesssim 10^8 M_\odot$, the density is low enough and R_{sh} is small enough that for small values of a the SNR can expand over the SMBH before appreciably decelerating. The centre of such a shock front is close to being aligned with the centre of symmetry of the gas distribution, which leads to a more symmetric evolution. This is seen in the fact that all L values converge at small a . However, by $M_\bullet \gtrsim 10^9 M_\odot$, the gas

¹⁰A recent example around Sgr A* is the object G2 (for example, Burkert et al. 2012); though, if a cloud, its mass is too small to have a significant impact on the overall density.

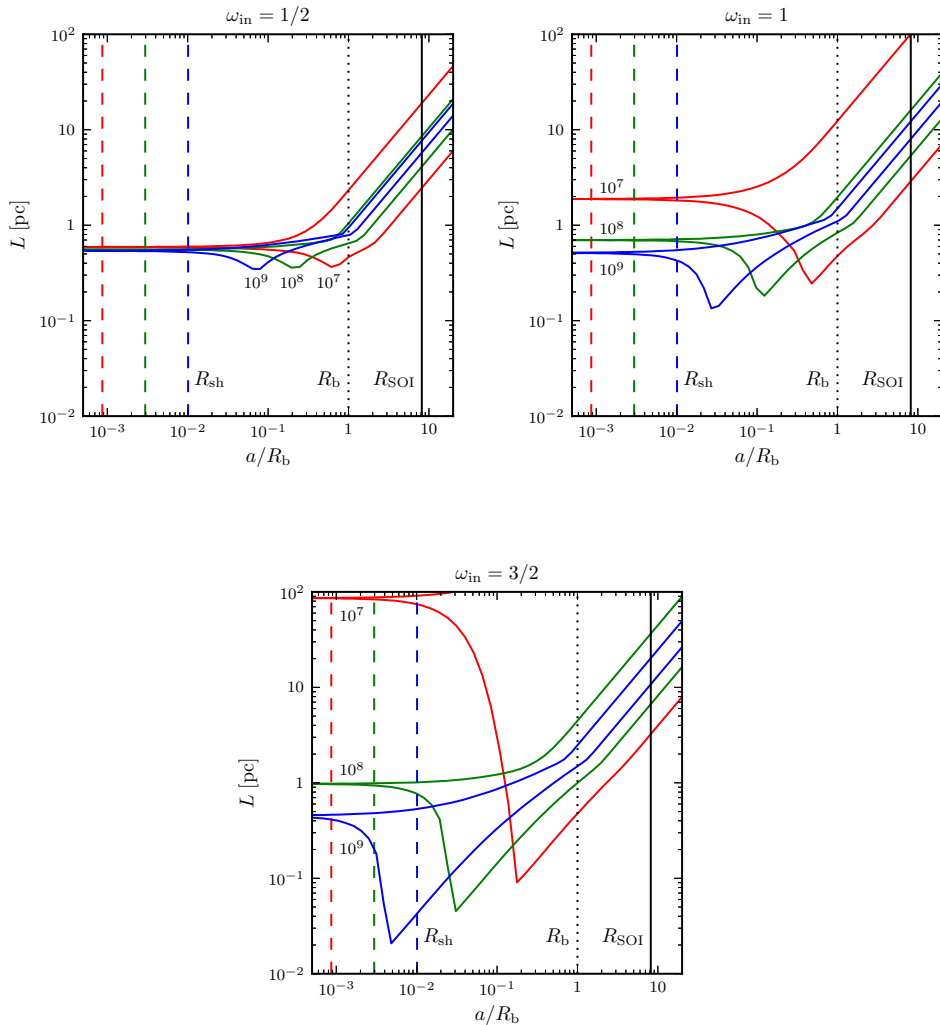


Figure 2.8: Deceleration lengths, L , as a function of the ratio of the explosion distance, a , to the break in gas density, R_b . Each set of axes is to the same scale, and corresponds to a different gradient near the SMBH: $\omega_{in} = 1/2$ (top left), $\omega_{in} = 1$ (top right) and $\omega_{in} = 3/2$ (bottom). As indicated in the top-left panel, red corresponds to the gaseous environment of an SMBH of $10^7 M_\odot$, green to $10^8 M_\odot$ and blue to $10^9 M_\odot$. Two curves are shown for each M_\bullet (each colour); the higher curve shows L for the direction away from the SMBH, and the lower curve shows L towards the SMBH. The dashed coloured lines correspond to R_{sh} for each value of M_\bullet . The dotted black line shows the break in gas density at R_b , while the solid black line shows the extent of the SOI (which is the same multiple of R_b for all M_\bullet). Unlike in Fig. 2.7, we also show results for a standard ADAF model ($\omega_{in} = 3/2$; bottom panel), since these density profiles can produce L values that fall within R_{SOI} .

density is high enough and R_{sh} extends far enough from the SMBH that explosions near the SMBH cannot pass over the singularity before being sheared, and this more symmetric expansion regime beyond the SMBH at small a is no longer present.

In general, with increasing overall density (around more massive black holes), we find the same trend observed for the Milky Way with denser gaseous environments: the ratio of L/a decreases, as does the maximum possible asymmetry (differences between upper and lower curves). On the other hand, increasing ω_{in} also tends to create greater asymmetries in the SNRs, as can be appreciated by comparing the three panels of Fig. 2.8. For higher ω_{in} , the ratio L/a is higher in the direction away from the SMBH as a result of the density being lower at any point further than R_0 , but it is lower towards the SMBH as the SNR sweeps through a steeper density gradient near the origin.

2.6.2 Morphological evolution

We turn now, using the numerical treatment of Section 2.4, to the subsequent adiabatically decelerating evolution of the remnant. We consider explosions both inside and outside the density break, R_b . The explosion distances are chosen such that, across all M_\bullet , the same a/R_b ratio is maintained for the examples inside R_b ($a/R_b = 0.6$) and outside R_b ($a/R_b = 2.5$); this will also be useful for comparison with the time-scale plots of Fig. 2.11.

Fig. 2.9 depicts the morphology for two explosion distances in the Milky Way environment. The explosion inside the density break does not decelerate before reaching the SMBH (as expected from Fig. 2.7, where $L > a$). Therefore it passes over the SMBH without any significant distortion. The SNR subsequently expands into the lower density region almost spherically, with the centre of the SNR being very near the SMBH. For the explosion outside the break in density, the trailing part of the shock decelerates before reaching the SMBH, while at the same time the parts expanding through the $\omega = 3$ region wrap around the SMBH and eventually self-interact. SNRs such as this, which explode far enough from the SMBH that $L < a$, show significant asymmetries during their evolution.

Fig. 2.10 shows examples of the variation in morphology of the remnant arising from differences in the black hole mass (and therefore the gas density). The values of M_\bullet are the same as those used in Fig. 2.8 for the deceleration lengths; the black hole mass increases from top to bottom. The data shown in Fig. 2.10 are summarized in Table 2.1.

It is evident that, in many cases, much of the mass of the remnant remains near the SMBH due to the focusing effect of the density gradient on the flowlines. Therefore, unlike expansion away from the SMBH, where the mass behind the shock is more tenuous due to the rapid shock expansion, the ejecta material near the SMBH is expected to be more concentrated.

In addition to the symmetries in L found in Section 2.6.1, explosions closer to

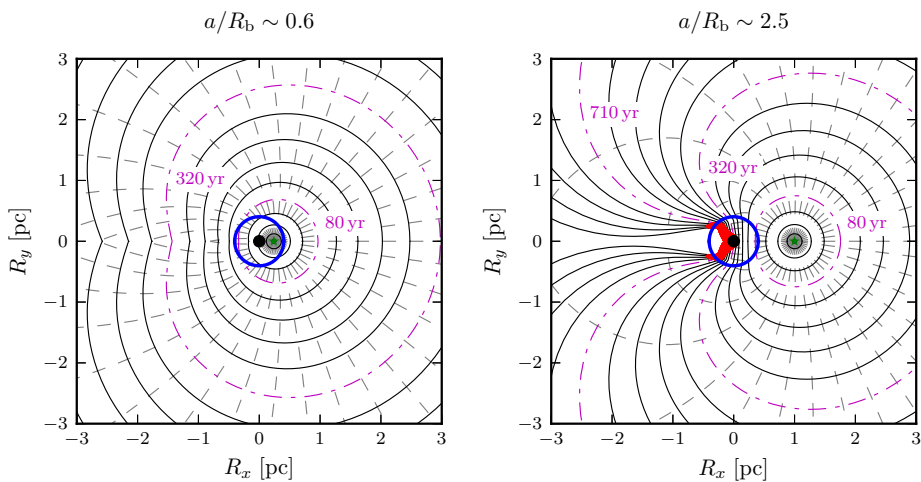
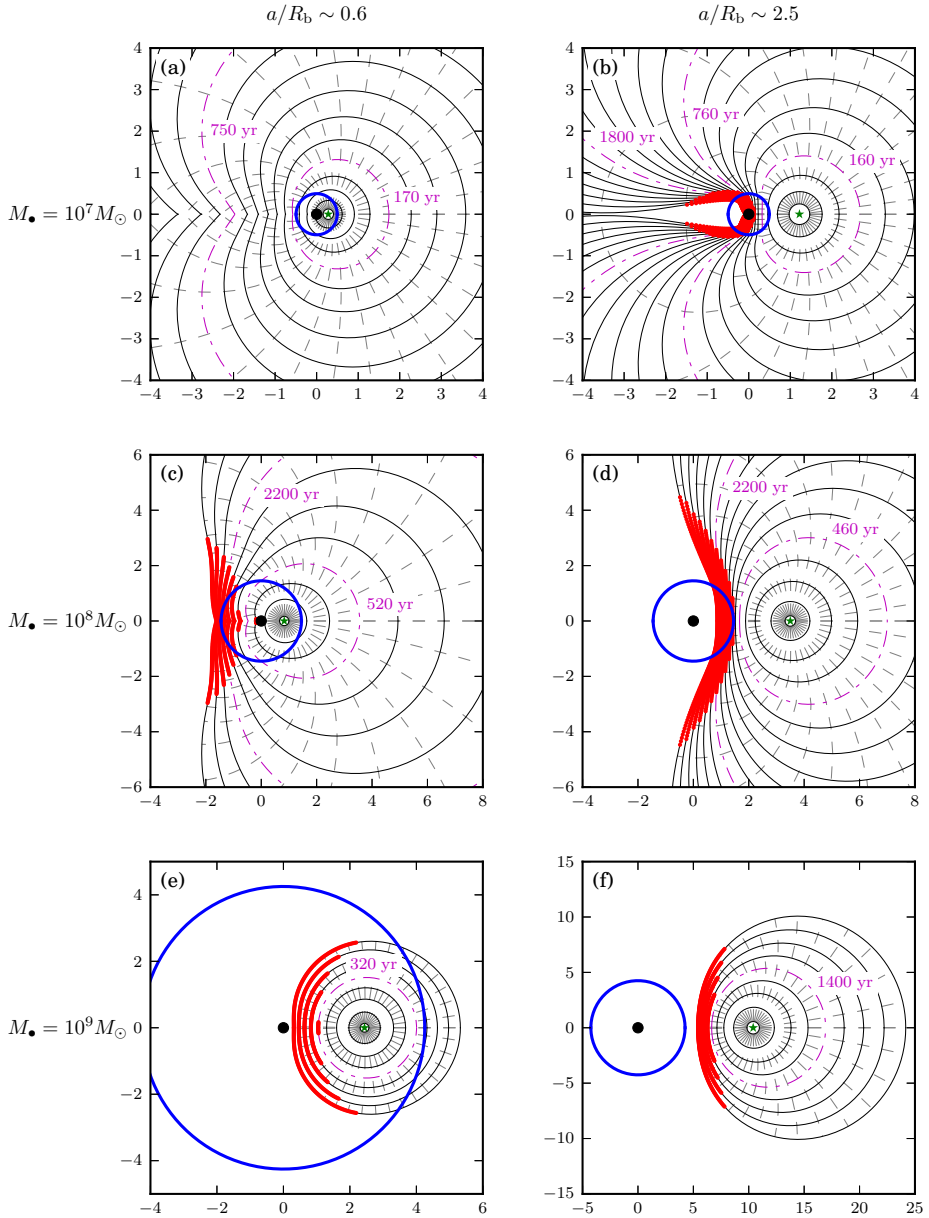


Figure 2.9: Morphological evolution for two explosion distances for the Milky Way, inside (left) and outside (right) R_b . The explosion distance in the left-hand panel is $a = 0.24$ pc, and in the right-hand panel, $a = 1.0$ pc. The black hole is marked with a black point at the origin and the supernova occurs at the green star. The break in density at R_b is shown as a thick blue circle. Snapshots of the shock front at different times are in solid black, and dashed lines show sample flowline paths. Flowlines flagged as having reached the shearing condition discussed in Section 2.6.3 ($v_{\text{SNR}} < v_K$) are shown as red points. Some example snapshot times are indicated next to corresponding dot-dashed magenta lines. In the left-hand panel, the initial snapshot shown is at 13 yr and the final at 620 yr; in the right-hand panel, the initial snapshot is at 13 yr and the final at 1100 yr. The spacing between snapshots is an equal multiple of the (variable) time step used. In the left-hand panel, the initial snapshot spacing is 16 yr, and the final spacing is 84 yr; in the right-hand panel, the initial snapshot spacing is 16 yr, and the final spacing is 120 yr. In both cases, the remnants expand well beyond the window shown, until they reach the radiative stage as discussed in Section 2.6.3.



panel	$M_{\bullet} (M_{\odot})$	a (pc)	t_{init} (yr)	Δt_{init} (yr)	Δt_{final} (yr)	t_{final} (yr)
a	1×10^7	0.28	14	23	160	1200 †
b	1×10^7	1.2	28	32	1000	3300 †
c	1×10^8	0.83	19	91	760	4300
d	1×10^8	3.5	24	58	580	5100
e	1×10^9	2.4	16	40	210	1000
f	1×10^9	10	70	170	900	4300

Table 2.1: Parameters used for the plots of Fig. 2.10, where M_{\bullet} is the mass of the SMBH and a is the distance of the explosion point from the SMBH. The snapshots that are plotted are at fixed multiples of the time step, although the time step is dynamic and increases with the size of the remnant. The first curve that is plotted is at a time t_{init} , and the difference between the first two snapshots is given in Δt_{init} . The difference between the final two snapshots is given in Δt_{final} , and the last curve that is plotted is at a time t_{final} . Additional examples of snapshot times are shown on Fig. 2.10 with corresponding magenta dot-dashed curves. Note that the values of Δt are not the time step used by the numerical treatment, which is much smaller. †: simulation ran until 10^4 yr, stopping due to the radiative onset threshold discussed in Section 2.6.3, but the last curve shown within these axis limits is at the stated time.

a lower-mass SMBH ($M_{\bullet} \lesssim 10^8 M_{\odot}$) are also found to be more symmetric during their adiabatic evolution compared to those further from the SMBH (compare panel ‘a’ of Fig. 2.10 to panel ‘b’). SNRs near lower M_{\bullet} expand over the SMBH largely unimpeded, and their centres are closely aligned with the centre of symmetry of the gas distribution when they enter the adiabatic phase.

Remnants around higher-mass SMBHs ($M_{\bullet} \gtrsim 10^9 M_{\odot}$) are more symmetric for the whole duration of their adiabatic lifetimes. The overall increase in density causes the scale of the remnant to be small (relative to the scale of the background gas distribution), and so, within the lifetime of the remnant, significant asymmetries have not yet developed. Indeed, by looking at the overall remnant size with respect to M_{\bullet} , there is a clear trend towards decreasing remnant size with increasing M_{\bullet} during this phase of evolution.

2.6.3 Adiabatic SNR lifetimes

During the adiabatic phase, the SNR can be observed as a hot, X-ray emitting object. The hard X-rays can penetrate the obscuring matter in galactic nuclei and allow us to detect the SNR. In particular, in quiescent nuclei, the SMBH light may not prevent the SNR detection in X-rays. We will refer to this temporal window during which the SNR can be observed in X-rays as the ejecta ‘adiabatic lifetime’ or simply its ‘lifetime’, because once the ejecta become radiative it cools rapidly and its X-ray emission ceases.

As previously mentioned, in a general environment, the adiabatic phase ends when the expansion has caused the internal temperature to decrease enough for radiative losses to become dynamically important. In the SOI, however, the tidal field can tear apart the ejecta well before the end of its radiative phase. In this case, the ejecta is dispersed and may not be immediately identified as such, at any wavelengths.

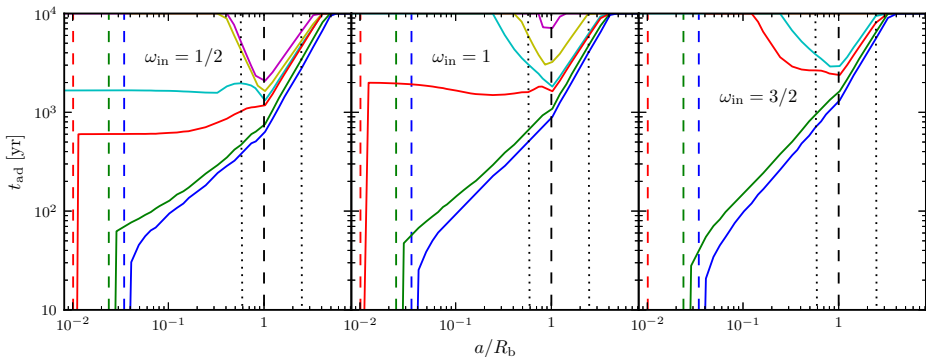


Figure 2.11: Time taken to shear a total ejecta mass $M_{\text{sh}} \geq M_{\text{ej}}/2$ for a range of M_{\bullet} and ω_{in} , for explosion distances a scaled to the break in gas density, R_b . Decreasing t_{ad} curves correspond to increasing M_{\bullet} , and the black hole masses shown are as follows; magenta: $5 \times 10^7 M_{\odot}$, yellow: $1 \times 10^8 M_{\odot}$, cyan: $5 \times 10^8 M_{\odot}$, red: $1 \times 10^9 M_{\odot}$, green: $5 \times 10^9 M_{\odot}$, blue: $1 \times 10^{10} M_{\odot}$. The curve for each M_{\bullet} represents data from simulations covering between 30 and 40 values of a . Dashed, vertical coloured lines show the corresponding R_{sh} . The dashed black line shows the location of R_b . The dotted black lines show the two regions of explosion distances investigated in Fig. 2.10. The right-hand limit of the horizontal axis is set at the SOI. By 10^4 yr, radiative losses become significant in all cases; if the shearing condition $v_{\text{sh}} < v_{\text{K}}$ has not yet been met by this time, the adiabatic stage ends due to the radiative transition discussed in Section 2.6.3. Note that the Galactic Centre SMBH is not shown on this plot, as we do not find $M_{\text{sh}} \geq M_{\text{ej}}/2$ at any value of a before the radiative stage sets in.

So far, we have been evolving the shock expansion without directly considering the gravitational field of the SMBH, but only considering its indirect influence in shaping the gas density profiles. This is a very good approximation as long as the internal pressure forces are significantly larger than the SMBH tidal forces. From momentum conservation, this means that we can ignore the SMBH gravitational field whenever the shock front is faster than the local Keplerian velocity, v_{K} . When, however, $v_{\text{s}} < v_{\text{K}}$, the dynamics of the shock front is dictated by gravity. As different adjacent parts move at different speeds $\sim v_{\text{K}} \propto R^{-1/2}$, the SNR is sheared in a dynamical time.

If the overall density is large enough, the swept up mass causes the shock front to decelerate before being sheared. As shown in Sections 2.6.1 and 2.6.2, most of the ejected mass is focused close to the SMBH (see Fig. 2.10), in regions of high Keplerian velocities, where this is more likely to occur. This effect is more prominent in the surrounding of more massive black holes.

Practically, we consider that the SNR has ended its life when half of the original ejecta mass satisfies the condition $v_{\text{s}} < v_{\text{K}}$. A fraction of the ejecta mass is assigned to each flowline (as per Section 2.4.1), and we monitor the total proportion of sheared mass M_{sh} to determine this time. The sheared portions of the remnants are marked with red points over the flowlines in Fig. 2.10. Fig. 2.11 describes the variation in lifetime for different explosion distances and M_{\bullet} . For models with $M_{\bullet} \lesssim 10^7 M_{\odot}$, no

SNR within the SOI ends its lifetime by shearing within the 10^4 yr shown on the plot.

There is a clear trend in the behaviour of the remnant lifetimes as a increases. The lifetimes for SNRs exploding within R_{sh} vanish, by the definition of the shearing radius. Just outside R_{sh} the lifetimes are short but they increase rapidly with a . This is because, at small a , the SNR expands at $v_{\text{init}} \approx 10^4 \text{ km s}^{-1}$ for the time that it is near the SMBH. Therefore, the amount of sheared ejecta is directly proportional to the fraction of the surface area of the SNR that enters the sphere of radius R_{sh} around the SMBH. This quickly decreases as a increases, causing the rapid increase in lifetime.

For $M_{\bullet} \lesssim 10^8 M_{\odot}$, there is a sudden jump to very long lifetimes at distances slightly larger than R_{sh} (in fact, within a range of small a , the $M_{\text{sh}} \geq M_{\text{ej}}/2$ condition is never met before the radiative stage sets in). Explosions at small a expand over the SMBH without any significant disruption due to their high initial velocity. They then almost entirely travel ‘downhill’ in density, and so $\geq 50\%$ of the remnant is never sufficiently decelerated by travelling into a sufficiently high density.¹¹

Further increasing a , the lifetime then drops significantly. This can be attributed to the aforementioned focusing of ejecta towards the SMBH (as seen in Fig. 2.10). Since the shock decelerates significantly in these same regions, a drop in the lifetime is seen, particularly near the break in gas density, R_{b} , in Fig. 2.11. For lower-mass SMBHs like Sgr A* ($M_{\bullet} \lesssim 10^7 M_{\odot}$), although 50% of the SNR is not found to be sheared, parts of SNRs at this region of a may be decelerated enough before reaching the SMBH that at least a small fraction ($\lesssim 20\%$) of the remnant is sheared. At large a values, much of the SNR spreads out to distances further from the SMBH before appreciably decelerating. Here, a combination of lower v_{K} and less deceleration of the shock conspire to lengthen the time taken to reach the shearing condition.

Inspection of the left-middle panel of Fig. 2.10 shows an intermediate behaviour around $M_{\bullet} \approx 10^8 M_{\odot}$. In this case, for explosions near the SMBH, the SNR can first pass beyond the SMBH and then become significantly sheared. However, once the SMBH mass is high enough ($M_{\bullet} \gtrsim 5 \times 10^8 M_{\odot}$), the higher densities and larger v_{K} mean that it is impossible to have large lifetimes for small a , as remnants are always significantly sheared before they expand far from the SMBH. As seen in Sections 2.6.1 and 2.6.2, they therefore never enter the more symmetric, ‘downhill’ expansion regime seen for lower values of M_{\bullet} . Therefore, around these higher mass SMBHs, the lifetime is generally $\sim 10^3$ yr or less in the entire inner density region.

We note that the most likely distances for core-collapse supernovae to occur are at or within R_{b} , as the density of massive stars falls much more steeply beyond this radius (see Section 2.6.3). The SNR lifetimes are shortest in this region (see Fig. 2.11). For more massive SMBHs the lifetime is also reduced significantly over the whole inner region.

Before concluding this section we note that the tidal shearing of an SNR might have a significant observational signature. One can expect that the sheared ejecta will

¹¹The amount of deceleration in such cases may be underpredicted by the Kompaneets approximation, as discussed in Section 2.4.

be largely accreted by the SMBH. This will temporarily enhance the accretion rate, leading to a period of about 100 yr in which a few solar masses are accreted by the black hole. This is a very large accretion rate that may lead to a flaring of the SMBH, reaching luminosities comparable to the Eddington luminosity over this period.

The radiative transition

As we are interested in the hot, X-ray stage of evolution, we test for the onset of increased radiative losses in the remnant. This was estimated by comparing the shock velocity to the threshold of 300 km s^{-1} outlined in Section 2.3.4. As with the shearing condition, we consider the adiabatic lifetime to have ended when more than half of the remnant is below this velocity.

For SNRs that are not destroyed by shearing, we find that this criterion is not satisfied before the SNR grows larger than the SOI. However, the density gradient will not continue to have a R^{-3} form indefinitely. Beyond the SOI, the SMBH no longer has any substantial influence on the environment and the density is expected to level off.

Therefore, to determine the onset of the radiative stage, we find the time when more than half of the shock reaches 300 km s^{-1} by extending the density uniformly beyond the SOI. If the SNR survives to these large radii, we find that they eventually expand nearly spherically, and that the shape in this late stage is largely indifferent to the processes that occurred near the SMBH. With a uniform density and approximately spherical evolution, the late-time kinematics closely follow the Sedov–Taylor solution. For densities that flatten outside the SOI to about $n \approx 1 \text{ cm}^{-3}$, we find that the SNRs transition to the radiative stage at $\sim 10^4$ yr, independently of M_\bullet . All adiabatic lifetimes therefore end at this age if the SNR has not already been destroyed by shearing from the SMBH.

Mean lifetimes

Deriving properties over the whole SOI is useful in the cases where, for more distant galaxies, individual SNRs may not be observationally resolved. Young SNRs will contribute to the total X-ray emission from these regions, which can be more easily observed.

To summarize the effect of the SMBH environment on SNRs, we calculate the lifetime for core-collapse SNRs averaged over the entire SOI:

$$\langle t_{\text{ad}} \rangle = \frac{\int_{R_{\text{sh}}}^{R_{\text{SOI}}} t_{\text{ad}}(R) n_{\text{cc}}(R) R^2 dR}{\int_{R_{\text{sh}}}^{R_{\text{SOI}}} n_{\text{cc}}(R) R^2 dR}, \quad (2.24)$$

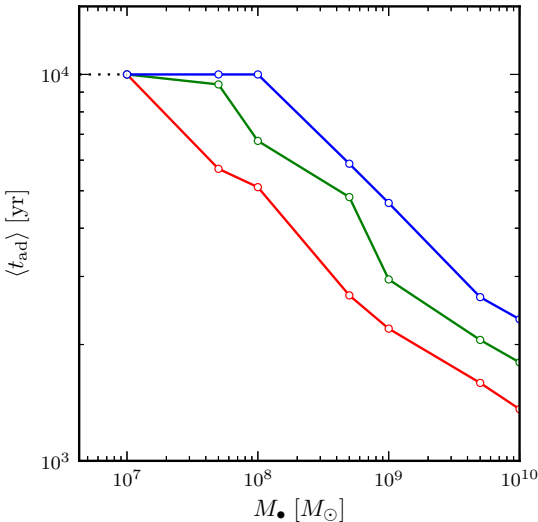


Figure 2.12: Estimated mean adiabatic lifetimes as a function of black hole mass in the present models, using equation (2.24) with the results for $t(R)$ in Fig. 2.11 and the stellar number density distributions $n(R)$ in Section 2.5.3. The red line is for $\omega_{\text{in}} = 1/2$, green for $\omega_{\text{in}} = 1$ and blue for $\omega_{\text{in}} = 3/2$. For lower M_{\bullet} ($\lesssim 10^7 M_{\odot}$), remnants throughout the SOI are not destroyed by the shearing condition by the time radiative losses start to become significant. The adiabatic lifetime therefore ends at 10^4 yr due to the radiative stage, which is indicated by the dotted black line.

where

$$n_{\text{cc}}(R) \propto \begin{cases} \left(\frac{R}{R_b}\right)^{-2} & R \leq R_b \\ \left(\frac{R}{R_b}\right)^{-4.5} & R > R_b \end{cases} \quad (2.25)$$

is the volume number density of stars with mass over $8M_{\odot}$ (see Section 2.5.3).

The average lifetime, $\langle t_{\text{ad}} \rangle$ is shown in Fig. 2.12, as a function of M_{\bullet} . Examining Fig. 2.11 and equation (2.25), we see that much of the reduction in $\langle t_{\text{ad}} \rangle$ is determined by the value of t_{ad} for explosions near and inside the break in gas density ($a \lesssim R_b$). The weighted contribution of t_{ad} to the mean lifetime is higher inside the break due to the higher density¹² of massive stars; additionally, much of the reduction in t_{ad} occurs near the break for lower values of M_{\bullet} , while t_{ad} is low throughout the inner region for higher M_{\bullet} . For $M_{\bullet} > 10^7 M_{\odot}$, the mean adiabatic lifetime of the SNR gets increasingly shorter, well below the canonical value of $\sim 10^4$ yr. By $M_{\bullet} \gtrsim 10^8 M_{\odot}$, the lifetime of most SNRs in the SOI is ended by disruption by the SMBH while the SNR is in the adiabatic stage. Shallower inner gas density profiles (green and red lines) amplify these trends.

2.7 Discussion and conclusions

In this chapter, we presented a novel numerical method based on the Kompaneets approximation for calculating the evolution of a shock in an arbitrary axisymmetric

¹²Note that $dN(M > 8) = n_{\text{cc}}(R)R^2 dR$ is constant for $R \leq R_b$.

configuration of density. Our approach has the benefit of being more flexible than analytic solutions (which only exist for some simple density stratifications) while being much faster than full hydrodynamical simulations.

We apply this numerical method to trace the evolution of SNRs in quiescent galactic nuclei, with properties similar to those of our Galactic Centre. We describe these nuclei as self-regulating and steady-state systems, where gas inflow from outside this region has been limited and unimportant during at least the last 100 Myr. In this scenario, most of the star formation occurs in situ, recycling the gas ejected in supernovae, and winds from massive stars feed the accretion flow, which forms most of the interstellar gas. We predict the morphological evolution of SNRs in these nuclei, and relevant time-scales such as their X-ray lifetimes.

We find that the supernova remnants that explode very near low-mass SMBHs ($\lesssim 10^8 M_\odot$, such as Sgr A*) will pass over the SMBH before appreciably decelerating and will continue expanding almost spherically. Although there can be prominent distortion during the early evolution of SNRs that explode further away from these SMBHs, SNRs at all explosion distances appear reasonably spherical by the onset of the radiative regime, much like SNRs in a typical interstellar medium. Notably, in the Galactic Centre, this implies that an SNR should be observable in X-ray for $\sim 10^4$ yr. The presence of a suspected SNR enveloping Sgr A*, known as Sgr A East (Maeda et al. 2002), fits with our prediction of SNRs being able to survive their adiabatic expansion through the Galactic Centre region.

If the SMBH mass is large enough ($\gtrsim 10^8 M_\odot$), we instead expect a wide range of SNR morphologies, depending on the explosion distance from the SMBH. There, SNRs typically end their life due to tidal shearing and disruption. The observable lifetime is therefore suppressed ($10^2 \sim 10^3$ yr) with respect to SNRs evolving around lower mass SMBHs. The reductions in SNR lifetime depend on the inner gradients of gas density as predicted by accretion theory. Conversely, therefore, observations of SNRs can be used to infer and constrain properties of their environment. For example, variations in the density gradients can produce different global quantities such as the mean lifetime of SNRs (Fig. 2.12) or their overall sizes in their early evolution (Figs 2.7 and 2.8).

The disruption of the SNR, or fraction of it, by the central SMBH, that takes place when this material slows down below the Keplerian velocity would lead to a period of enhanced accretion on to the central black hole. If a significant fraction of the sheared material is trapped by the SMBH we expect accretion of a few solar masses on to the SMBH over a period of ~ 100 yr, yielding (assuming efficiency of 0.1) a luminosity of the order of 0.7×10^{44} erg s $^{-1}$. This enhanced accretion would be at the sub-Eddington rate for the higher mass black holes (above $0.5 \times 10^6 M_\odot$) but still very significant and at a level comparable to a powerful AGN. This may lead to a period of flaring of the otherwise quiescent black hole. Such events would happen even around the Galactic Center and other small-mass SMBHs. While SNRs are not completely disrupted around such black holes we still expect events in which up to 20% of the

SNR material is accreted on to the central black hole over a period of about a hundred years leading to significant flaring.

Beyond the Milky Way, an excellent example of an SNR that is resolved in a galactic nucleus is S Andromedae (SN 1885A), which has an angular diameter of about 0.7 arcsec and has a morphology resolvable by the *Hubble Space Telescope* (Chevalier and Plait 1988; Fesen et al. 1999, 2007). The SNR is only 60 parsecs from the centre of the bulge of the Andromeda galaxy, though not quite within the SMBH SOI. Although SNRs such as S Andromedae are resolvable in other galactic nuclei with the current generation of instruments, individual SNRs may not be distinguished in more distant galaxies.

For those distant galaxies, it is possible to use our formalism to predict global quantities that can be observed, such as the number of SNRs expected at a given time and therefore their total X-ray luminosity. Exploiting the link between SNRs and young massive stars, it is also possible to estimate the expected SFR in the spheres of influence of quiescent SMBHs. These studies, which will be presented in Chapter 3, and their comparison with observation, can inform theory of nuclear assembly and galaxy formation in general.

Acknowledgements

This work was supported by the Netherlands Research Council (NWO grant numbers 612.071.305 [LGM] and 639.073.803 [VICI]) and by the Netherlands Research School for Astronomy (NOVA). TP was supported by the ISF I-Core centre for excellence and by a grant from the Israel Space Agency (ISA). We thank an anonymous referee for helpful comments.

Appendix 2.A: Integrals of density in the ejecta-dominated stage

Here, we elaborate on the treatment of the integrals over the density discussed in Section 2.3.1. The general angle-dependent approach is given, as well as the integrations over a sphere for reference.

Angle-dependent integrals

Beginning with equation (2.3), we consider explosions either outside or inside the break in density. In general, the integrals along R' can be partitioned into segments between some radii R'_{lower} and R'_{upper} ,

$$M_{\text{part}} = \rho_a a^\omega \int_{R'_{\text{lower}}}^{R'_{\text{upper}}} R^{-\omega} R'^2 dR', \quad (2.26)$$

which, when summed to compose the full integral from $R' = 0$ to $R' = L$, give the full mass swept out over the path. The integrals are split in such a way to calculate sections that are entirely within one of the two possible density gradients ω .

For explosions outside the break in density, if a shock segment has an initial angle $\psi_0 > \sin^{-1}(R_b/a)$, the segment will not cross into the region interior to the break, and the integral is fully through the $\omega = 3$ region. However, if $\psi_0 \leq \sin^{-1}(R_b/a)$, the element of the shock crosses the break. In such cases, the radius R' extending from $R = a$ has either one or two¹³ solutions for the intersection with the sphere of radius (measured from the SMBH) equal to R_b :

$$R'_{b\pm} = \frac{1}{2} \left(s \pm \sqrt{s^2 - 4(a^2 - R_b^2)} \right), \quad (2.27)$$

where $s \equiv 2a \cos \psi_0$. For explosions outside the break, the integral can be split into three possible regions (with $R'_{b\pm}$ provided by equation 2.27): $R' < R'_{b-}$, or $R'_{b-} < R' < R'_{b+}$, or $R' > R'_{b+}$. These ranges define the integral limits, where each integral has the general form

$$M_{\text{part}} \propto a^\omega \int \frac{r^2}{(a^2 + R'^2 - sR')^{\omega/2}} dR'. \quad (2.28)$$

The same holds for explosions inside the break, except that there is only one solution, R'_b for the intersection with the surface at $R = R_b$ and equation (2.28) has only two sets of limits: $R' < R'_b$, and $R' > R'_b$. The general solutions to the angle-dependent integrals using these limits are lengthy and are not reproduced here.

Integrals over a sphere

Due to the introduction of an axis of symmetry by the offset position of the sphere, the mass integral may be simplified using cylindrical coordinates with this symmetry axis (the cylindrical z) aligned on the explosion point. A spherically symmetric density field (having an origin coincident with that of this cylindrical coordinate system) remains constant over the cylindrical polar angle φ , for a given cylindrical¹⁴ r and z , since the spherical $R (= \sqrt{r^2 + z^2})$ is constant. Thus the expression for mass is reduced to a double integral.

In such a coordinate system, for a single power-law density of exponent $-\omega$, the mass swept up (M_s) by a spherical shock front that has expanded through a radial distance L (measured from the explosion point, a)

$$M_s = 2\pi\rho_a a^\omega \int_{a-L}^{a+L} \int_0^{\sqrt{L^2 - (z-a)^2}} r (r^2 + z^2)^{-\omega/2} dr dz. \quad (2.29)$$

¹³For $\psi_0 = \sin^{-1}(R_b/a)$ and $\psi_0 < \sin^{-1}(R_b/a)$, respectively

¹⁴Note that we use R to designate the spherical radial coordinate, and r to designate the cylindrical one.

For the single density distributions of $\omega = 1$ and 3, this evaluates to

$$M_s = \begin{cases} \frac{2\pi\rho_a}{3} \left[(a+L)^3 - |a-L|^3 - 6a^2L \right], & \omega = 1 \\ 2\pi\rho_a a^3 \left[\ln\left(\frac{a+L}{a-L}\right) - \frac{2L}{a} \right], & a > L, \quad \omega = 3. \end{cases} \quad (2.30)$$

In the case $a > L$ for the $\omega = 1$ solution, the term in brackets reduces to $2L^3$ such that $M_s = 4\pi\rho_0 L^3/3$, which is the trivial $\omega = 0$ solution.

For a model density in which there is a broken power-law distribution, the integral over a sphere centred at $z = a$ is less straightforward. To avoid introducing complicated integral limits to equation (2.29), one approach is to determine the over-all quantity by summing integrals over two density distributions, where the integrand for each is restricted using Heaviside step functions, H , that break the distribution at specified (spherical) radii, R . Using the cylindrical integral of equation (2.29), and taking a density distribution that is non-zero between two spherical radii from the origin, $R = P$ and $R = Q$, this effectively constrains the density as

$$\rho \rightarrow \rho \times \left[H\left(\sqrt{r^2 + z^2} - P\right) - H\left(\sqrt{r^2 + z^2} - Q\right) \right]. \quad (2.31)$$

For a two-section broken power-law density with ω_{in} and ω_{out} , the total swept-up mass will be $M_s = M_{\text{in}} + M_{\text{out}}$. The solutions for $\omega = 1$ and 3 are given below.

As an alternative method, solutions for $\omega = 1/2$ and $3/2$ were obtained using integrals of the unconstrained density by instead splitting the integrated regions into spherical caps, and adjusting the integral limits appropriately. These curves match the behaviour of those for $\omega = 1$ and 3, showing agreement between the two methods of integration.

Solution for $\omega = 1$

For an explosion at $R = a$ and an outer break at $R = c$:

$$\begin{aligned} M_1 = \frac{\pi\rho_0}{3} & \left[H(a+L) \left\{ (a+L)^2 [2(a+L) - 3a] \right\} \right. \\ & - H(a+L-c) \left\{ (a+L-c)^2 [2(a+L) + c - 3a] \right\} \\ & - H(|a-L|) \left\{ (a-L)^2 [2|a-L| - 3a] \right\} \\ & \left. + H(|a-L|-c) \left\{ (|a-L|-c)^2 [2|a-L| + c - 3a] \right\} \right]. \quad (2.32) \end{aligned}$$

Solution for $\omega = 3$

In this case, an inner density break at $R = c$ needs to be applied:

$$\begin{aligned}
 M_3 = 2\pi\rho_0 a^3 \left[H(a+L-c) \left\{ \frac{(c-a-L)^2}{2ac} \right. \right. \\
 \left. \left. - \ln\left(\frac{c}{a+L}\right) - \frac{a+L}{c} + 1 \right\} \right. \\
 \left. + H(a-L-c) \left\{ \ln\left(\frac{c}{a-L}\right) + \frac{a-L}{c} - 1 \right\} \right. \\
 \left. + H(|a-L|-c) \left\{ \frac{(c-|a-L|)^2}{2ac} \right\} \right]. \quad (2.33)
 \end{aligned}$$

Analytic volume, time and velocity expressions in the Kompaneets approximation

Solutions for the volume, time and velocity are given in K92, with the given coordinate transformation, for power laws of $\omega = 0$ and 4. Instead, $\omega = 1$ and 3 are relevant for the presently considered density profiles, and we outline here the corresponding solutions.

In a general radial power-law profile, the solution for the volume is (see equation 2.8, as well as equation 16 in K92)

$$\begin{aligned}
 V &= 2\pi \int_{R_-}^{R_+} (1 - \cos\theta) R^2 dR \\
 &= 2\pi \int_{R_-}^{R_+} \left\{ 1 - \cos\left(\frac{1}{\alpha} \cos^{-1}\left[\frac{1-x^2 + \left(\frac{R}{a}\right)^{2\alpha}}{2\left(\frac{R}{a}\right)^\alpha}\right]\right) \right\} R^2 dR, \quad (2.34)
 \end{aligned}$$

recalling that $\alpha \equiv (2 - \omega)/2$. For $\omega = 1$ and 3,

$$R_{\pm} = \begin{cases} a(1 \pm x)^2, & \omega = 1 \\ \frac{a}{(1 \mp x)^2}, & \omega = 3 \end{cases} \quad (2.35)$$

are the leading (R_+) and trailing (R_-) points of the shock (along $\theta = 0$, using equation 2.8). When comparing the equations for $\omega = 1$ and 3 with the ψ_0 parametrisation, it is important to note that a phase shift of π in ψ_0 is required to obtain correspondence (of the definition of R_- and R_+ , for example) between the two cases. In terms of x ,

this gives the following solutions:¹⁵

$$V(x) = \kappa_V \times \begin{cases} x^3 (1 + x^2), & \omega = 1 \\ x^3 \frac{(1 + x^2)}{(x^2 - 1)^6}, & \omega = 3 \end{cases} \quad (2.36)$$

for

$$\kappa_V \equiv \frac{32\pi a^3}{3}. \quad (2.37)$$

Therefore the time can be found from the following integrals of equation (2.6):

$$t(x) = \kappa_t \times \begin{cases} \int_0^x \sqrt{u^3 (1 + u^2)} \, du, & \omega = 1 \\ \int_0^x \sqrt{\frac{u^3 (1 + u^2)}{(u^2 - 1)^6}} \, du, & \omega = 3 \end{cases} \quad (2.38)$$

for

$$\kappa_t \equiv \sqrt{\frac{256\pi a^5 \rho_0}{3\lambda E (\gamma^2 - 1)}}. \quad (2.39)$$

The $\omega = 1$ result may be written via a power-series expansion about $x = 0$,

$$t_1(x) = \kappa_t \left(\frac{2x^{5/2}}{5} + \frac{x^{9/2}}{9} - \frac{x^{13/2}}{52} + \dots \right). \quad (2.40)$$

The integral for $\omega = 3$ is divergent for $x \rightarrow 1$, and is represented by the power series about $x = 0$

$$t_3(x) = \kappa_t \left(\frac{2x^{5/2}}{5} + \frac{x^{9/2}}{9} + \frac{59x^{13/2}}{52} + \dots \right). \quad (2.41)$$

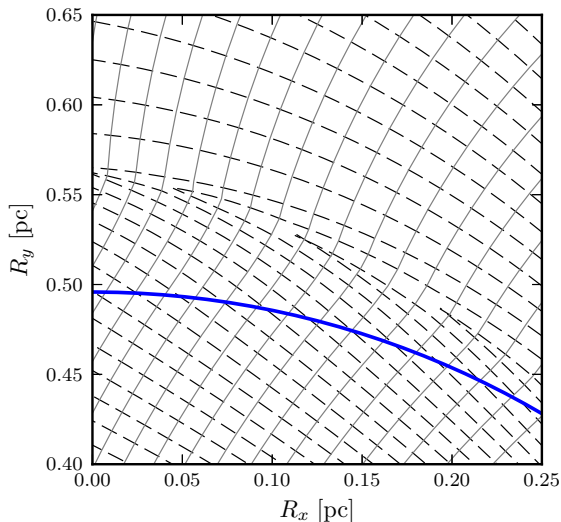
For $\omega = 1$, the value of $x = 1 \leftrightarrow y = y_c$ signifies the moment at which the trailing point of the shock reaches the density singularity ($R_- = 0$). This is, therefore, also the onset of shock self-interactions as other parts of the shock wrap around this point. This occurs in a finite time t , and, unlike in the $\omega = 3$ case, solutions still exist beyond $x = 1$ (there is no blow-out of the shock front, as in the case of $\omega = 3$ where the leading point $R_+ \rightarrow \infty$).

In terms of x , we therefore have

$$v_n(x) = \kappa_v \times \begin{cases} \sqrt{\frac{1}{x^3 (1 + x^2)}}, & \omega = 1 \\ \sqrt{\frac{(x^2 - 1)^6}{x^3 (1 + x^2)}}, & \omega = 3 \end{cases} \quad (2.42)$$

¹⁵The identity $\cos(2 \cos^{-1} z) = 2z^2 - 1$ is useful for the solution to these integrals.

Figure 2.13: Example of flow-line intersection and merging due to the presence of a boundary (thick blue line) between two power-law densities. Dashed lines show flow-line paths, which lie perpendicular to the shock front (sample shock snapshots are given as solid grey lines). In this example, the break is between power laws of $\omega_{\text{in}} = 1/2$ and $\omega_{\text{out}} = 3$, for an explosion around a $10^7 M_{\odot}$ SMBH at $R_x = 0.6$ pc, $R_y = 0$.



for

$$\kappa_v \equiv \sqrt{\frac{3\lambda E (\gamma^2 - 1)}{64\pi a^3 \rho(R)}}. \quad (2.43)$$

Together, these expressions allow a transformation of the solution in terms of x into physical units. We are now in a position to compare the numerical solutions with analytic ones, as is done in Section 2.4.2.

Appendix 2.B: Numerical treatment of shock self-interactions

Here, we outline the treatments of self-interacting segments of the shock front in our numerical scheme. In an axisymmetric arrangement, self-interactions can happen in two ways. In the first case, any parts of the shock that pass over the axis of symmetry (the x -axis in our coordinates) will collide with the complementary part of the shock travelling over the axis in the opposite direction. This can happen as the shock wraps around the SMBH, where the density is at its highest. Other shock self-interactions can be caused by variations in the density profile that force flowlines to converge, such as near a break in power-law densities (see Fig. 2.13 for an example).

We therefore need a routine that can detect self-interactions in a general way. A simple implementation would be to examine the location histories of the flowlines to determine if any have intersected. In our experience, storing these histories puts too high a demand on memory. Instead, two methods for detecting interacting regions in the shock front were investigated.

The first approach is an anticipatory one, which tests the spatial divergence of the velocity of the shock front at each time step. This quantity gives an indication of whether portions of the shock front are converging. However, care is required in choosing the threshold of divergence used to define merging regions of the shock, which results in this divergence method being difficult to tune.

In practice, it is more straightforward to use a reactive detection of self-interactions. The shock front, defined by the positions of the flowlines at one point in time, is constrained algorithmically to be a simple piecewise linear curve. Any intersections along the curve can be detected, as we monitor the ordering of the points. Loops arising from intersections of the shock front are removed, which is equivalent to an effective merger of all flowlines involved in the intersecting loop into a single resultant flowline.

In all cases of self-interactions, the merged flowlines are replaced by a single flowline with an average of their positions. The ejecta mass represented by the new flowline is taken to be the sum of the masses assigned to the previously merging flowlines.

Fig. 2.13 shows an example of regions along a sample shock solution in which flowlines are converging and being merged. This specific example models fluid elements (flowlines; dashed curves) at the shock front (solid grey lines) colliding due to the change in gradient of the background density (thick line).

3 The contribution of young core-collapse supernova remnants to the X-ray emission near quiescent supermassive black holes

A. Rimoldi, E. M. Rossi, E. Costantini, S. F. Portegies Zwart
Monthly Notices of the Royal Astronomical Society, 456, 3 (2015)

Appreciable star formation, and, therefore, numerous massive stars, are frequently found near supermassive black holes (SMBHs). As a result, core-collapse supernovae in these regions should also be expected. In this chapter, we consider the observational consequences of predicting the fate of supernova remnants (SNRs) in the sphere of influence of quiescent SMBHs. We present these results in the context of ‘autarkic’ nuclei, a model that describes quiescent nuclei as steady-state and self-sufficient environments where the SMBH accretes stellar winds with no appreciable inflow of material from beyond the sphere of influence. These regions have properties such as gas density that scale with the mass of the SMBH. Using predictions of the X-ray lifetimes of SNRs originating in the sphere of influence, we make estimates of the number of core-collapse SNRs present at a given time. With the knowledge of lifetimes of SNRs and their association with young stars, we predict a number of core-collapse SNRs that grows from ~ 1 around Milky Way-like ($4.3 \times 10^6 M_{\odot}$) SMBHs to ~ 100 around the highest mass ($10^{10} M_{\odot}$) SMBHs. The presence of young SNRs will amplify the X-ray emission near quiescent SMBHs, and we show that the total core-collapse SNR emission has the potential to influence soft X-ray searches for very low-luminosity SMBHs. Our SNR lifetime estimates also allow us to predict star formation rates in these regions. Assuming a steady-state replenishment of massive stars, we estimate a star formation rate density of $2 \times 10^{-4} M_{\odot} \text{ yr}^{-1} \text{ pc}^{-2}$ around the Milky Way SMBH, and a similar value around other SMBHs due to a weak dependence on SMBH mass. This value is consistent with currently available observations.

3.1 Introduction

Supermassive black holes (SMBHs) are thought to exist in almost all massive galaxies (Ferrarese and Ford 2005; Marleau et al. 2013). In the local Universe, the vast majority of these SMBHs are now quiescent, and radiate at many orders of magnitude less than the Eddington luminosity; most notably, this is observed for the Galactic Centre SMBH, Sgr A* (Melia and Falcke 2001; Alexander 2005; Ho 2009; Genzel et al. 2010).

Increased star formation rates (SFRs), along with massive stars, are seen towards the centre of many galaxies (Sarzi et al. 2005; Walcher et al. 2006; Schrubba et al. 2011; Kennicutt and Evans 2012; Neumayer and Walcher 2012). The best studied nucleus containing these features is that of the Milky Way, where massive stars have been observed in a high concentration out to half a parsec from the SMBH (for example, Do et al. 2013b,a; Lu et al. 2013). It is generally believed that winds from these stars are accreted on to the SMBH through a radiatively inefficient flow, which results in a gas density that is a decreasing power-law function of radius from the SMBH (Quataert 2004; Cuadra et al. 2006; Genozov et al. 2015).

These massive stars are also the eventual progenitors of core-collapse supernovae (SNe) in galactic nuclei. Within the sphere of influence of Sgr A* (the region within which the gravitational potential of the SMBH is dominant), evidence for at least one supernova event has been observed in the supernova remnant (SNR) Sgr A East. This SNR appears to be engulfing Sgr A* with a radius of several pc, and its age has been estimated to be $\sim 10^4$ yr (Maeda et al. 2002; Herrnstein and Ho 2005; Lee et al. 2006; Tsuboi et al. 2009). Recently, *XMM-Newton* observations over a larger scale in the Galactic Centre have been interpreted to suggest the presence of a second SNR, some 20 pc across (Ponti et al. 2015).

In addition, a number of stellar remnants have been detected in the Sgr A* sphere of influence, pointing again towards supernova explosions in the past of this nucleus. The Cannonball neutron star (CXOGC J174545.5-285829) has been proposed as originating from the supernova event that created Sgr A East, and is currently close to the edge of the SNR ejecta shell (Park et al. 2005); tracing its motion back to the centre of the shell suggests an age of 9000 yr (Zhao et al. 2013). Recently, a magnetar (SGR J1745–2900) was discovered at $\lesssim 2$ pc from Sgr A*, and this has been postulated as being associated with the possible 20 pc SNR (Ponti et al. 2015). The presence of stellar remnants within the sphere of influence has also been confirmed from the observation of at least four X-ray binaries (XRBs) within 1 pc of the SMBH, though whether they are high- or low-mass XRBs is uncertain (Muno et al. 2005).

Unlike those in the solar neighbourhood, the SNRs in galactic nuclei evolve in an exceptional gaseous environment that is dominated by a radiatively inefficient accretion flow around the SMBH. The importance of understanding how SNRs evolve in these environments is highlighted, for example, in recent work by Gaggero et al. (2015) modelling the Galactic Centre γ -ray excess using a high supernova rate in the

region. In the previous chapter (Rimoldi et al. 2015), we developed a numerical shock solver to predict the evolution of SNRs in quiescent galactic nuclei, and showed how their age, size and shape are influenced by the accretion flow properties. Leveraging the results from that work, here we propose the use of X-ray emission from young SNRs to study the close environment of quiescent SMBHs.

In searches for low luminosity SMBHs, X-rays are often used to avoid extra-nuclear contaminants that affect optical emission (for a recent example, see Miller et al. 2015); however, these X-ray searches are not without their own contaminants, and the emission from XRBs is regularly discussed as a prominent contribution. Yet, if we could observe our Galactic Centre from a more distant perspective, SNR emission would in fact be the dominant contaminant, as the Sgr A East SNR is brighter than both Sgr A* and individually detected XRBs in the sphere of influence.

We are, therefore, interested in how the lifetimes of SNRs in other galactic nuclei can be used to estimate the contribution of SNRs to the nuclear X-ray emission. Most importantly for us, a dominant contribution from SNRs may allow us to use the detected X-ray emission to constrain the gas properties and SFR. This information may ultimately help us to understand whether there is a connection between the gas component, the young stellar population and the SMBH that is universal, as well as the nature of this relationship. More generally, this would be an important step forward in the understanding of the interplay between SMBHs and their host galaxies.

In this chapter, we assume that massive star and gas distributions are self-similar in the sphere of influence of quiescent SMBHs, of which our Galactic Centre provides an observational basis. The universality of this model does not differentiate between SMBH environments by galactic morphology. Therefore, a discussion of core-collapse SNe in elliptical galaxies may, at first, appear at odds with the current picture of ellipticals. The morphology of a galaxy is typically a very decisive factor regarding which type of SNe are seen on a galactic scale, and in elliptical galaxies, observational identifications of core-collapse SNe are very rare. They cannot be ruled out completely, however, as shown by the observation of a probable stripped core-collapse (Type Ib) supernova SN 2005cz in the outskirts of the elliptical galaxy NGC 4589, which appears to have undergone some recent star formation due to a merger (Zhang et al. 2008; Kawabata et al. 2010).

Although most of the volume of elliptical galaxies is devoid of star formation, in the vicinity of the SMBH, star formation may still be present within sufficiently cooled accretion flow of stellar winds (analogous to the possible *in situ* origin of the young stars in the Galactic Centre). Surveys of the nuclear regions of local elliptical galaxies suggest an inverse correlation between their nuclear activity and the presence of sufficiently cooled interstellar material near the SMBH (Zhang et al. 2008). In the case of active nuclei, the central engine may prevent the cooling of gas, and, in turn, star formation (Werner et al. 2014). Therefore, it is worth reiterating that our results are only in the context of quiescent nuclei.

Justifications and details of our self-regulating, ‘autarkic’ model are given in Sec-

tion 3.2, where we present our framework for quiescent SMBH environments (see also Chapter 2). In this context, we then predict the total number of SNRs expected in that region at any given time (Section 3.4) and their total X-ray luminosity, of which we also assess the detectability (Section 3.5). Finally, we derive the associated SFRs (Section 3.6). Further elaboration on our findings, and our conclusions, can be found in Section 3.7.

3.2 Galactic nuclear environments

The spheres of influence of quiescent SMBHs have not experienced major continuous inflows of gas for at least the last $10^7 \sim 10^8$ yr, roughly the estimated duty cycle of an active galactic nucleus (Shankar et al. 2009). During this time, the SMBH mass and its sphere of influence have not appreciably grown in size, and the life cycles of a few to many generations of massive stars have passed.

After most of the original accretion disc has been consumed, the SMBH starts accreting from the winds of massive stars at a very sub-Eddington level. The resulting gaseous environment takes the form of an almost spherical, steady-state and radiatively inefficient flow, at least up to a substantial fraction of the sphere of influence (Quataert 2004; Cuadra et al. 2006).

Therefore, massive star and gas properties reflect the current and local environmental conditions within the sphere of influence. In particular, they have had time to create a steady-state system where massive stars are born from the gas in the local accretion flow and give it back in form of winds and SNe. Since, from these components, our model describes quiescent nuclei as closed, self-regulating systems, we call this an ‘autarkic’ model.

As a consequence of this autarkic behaviour, massive star and gas distributions should trace each other and their profile be universal among quiescent spheres of influence, with the total number of stars and the accretion rate proportional to the mass of the SMBH. We therefore expect the same properties, regardless of the global galaxy morphology and assembly history of the nucleus, which should instead be imprinted in the low-mass stellar component of the nucleus.

Due to our vantage point, we have some knowledge of the gas and star distributions in the Galactic Centre. Practically, we can therefore use those observations (Section 3.2.1) to quantitatively develop a general description of quiescent galactic nuclei (Section 3.2.2), extending a method first proposed in Chapter 2.

3.2.1 Galactic Centre observations

The archetypal quiescent galactic nucleus for this work is our Galactic Centre. The SMBH mass (M_\bullet) of Sgr A* is $4.3 \times 10^6 M_\odot$, resulting in a sphere of influence (hereafter SOI) a few parsecs in radius, within which some $M_* \approx 2M_\bullet \approx 10^7 M_\odot$ worth

of stars reside (Schödel et al. 2002, 2003; Ghez et al. 2003; Eisenhauer et al. 2005; Ghez et al. 2008; Gillessen et al. 2009).

The number density distribution of massive stars in the sphere of influence of Sgr A* appears to follow the form of a two-part power law, broken at a radius defined here as R_b (Buchholz et al. 2009; Do et al. 2013b):

$$n_{\text{cc}}(R) = \kappa_n \times \begin{cases} \left(\frac{R}{R_b}\right)^{-2} & R \leq R_b \\ \left(\frac{R}{R_b}\right)^{-4.5} & R > R_b, \end{cases} \quad (3.1)$$

for some constant κ_n , that will be constrained in Section 3.4. The steepness of the gradient outside R_b is more uncertain, due to the low number of stars at this distance; however, for the same reason, the value of the outer gradient does not have a substantial influence on our results.

The gaseous environment in the SOI is dominated by the accretion flow. The measured density at approximately the scale of the Bondi radius (~ 0.04 pc) is $\sim 130 \text{ cm}^{-3}$, where the mass flow has an Eddington ratio of $\dot{M}/\dot{M}_{\text{Edd}} \approx 10^{-5}$ (Baganoff et al. 2003; Wang et al. 2013). We take this radius, hereafter referred to as R_0 , as a reference point for the density. A break in the gas density is expected at $R_b \approx 0.4$ pc where the density of high-mass stars drops off (Quataert 2004; Cuadra et al. 2006). Within R_b , the density gradient depends on the mode of energy transport. In standard advection-dominated accretion flows, the inner power law follows $\omega_{\text{in}} = 3/2$ (Narayan et al. 1995; Narayan and Yi 1995). For convection-dominated flows (Quataert and Gruzinov 2000; Ball et al. 2001) or those with substantial outflows, as in the adiabatic inflow–outflow solution (ADIOS; Blandford and Begelman 1999; Begelman 2012), the inner gradient is shallower at $\omega_{\text{in}} = 1/2$. Although more recent observations tend to favour a density gradient of $R^{-\omega_{\text{in}}}$ with $\omega_{\text{in}} = 1/2$ (Wang et al. 2013), we also explore the whole possible range $\omega_{\text{in}} \in \{1/2, 1, 3/2\}$. Outside R_b , instead, we follow results from simulations and we take R^{-3} (Quataert 2004; Cuadra et al. 2006).

Finally, it is now well established that a molecular torus exists around Sgr A*, which extends from just inside the SOI (~ 2 pc) to about 5 pc from the SMBH (Jackson et al. 1993; Christopher et al. 2005; Liu et al. 2013). The torus has a wedge-like profile, where the inner edge is narrower (~ 0.4 pc thick) than the outer edge (~ 2 pc), and contains molecular hydrogen with a density of $n_{\text{H}_2} \approx 10^4 \text{ cm}^{-3}$.

3.2.2 Quiescent galactic nuclei as autarkic systems

We now consider environments of other quiescent galactic nuclei, and we show how their properties can be scaled with the mass of the SMBH (see also Chapter 2).

The particular region we are most interested in is the SMBH sphere of influence, which contains a total mass in stars of $M_* \approx 2M_\bullet$, and the size of which can be

estimated as a function of SMBH mass, using the M - σ relation (Ferrarese and Merritt 2000; Gebhardt et al. 2000):

$$R_{\text{SOI}} \approx 2.7 \left(\frac{M_{\bullet}}{4.3 \times 10^6 M_{\odot}} \right)^{7/15} \text{ pc.} \quad (3.2)$$

Our reference value for the Milky Way SOI radius is $R_{\text{SOI,MW}} = 2.7$ pc. In the self-similar spirit of our model, we will also scale the break and density reference radii (R_{b} and R_0) proportionally with the SOI size. As for the Milky Way, we associate R_0 with the Bondi radius. This scaling with R_{SOI} therefore implies that the temperature of the gas is proportional to σ^2 . We will comment on some implications of this later in this section.

Within the sphere of influence, the number density distribution of massive stars has the form of equation (3.1), and the total number of these stars is $N_{\text{cc}} \propto M_* \propto M_{\bullet}$. This will be quantified in Section 3.4, where we will predict the associated steady-state supernova rate and compare with observations.

The gas density profile around the black hole is universally set by accretion physics for a radiatively inefficient flow, and it is described in the previous section. The number density, n , however, should be estimated through the continuity equation,

$$\dot{M} \approx 4\pi R^2 m_{\text{p}} n(R) v_{\text{K}}(R), \quad (3.3)$$

where the radial velocity in a geometrically thick accretion flow is approximately the Keplerian value v_{K} . Since the accretion rate \dot{M} is powered by stellar winds, it increases with the stellar number and therefore with the black hole mass in a proportional fashion, $\dot{M} \propto M_{\bullet}$. This implies that such self-similar quiescent SMBHs emit at the same Eddington ratio. It follows that the number density in terms of the Milky Way value at the radius R_0 is

$$n(R_0) \approx 130 \left(\frac{M_{\bullet}}{4.3 \times 10^6 M_{\odot}} \right)^{1/2} \left(\frac{R_{\text{SOI}}}{R_{\text{SOI,MW}}} \right)^{-3/2} \text{ cm}^{-3}. \quad (3.4)$$

Equation (3.4) allows us to express the density distributions around other quiescent SMBHs purely as a function of their mass.

Although other kinds of scaling are possible, this simple scaling with M_{\bullet} is consistent with recent, more in depth treatments of quiescent SMBH circumnuclear media (see Generozov et al. 2015, where their stagnation radius is comparable to the Bondi radius). Moreover, our scaling of R_0 with M_{\bullet} (such that $R_0 \ll R_{\text{b}}$) is compatible with the results in Generozov et al. (2015) in the high-heating limit, which corresponds to continuous star formation in their work (which is also assumed here based on observational evidence in the Milky Way; Figer et al. 2004; Figer 2009; Pfuhl et al. 2011).

In all these galactic nuclei, the density is expected to flatten from the R^{-3} gradient around the scale of the SOI. In this chapter, we more carefully model the ambient

density near and beyond the SOI with respect to Chapter 2. We considered a few possible variations for the way the density levels off: a floor of 1 cm^{-3} (irrespective of radius), a fixed value of 1 cm^{-3} beyond R_{SOI} , and a fixed value of $n(R > R_{\text{SOI}}) = n(R_{\text{SOI}})$. Regardless of the choice, we found the variations in our final results (such as the variation in the predicted temperatures of Section 3.5.1) were minimal. In the remaining work, we impose a floor in the density at the value $n = 1 \text{ cm}^{-3}$.

In this chapter, we additionally embed a molecular torus within the power-law ambient medium. The torus is taken to begin at R_{SOI} and extend to $5 (R_{\text{SOI}}/R_{\text{SOI,MW}})$ pc from the SMBH, with the inner and outer thicknesses described as above (also scaled by $R_{\text{SOI}}/R_{\text{SOI,MW}}$). The density within the torus is taken to be $2 \times 10^4 m_{\text{p}} \text{ cm}^{-3}$ independent of the SMBH mass, as it is a property of the molecular cloud.

3.3 SNR dynamical evolution

For our purposes, we need to trace the evolution of SNRs (including their morphology and shock velocity) in the ambient medium of galactic nuclei explained in Section 3.2. To this end, we use the method developed in Chapter 2, where the reader can find a detailed description.

In short, this method exploits the Kompaneets approximation to follow the evolution of a strong shock from a SNR in an axisymmetric configuration of density. In this chapter, we explode the SNRs at different distances along the axis of symmetry of the molecular torus. Along with the power-law background, this preserves the axisymmetry of the problem that was originally exploited in the design of our code.

Once the shock decelerates, the temperature of the shocked gas becomes sufficiently low for line cooling to efficiently radiate energy from the SNR. Prior to this stage, the SNR is deemed ‘adiabatic’, as the energy lost is a very small fraction of the total energy in the shocked gas. We define the end of the adiabatic stage to occur when the SNR has succumbed to one of two outcomes: either ≥ 50 per cent of the SNR, measured by ejecta mass fraction, has reached this radiative stage ($T \lesssim 10^6 \text{ K}$; $v \lesssim 300 \text{ km s}^{-1}$), or ≥ 50 per cent has been sheared apart from decelerating enough that the velocity is comparable to the local Keplerian velocity around the SMBH. If deceleration is not appreciable, then the SNR shearing happens at a radius

$$R_{\text{sh}} = 1.9 \times 10^{-4} \left(\frac{M_{\bullet}}{4.3 \times 10^6 M_{\odot}} \right) \left(\frac{v_{\text{init}}}{10^4 \text{ km s}^{-1}} \right)^{-2} \text{ pc}, \quad (3.5)$$

where we assumed an ejection velocity of 10^4 km s^{-1} . In all our calculations, R_{sh} is the minimum explosion radius at which a SNR can survive.

We have found that including a molecular torus in our simulations does not have a large effect on the SNR dynamics or morphology, as the shock front effectively diffracts around the barrier and continues its outward motion after self-intersecting on the far side. Therefore, we do not expect tori of the dimensions considered here to

confine or strongly shape the SNR once it has expanded to the scale of the sphere of influence.

3.3.1 X-ray emitting lifetime

Improving on Chapter 2, the more careful modelling of the environment just outside the SOI allows us to more robustly quantify the adiabatic lifetime for SNRs that expand beyond the SOI, and survive through to the radiative stage. We find that, regardless of the specific choice in the way the density flattens (Section 3.2.2), the adiabatic stage ends after a similar time, around 2×10^4 yr.

More generally, we calculate the adiabatic lifetime $t_{\text{ad}}(R)$ of a SNR as a function of distance within the SOI, regardless of its fate (whether sheared or not). We then compute, for a given black hole mass, the mean adiabatic lifetime $\langle t_{\text{ad}} \rangle$ by weighting $t_{\text{ad}}(R)$ by the number density of massive stars at that location (equation 3.1; for more detail see Section 2.5.3 in Chapter 2). The result is shown in Fig. 3.1, with the circles and dashed lines (left-hand axis). The three inner density gradients $\omega_{\text{in}} \in \{1/2, 1, 3/2\}$ are shown, where the red line, $\omega_{\text{in}} = 1/2$, corresponds to that favoured by observations in the Milky Way. For $M_{\bullet} < 10^8 M_{\odot}$, the average SNR ends its life evolving through the radiative phase, while for $M_{\bullet} > 10^8 M_{\odot}$ the combination of ambient medium deceleration and black hole tidal forces disperse the SNR before the radiative stage, shortening the duration of its X-ray emitting phase. The suppression of adiabatic lifetime increases with M_{\bullet} and at $M_{\bullet} = 10^9 M_{\odot}$ is an order of magnitude smaller for $\omega_{\text{in}} = 1/2$.

3.4 Number of adiabatic remnants in a snapshot observation

Using results for the lifetimes of SNRs as a function of distance within the SOI, we proceed to calculate the average number (N_{SNR}) of core-collapse SNRs that could be observed at any given time in X-ray, within the SOI of an SMBH. Knowledge of N_{SNR} will allow us to later determine the expected contribution of young SNRs to the X-ray emission near the SMBH.

We assume here that the accretion flow refilling time-scale from stellar winds is similar to, or shorter than, the supernova rate, such that, on average, previous SNRs do not significantly effect the gaseous environment of subsequent SNRs. This appears to be the case for the Milky Way, where simulations show that a quasi-steady-state gas distribution matching the one we assume here is reached over a time-scale (2×10^3 yr), which is an order of magnitude shorter than the expected supernova rate of one per $\sim 10^4$ yr (Cuadra et al. 2006). In more massive nuclei, we expect the time between SNe to shorten proportionally to the mass input from stellar winds, sustaining the competing effects of supernova sweeping and wind refilling.

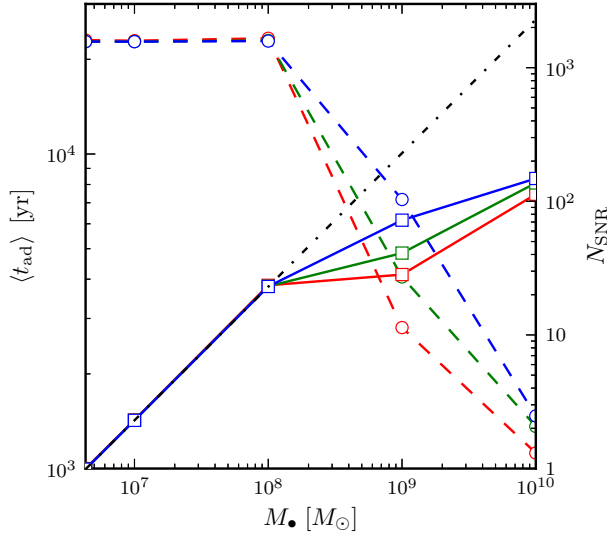


Figure 3.1: Circles with dashed lines (left-hand axis) show the mean adiabatic lifetime of SNRs as a function of M_{\bullet} and ω_{in} , measured by shearing a total of $M_{\text{ej}}/2$. By $\sim 2 \times 10^4$ yr, radiative losses become significant in all cases; if the shearing condition $v_{\text{sh}} < v_{\text{K}}$ has not yet been met by this time, the adiabatic stage ends due to the radiative transition (indicated by a dotted black line at low M_{\bullet}). The squares with solid lines (right-hand axis) show the expected number of adiabatic SNRs in galactic nuclei as calculated in equation (3.6), with a scaling based on the observation of one core-collapse SNR in the Milky Way. In each case, the red line corresponds to an inner gas gradient $\omega_{\text{in}} = 1/2$, the green line is for $\omega_{\text{in}} = 1$ and the blue line is for $\omega_{\text{in}} = 3/2$. The reduction in lifetime by SMBH shearing is compared with the value expected if SNRs ended their adiabatic stage from radiative losses alone ($\sim 2 \times 10^4$ yr), shown as a black dot-dashed line.

In a steady state case, the massive stars are replenished by star formation at the same rate as they explode as SNe, and their number at any location is independent of time. In this case, $dN(M > 8) = n_{\text{cc}}(R)R^2 dR$ in any spherical shell of distance R from the SMBH.¹ The number of ‘adiabatic’ remnants, N_{SNR} , expected at any time in the SOI is thus

$$N_{\text{SNR}} = 4\pi \int_{R_{\text{sh}}}^{R_{\text{SOI}}} \frac{n_{\text{cc}}(R) t_{\text{ad}}(R)}{\langle t_{*}(M > 8) \rangle} R^2 dR, \quad (3.6)$$

where $\langle t_{*}(M > 8) \rangle$ is the stellar lifetime $t_{*}(M) \approx 10^{10} (M/M_{\odot})^{-2.5}$ yr, weighted over the stellar initial mass function (IMF), $\varphi(M)$, for $M > 8 M_{\odot}$. As for the stellar and gas distributions, we take a universal current IMF in black hole SOIs.

¹We assume that the location of the SMBH coincides with the centre of the stellar distribution.

To solve generally for N_{SNR} , the total number of massive stars,

$$N_{\text{cc}} = 4\pi \int_{R_{\text{sh}}}^{R_{\text{SOI}}} n_{\text{cc}} R^2 dR, \quad (3.7)$$

as a function of M_{\bullet} is required. This will allow us to determine $\kappa_{\text{n}}(M_{\bullet})$ in the definition of n_{cc} (equation 3.1), which in turn is to be used in equation 3.6. For $M_{\bullet} = 4.3 \times 10^6 M_{\odot}$, equation (3.6) is simplified by the fact that our simulations, as summarized in Fig. 3.1, show $t_{\text{ad}}(R)$ to be constant (2×10^4 yr) over R within the SOI, since there is no explosion location where SNRs are destroyed by shearing. We can therefore divide through by $t_{\text{ad}}(R)$ and write equation (3.6) as a supernova rate:

$$\mathcal{R}_{\text{SN}} = \frac{N_{\text{SNR}}}{t_{\text{ad}}(R)} = \frac{N_{\text{cc}}}{\langle t_{*}(M > 8) \rangle}. \quad (3.8)$$

From these equalities, we estimate N_{cc} , using observations to set a value for $\langle t_{*}(M > 8) \rangle$ and N_{SNR} , as explained below.

For $\langle t_{*}(M > 8) \rangle$, the mass distribution of core-collapse progenitors is needed. Pfuhl et al. (2011) find that the long-term star formation in the Milky Way nuclear star cluster is best fit by an approximately Chabrier/Kroupa IMF,

$$\begin{aligned} \varphi(M) &= \frac{dN}{dM} \propto M^{-\alpha}, \\ \alpha &= \begin{cases} 1.3, & 0.1 M_{\odot} \leq M \leq 0.5 M_{\odot} \\ 2.3, & 0.5 M_{\odot} < M. \end{cases} \end{aligned} \quad (3.9)$$

With this IMF, the mean stellar lifetime for core-collapse progenitors is

$$\begin{aligned} \langle t_{*}(M > 8) \rangle &= \frac{10^{10} \int_{8M_{\odot}}^{50M_{\odot}} (M/M_{\odot})^{-(2.5+\alpha)} dM}{\int_{8M_{\odot}}^{50M_{\odot}} (M/M_{\odot})^{-\alpha} dM} \text{ yr} \\ &= 2 \times 10^7 \text{ yr}, \end{aligned} \quad (3.10)$$

where stars above $\sim 50 M_{\odot}$ are taken to form black holes directly without a corresponding supernova (Fryer 1999; Yungelson et al. 2008).² Note that this mass function does not describe the current stellar content of the Galactic Centre, since the majority of the total stellar mass is in the longer-lived low-mass stars, most of which formed more than 5 Gyr ago (Pfuhl et al. 2011). The present-day mass function is also modified by accumulated stellar remnants.

As mentioned in Section 3.2.1, there are one or two potential SNRs within the SOI of Sgr A*: the Sgr A East shell and a possible SNR suggested by Ponti et al. (2015) in observations of the ~ 20 pc X-ray emitting lobes. Sgr A East has been argued to be a $\lesssim 10^4$ -year-old Type II SNR that is transitioning to the radiative evolutionary

²The numerical result does not change appreciably if the integration limit is ∞ .

phase (Maeda et al. 2002). The 20 pc structure may be an SNR of similar age, possibly associated with the $\sim 10^4$ -yr-old magnetar SGR J1745–2900 in the sphere of influence (Ponti et al. 2015). Taking at least one of these two possible SNRs to have been generated by a core-collapse supernova in the SOI, we set $N_{\text{SNR}} = 1$. Through equation (3.8), we then derive $N_{\text{cc}} \approx 1000$ for the Milky Way.

There is, however, evidence to suggest that the IMF of, at least, the recently formed stellar disc(s) is more top-heavy ($\alpha \approx 0.45$; Paumard et al. 2006; Bartko et al. 2010). Therefore, we also consider the effect of using $\alpha = 0.45$ in equation (3.9). This reduces the mean stellar lifetime to $\langle t_*(M > 8) \rangle = 9 \times 10^6$ yr, and, therefore, N_{cc} is reduced to ~ 500 . These values of N_{cc} are slightly higher than the number of sufficiently massive stars found in recent censuses of the inner half parsec (around a few hundred; Do et al. 2013a), though some discrepancy may be expected if current K -band spectroscopic limits restrict these observations to very early-type stars and the innermost region (Lu et al. 2013).

Since N_{cc} is proportional to the total stellar mass and $M_* \propto M_\bullet$, the scaling with the mass of the SMBH is simply

$$N_{\text{cc}} \approx 10^3 \left(\frac{M_\bullet}{4.3 \times 10^6 M_\odot} \right). \quad (3.11)$$

Equation (3.6) can now be solved generally for quiescent nuclei as a function of M_\bullet , and our result is shown in the solid lines (right-hand axis) of Fig. 3.1. The number of observed SNRs at any given time grows with M_\bullet from $N_{\text{SNR}} = 1$ for $M_\bullet = 4.3 \times 10^6 M_\odot$ to around 10^2 for $M_\bullet = 10^{10} M_\odot$. This trend is the result of two competing effects: as M_\bullet increases, SNR lifetimes become shorter but the total number of massive stars increases (equation 3.11). Since the latter grows faster, the net behaviour is a positive gradient.

The dot-dashed black line in Fig. 3.1 shows a comparison with the case if SNR lifetimes were not ended by shearing, but instead continued through a final radiative phase ($\gtrsim 10^4$ yr), as is typical in a constant ISM. In this case, $N_{\text{SNR}} \propto M_\bullet$, while our results (solid lines) show a sublinear growth. The reduction is most prominent at the highest masses, where the mean X-ray lifetime of a SNR is several times smaller than 10^4 yr. A spread in the expected number of remnants can be seen to be dependent on the choice of inner gas gradient around $M_\bullet = 10^9 M_\odot$, where the red and blue lines differ by a factor of 3. We will show later that most of local galaxies suitable for X-ray observations have SMBHs around that mass (Section 3.5.3). Therefore, our result suggests that, in principle, it may be possible to use these nuclei to probe the inner accretion flow. We will elaborate on this point later, when we discuss our results on the expected total luminosities (Sections 3.5.3 and 3.7).

In the remainder of this chapter, however, we will only present results for $\omega_{\text{in}} = 1/2$, as this is the most favoured value from recent observations of the Galactic Centre (Wang et al. 2013). Also, this gives a conservative lower limit for our predictions, and, as will be apparent later, our luminosity estimates are more uncertain than the difference between results from alternative gas density profiles.

3.5 X-ray luminosity from SNRs in the sphere of influence

Simultaneous SNRs in their adiabatic phase (Fig. 3.1) should contribute to the X-ray emission from quiescent nuclei. Here, we aim to quantify their total soft and hard X-ray luminosity, compare it to other sources and assess its detectability. In the X-ray band, the SNR dominant emission mechanism is bremsstrahlung radiation, unless the SNR is sweeping into a very rarefied environment (Vink 2012).

Therefore, to make an estimate of their relative brightness in the hard and soft band, we first make predictions of the gas temperature behind the SNR shocks. We calculate this temperature as a function of time as well as the most probable age of a SNR in a single observation, as very young SNRs are hotter than old ones.

3.5.1 SNR spectral properties

We characterize the temperature of SNRs in the sphere of influence of an SMBH by analysing data from the simulations outlined in Chapter 2. The challenge is that the medium is not uniform and different parts of the remnant hold different temperatures and luminosities, and these quantities change with time. Since we want to characterize the emission in a snapshot observation, we need a measure of the temperature that most contributes to the SNR spectrum, at its most probable age. We proceed as follows.

We first determine the temperature behind each point along the shock using the shock front velocity, v_s , via

$$T' = \frac{3m_u\mu}{16k_B}v_s^2, \quad (3.12)$$

for an adiabatic exponent of $\gamma = 5/3$, and where m_u is the atomic mass unit, μ is the mean molecular mass, and k_B is Boltzmann's constant.

At a given moment in time, the SNR mean temperature is found by weighting the temperature behind the shock, T' , at each point along the shock front, by the rate of radiative cooling over the line-dominated (low temperature) and bremsstrahlung-dominated (high temperature) regimes,

$$\Lambda_{\text{li,br}}(\rho', T') \propto \begin{cases} (\rho')^2 (T')^{-1}, & T \leq 3 \times 10^7 \text{ K} \\ (\rho')^2 (T')^{1/2}, & T > 3 \times 10^7 \text{ K}, \end{cases} \quad (3.13)$$

where ρ' is the density behind the shock. For a strong shock, the postshock density is found simply from the compression ratio $\rho'/\rho = 4$. Next, T' is weighted by the surface area, 'A', of each section of the SNR, which is the conical frustum (excluding circular caps) obtained by rotating the small cross-sectional segments of the shock front at that position about the axis of symmetry. The spatial mean of T' is computed along the entire evolution of the SNR.

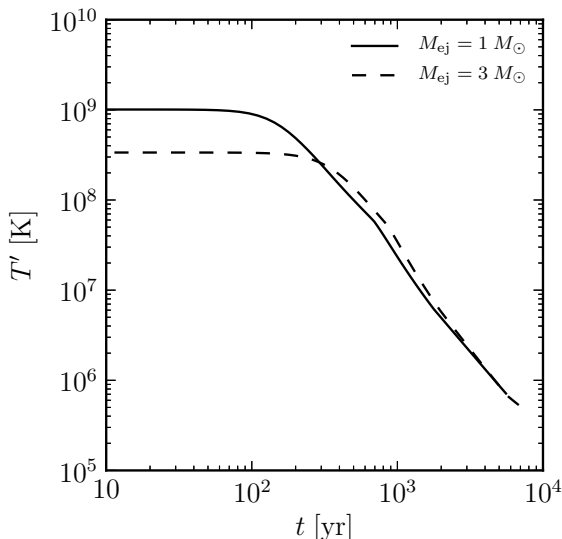


Figure 3.2: Temperature of an SNR, averaged by emissivity over the SNR surface as described in Section 3.5.1. The SNR shown here explodes at 10 pc from an SMBH of mass $10^9 M_\odot$. The solid line represents an ejecta mass behind the shock of $1 M_\odot$, while the dashed line shows a mass of $3 M_\odot$. In each case, the adiabatic evolution stops when more than 50 per cent of this mass is tidally sheared (which defines the last time point on this figure).

Two examples of this temperature evolution are plotted in Fig. 3.2, both at an explosion distance of 10 pc away from an SMBH of mass $M_\bullet = 10^9 M_\odot$. They clearly show how initially a supernova may be tens of keV hot, while thousands of years later its temperature can be well below 1 keV. The SNR depicted with the solid line has an ejecta mass of $1 M_\odot$, while the dashed line shows the case for an ejecta mass of $3 M_\odot$, to investigate variation in ejecta mass behind the shock front.

The shock velocity at the start of the ejecta-dominated stage in our simulations is determined by depositing the $\sim 10^{51}$ erg of explosion energy as kinetic energy into the given ejecta mass. Therefore, the higher mass of ejecta has a lower initial velocity, but takes longer to decelerate due to the need to sweep up more material before reaching the adiabatic stage. We ran simulations over all the $\omega_{\text{in}} = 1/2$ initial conditions with $M_{\text{ej}} = 3 M_\odot$ for comparison. We find that the late-time evolution of the SNR is relatively indifferent to the ejecta mass, resulting in a negligible difference in the SNR lifetimes compared to those with $M_{\text{ej}} = 1 M_\odot$.

Additionally, we weight the spatial mean by the time spent at that temperature (dt , at the resolution of the simulation snapshots), giving

$$\langle T'(R) \rangle = \frac{\iint T' \Lambda_{\text{li,br}}(\rho', T') dA dt}{\iint \Lambda_{\text{li,br}}(\rho', T') dA dt}. \quad (3.14)$$

This is the expected temperature observed in a single observation of a SNR, exploding at a given radius R from the SMBH.

Finally, we calculate the expected temperature of young SNRs in a given galactic nucleus by weighting $\langle T'(R) \rangle$ by the likelihood of a core-collapse supernova at each

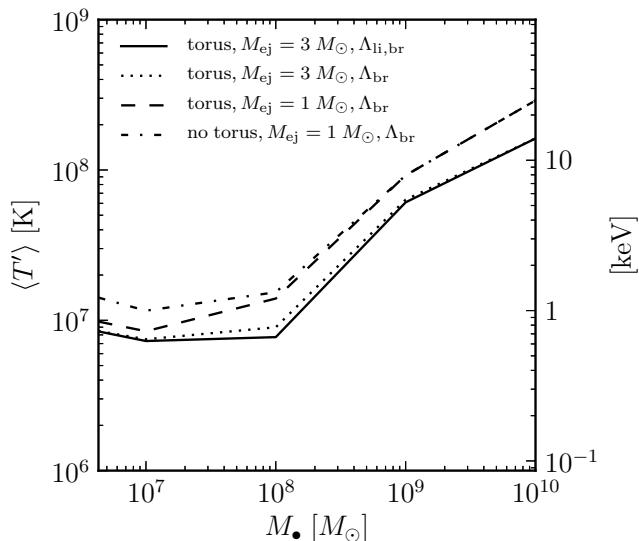


Figure 3.3: Mean temperature (left-hand axis) and corresponding energy (right-hand axis) for X-ray emitting SNRs exploding in the sphere of influence as a function of SMBH mass. Weighted mean temperatures are calculated using equation (3.14) at a given explosion distance, and then equation (3.15) for the entire sphere of influence. Four cases are compared. The solid line shows a molecular torus environment as outlined in Section 3.2 with $M_{ej} = 3 M_{\odot}$ and a cooling function ($\Lambda_{li,br}$) that transitions between the line cooling (T^{-1}) and bremsstrahlung ($T^{1/2}$) relations (equation 3.13). The remaining three curves are calculated with a purely bremsstrahlung cooling relation (Λ_{br}): the same molecular torus profile again with $M_{ej} = 3 M_{\odot}$ (dotted line), a density profile with a molecular torus and $M_{ej} = 1 M_{\odot}$ (dashed line) and a simple power-law density profile with no torus (dot-dashed line) and $M_{ej} = 1 M_{\odot}$.

location, which is proportional to the number density of massive stars, n_{cc} :

$$\langle T' \rangle = \frac{\int_{R_{sh}}^{R_{SOI}} \langle T'(R) \rangle n_{cc}(R) R^2 dR}{\int_{R_{sh}}^{R_{SOI}} n_{cc}(R) R^2 dR}. \quad (3.15)$$

This gives the expected temperature per galactic nucleus, which we plot in Fig. 3.3. In Fig. 3.3, we consider the effects of not only adding the torus and varying the ejecta mass, but also simplifying the cooling function used. The solid and dotted lines of Fig. 3.3 show that replacing the cooling function by a purely bremsstrahlung form, $\Lambda_{br}(\rho', T') \propto (\rho')^2 (T')^{1/2}$, produces only a very minor difference in the result (the density in the ambient medium when the SNR has appreciably decelerated also tends to be low, which reduces the low temperature emissivity). Therefore, for simplicity in the rest of this work, we perform our calculations with the bremsstrahlung-dominated function, $\Lambda_{br}(\rho', T')$.

There is a clear trend in Fig. 3.3 from low to high $\langle T' \rangle$ as the SMBH mass in-

creases. This is due to the shortening of SNR X-ray lifetimes with increasing SMBH mass discussed in Section 3.3.1. SNRs with shortened lifetimes do not spend a long time as cooler, softer X-ray objects, and therefore the expected temperature of an observed SNR is higher. On the other hand, for M_{\bullet} closer to that of Sgr A*, the SNRs do evolve through to the radiative stage, and spend much of their adiabatic life in the softer X-ray stage, reducing the overall expected temperature.

This effect suggests that SNRs around more massive SMBHs will have an influence on harder X-ray observations (for observations that extend to these high energies), while SNRs around lower mass SMBHs are more likely to influence soft X-ray observations. To test the robustness of our results, we again investigate the effect of varying the ejecta mass. We also test the impact of imposing the molecular torus on the density profile. It is evident from all the plotted curves that the final result does not strongly depend on either the presence of a torus or the ejecta mass.

As a caveat, we note that the electron temperature important for bremsstrahlung emission behind the shock front is dependent on the degree of energy equipartition with the shocked ionic component. There is some debate on the degree of equipartition in observed SNR plasmas, in part motivated by the fact that the thermal bremsstrahlung from very young SNRs has not been seen to exceed about 4 keV (for a recent review, see Vink 2012). Therefore, the hotter post-shock temperatures predicted here may be somewhat suppressed when considering the electron temperature relevant for radiative processes.

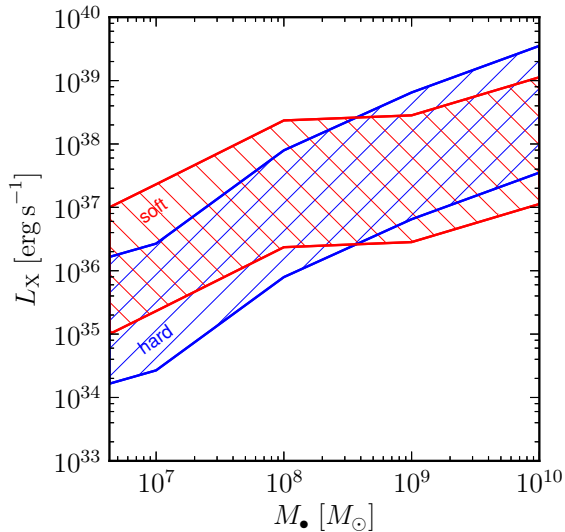
For comparison with observations, we note that the spectrum of Sgr A East has been described with either a plasma with a $k_{\text{B}}T \approx 2$ keV electron temperature (Maeda et al. 2002) or a two-temperature, thermal plasma of 1 and 4 keV (Sakano et al. 2004). The temperature of the bipolar lobes, and possible second SNR, in the Galactic Centre is also fit with a hot component of a comparable value (Ponti et al. 2015). A pervasive X-ray emission at ~ 1 keV is well-known to exist throughout the Galactic Centre region, which has also been attributed to SNRs (Muno et al. 2004; Ponti et al. 2015). These temperatures are in good agreement with the mean expected value for a SNR in the Galactic Centre predicted here.

3.5.2 SNR X-ray luminosity

With a prediction of the total number of SNRs in a sphere of influence as well as their mean temperatures, we can now consider the total integrated X-ray emission from SNRs. As in the previous section, we assume that each SNR contributes an X-ray luminosity that is unaffected by previous SNRs.

Our simulations focus on the dynamical properties of the SNR shock fronts, which allowed us to determine the post-shock temperature in Section 3.5.1. However, in the absence of, at least, a detailed model of plasma properties within the SNR volume as well as associated radiative processes to predict the luminosity from first principles, we turn to X-ray observations of young SNRs to guide our estimates for the total

Figure 3.4: X-ray luminosities for SNRs in the soft (0.35 to 2 keV) and hard (2 to 8 keV) bands. The red back-hatched ('\\') band shows the soft band limits determined from observations of young SNRs. The blue forward-hatched ('/') band shows the range of L_X expected in the hard band; as for Fig. 3.5, this emission is determined from the soft band luminosities scaled using a thermal bremsstrahlung spectrum with the temperature found in Section 3.5.1.



luminosities.

There is a large variation in luminosities observed for young core-collapse SNRs (Dwarkadas and Gruszko 2012). Some of this variation can be attributed to different supernova types. For example, Type II_n SNe are generally brighter in X-rays in the initial $10^3 \sim 10^4$ d compared to other core-collapse types;³ however, even just within the Type II_n classification, there can be variations of orders of magnitude in the early X-ray luminosity. For the most common core-collapse SNe, Type IIP, X-ray luminosities for Galactic SNRs have been estimated to start at $\sim 10^{38}$ erg s⁻¹ and decrease up to an order of magnitude within the first $\sim 10^3$ d (Dwarkadas and Gruszko 2012).

The compilation in Dwarkadas and Gruszko (2012) reports L_X over a range of different bands dependent on the X-ray observatory used. For a broader set of data, we also consider the *Chandra* ACIS Survey of M33 (ChASeM33), which studied a large number of young SNRs (Long et al. 2010). With a survey threshold of $L_{X,0.35-2\text{keV}} \approx 2 \times 10^{34}$ erg s⁻¹ (as well as the fact that M33 is a large, face-on spiral belonging to the Local Group) this provides a large sample of known extragalactic SNRs in soft X-rays. A total of 137 SNRs and SNR candidates were identified, with a median diameter of 44 pc (comparable to a middle-aged SNR) and inferred luminosities ranging from $2.4 \times 10^{34} \sim 1.2 \times 10^{37}$ erg s⁻¹ in the soft X-ray band (0.35–2 keV), with increasing number density for decreasing $L_{X,0.35-2\text{keV}}$. The brightest of these were of intermediate diameter (15 \sim 40 pc) but exhibited localised, enhanced X-ray emission suggestive of interactions with denser material.

There is some variation in the numbers of SNRs at the uppermost values of L_X

³This, along with the narrow hydrogen emission lines observed in their spectra, is attributed to interaction with high-density surrounding material.

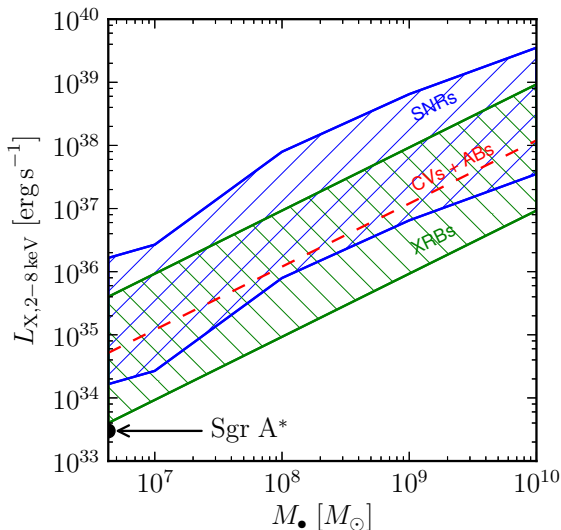


Figure 3.5: X-ray luminosities in the 2–8 keV band for SNRs and XRBs in quiescent SOIs. The blue forward-hatched (‘/’) band shows the limits of L_X if all SNRs were either emitting at the low or high end of observed luminosities for core-collapse SNRs. The hard band emission is determined from observations of X-rays in the soft band scaled using a thermal bremsstrahlung spectrum with the temperature in Section 3.5.1. The green back-hatched (‘\’) band shows the contribution from XRBs based on observations of the Galactic Centre and scaled by total stellar mass. The red dashed line shows the hard component of unresolved emission from the old stellar component (mostly cataclysmic variables and active binaries) in the sphere of influence, as estimated in Ge et. al. (2015). The black point shows the X-ray luminosity observed for Sgr A*.

in the 0.35–2 keV band in M33 compared to the Magellanic Clouds. As suggested in Long et al. (2010), this variation may be attributed to small-number statistics, though there may also be some variation due to differing galactic morphological types. Long et al. (2010) note that three well-known, young SNRs in the Milky Way—Cas A, Kepler and Tycho—are all emitting at around a few $10^{36} \text{ erg s}^{-1}$ in the 0.35–2.0 keV band.

These results from nearby galaxies suggest that, in the soft band, young SNRs are typically seen at $\lesssim 10^{37} \text{ erg s}^{-1}$. We therefore take this value as a conservative upper limit for our SNR luminosities. A lower limit is more difficult to define, in part because there is no definitive boundary between the ‘adiabatic’ and ‘radiative’ stages, and similarly no break in the X-ray luminosities at any such point. SNRs below $10^{35} \text{ erg s}^{-1}$ in the soft band (close to the lower threshold of the ChASem33 survey) are found to be middle-aged and of a well-evolved size. Therefore, we take this luminosity as a lower limit for SNRs in this band.⁴ These upper and lower limits define the hatched regions

⁴Our upper limit is the more important prediction, as we are interested in high end of contaminating SNR luminosities in X-ray searches for quiescent SMBHs.

of SNR X-ray emission in Figs. 3.4 and 3.5 for the total SNR emission in the SOI. This covers the extreme estimates of L_X if all of the N_{SNR} remnants were emitting at the very low or high ends of the expected luminosity from young core-collapse SNRs.

We note that our upper limit is conservative for at least two reasons. The first is that the ambient densities seen in SOI regions are larger than those seen in the typical ISM hosting the SNRs in these surveys. With a higher ambient density, the luminosity of the SNR is also expected to be higher. The second is that, although the luminosities seen in the ChASeM33 survey (and as seen in the LMC and SMC) do not exceed $\sim 10^{37}$ erg s $^{-1}$, luminosities at least an order of magnitude higher have been seen for very young SNRs in the Milky Way (as noted in the aforementioned compilation of Dwarkadas and Gruszko 2012).

In our Galactic Centre, Sgr A East, has a present-day luminosity of $L_{X, 2-10 \text{ keV}} \approx 10^{35}$ erg s $^{-1}$ (Maeda et al. 2002). This is the only well-known SNR near an SMBH, and it appears to be well into its adiabatic lifetime. The luminosity for Sgr A East reassuringly lies between our upper and lower limits for the Milky Way value.

As we aim to compare with XRBs observed in the hard band, we convert between the soft (0.35–2 keV) and hard (2–8 keV) bands using a thermal bremsstrahlung spectrum with the temperature we determined in Section 3.5.1 (given in Fig. 3.3). We integrate the bremsstrahlung emissivity over these frequency bands (ν_{min} to ν_{max}) for a given temperature $\langle T' \rangle$, taking the free–free Gaunt factor to be approximately constant over these bands. For a luminosity in the soft band, the corresponding luminosity in the hard band at $\langle T' \rangle$ is then given by the ratio

$$\frac{L_{X,\text{hard}}}{L_{X,\text{soft}}} = \frac{\exp\left(\frac{-h\nu_{\text{min,hard}}}{k_B\langle T' \rangle}\right) - \exp\left(\frac{-h\nu_{\text{max,hard}}}{k_B\langle T' \rangle}\right)}{\exp\left(\frac{-h\nu_{\text{min,soft}}}{k_B\langle T' \rangle}\right) - \exp\left(\frac{-h\nu_{\text{max,soft}}}{k_B\langle T' \rangle}\right)}. \quad (3.16)$$

In Fig. 3.4, we compare the SNR luminosity in the hard and soft bands by scaling the luminosity from a single SNR by N_{SNR} , using the above conversion from soft to hard band luminosities. This comparison makes it clear that around lower mass SMBHs, where the SNRs tend to evolve through to the radiative stage (and are therefore, on average, cooler), the expected emission favours the soft band. On the other hand, SNRs around more massive SMBHs tend to be younger and hotter on average, and therefore the emission is stronger in the hard band. Therefore, it is clear that SNRs may influence either soft or hard bands in SMBH searches, depending on the SMBH mass.

The sources of X-ray luminosity in the very dense and complex environments of galactic nuclei can be difficult to untangle. As summarized in Ponti et al. (2015), the hard X-ray emission towards the Galactic Centre is substantially influenced by point sources (Muno et al. 2005), and much of the hot thermal bremsstrahlung (~ 7.5 keV) emission seen in the region has been attributed to, at least at a ~ 100 pc scale, the integrated luminosities of unresolved sources (Heard and Warwick 2013a). The light from bright XRBs may additionally be scattered by the neighbouring ISM and molecular

clouds, also at the scale of ~ 100 pc (Sunyaev et al. 1993; Molaro et al. 2014).

A bipolar outflow has also been observed about $14 \sim 20$ pc to either side of Sgr A*, with $L_X \approx 10^{34}$ erg s $^{-1}$ (Morris et al. 2003, 2004; Markoff 2010; Heard and Warwick 2013b; Ponti et al. 2015). This has been attributed to either shock-heated winds from massive stars or tidal disruption events (Heard and Warwick 2013b), or as another possible SNR due to the recently revealed presence of a shock at the lobe boundaries (with a possible $2 \sim 4$ keV component; Ponti et al. 2015).

Here, we restrict our comparison to two other possible X-ray sources that are of interest as contaminants in X-ray searches for quiescent SMBHs: resolved XRBs and unresolved emission from the old stellar component of the nucleus. Munro et al. (2005) have reported the detection of four XRBs within only 1 pc of the Galactic Centre. To characterize these as XRBs, the selection of sources was restricted to those with large outbursts to distinguish them from other, consistently bright point sources. These sources had peak emissions between $L_{X, 2-8 \text{ keV}} \approx 10^{33}$ and 10^{35} erg s $^{-1}$, which is in fact a peculiar range that is between typical values of quiescent and outbursting XRBs; this also makes it unclear whether these are high- or low-mass XRBs (Campana et al. 1998; Munro et al. 2005).

Fig. 3.5 shows an estimate of the combined emission from known point-source, active XRBs at a given time, based on these observations. We use the range of peak luminosities of the four active XRBs seen in the inner ~ 1 pc of the Galactic Centre ($10^{33} \sim 10^{35}$ erg s $^{-1}$), which is represented as a green back-hatched (‘\’) band. As these four XRBs did in fact vary in luminosity over the observed *Chandra* period, taking their peak luminosities for the band on Fig. 3.5 will therefore likely be a conservatively high estimate of the total luminosity. This estimate also implicitly incorporates the remainder of the XRB population as being in quiescence and below the detection threshold at a given time. The X-ray emission for other nuclei is calculated by taking the same ratio of confirmed XRBs to total stellar mass (which scales linearly with M_\bullet) as that observed in the Galactic Centre.

Unresolved X-ray emission also originates from the old stellar population in the region, and is contributed to mainly by cataclysmic variables (CVs) and active binaries (ABs). The associated luminosity has been found to roughly scale with the stellar mass in observations of the Local Group (Revnivtsev et al. 2006, 2009; Ge et al. 2015). We take the hard-band relation $L_{X, 2-8 \text{ keV}} \approx 10^{27}$ erg s $^{-1}$ M_*/M_\odot given in Ge et al. (2015), using the scaling $M_* \approx 2M_\bullet$ in the SOI (Section 3.2). This estimate is given in Fig. 3.5 as the red dashed line.

It is clear from Fig. 3.5 that if nuclei scale similarly with the Galactic Centre, then it is possible for SNRs to compete with the X-ray emission from XRB point sources as well as the unresolved X-ray emission in the hard band. Furthermore, the emission from all of these source types is more luminous than the current X-ray luminosity of Sgr A* itself (a few 10^{33} erg s $^{-1}$). Therefore, for other SMBHs of similar Eddington ratios and L_X/L_{Edd} as Sgr A*, the emission from the central engine can be overwhelmed by contamination from both XRBs and young SNRs.

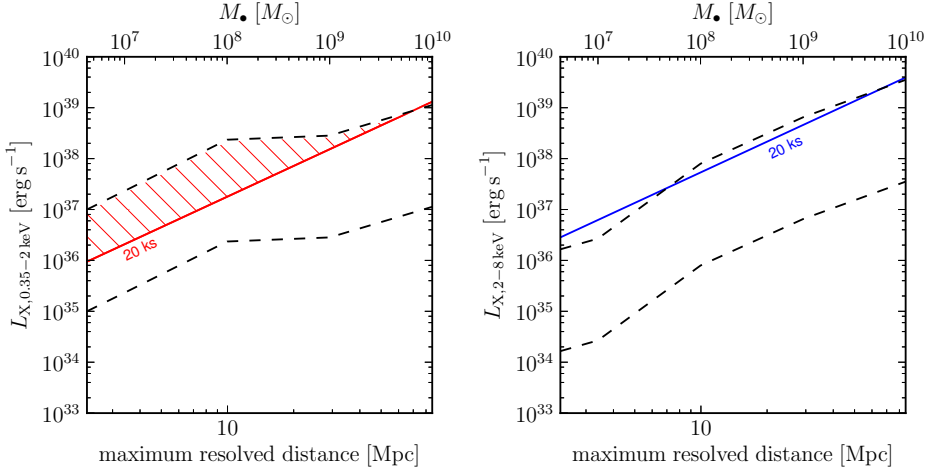


Figure 3.6: Observable limits of the combined X-ray luminosities from young SNRs as a function of SMBH mass (upper axes) or maximum resolved distance (lower axes). The maximum resolved distance is that at which the SOI of the SMBH is within the core of the PSF of *Chandra*. The left-hand panel shows luminosities in the soft X-ray (0.5–2 keV), while the right-hand panel shows hard luminosities (2–8 keV). SNR luminosity limits are the dashed black lines (shown also in Fig. 3.5). Flux-limited detection thresholds from *Chandra* exposure times of 20 ks for galaxies at the distance limit are given as solid lines. The shaded region in the left-hand panel highlights the observable range of luminosities in the soft band.

3.5.3 Detectability

We now consider whether these predictions can be observed, exploiting the high spatial resolution (0.49 arcsec) of the *Chandra* satellite. Fig. 3.6 shows the expected soft (0.5–2 keV) and hard (2–8 keV) X-ray luminosity as a function of the black hole mass. The upper and lower limits of the SNR luminosities in Fig. 3.6 are found in Section 3.5.2 and are the same as those plotted on Fig. 3.4. The solid lines of Fig. 3.6 show the range of luminosities that can be detected by *Chandra*-ACIS-S with 20 ks exposures (based on flux limits of $3 \times 10^{-15} \text{ erg cm}^{-2} \text{ s}^{-1}$ and $9 \times 10^{-15} \text{ erg cm}^{-2} \text{ s}^{-1}$ for a 10 ks exposure). The lower horizontal axes are given in terms of the maximum resolvable distance of the SOI. This is the distance at which the (diameter of the) SOI of the SMBH is just within the core of the point-spread function of *Chandra*. For example, the SOI of a $10^8 M_{\odot}$ SMBH is resolvable at any distance below ~ 10 Mpc; and, at 10 Mpc, the lower limit of detectable soft X-ray emission is given by the red line. At any distance less than 10 Mpc, this detection threshold drops and so fainter emission from SNRs would be detectable.

From Fig. 3.6, it is evident that, even at the maximum resolved distance, the upper

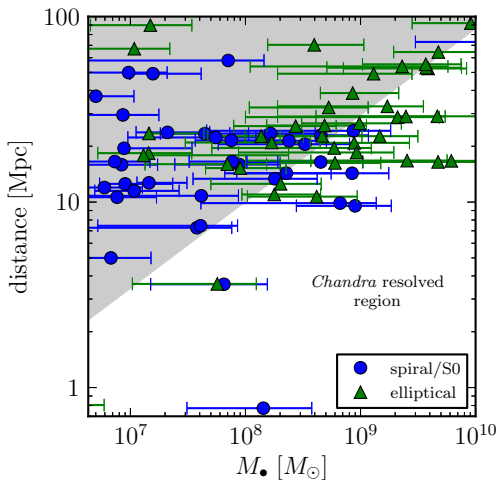


Figure 3.7: Distances and masses (with errors) of known SMBHs over the same mass range considered in this chapter. Data were taken from tables in the review of Kormendy & Ho (2013). Masses were estimated primarily from stellar dynamics, with, in some cases, measurements of gas motions near the SMBH. Blue circles represent spiral or lenticular (S0 Hubble type) galaxies, while green triangles represent elliptical galaxies. The grey region shows the combinations of M_{\bullet} and distance for which the angular size of the SOI is within the core of the *Chandra* point-spread function and the SOI is unresolved. The white region therefore shows the conditions for which the SOI is resolved.

limit of SNR emission is detectable as it is above the 20 ks threshold in the soft band through most of the M_{\bullet} range (although the low end of possible X-ray luminosities is possibly not within the detection threshold of *Chandra*). In the hard band, the *Chandra* 20 ks threshold follows very closely the high limit of predicted SNR emission. This suggests that, for galaxies at the maximum resolved distance, the emission would not be detectable in the hard band. Again, however, if a galaxy is closer than this maximum distance, the threshold marked by the blue solid line will drop; therefore, hard X-ray luminosities are still potentially detectable for more nearby galaxies.

To compare this with the number of SMBHs known at these distances, in Fig. 3.7 we plot the distances and masses of well-established SMBHs constructed from Tables 2 and 3 in the review of Kormendy and Ho (2013) and the references therein. We show in the grey region the cases where the SOI of the SMBH is not resolved by *Chandra*. As for the upper axes in Fig. 3.6, the limit between the grey and white area is determined by the distance at which the SOI of the SMBH equals in size the core of the point-spread function of *Chandra*.

Although the majority of known SMBH SOIs lie in this unresolvable region, a large fraction (~ 30) of the candidates stand out and may be targets to compare with our predictions. Many potential candidates within the axis limits of Fig. 3.7 are members of the Virgo and Fornax clusters (Jordán et al. 2007; Ferrarese et al. 2012). Most of the resolvable SOIs belong to SMBHs with masses $10^8 \sim 10^9 M_{\odot}$, many of which lie well within the maximum resolved distance.

We therefore conclude that our predictions and thus the ansatz of self-regulation and self-similarity for quiescent galactic centres may be testable, currently, for a reasonable population of galaxies.⁵ An obvious next step would be to perform a systematic

⁵One additional hindrance to observing nuclear sources is the inclination of late-type galax-

search of *Chandra* archives for specific examples, but this is beyond the scope of the current work.

3.6 The sphere of influence SFR

Since massive stars trace the star formation history of a region, our previous results also allow us to estimate the SFR in the SOI as a function of the black hole mass. In steady state, the supernova rate, \mathcal{R}_{SN} , is equal to the rate of formation of new stars:

$$\begin{aligned} \mathcal{R}_{\text{SN}} &= \frac{N_{\text{cc}}}{\langle t_*(M > 8) \rangle} = \text{SFR} \frac{\int_{8M_{\odot}}^{50M_{\odot}} \varphi(M) dM}{\int_{0.1M_{\odot}}^{100M_{\odot}} M\varphi(M) dM} \\ &= 1.2 \times 10^{-2} \text{yr}^{-1} \left(\frac{\text{SFR}}{M_{\odot} \text{yr}^{-1}} \right), \end{aligned} \quad (3.17)$$

where ‘SFR’ is the total SFR spread over our fiducial IMF (equation 3.9), and

$$\frac{N_{\text{cc}}}{\langle t_*(M > 8) \rangle} \approx 5 \times 10^{-5} \left(\frac{M_{\bullet}}{4.3 \times 10^6 M_{\odot}} \right) \text{yr}^{-1}, \quad (3.18)$$

combining equations (3.10) and (3.11). This allows us to write the SFR as a function of the black hole mass:

$$\text{SFR} \approx 4 \times 10^{-3} \left(\frac{M_{\bullet}}{4.3 \times 10^6 M_{\odot}} \right) M_{\odot} \text{yr}^{-1}. \quad (3.19)$$

The total SFR as a function of M_{\bullet} is shown as the solid line (left-hand axis) in Fig. 3.8. This corresponds to an SFR density averaged over the whole SOI, Σ_{SFR} , that stays approximately constant around $10^{-4} M_{\odot} \text{yr}^{-1} \text{pc}^{-2}$ in the whole mass range of interest (dashed line, right-hand axis of Fig. 3.8). Making the IMF more top-heavy ($\alpha = 0.45$) does not change the multiplicative factor in the right-hand side of equation (3.17) within the given precision (1.2×10^{-2}), and so the predicted SFR is unaffected.

Few observations of stellar populations at the scale of quiescent SOI are available for comparison with these predictions, not only due to the challenge of resolving parsec-scale properties but also due to obscuration of the nuclear star clusters. We gather some observations below.

For the SOI of the best-studied SMBH, Sgr A*, equation (3.19) predicts an SFR of $4 \times 10^{-3} M_{\odot} \text{yr}^{-1}$, equivalent to an SFR per unit area of $\Sigma_{\text{SFR}} = \text{SFR} / (\pi R_{\text{SOI}}^2) \approx 2 \times 10^{-4} M_{\odot} \text{yr}^{-1} \text{pc}^{-2}$. This is in agreement with the observationally inferred SFR of $7 \times 10^{-4} M_{\odot} \text{yr}^{-1} \text{pc}^{-2}$ in the innermost 1.2 pc (which we expect to have a higher SFR density than the outer sphere of influence), in the last $\sim 10^7$ yr (Pfuhl et al. 2011).

ies to our line of sight. The nuclei of edge-on galaxies are potentially more contaminated by unresolved X-ray point sources and hot, X-ray emitting gas.

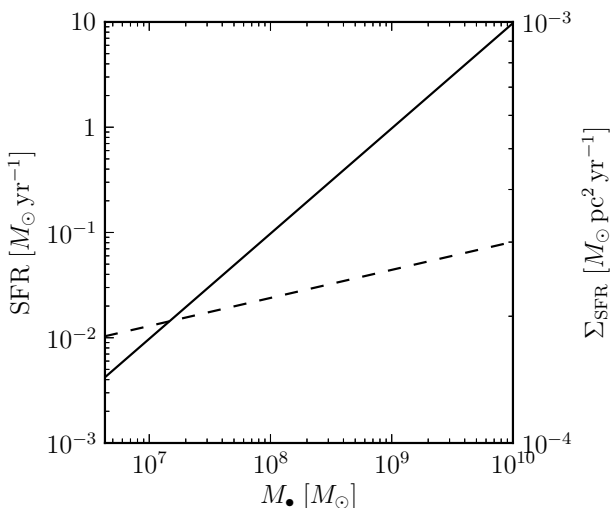


Figure 3.8: Total (solid line; left-hand axis) and surface density (dashed line; right-hand axis) SFRs within the SMBH sphere of influence as a function of SMBH mass.

A sharp increase in SFR is seen with decreasing distance from the centre of many nearby spiral galaxies (Schruba et al. 2011), even if the SOI of the putative SMBH is not resolved. Extrapolating the values of SFR towards the centre of the Milky Way and NGC 6946, shown in Kennicutt and Evans (2012), gives values in line with those predicted here. In small-bulged, late-type spirals, Walcher et al. (2006) can directly resolve the nuclear star clusters within the SOI, because they are not obscured by the presence of a massive bulge. Extending the results to lower mass, the values we find are reasonable for these galaxies. We compare with Walcher et al. (2006) by using their SFR calculated over the most recent 10^8 yr. This gives $\Sigma_{\text{SFR}} \approx 6 \times 10^{-5} M_{\odot} \text{ yr}^{-1} \text{ pc}^{-2}$, for a mean $M_{\bullet} \approx 10^5 M_{\odot}$, where we use the M_{\bullet} estimates in Neumayer and Walcher (2012), and we take a radius equal to the mean effective radius of 3.5 pc from Böker et al. (2004).

Despite the limited observations of SNRs in the Galactic Centre available to anchor our results, these comparisons give support to our autarkic scenario for quiescent galactic nuclei. Ideally, a combination of X-ray observations of SNRs and nuclear SFRs would be needed to refine these predictions.

3.7 Discussion and conclusions

Quiescent galactic nuclei such as that of the Milky Way are frequently seen to harbour massive stars. We have demonstrated, elaborating on work presented in Chapter 2, that their presence can be exploited to gain insights into these common, but not well understood, environments.

Our model for SNR evolution, developed in Chapter 2, can be applied to a diverse

range of descriptions of the regions near SMBHs. However, in particular, we have chosen an ‘autarkic’ framework that is consistent with observations of the Galactic Centre. This describes quiescent SMBH environments that are self-regulating and uninfluenced by any inflows of material beyond the sphere of influence. The gas in the accretion flow is supplied by stellar winds, which also provides part of the material from which new stars are formed. In this model, we take the total rate of star formation, and therefore number of massive stars in steady state, to scale with the total stellar mass in the sphere of influence. As a consequence, the accretion rate is the same fraction of Eddington ($\dot{M}/\dot{M}_{\text{Edd}} \approx 10^{-5}$) as that of Sgr A* in the Galactic Centre.

For SNe exploding in such environments, our dynamic modelling predicts the ‘adiabatic’ lifetimes and therefore total number of core-collapse SNe seen at one time. We find $1 \sim 10^2$ SNRs in the sphere of influence of SMBHs over the mass range 10^6 to $10^{10} M_{\odot}$. As the SMBH mass increases, the reduced lifetime of SNRs competes with the increase in core-collapse progenitors in the region, resulting in a sublinear increase of the observed number of SNRs.

In galactic nuclei beyond the Local Group, for which the resolution of individual SNRs may be more challenging, the presence of hot SNRs can affect the total X-ray emission from the sphere of influence. Therefore, we use the total number of SNRs to estimate the total X-ray emission expected from these regions. One caveat, noted also in Chapter 2, is that the Kompaneets approximation may overestimate the ‘adiabatic’ lifetimes of SNRs. Correcting for this may reduce the X-ray luminosities predicted here, in particular for low-mass SMBHs (which have, on average, longer lived SNRs).

We find that, for nuclei with properties like that of our Galactic Centre, core-collapse SNRs can compete with the emission from X-ray binaries as well as unresolved sources, and can potentially outshine the emission from the central engine itself. This is indeed what is observed for the known X-ray sources in the Galactic Centre, where different X-ray sources be more easily distinguished; the X-ray luminosity within the Sgr A East shell ($\sim 10^{35} \text{ erg s}^{-1}$; Maeda et al. 2002) is higher than that observed from Sgr A* (a few $10^{33} \text{ erg s}^{-1}$; Baganoff et al. 2003; Wang et al. 2013). We predict that this emission could be detectable, particularly in the soft band, out to the maximum distance at which the SMBH sphere of influence is resolved by *Chandra*. Though beyond the scope of the current work, a natural follow-up would be to examine *Chandra* data for specific galaxies.

Knowledge of SNR lifetimes can be used to estimate the SFR and core-collapse progenitor numbers in these environments. For a Milky Way-type galaxy, our estimated SFR density of a few $10^{-4} M_{\odot} \text{ yr}^{-1} \text{ pc}^{-2}$ is in good agreement with other approaches (Pfuhl et al. 2011). This corresponds to a core-collapse progenitor population of $N_{\text{cc}} = 500 \sim 1000$ within the sphere of influence. The SFR obtained for other galactic nuclei shows concordance with available data on SFR in nuclear clusters. Kennicutt and Evans (2012) show the SFR as a function of radius for the specific examples of the Milky Way and NGC 6946, which, at small radii, tend towards the values we predict. Ideally, a combination of X-ray measurements and estimates of SFRs can then be used

to compare with our predictions and understand at what extent quiescent nuclei are autarkic.

The gas models in this chapter were refined by adding molecular tori around the scale of the black hole sphere of influence. Our results with the molecular tori show that they do not generally have a substantial effect on the lifetimes of SNRs or on the overall morphology of the SNR. The minimal impact of the torus on SNR expansion in the Galactic Centre suggests that large-scale asymmetries, such as those seen in Sgr A East or the 20 pc lobes, are not due to dynamical confinement from the molecular torus alone.

One potential improvement to our current approach relates to the X-ray luminosity predictions, which rely on data and are not calculated *ab initio*. Although the use of observations allowed us to make qualitative inferences on the importance of SNRs, more detailed predictions would require a more accurate modelling of the radiative processes within the SNR. This prevents us from quantifying more conclusively the contribution to X-ray of SNRs (Fig. 3.6), or to draw conclusions on the feasibility to use X-ray observations to constrain the gaseous ambient medium gradient. This possibility of using SNRs to constrain the gaseous environment can be seen, for example, in the differences of a factor of a few in the predicted N_{SNR} around a $10^9 M_{\odot}$ SMBH in Fig. 3.1. Constraining the inner gaseous medium bears the exciting promise of pinning down the physics that describes radiatively inefficient accretion flows.

In this work, we have not taken into account additional processes over short time-scales that may affect the accretion rate and luminosity of the SMBH. Temporary increases in accretion rates can occur from the input of small amounts of stellar or gaseous mass from outside the sphere of influence. For example, stellar tidal disruption events like that of *Swift* J1644+57 produce SMBH flaring observed in radio through to X-rays (Komossa 2002; Burrows et al. 2011). An inwards deposition of molecular gas, tidally disrupted into a disc, might also be responsible for the formation of some of the young stars around SMBHs (Levin and Beloborodov 2003; Paumard et al. 2006). We also emphasize that, although SNRs tend to sweep gas out of their environment, explosions near the SMBH may also, at a smaller scale, deposit some material near the SMBH, enhancing accretion and causing temporary flaring.

With respect to outflows, a simple estimate of their importance can be made by comparing the gravitational binding energy of the SMBH-gas systems with that of the total supernova energy. Doing this calculation, we find that the supernova energy is larger than the binding energy at low M_{\bullet} , and that the gravitational binding energy of the gas grows faster than the supernova energy input, but the two values only become comparable by large SMBH masses ($\sim 10^9 M_{\odot}$). If the supernova energy is efficiently deposited into kinetics of the nuclear gas, then outflows due to SNe in quiescent nuclei may be important around lower mass SMBHs. Large-scale expulsion of gas may temporarily reduce the rate of accretion from stellar winds; however, as has been shown for lower mass SMBHs like Sgr A* (Section 3.4), the gas refilling time-scale is shorter than the supernova rate. Such core-collapse-induced outflows from

low-mass SMBHs are a potentially interesting topic of future work.

Finally, our model is anchored to Galactic Centre observations and influenced by uncertainties on the number of current SNRs in the adiabatic phase. These uncertainties certainly propagate through our predictions. With the constant monitoring of the Galactic Centre, as seen in the recent results of Ponti et al. (2015), this model will no doubt become better informed.

We have shown that this autarkic model applied to young stars, gas, and the SNRs amongst them, is a promising framework to understand how these nuclei function and evolve. The predictions of our model can be tested and refined by X-ray observations and SFR estimates of quiescent galactic nuclei.

Acknowledgements

This work was supported by the Netherlands Research Council (NWO grant numbers 612.071.305 [LGM] and 639.073.803 [VICI]) and by the Netherlands Research School for Astronomy (NOVA). The authors thank the anonymous referee for very helpful comments on the manuscript. We also gratefully acknowledge Tsvi Piran for feedback that shaped an early version of this work, and we wish to thank Elena Gallo and Gabriele Ponti for helpful discussions.

4 Simulations of stripped core-collapse supernovae in close binaries

A. Rimoldi, S. F. Portegies Zwart, E. M. Rossi
Computational Astrophysics and Cosmology, 3, 1 (2016)

We perform smoothed-particle hydrodynamical simulations of the explosion of a helium star in a close binary system, and study the effects of the explosion on the companion star as well as the effect of the presence of the companion on the supernova remnant. By simulating the mechanism of the supernova from just after core bounce until the remnant shell passes the stellar companion, we are able to separate the various phenomena leading to the final system parameters. In the final system, we measure the mass stripping and ablation from, and the additional velocity imparted to, the companion stars. Our results agree with recent work showing smaller values for these quantities compared to earlier estimates. We do find some differences, however, particularly in the velocity gained by the companion, which can be explained by the different ejecta structure that naturally results from the explosion in our simulations. These results indicate that predictions based on extrapolated Type Ia simulations should be revised. We also examine the structure of the supernova ejecta shell. The presence of the companion star produces a conical cavity in the expanding supernova remnant, and loss of material from the companion causes the supernova remnant to be more metal-rich on one side and more hydrogen-rich (from the companion material) around the cavity. Following the impact of the shell, we examine the state of the companion after being heated by the shock.

4.1 Introduction

There is substantial evidence that most massive stars evolve in binary systems (Duquennoy and Mayor 1991; Rastegaev 2010; Sana et al. 2012). Therefore, the presence of companion star is an important consideration in the theory and observation of supernovae and supernova remnants (SNRs). In particular, while Type Ia (white-dwarf; WD) supernovae may have a companion which has deposited sufficient mass onto the WD to trigger a ‘single-degenerate’ explosion, many Type Ibc (stripped core-collapse) supernovae may have close companions that have been at least partly responsible for the loss of mass from the progenitor (Bersten et al. 2014; Fremling et al. 2014; Eldridge et al. 2015; Kim et al. 2015; Kuncarayakti et al. 2015).

Observational searches for supernova companions have typically focused on Type Ia explosions. Possible companions have been a subject of scrutiny in order to determine the frequency of the two main suspected (single-degenerate or double-degenerate) explosion channels (Maoz et al. 2014). Hydrogen enrichment from a companion has been searched for in Type Ia SNRs, but so far there has been no evidence of hydrogen lines (Mattila et al. 2005; Leonard 2007; Lundqvist et al. 2015). As noted in García-Senz et al. (2012), detection of H_α lines may be difficult due to confusion with Fe and Co lines due to the mostly slow ($< 10^3 \text{ km s}^{-1}$) hydrogen mixing with iron-peak elements.

The presence of a supernova companion is difficult to directly detect if they are low-mass stars at very large distances, and so far definitive evidence of close companions to any supernova progenitor, let alone those of Type Ibc, has been lacking. Tycho G is probably the best example of a directly imaged, suspected companion, associated with the galactic Type Ia supernova, Tycho (SN 1572; Ruiz-Lapuente et al. 2004), though recent observations put its status as a supernova companion into dispute (Kerzendorf et al. 2013; Xue and Schaefer 2015). On the other hand, some direct searches for single-degenerate companions have ruled out giant/subgiant (evolved) stars (SN 2011fe and SNR 1006; Li et al. 2011; González Hernández et al. 2012) and even main sequence companions (SNR 0509-67.5; Schaefer and Pagnotta 2012).

The presence of a companion due to increased emission, and therefore modification of the standard light curve, from the ejecta interacting with the companion has also been ruled out in observations of Type Ia supernovae (Olling et al. 2015). However, a recently observed supernova (iPTF14atg; Cao et al. 2015) does show evidence of interaction with a companion through the detection of an ultraviolet burst in the first several days.

Though much of the focus of previous work has been on Type Ia explosions, the phenomena of companion interactions with single-degenerate Type Ia ejecta has parallels with core-collapse supernovae in binaries, and therefore this scenario still provides a useful context. A similarity between Type Ia supernovae and Type Ibc supernovae is that the explosion energy in both is believed to be $E_{\text{SN}} \sim 10^{51} \text{ erg} \equiv 1 \text{ foe}$

(Smartt 2009; Dessart et al. 2014).¹ Also, in single-degenerate Type Ia and binary Type Ibc explosions, main sequence companions are typically at small orbital separations. In the former, this is simply due to the requirement for Roche-lobe overflow in the companion in order to transfer mass to the WD; in the latter, this is due to binary interactions and associated dissipative processes leading to circularised close binaries (Tauris and Takens 1998, hereafter, TT98). However, while simulations of Type Ia supernovae have placed the companion at the point of Roche-lobe overflow, the orbital separations in Type Ibc supernovae can be larger than this. Therefore, simulations of the latter are needed to test the distance-dependence of results that have been extrapolated from Type Ia simulations, such as those used in Tauris (2015).

TT98 analytically investigated the consequences of a supernova in a close, circularised binary, with the goal of finding the runaway velocities of the components of a binary disrupted by a Type Ibc supernova. These predictions were based on early simulations of the effect of a supernova shell impact on a star (Fryxell and Arnett 1981) in order to determine the amount of mass lost and the change in velocity of the companion. Motivated by this problem, we perform simulations of supernovae in binary systems with properties comparable to those used in TT98.

Simulations of supernovae have been performed at many scales, ranging from hundreds of kilometres around the nascent neutron star (Janka 2012) to the impact of the ejecta shell on a companion (and the influence of the companion on the overall structure of the ejecta). The impact of Type Ia ejecta on companions has, in particular, been well studied (Marietta et al. 2000; Pakmor et al. 2008; Liu et al. 2012; Pan et al. 2012). Hirai et al. (2014) investigated the fraction of mass stripped from a giant companion star due to the effect of a core-collapse (Type II) supernova using a two-dimensional grid-based Eulerian code. Recently, Liu et al. (2015) also presented results on the consequences of a Type Ibc supernova interacting with a binary companion using smoothed-particle hydrodynamics (SPH). These studies have often focused on the companion star without following the explosion from the moment of the supernova. As a consequence, the ejecta shell is initialised artificially via analytic prescriptions near the surface of the companion, without considering its earlier evolution. In addition, the response of the binary companion and subsequent SNR evolution is analysed in these cases from a static configuration rather than placing the binary in an orbit.

For close binary orbits it is typically assumed that the binary has circularised by this point in its evolution, so that the eccentricity of the orbit can be set to zero (TT98). We follow the same assumption in this work. Moreover, despite these close separations and, therefore, short orbital periods, in theoretical work the binary period is taken to be much shorter than the timescale over which the ejected shell impacts the companion. This can be made more explicit (as in, for example, Colgate 1970) by noting that the

¹More recently, the ‘Bethe’, B, has also been proposed as an equivalent unit in honour of Hans Bethe’s work on supernovae (Weinberg 2006; Woosley and Heger 2007).

ejecta velocity must be larger than the escape velocity of the primary star,

$$v_{\text{ej}} > v_{\text{esc}} = \sqrt{\frac{2GM_1}{R_1}}, \quad (4.1)$$

where M_1 and R_1 are the mass and radius of the primary. Since the distance, a , of the companion from the primary is larger than R_1 , and since the orbital velocity at that distance is

$$v_{\text{orb}} = \sqrt{\frac{GM_1}{a}}, \quad (4.2)$$

then it must be that $v_{\text{ej}} > v_{\text{orb}}$. In practice, typical ejecta velocities ($10^3 \sim 10^4 \text{ km s}^{-1}$) are much larger than the orbital velocities ($\sim 10^2 \text{ km s}^{-1}$), hence the latter is typically ignored in analytic impact velocity calculations. However, matter in the ejecta in fact have a radially dependent velocity (approximately, in the homologous regime, $v_{\text{ej}}(R, t) \propto R/t$). Therefore, during the late-time interactions of the lower-density, slower (and presumably high-metallicity) ejecta with the companion, we may no longer be justified in ignoring the orbital velocity.

Also, it is likely that the companion stars in such close orbits have been synchronised with the orbital period by tidal friction (Zahn 1977). In one of the most compact binaries we consider here, a $4 M_{\odot}$ helium star separated by $4 R_{\odot}$ from a $1 M_{\odot}$ companion, the orbital period is $4 \times 10^4 \text{ s}$, which is still much longer than the timescale of the interaction of the supernova ejecta ($\lesssim 2 \times 10^3 \text{ s}$). With synchronisation, the surface of a star at $\sim 1 R_{\odot}$ would therefore rotate at $2\pi R_{\odot}/(4 \times 10^4 \text{ s}) \approx 100 \text{ km s}^{-1}$. As this is also orders of magnitude smaller than the ejecta velocity, we do not expect rotation to induce any substantial asymmetries during the shell interaction and do not consider it here.²

An additional important factor in the dynamics of supernovae in binaries is a possible kick imparted to the newly formed neutron star. This is likely due to a ‘gravitational tugboat’ effect from asymmetry in the ejecta surrounding the neutron star after the core bounce, and perhaps also high magnetic fields and the asymmetric emission of neutrinos from the proto-neutron star (Kusenko and Segrè 1996; Scheck et al. 2004, 2006; Maruyama et al. 2011; Wongwathanarat et al. 2013). For *ultra*-stripped supernova progenitors, which have very small ejecta masses, the shock expands very rapidly and the tugboat effect on the neutron star has been shown to be minimal (Suwa et al. 2015). For the range of hydrodynamic simulations in this chapter we do not apply any additional kick to the neutron star.

To study this problem hydrodynamically, we simulate a supernova in an orbiting binary from just after the moment of core bounce in the supernova. To this end, we first

²As shown by Pan et al. (2012) for the Type Ia case, both orbital motion and rotation produce no substantial difference in the impact velocity gained by the companion. However, it is possible that a high rotation rate in the companion can help unbind a small additional amount of shock-heated material from the surface of the companion due to the additional rotational energy.

generate stellar structure models of the binary components using a one-dimensional stellar evolution code, where we strip an evolved massive progenitor of the majority of its envelope. We then convert these stellar structures to three-dimensional stars in an SPH code, and run simulations from the moment of the supernova. We vary the mass of the primary star as well as the orbital separation independently. In particular, we are interested in investigating the dependence of the companion's removed mass and impact velocity (the radial component in velocity of the companion induced by the impact of the shell) on the initial orbital separation of the binary. We describe our numerical method in more detail in the following section.

4.2 Method

Throughout this work we use the Astrophysical Multipurpose Software Environment³ (AMUSE; Portegies Zwart et al. 2009; Pelupessy et al. 2013; Portegies Zwart et al. 2013b) to perform our simulations. We first outline the technique used to generate the stellar models in our binary systems (Section 4.2.1). We then describe the set up of the initial hydrodynamical models from the stellar structure (Section 4.2.2). Finally, we describe the simulation of the supernova in the binary, with some discussion on the initial convergence tests that were performed (Section 4.2.3).

4.2.1 Stellar models

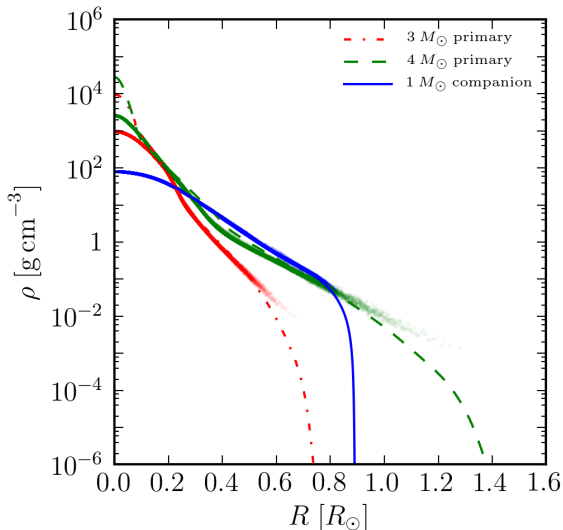
In order to generate an SPH realisation of the binary, we require a stellar evolution code that can return the internal structure of the star. Two evolution codes in AMUSE fit this criterion: MESA (Paxton et al. 2011) and EVtwIn (Eggleton 1971, 2006). We chose MESA to evolve the models to their final stellar structure, motivated by difficulties in previous work in using EVtwIn to obtain solutions past the carbon flash in more massive stars (de Vries et al. 2014).

Due to interactions with the binary companion (and potentially also through stellar winds), much of the mass of the primary star is lost over its lifetime, resulting the helium star progenitor of a Type Ibc supernova (for some observationally-motivated examples, see Kim et al. 2015). To obtain an estimated lifetime of the progenitor, we first use SSE, which is a fast predictor of stellar properties based on parametrised stellar evolution tracks (Hurley et al. 2000). With the intent of generating $3 M_{\odot}$ and $4 M_{\odot}$ Helium-star progenitors, we begin with a $12.9 M_{\odot}$ and $16.0 M_{\odot}$ zero-age models with metallicity $Z = 0.02$,⁴ which are predicted by SSE to end with the required helium core masses.

³www.amusecode.org

⁴This 'canonical' value of the solar metallicity may be an overestimate; see Asplund et al. (2009) for a review.

Figure 4.1: Comparison of the internal stellar structures of the $3 M_{\odot}$ and $4 M_{\odot}$ primary stars, as well as the $1 M_{\odot}$ companion. Lines correspond to the one-dimensional models given by MESA, where the solid line is the companion star, the dot-dashed line is the $3 M_{\odot}$ primary and the dashed line is the $4 M_{\odot}$ primary. Overlaid in the same colour are points representing the densities calculated at the location of each SPH particle in the relaxed SPH models constructed from the MESA models (which excludes the neutron star at the origin).



We do not model or speculate on the specific mechanisms of the mass loss from the primary star, but instead apply a constant mass loss (removed from the outer mass shells of the MESA structure model) until the final helium star mass is reached. Because the lifetime in SSE may be an overprediction compared to the actual lifetime reached in MESA, we apply this mass loss between 80 and 90 per cent of the predicted SSE lifetime so as to not reach the end of the MESA evolution before all of the required mass is stripped. The stellar evolution is then continued until the final lifetime found in MESA.

For our helium star models, the very final stage of evolution involves a rapid expansion of the remaining, tenuous envelope. Due to interaction with the close binary companion, this small amount of material in the envelope is in fact expected to be lost from the system. For our progenitors, we use models just prior to this stage, at which the outer radius of the helium star is still compact (this corresponds to an age of 19 Myr and 14 Myr for the $3 M_{\odot}$ and $4 M_{\odot}$ helium stars, respectively). For consistency, we evolve our ($Z = 0.02$, $M_2 = 1 M_{\odot}$) companion star to the same age as that used for the primary star. This means the companion is still very early on the main sequence, and therefore the effect of this small duration of stellar evolution on the structure and composition of the companion is negligible.

4.2.2 Hydrodynamical model set-up

We model the hydrodynamics of the supernova using the SPH code GADGET-2 (Springel 2005a), running in the AMUSE framework. The SPH formalism has been shown to be effective in three-dimensional simulations of stellar phenomena (Pakmor et al. 2012,

for example). One reason is that computational resources are not expended on regions of vacuum or negligible density (for example, Lai et al. 1993; Church et al. 2009), which constitute a significant fraction of the simulation volume in the current problem. Modelling a binary in a vacuum is easily handled in SPH, without the need for (low density) background fields in grid codes, which can exhibit artificial shocks from motions of other bodies within this background.

The Lagrangian nature of SPH describes advection naturally, without suffering from complications of numerical diffusion found in Eulerian codes, and we do not have to restrict the simulation to a fixed volume, which is useful in the present problem of a rapidly expanding shell of gas. A benefit to running the simulation in three dimensions is the absence of any boundary effects, which can produce on-axis artefacts (Marietta et al. 2000) or preferential wave numbers in the formation of instabilities (Warren and Blondin 2013). As with all hydrodynamical codes, the SPH method also has its drawbacks, and some of these are discussed further in the context of our convergence studies in Section 4.2.5.

The stellar models created in MESA are converted into SPH particles using the `star_to_sph` routine in AMUSE, in a similar method to that outlined in de Vries et al. (2014). The routine first extracts the one-dimensional hydrostatic structure of the star, represented as a function of mass coordinates, from the data generated by the stellar evolution code. The SPH particles are initialised in a homogeneous sphere constructed from a face-centred cubic lattice, and the radial positions of the particles are then adjusted so as to match the density profile from the evolution code.⁵ The internal energies of the particles are then assigned from the temperature (and mean molecular weight) distribution from the stellar evolution code. We use equal-mass particles throughout these simulations (unequal-mass particles can cause additional complications such as spurious mixing; Rasio and Lombardi 1999).

The primary star is configured with a purely gravitational core particle of $1.4 M_{\odot}$ to model the neutron star. The softening length ϵ is chosen to be equal to the smoothing length, such that, due to the compact support of the cubic spline, the smoothing kernel reaches zero at 2.8ϵ . This equality is also maintained for the SPH particles to preserve equal resolution of the gravitational and pressure forces. The zero-kinetic-energy models are relaxed over 2.5 dynamical timescales of the gas using critical damping on the velocities of the particles, where at each step the magnitude of damping is reduced so that in the final step no constraint on the velocity is imposed (for a similar approach, see de Vries et al. 2014). This is required due to effects of mapping the one-dimensional stellar structure on to the particle grid, and differences in physics between the codes, such as the value of the adiabatic exponent (which, in the SPH code, is a fixed value of $\gamma = 5/3$).

We show the one-dimensional stellar structures as well as the relaxed SPH particle

⁵Randomisation of the angular orientation of the particles has the undesirable effect of the additional shot noise it generates in the initial density distribution; however, the further step of damped relaxation used here will ultimately result in a glass-like configuration.

densities in Fig. 4.1. Note that for the primary stars, the density according to the SPH gas particles levels off towards the centre compared with the MESA profiles, as the central density in this region is dominated by the single core particle (which is excluded from the densities in the plot).

We set up the binary models at different orbital separations, a , where the minimum separation is chosen to be greater than the limit of Roche-lobe overflow (RLOF) of the companion star, given by the Eggleton (1983) relation,

$$a_{\text{RLOF}} = \frac{0.6 q^{2/3} + \ln(1 + q^{1/3})}{0.49 q^{2/3}} R_2, \quad (4.3)$$

where R_2 is the companion radius and q is the binary mass ratio M_2/M_1 . Once both stars have been constructed in the SPH code, orbital velocities are determined for a circular orbit at the specified separation and applied to each star.

4.2.3 Simulation of the supernova explosion

The supernova is initiated using the ‘thermal bomb’ technique (Young and Fryer 2007; Hirai et al. 2014), which assumes the core bounce has just occurred, at which moment we inject energy into a shell of particles around the neutron star. As discussed in Young and Fryer (2007), thermal bomb approaches (along with alternative, piston-driven shocks) are not intended to embody the physical mechanism that drives the supernova. Indeed, the actual processes by which the energy gain occurs near the proto-neutron star are still not fully understood, though recent observations and insights from simulations have shed some light on the role of instabilities, asymmetries and jets in driving this process (Janka 2012; Bruenn et al. 2013; Hanke et al. 2013; Lopez et al. 2013; Milisavljevic et al. 2013; Couch and O’Connor 2014; Couch and Ott 2015).

The boundary of energy injection is specified by radius (which is equivalent to a fixed enclosed mass) instead of particle number. This allows scaling of the problem over a range of SPH particle numbers while keeping fixed the mass fraction that receives the supernova energy. The total thermal energy (a canonical 10^{51} erg \equiv 1 foe) is distributed evenly amongst these N_{SN} particles, so that the specific internal energy per particle is increased by $(1 \text{ foe}) / (N_{\text{SN}} m_{\text{SPH}})$.

We found that a careful investigation of the effect of the injection radius was necessary. Too small a radius (and therefore N_{SN}) results in large asymmetries in the shock front that grow from intrinsic small-scale asymmetries in the initial particle distribution. On the other hand, too large a radius results in the internal energy of the supernova being distributed amongst a large number of particles, lowering the specific internal energy and therefore reducing the overall temperature in the region and weakening the shock. We found that, for the helium star models used here, injecting the supernova energy into a region $R_{\text{SN}} \lesssim 0.05 R_{\odot}$ generates a sufficiently spherical shock while still keeping N_{SN} sufficiently small.

To check the strength of the resulting shock, we calculated the Mach number at various stages through one of our supernovae (the $3 M_{\odot}$ primary). After 2 s, in the

high-temperature core the Mach number is ~ 3 , but quickly grows as the shock traverses down the temperature gradient of the star (where the sound speed is lower). The Mach number exceeds 10 by shock breakout. Increasing the radius of energy injection would reduce the initial energy density and therefore the initial Mach number. However, provided the Mach number remains high (as seen in our simulations), the strong-shock conditions are upheld.

4.2.4 Measured parameters

With the results of these simulations it is possible to predict the final velocities (formally, at infinity) of the runaway components of supernova-disrupted binaries. For masses m relative to the neutron star mass (i.e. $m \equiv M/M_{\text{NS}}$), TT98 calculate these values in terms of the following initial parameters:

- a : the pre-supernova binary orbital separation
- v : the pre-supernova relative orbital velocities
- w : the magnitude of the kick applied to the NS
- θ and ϕ : the spherical polar angles of the NS kick vector with respect to the ‘ x ’-axis aligned along the NS orbital velocity vector at the moment of the kick
- v_{im} : the magnitude of the radial velocity component imparted to the companion due to the impact of the supernova shell (we refer to this as the ‘impact velocity’)
- v_{ej} : the magnitude of the radial velocity of the ejecta shell
- m_2 , m_{2f} and m_{shell} : the initial mass of the companion, the final mass of the companion after mass loss, and the mass of material in the shell, respectively (all relative to the neutron star mass)

In the original work of Wheeler et al. (1975), during the supernova shell passage over the companion star, the mass removed from the companion is parametrised by the fraction of companion radius $x = R/R_2$ as a function of the angle around the star. Above some critical fraction of the companion radius, x_{crit} , a fraction F_{strip} of the mass is stripped by the shell impact, and below it a fraction F_{ablate} of mass is ablated. The values of F_{strip} and F_{ablate} are calculated in Wheeler et al. (1975) using a polytropic star of index $n = 3$. The predictions in TT98 are based on the work of Wheeler et al. (1975) as well as mass-loss estimates from simulations of a planar slab of material hitting a star Fryxell and Arnett (1981), which have a low resolution compared with modern simulations. These results also need a corrective factor due to the shell in reality having some curvature. Higher resolution simulations, such as those presented here, provide a test of these earlier estimates, which are one of the sources of uncertainty in the results of TT98.

The magnitude of the radial impact velocity imparted to the companion by the shell, v_{im} , is theoretically determined to be

$$v_{\text{im}} = \eta v_{\text{ej}} \left(\frac{R_2}{2a} \right)^2 \frac{M_{\text{ej}}}{M_2} x_{\text{crit}}^2 \frac{1 + \ln(2v_{\text{ej}}/v_{\text{esc}})}{1 - F^*}. \quad (4.4)$$

Here, we use the expression from Wheeler et al. (1975) in the form adopted by Tauris (2015), which applies the substitution $(F_{\text{strip}} + F_{\text{ablate}}) = F \rightarrow F^* = (F_{\text{strip}} + F_{\text{ablate}})^\alpha$ for some α , as well as a free parameter η to account for the fact that this tends to over-predict the value of v_{im} . Effectively, η represents the final change in momentum, Δp , of the companion as a fraction of the incident momentum in the shell. As noted in Wheeler et al. (1975), corrections must be applied to this formula as it neglects the presence of a rarefaction wave back through the ejecta, geometrical effects of curvature in the shell (more important for small a), inhomogeneities in the ejecta and radiative losses behind the shock. Further phenomena can also modify the final impact velocity, such as the deformation of the companion by the shock passage (altering its cross-sectional area), the formation of a bow shock in the ejecta (during which time the flow deflects around the companion star), and shock convergence on the far side of the star (causing the asymmetric emission of material from this side of the star).

In our simulations, the two main measurements we make are, therefore, the mass loss from and impact velocity imparted to the companion, as a function of orbital separation. We measure the removed mass by calculating the specific energy for each particle,

$$e_{\text{tot}} = e_{\text{kin}} + e_{\text{therm}} + e_{\text{pot}} = \frac{1}{2}v^2 + u - \phi, \quad (4.5)$$

where v is the particle velocity, u is its specific internal energy and ϕ is the gravitational potential at its position. Bound particles have a negative value of e_{tot} . The amount of bound mass in the companion is time-dependent over the course of the simulation due to energy exchange between particles. The stabilisation of mass bound in the companion determines the end of our simulation, which occurs within 10 dynamical timescales of the companion star ($\sim 2 \times 10^4$ s). The mass-loss results will be discussed in Section 4.3.2. Measurements of the radial impact velocity that is gained by the companion will be discussed in Section 4.3.3.

4.2.5 Convergence test

One feature of SPH that requires caution is that the resolution is dependent on the local density, and therefore the method loses resolution in the lower-density, uppermost layers of the stars in our simulations. In the current problem, the mass stripped by the secondary is from these same layers. Therefore, a good test for the resolution of the simulations is to look for convergence in the quantity of mass stripped from the companion.

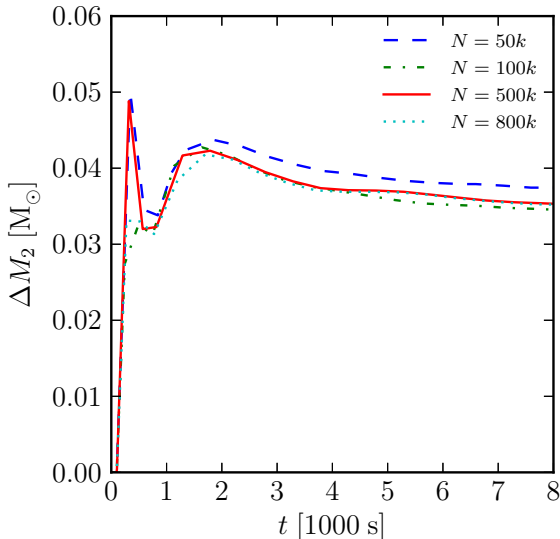


Figure 4.2: Results for a convergence study using the amount of mass stripped from the companion. The primary star mass was $3 M_{\odot}$ and the orbital separation was $4 R_{\odot}$ in all cases. The number of SPH particles used in each run is given in the legend.

During the supernova, Richtmyer–Meshkov (the impulsive form of Rayleigh–Taylor) instabilities (RMI) are expected to be present, which have been found to appear once reverse shocks form at the interfaces between discontinuities in the density gradient (Kane et al. 1999). Such discontinuities are present in Type Ibc progenitors at the interface between the carbon–oxygen boundary in the core and, if any substantial fraction of hydrogen remains in the envelope, also at the helium–hydrogen boundary. However, these discontinuities tend to be smoothed during the conversion from the one-dimensional stellar model and subsequent relaxation of the SPH particles. Proper treatment of the RMI requires a prescription of artificial conductivity that is not included in the current SPH codes in AMUSE. This instability is expected to be a significant factor in the mixing of stellar material early in the evolution of SNRs, and so any evaluation of the fate of the composition of the supernova ejecta must take this into account.

Unless the growth of RMI is explicitly seeded by some structure at the density interface, these instabilities will grow from perturbations at the numerical level of the simulation and may not, in such cases, grow substantially (Kane et al. 1999). Therefore, there is the potential for instabilities to be dependent on numerical effects such as the resolution of the simulation. Additionally, during the stripping of mass from the companion star, the initial deceleration of the shell impacting the companion may be Rayleigh–Taylor unstable, but also that the subsequent flow of the shell over the surface of the star may induce some shearing (Kelvin–Helmholtz) instabilities (KHI).

Due to the smoothing of discontinuities after relaxation of the SPH models, a

$M_1 (M_\odot)$	$M_{\text{ej}} (M_\odot)$	$a (R_\odot)$	$\Delta M_2 (M_\odot)$	$v_{\text{im}} (\text{km s}^{-1})$
4.0	2.6	4.5	0.021	78
4.0	2.6	5.5	0.013	57
4.0	2.6	6.5	0.0096	47
3.0	1.6	4.0	0.037	83
3.0	1.6	5.0	0.020	60
3.0	1.6	6.0	0.013	48

Table 4.1: Simulation initial conditions and main results. The first three columns indicate the initial conditions, where M_1 is the mass of the primary (helium star) and before the supernova, M_{ej} is the total ejecta mass, and a is the initial orbital separation. The last two columns are the amount of mass stripped from the companion star and the (magnitude of the) impact velocity.

lack of artificial conductivity⁶ in GADGET-2 and the only perturbations being from noise in our SPH distribution, we expect that instabilities will not be fully captured in our simulations. As a result, we expect that the influence of instabilities on our results should also be reduced.

Fig. 4.2 shows a test of varying the SPH particle number, N , based on the amount of mass lost from the companion star (evaluated using equation 4.5). For low N , there is noticeable noise in the bound mass determination over time, but for $N \geq 10^5$ particles, this is no longer appreciable. As shown in Fig. 4.2, we did not find any substantial difference in the results increasing N from 5×10^5 to 8×10^5 . Accounting for this, as well as available computational resources, our simulations were run with 5×10^5 particles.

4.3 Results

After reviewing the initial conditions used for our simulations, we examine the early stages of the supernova (Section 4.3.1). We then investigate the magnitude of mass lost from the companion as a function of the orbital separation (Section 4.3.2), as well as the velocity imparted to the companion and the fraction of imparted momentum compared to the incident shell (Section 4.3.3). Next, we examine the newly formed SNR for asymmetries in morphology and metallicity (Section 4.3.4). Finally, we consider the subsequent evolution of a star altered by a supernova shell impact (Section 4.3.5).

Table 4.1 shows the initial conditions used in our simulations. The choice of primary and companion masses is motivated by the binary parameters used in TT98 and Tauris (2015), while the minimum orbital separations are chosen to be outside the

⁶This smooths thermal energy discontinuities and is used in capturing the vortices seen in KHI. However, there has been some debate on the causes of KHI suppression in SPH; see, for example, the discussion in Gabbasov et al. (2014).

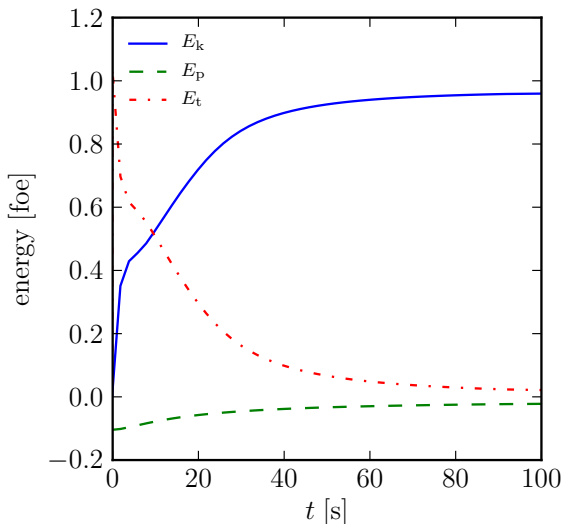


Figure 4.3: Distribution of total energy in the gas, in units of foe (10^{51} erg), as a function of time following the supernova event. The energy is broken down into kinetic (E_k), potential (E_p) and internal (thermal; E_t). This example corresponds to a primary of mass $4 M_\odot$ and an orbital separation of $4.5 R_\odot$.

RLOF value (equation 4.3). The final two columns show the effects on the companion due to the shell impact, discussed in more detail in the remainder of this section.

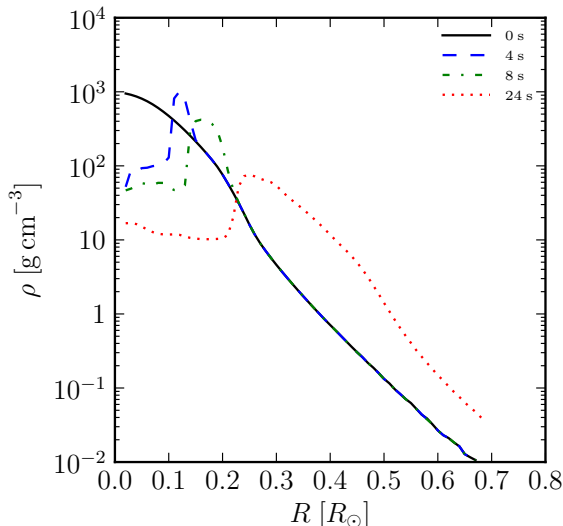
4.3.1 Shock breakout

Approximately 20 s after the supernova is initiated, the forward shock has broken out of the surface of the helium star, during which time the fraction of SPH particles bound to the $1.4 M_\odot$ neutron star drops smoothly to almost zero. We find at late times that there is some fall-back of a small amount of material, which remains bound to the neutron star. As we do not model here the complexities of the magnetic field of the new neutron star or any form of pulsar wind, it is possible that other mechanisms later expel some or all of the residual bound gas.

In Fig. 4.3, it can be seen that there is a rapid conversion of energy from internal (thermal) energy from the moment of explosion to kinetic and potential energy as the shock passes through the star and the subsequent shell expands. By approximately 100 s following the supernova explosion, very little of the original thermal energy remains in the gas as it has been almost entirely converted into kinetic energy in the expanding shell.

Fig. 4.4 shows the changes in density through the $3 M_\odot$ helium star from shortly after core bounce until after the forward shock has reached the outer layers of the star. A lower density cavity with a very shallow gradient is seen to lag behind the expanding ejecta shell. After the shock has reached the surface (24 s), the expansion proceeds towards the companion in a self-similar manner—the variation in gradient is maintained over time, although the overall magnitude of the density drops during

Figure 4.4: The radial density structure of SPH particles (excluding the core particle) at 4 s, 8 s and 24 s following a supernova in a $3.0 M_{\odot}$ primary.



the expansion. We investigate the density and velocity distributions within the ejecta in more detail in Section 4.3.3.

4.3.2 Impact and mass loss from the companion

We now consider the phenomena occurring during the supernova shell impact on the companion, as well as the removal of mass during this interaction. The passing shell first strips material from the outer layers of the companion. The compression of the companion along the direction of motion of the shock causes heating of the stellar material, which results in a subsequent mass loss through ablation. This ablation of material is found to be a slower form of mass loss than the initial stripping phase.

The passage of the shock through the companion can be seen in the density slices of Fig. 4.5. The black vectors in this figure show the velocities for a random sample of all the SPH particles that were originally in the companion which have subsequently become unbound. These vectors have had the orbital velocity vector of the companion subtracted, and they are then projected onto the orbital plane. Because each SPH particle has the same mass, these vectors also indicate the relative momentum of the unbound particles.

Aside from the mass stripping from the sides of the star as predicted in Wheeler et al. (1975), there is also mass loss from the far side after the shock has passed through the star. Panel (b) of Fig. 4.5 shows that, once the shock passes through the centre of the companion, it converges at the far side of the star as it accelerates down the density gradient (similar shock convergence is seen around other spherically symmetric density gradients, such as in Chapter 2). This increases the local pressure on this axis, resulting

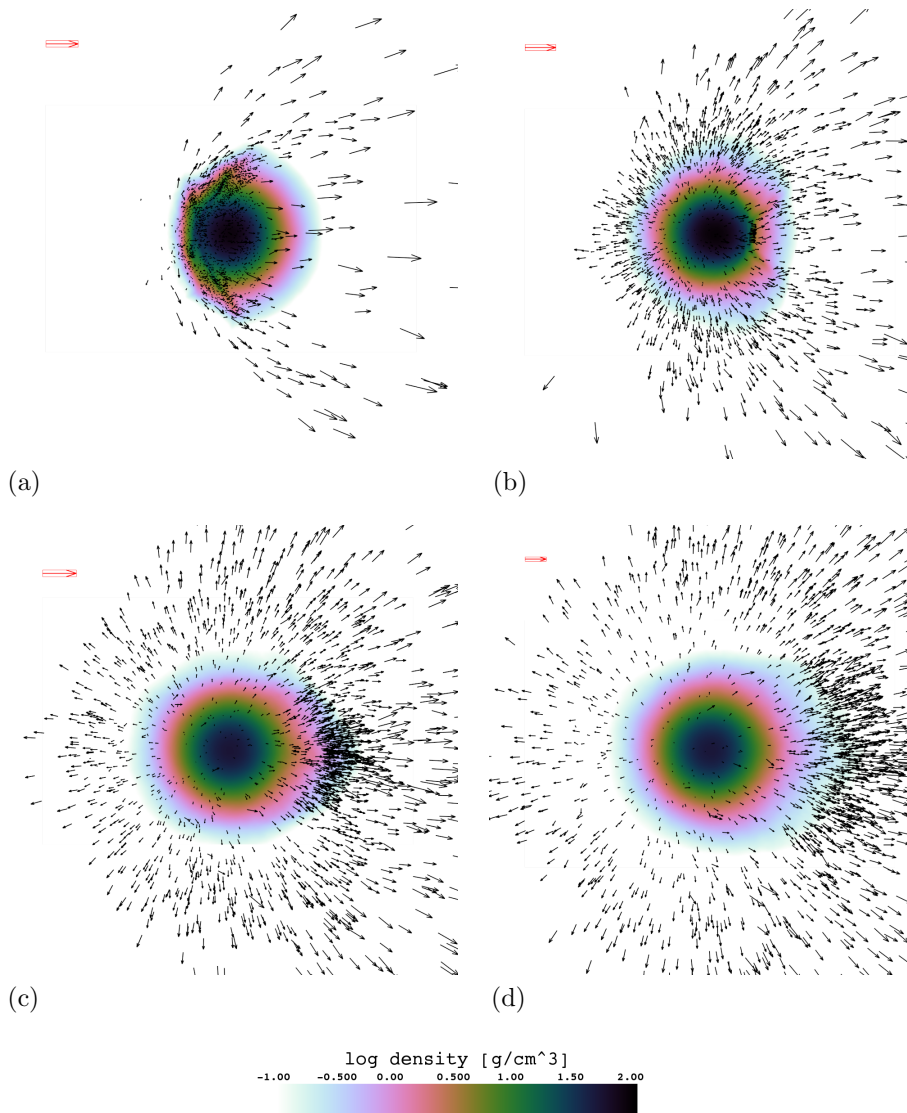
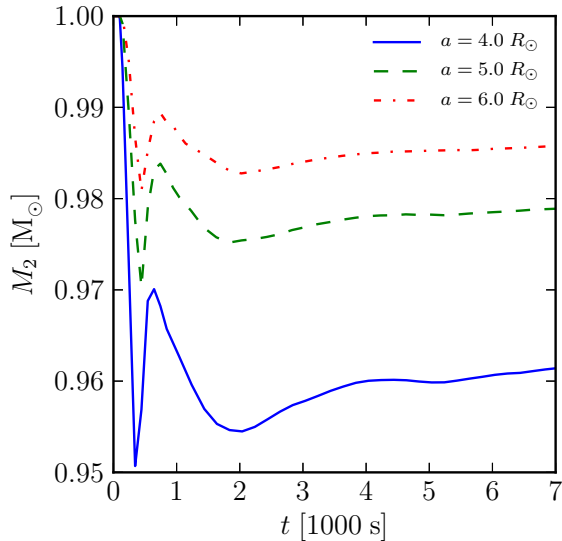


Figure 4.5: A slice through the x - y (initial orbital) plane during the passage of the supernova shock through a $1.0 M_{\odot}$ companion star after a 1 foe supernova in a primary star of $3.0 M_{\odot}$ at a distance of $4 M_{\odot}$. The snapshots correspond to times of (a) 433 s, (b) 1028 s, (c) 1628 s and (d) 2028 s. The shock enters the companion star from the left. The black vectors show the magnitude of the velocity projected onto the orbital plane (and with the orbital velocity of the companion subtracted) for a small random sample of all the particles removed from the companion. In each case, a reference vector (red, boxed) is given in the upper left corner; these correspond to (a) $1 \times 10^4 \text{ km s}^{-1}$, (b) $3 \times 10^3 \text{ km s}^{-1}$, (c) $2 \times 10^3 \text{ km s}^{-1}$ and (d) $1 \times 10^3 \text{ km s}^{-1}$.

Figure 4.6: Mass bound to the companion using equation (4.5) as a function of time since the supernova explosion for a primary helium star of $3.0 M_{\odot}$ and a range of orbital separations.



in expulsion of material from the far side of the star (panels c and d) and can counter the effect of the outward kick imparted by the incident shell of material (see also Marietta et al. 2000).

In the last panel of Fig. 4.5, the central density of the companion has dropped and it has noticeably expanded from the shock heating. During this later stage (final three panels), ablation occurs for material which has been heated to the point where the thermal energy is greater than the binding energy. Due to the shock heating, the companion becomes extended, similar to a pre-main sequence star (though its internal structure will differ from a pre-main sequence star), and its luminosity is expected to increase temporarily as it reverts to thermal equilibrium (Marietta et al. 2000, see also Section 4.3.5). Finally, we find a quadrupole oscillation of the companion that is induced by the distortion from compression due to the shock. This ringing subsides after about one dynamical timescale of the companion star.

Fig. 4.6 shows an example of the variation in companion mass due to the shell impact. The stripping of mass by the passing shell causes a rapid mass loss in the initial phase. There is then a brief increase in the bound mass, which has also been seen in past simulations (Pakmor et al. 2008; Pan et al. 2012; Liu et al. 2015). One possible cause of this is the formation of a reverse shock in the ejecta, which slows material with respect to the companion and increases the amount of bound mass (Pan et al. 2012). A more gradual mass loss then ensues due to the later ablation of shock-heated material. The proportion of mass lost drops rapidly even by moderate orbital separations.

In Fig. 4.7, we show the amount of mass lost from the companion (as a fraction of its initial mass) as a function of orbital separation. The lost mass is found by sub-

tracting the final bound mass at the last snapshot of each simulation (which occurs at 2×10^4 s) from the initial mass. We use the last time possible from the simulation as the final mass takes much of the total simulation time to reach its steady-state value. A least-squares regression gives a fit to our data of $1.3 (R/R_\odot)^{-2.6} M_\odot$ for the $M_{\text{ej}} = 1.6 M_\odot$ data and $0.58 (R/R_\odot)^{-2.2} M_\odot$ for the $M_{\text{ej}} = 2.6 M_\odot$ data. A variation of only 3 per cent in the values of lost mass is sufficient to obtain agreement between the fitted gradients, and therefore caution should be exercised in interpreting any difference between the two gradients. The dashed line in Fig. 4.7 shows the prediction from TT98, the dotted line shows the fit obtained from Type Ia simulations compiled by Tauris (2015), and the dot-dashed green line is from Liu et al. (2015). The values of lost mass we find are comparable to those seen in Liu et al. (2015). Likewise, we find values of ΔM_2 less than the values that are extrapolated from simulations of Type Ia supernovae, indicating that these values should be revised for the conditions of Type Ibc supernovae considered here.

There are some differences between our initial conditions and those from the previous work shown in Fig. 4.7. Compared with previous Type Ia simulations, our explosion energies and ejecta masses are both slightly different. Additionally, the companion radius, R_2 , shrinks slightly after relaxation of the SPH models compared with the radius from the MESA model. The predictions in TT98 and Tauris (2015) depend on these quantities in particular within the geometric parameter Ψ , used originally by Wheeler et al. (1975), defined as

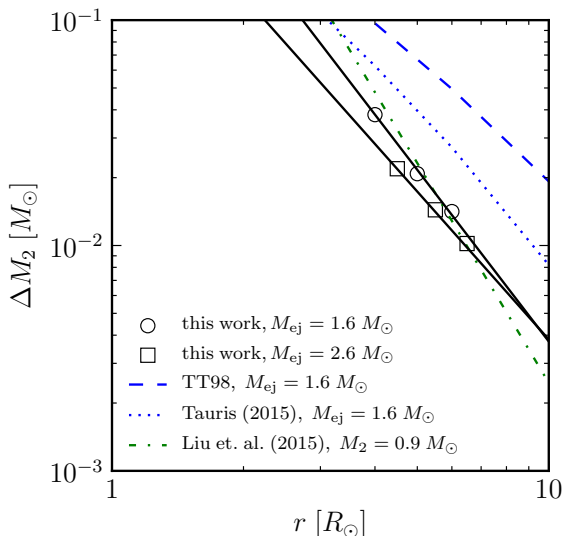
$$\Psi = \left(\frac{R_2}{2a} \right)^2 \left(\frac{m_{\text{shell}}}{m_2} \right) \left(\frac{v_{\text{ej}}}{v_{\text{esc}}} - 1 \right). \quad (4.6)$$

This parameter is used in the determination of x_{crit} as well as F_{strip} and F_{ablate} in Wheeler et al. (1975) using tabulated data for an $n = 3$ polytrope. For our comparisons, we adjust these quantities (and therefore Ψ) in the TT98 and Tauris (2015) estimates to match the initial conditions of our simulations. Furthermore, the simulations in Liu et al. (2015) also use a slightly different companion mass and ejecta mass, and so their results are not completely equivalent to ours. The structure of the companion star has been shown to substantially effect the magnitude of removed mass in simulations of Type Ia supernovae (Meng et al. 2007; Pan et al. 2012; Liu et al. 2012). Slight differences in companion models can therefore be responsible for some of the discrepancies.

4.3.3 Momentum transfer and the velocity of the companion

When the orbital separation is very small, the impact of the ejecta causes not only a significant loss of mass from the companion star but also a large change in velocity. The largest change in velocity of the companion occurs during the transfer of momentum from the shell in the initial impact. However, as the end of the shell passes over the far side of the companion, there is an overpressure acting on this side of the star when the

Figure 4.7: Final mass lost from the companion as a function of orbital separation. Circles show results with a primary star of $3 M_{\odot}$ and squares show results for a primary star of $4 M_{\odot}$. The secondary is $1 M_{\odot}$ in each case. The solid lines show the best fit power-laws for each ejecta mass. The comparison curves are from the theoretical predictions of WLK75 as adapted by TT98 and Tauris (2015) (rescaled to our initial conditions), as well as the simulation results of Liu et al. (2015) for a $0.9 M_{\odot}$ companion star. Note that the comparison with Liu et al. (2015) is not fully equivalent, as both the ejecta mass and companion mass (and therefore radius) are slightly different.



shock converges on this axis. This causes the companion to receive a slight change in momentum in the direction opposite to the shell motion (which has been suggested in other simulations such as Fryxell and Arnett 1981; Marietta et al. 2000). In the theory of TT98, v_{im} is defined to be an *effective* velocity that not only accounts for the momentum imparted to the companion by the passage of the shell but also the subsequent change in momentum due to (potentially asymmetric) mass loss.

We found that measuring the velocity of the companion with respect to the neutron star is complicated by the difficulty to define the baryonic centres of the binary system with the ejecta that had not yet left the binary system, the oscillatory behaviour of the companion star as a result of the shell impact, and the Brownian motion of the neutron star due to the shot-noise of the limited resolution in its vicinity.

As an alternative technique, we set up a co-rotating frame of reference that matches the original circular orbital motion. Up until the shell impact, there is no component of velocity of the companion perpendicular to this direction of motion. During and after the impact, the companion (as well as the mass unbound from it) gains a component of velocity, and therefore momentum, in the radial direction with respect to this frame. We use this to measure the momentum delivered to the companion and the material removed from the companion, as well as the radial impact velocities.

The left-hand panel of Fig. 4.8 shows the component of momentum in the radial direction for material unbound from the companion that was not unbound in the previous time step. The first peak is due to the large amount of material initially stripped from the companion star by the shell impact. This figure also clearly indicates the burst of material out of the back of the star, seen as the second peak in the left-hand panel.

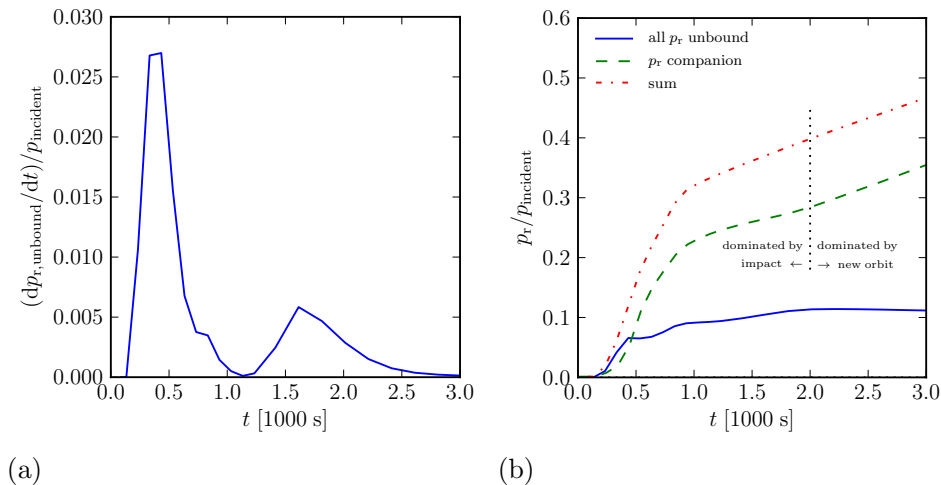


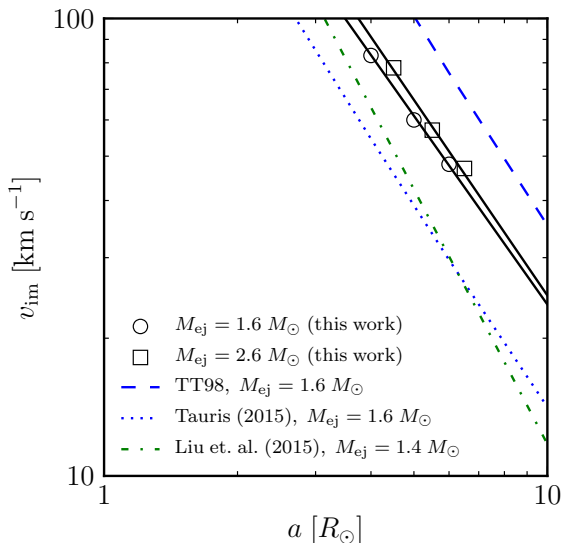
Figure 4.8: Components of momenta in the radial direction of (a) newly unbound material from the companion (material that was not unbound the previous snapshot) and (b) the total unbound mass from the companion, and bound mass in the companion, and the sum of these two values. Values are shown as a fraction of the total incident momentum calculated for the cross-section of shell material that impacts the companion. The example shown is for a $3 M_{\odot}$ primary and an orbital separation of $6 R_{\odot}$.

The right-hand panel shows the breakdown of momenta in the radial direction for unbound and bound material originally from the companion (and their sum). This gives an alternative indication of η , where we see that although less than half of the total incident momentum in the shell is delivered to this material in total, only $\lesssim 30$ per cent of the momentum is delivered to the (bound material of the) companion star.

As the interaction of the shell with the companion is not instantaneous, we must define a point at which we measure the impact velocity. Up until the second peak seen in the left-hand panel of Fig. 4.8, the radial velocity gained by the companion is dominated by the interaction with the passing shell. Once this interaction has ended, there is an additional, growing radial component in velocity from the eccentricity induced in the orbit. The change in gradient of p_r for the companion, seen in the right-hand panel of Fig. 4.8, marks the end of the impact phase, which corresponds to just after the second peak in the left-hand panel. We define this to be the point at which we measure the impact velocity. Up to this point, the contribution to the radial velocity from any induced eccentricity is small.

Our final impact velocity magnitudes are shown in Fig. 4.9. A least-squares regression gives a fit to these data of $556 (R/R_{\odot})^{-1.4} \text{ km s}^{-1}$ for the $M_{\text{ej}} = 1.6 M_{\odot}$ data and $652 (R/R_{\odot})^{-1.4} \text{ km s}^{-1}$ for the $M_{\text{ej}} = 2.6 M_{\odot}$ data. The velocities for both ejecta mass conditions follow a similar gradient to earlier work presented in TT98 and Taurus (2015), although it is not quite as steep as the -1.9 power-law of Liu et al. (2015). The

Figure 4.9: Magnitude of the impact velocity, v_{im} , imparted to the companion star as a function of orbital separation a . Markers and line styles correspond to those used in Fig. 4.7. Again, as for Fig. 4.7, the comparison with Liu (2015) is not fully equivalent due to the slightly different ejecta mass and companion parameters.



overall scaling differs from previous work, however. The early estimate from TT98 of the impact velocities used a value of $\eta \approx 0.5$ (see equation 4.4), whereas fits in Tauris (2015) and Liu et al. (2015) sit closer to $\eta \approx 0.2$. Our impact velocities lie in between these values, corresponding to $\eta \approx 0.3$. At the point of measurement of v_{im} , there will already be a small contribution in the measured v_{im} from the growing radial velocity component due to the eccentricity of the new orbit. However, even if we were to define the measured impact velocity to be earlier (before the shock convergence at the far side of the star), this still produces values of v_{im} that are larger than those seen in Liu et al. (2015). We consider a possible cause of differences in results in Section 4.3.3.

Finally, we also consider the effect of drag from the remaining material on the companion velocity, noting that there is still a non-negligible density of gas interior to the ejecta shell. For a conservative estimate of this drag force from the innermost ejecta, we neglect any outward velocity of this gas, and take a density of $10^{-3} \text{ g cm}^{-3}$ in this material. With these values, the drag force on the companion will be

$$F_{\text{drag}} = \frac{1}{2} \rho v_2^2 C_{\text{drag}} A_2 \approx 2 \times 10^{28} \text{ N}, \quad (4.7)$$

for $v_2 = 300 \text{ km s}^{-1}$, where we approximate the drag coefficient of the star with a solid sphere value of $C_{\text{drag}} \approx 0.5$. For a companion mass of $M_2 = 1 M_{\odot}$ the acceleration associated with this drag is therefore only $10^{-5} \text{ km s}^{-2}$. Although small, drag induced by the lower-velocity ejecta may appreciably alter the final velocity of the companion when integrated over a long timescale.

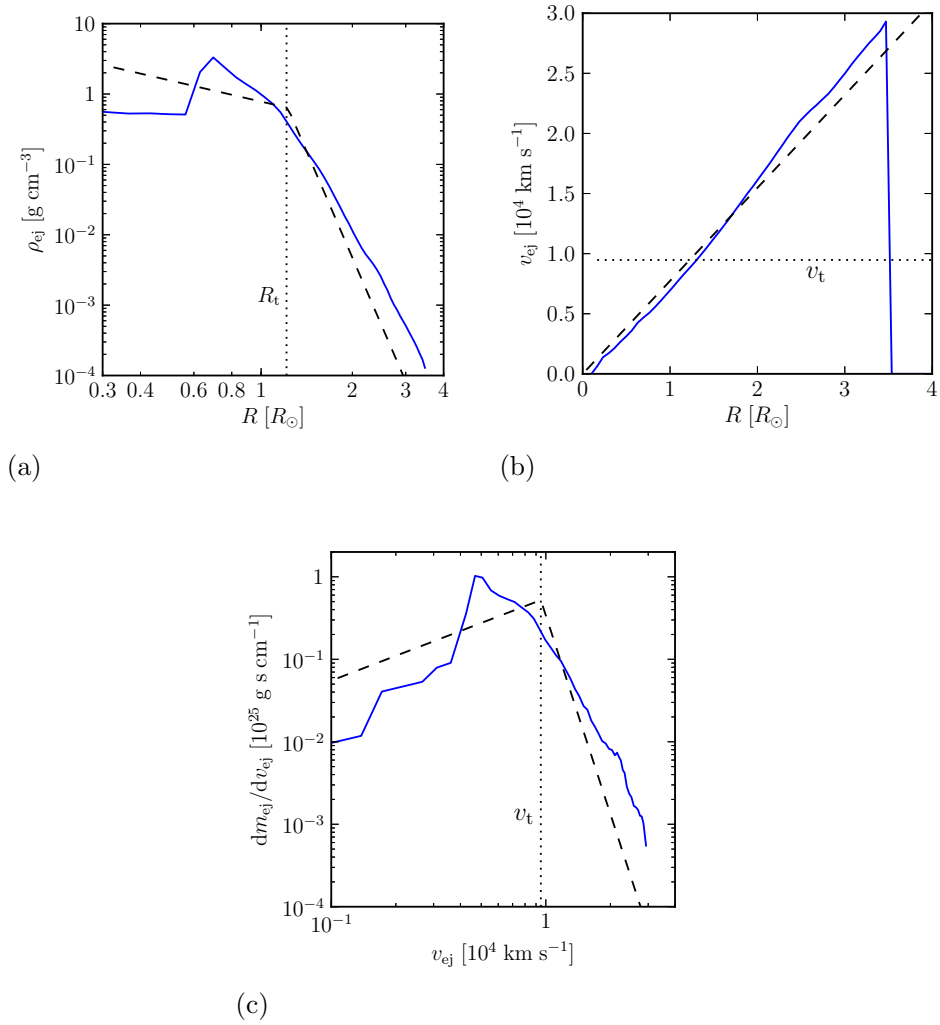


Figure 4.10: Solid blue lines show the profiles of (a) density, (b) magnitude of velocity and (c) the mass distribution of velocity within the ejecta for our simulations (binned in radial shells from the centre of mass of the ejecta). Dashed black lines show the power-law profiles used in Liu et al. (2015). Both cases were calculated for a time of 90 s after the supernova. The transition velocity (and radius at which this occurs) in the Liu et al. (2015) profiles are given as dotted lines.

Ejecta profiles

We investigate in more detail our ejecta profiles as a potential cause of the discrepancy between our impact velocities and those of Liu et al. (2015). Previous work, such as that of Liu et al. (2015), has often initialised the ejecta with the assumption that it is in a homologous expansion by the time it impacts the companion, so that, for a given t , $v \propto R$. The density and velocity profiles in this ejecta are constructed from broken power-law fits to analytic treatments of the shock through the progenitor. These treatments have, in particular, been based on the polytropic envelopes (or one-dimensional structure models) of supergiant stars, and the power-law fits are to the (small and large R) asymptotic limits of a varying density gradient in the ejecta (Chevalier and Soker 1989; Matzner and McKee 1999).

In Fig. 4.10, we show the variation of ejecta density and velocity as a function of radius from the centre of mass (by averaging the SPH particles over concentric shells) and compare with an analytic function from the equations used in Liu et al. (2015). We also show, in the bottom panel of Fig. 4.10, the distribution of velocity over mass in the ejecta. It is clear from Fig. 4.10 that in the ejecta from our helium star models we have a shallower density gradient through much of the outer regions compared with the power-law profiles. In this outer ejecta, the velocity and density are also higher in our models. As the impact velocity has a strong dependence on this high-velocity ejecta (Liu et al. 2015), this can explain the increased impact velocities seen in our simulations.

Finally, we examined the ejecta for large-scale asymmetries by determining the shell-averaged radial profiles of density and velocity in hemispheres corresponding to the directions toward and away from the companion star. We found that the values in either direction agreed to within a few per cent, and therefore do not produce a discernible difference on the logarithmic plots in Fig. 4.10.

4.3.4 Properties of the larger-scale SNR

Fig. 4.11 shows a 3D rendering of the SNR and companion at 10^3 s after the moment of the supernova. At this point, a hole has been created in the passing shell due to the presence of the companion, which is seen to persist at later times. The hole in the ejecta caused by the companion is approximately 30 degrees in size for the minimum orbital separations.

Even if an ejecta hole cannot be detected morphologically, the presence of a hole in SNR ejecta may allow the inference of a companion from a burst of radiation generated during the impact with the companion, which can escape through the less optically thick region of the companion shadow cone (Kasen 2010). The hole may persist to late stages of the SNR despite some amount of refilling due to the subsequent rarefaction wave along with hydrodynamic instabilities (Kasen 2010; García-Senz et al. 2012).

Not only do we observe a hole in the SNR due to the companion star, but we also see an increase in the density in a ring surrounding the hole, as shown most clearly

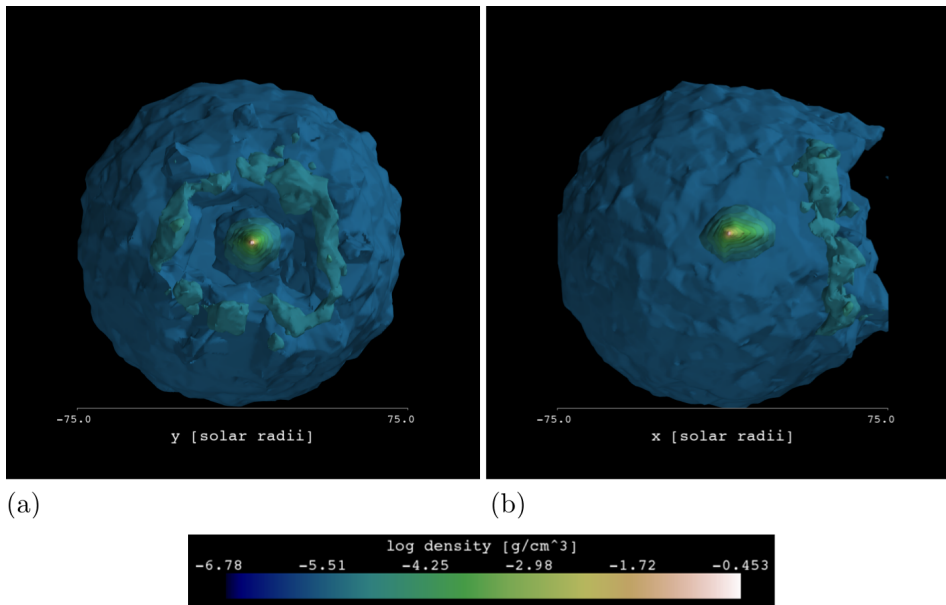


Figure 4.11: A 3D rendering of the gas density in the system 10^3 s after the supernova, viewed down the x -axis (a; the original axis of the binary) and y -axis (b). The companion is still distorted due to the impact, and has produced a hole in the expanding ejecta. We used the software Mayavi2 (Ramachandran and Varoquaux 2011) for the visualisation.

in Fig. 4.11. As shell material impacts the outer part of the companion star, where material is stripped and swept up with the ejecta, this ring of gas is also compressed in contrast with the freely expanding ejecta that do not interact with the companion. Aside from augmentation of the early supernova light curve, our results also suggest that ring-like enhancements in density of the SNR could indicate the presence of a companion star. Ring-like structures may be easier to detect than a hole in the SNR as the enhancement in density may also be associated with an increase in radiative losses in the ring.

The amount of accretion on the companion has previously been shown to decrease with increasing shell velocity (Fryxell and Arnett 1981); therefore, the high ejecta velocities in Type Ibc supernovae lead us to expect little pollution of the companion with supernova material. Indeed, we find negligible pollution of the companion star. The converse—pollution of the SNR with material from the companion—can be appreciable. A few $10^{-2}M_{\odot}$ of hydrogen-rich material may be lost from the companion by the passing shell in our simulations, which may be detectable as an asymmetry in the metallicity of the SNR on the side of the companion.

As the full composition (the mass fraction of each species as determined by the MESA model) is recorded for each SPH particle, we are able to trace the dispersion of this material from the progenitor in the subsequent SNR. We do not, however, cal-

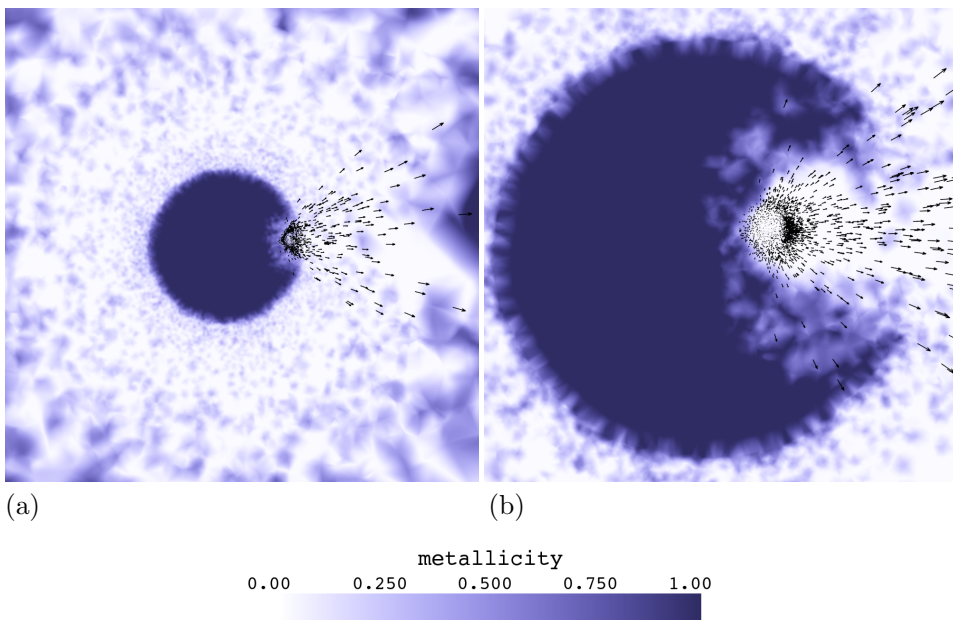


Figure 4.12: A $30 R_{\odot}$ by $30 R_{\odot}$ slice through the x - y (initial orbital) plane showing the mean metallicity ($1 - X_{\text{H}} - X_{\text{He}}$) within $1 R_{\odot}$ of the plane at (a) 733 s and (b) 2028 s after a supernova in a $3 M_{\odot}$ primary at an orbital separation of $4 R_{\odot}$. Black vectors show samples of the momentum of the material unbound from the companion star projected onto the orbital plane, as in Fig. 4.5.

culate the changes in composition during the supernova itself; as much of this process involves transmutation of one metal species to another in the stellar interior (where the metallicity remains $Z \sim 1$), we therefore limit the present discussion to the overall metallicity of the material.

Fig. 4.12 illustrates that the metallicity of the SNR is highest in the innermost regions, where the ejecta represents material nearest the core of the supernova progenitor. A hole develops in this high-metallicity ejecta, at first primarily due to the shadow of the companion star (panel a). At later times (panel b), the ablation of companion material further reduces the metallicity of a large fraction of the inner part of SNR in the direction of the companion. The orbital motion of the companion star within the inner SNR during this longer period of ablation can also enlarge the region over which the gas is enriched with hydrogen.

4.3.5 Post-impact state of the companion

Following the stripping and ablation of mass from the outer layers of the companion star, we used AMUSE to investigate the stellar evolution of the companion and compare with an unperturbed stellar model evolving from the main sequence. As we associate

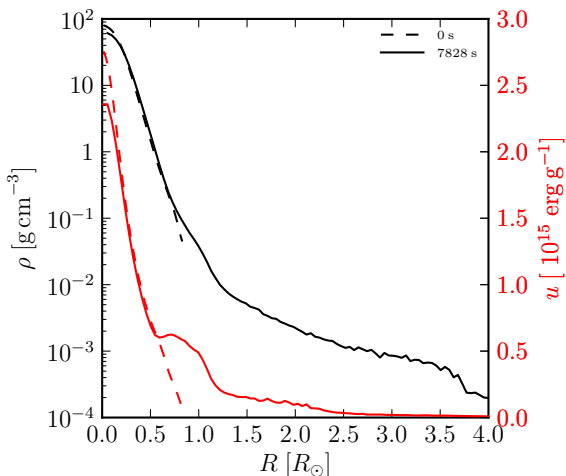


Figure 4.13: Density (left-hand axis) and internal energy (right-hand axis) of the companion star before (dashed lines) and 7828 s after (solid lines) the supernova explosion. These properties were determined by averaging across radial shells concentric with the centre of mass of the companion. All SPH particles bound to the companion were within a radius of $4.5 R_{\odot}$.

composition with each SPH particle from the original stellar model, we were able to convert the final SPH state of the companion back to a one-dimensional structure model by an inversion of the method to construct the SPH model outlined in Section 4.2.2. After the model is loaded back into MESA, we continue the stellar evolution and compare this with an undisturbed companion model.

As we find negligible contamination of the companion with ejecta material, the difference in evolution is effectively due to the reduction in mass of the star. A $1 M_{\odot}$ star with metallicity $Z = 0.02$ evolves to the through to a carbon-oxygen WD at 12.1 Gyr in MESA. On the other hand, the $1 M_{\odot}$ model which has lost $0.04 M_{\odot}$ of material from the supernova impact reaches this stage at a later age of 14.0 Gyr. Although the final age of the stars is noticeably different, there is little evolutionary difference between the two models on an HR diagram. It may, therefore, be difficult to distinguish a companion that has lost part of its envelope due to a supernova from T_{eff} and L alone. Nevertheless, the stripping and contamination in the outer layers of the star still has the potential to produce differences in chemical abundances that are spectrally distinguishable from the coeval stellar population (see also, for example, Pan et al. 2012).

More immediately, after the impact of the shell on the companion, a large amount of thermal energy is deposited in the outer layers of the star, which will dramatically affect its appearance over approximately the thermal timescale of the outer layers. To investigate this in more detail, in Fig. 4.13 we plot the density and internal energy of a companion star subjected to a supernova in a $3 M_{\odot}$ primary star at a separation of $4 R_{\odot}$. For this example, the total excess internal energy, integrated over the spherical shell $\gtrsim 0.6 R_{\odot}$, is $\Delta U \approx 10^{47}$ erg. If this were instantaneously converted to radiation, the excess energy would be released on a diffusion timescale, which we calculate to

be ~ 10 yr in these low-density outer layers of the star.⁷ The thermal timescale of the diffuse outer layers of such an expanded star is shorter than the canonical solar thermal timescale, and is of the order $t_{\text{therm}} \approx 10^3 \sim 10^4$ yr (Marietta et al. 2000; Podsiadlowski 2003). Nevertheless, as the thermal timescale is still orders of magnitude larger than the diffusion timescale, we expect the luminosity due to this excess energy to be limited by the former. A rough estimate of the luminosity can then be found from $\Delta U/t_{\text{therm}} \approx 10^2 \sim 10^3 L_{\odot}$. In practice, however, the luminosity will gradually decline from a peak value to the main-sequence luminosity⁸ over roughly the thermal timescale (Podsiadlowski 2003).

Finally, we note that in the example of Fig. 4.13, the furthest extent of the SPH particles in the companion was $\sim 4 R_{\odot}$. If the companion star were to continue expanding to a larger extent, its radius would encompass the neutron star in systems that remain bound, complicating the subsequent evolution of the system. This could increase the likelihood of accretion of material onto the neutron star, or even result in a merger between the neutron star and the companion. The interaction may also re-circularise the orbit after an eccentricity was gained from a kick to the neutron star during the supernova.

4.4 Discussion and conclusions

For supernovae in close binaries, the impact of the ejecta shell can have non-negligible effects on the mass and velocity of the companion star. The change in momentum of the companion is used in predictions of the final velocities of runaway stars from supernova-dissociated binaries, as seen in the recent work of Tauris (2015). These predictions are important for determining the level of contamination from these stars in searches for hypervelocity stars from other origins, such as the Hills mechanism with the supermassive black hole in the Galactic Centre (Hills 1988; Yu and Tremaine 2003).

We have performed SPH simulations of supernovae in close binaries to study the consequences of the shell impact on the companion. The overall hydrodynamic phenomena and trends we observe during these simulations are broadly consistent with previous studies of Type Ia (Marietta et al. 2000; Pakmor et al. 2008; Pan et al. 2012; Liu et al. 2012), Type Ibc (Liu et al. 2015) and Type II (Hirai et al. 2014) supernovae. In addition, we find that the gradient in the impact velocity predicted by Wheeler et al. (1975) matches our results well, with some modification of the η parameter representing the total momentum received by the companion.

⁷To obtain this value, we integrated from $0.6 R_{\odot}$ to the surface of the star assuming a Thomson cross-section.

⁸In fact, the luminosity from nuclear energy generation can drop lower than the main-sequence value, due to the reduction in central temperature and pressure following the initial expansion (Marietta et al. 2000).

While this work was in preparation, Liu et al. (2015) presented work on the effect of a Type Ibc supernova shell impacting a companion star. As with Liu et al. (2015), we find that the magnitude of mass loss and impact velocity of the companion is less than early estimates. However, the velocity induced onto the companion due to the shell impact in their work is a factor of $1.5 \sim 2$ lower than our results. Although it is not straightforward to separate the causes of such discrepancies, there are a number of differences between our calculations. One is the structure of the companion star, which is known to affect both the mass loss and impact velocity results (Meng et al. 2007; Pan et al. 2012; Liu et al. 2012, 2015). A more notable difference is that in our simulations the shell is naturally formed from the supernova explosion mechanism, as opposed to the introduction of the supernova ejecta by an analytic description. This results in a different ejecta structure, and more momentum carried in the leading edge of the ejecta, which is important in determining the final impact velocity (Liu et al. 2015).

Using the predictions from our simulations, we return to the question of runaway velocities of the components of supernova-disrupted binaries considered in TT98 and Tauris (2015). We have created a python code that calculates the final speeds derived by TT98 in order to investigate the analytic predictions with our simulation results. In this Monte Carlo code, an impulsive increase in velocity, w , is imposed to the neutron star, randomly oriented from an isotropic distribution over a sphere. This is achieved by mapping from a uniform random distribution over $t \in (0, 1]$ to $2\pi t$ for the angle ϕ , and from a uniform random distribution over $u \in [0, 1]$ to $\cos^{-1}(2u - 1)$ for the angle θ . Fig. 4.14 shows a comparison of the distributions of speeds with (red) and without (blue) the effect of applying v_{im} and mass loss in the companion star.

From Fig. 4.14, it is evident that, although adding an impact velocity to the companion (perpendicular to its orbital velocity) increases the minimum companion speed, it also in fact reduces the maximum companion speed. To clarify the discrepancies in the distributions that occur when adding v_{im} , we consider the effect of NS kick angles on the final velocity of the companion star in disrupted binaries in Fig. 4.15, analogous to Fig. 4 in Tauris (2015). The white regions for high θ in each panel represent binaries that remain bound after the NS kick (and thus the runaway velocity is undefined). The grey regions represent NS kick angles for which the NS and companion star merge after the supernova. It can be seen from the lower panel that the effect of applying an impact velocity to the companion star can stabilise the systems where the NS kick is counter-aligned with the NS orbital velocity. In fact, the small region of parameter space giving large values of v_2 at $\phi = 0$ and high θ is removed after adding v_{im} (due to these systems now remaining bound). This explains the potentially counter-intuitive result that by adding an additional velocity to the companion star in fact reduces the maximum possible velocity of runaway stars.

The main results of our work are as follows:

- We follow the supernova from just after the core bounce in a helium star generated from a stellar evolution model. Exploding a supernova in such a model pro-

Figure 4.14: Comparison of Monte Carlo sampling over NS kick orientation for the case with no impact effects on the companion (blue) and with impact effects as determined from our simulations (red). Both cases show 10^4 samples of NS kick orientation with a uniform on distribution over the unit sphere. The magnitude of the NS kick velocity, w , is fixed at 800 km s^{-1} throughout. Mean values of the runaway velocities, as well as percentages of cases where the binary components remain bound and merged (and, in parentheses, merged cases that were calculated as bound). Neither bound nor merged cases appear in these distributions.

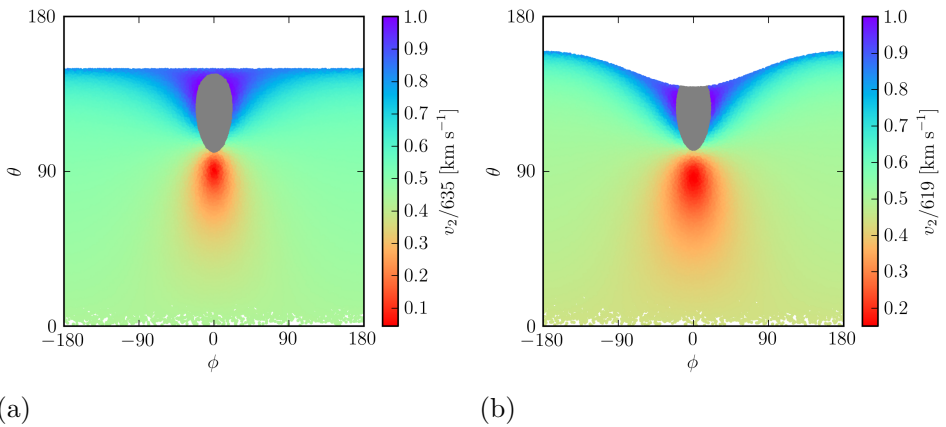
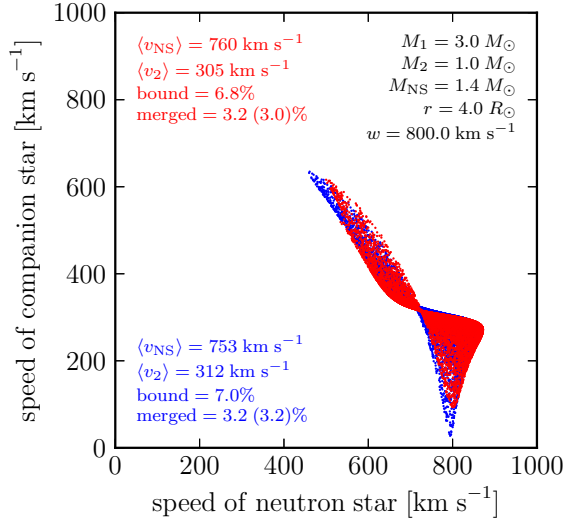


Figure 4.15: Distribution of NS kick angles from the x -axis (aligned with the pre-kick NS orbital vector) for the same parameters as the Monte Carlo runs shown in Fig. 4.14 (but with 2×10^5 samples to better fill the space in angles). The span of θ over $\phi = 0$ defines the orbital plane, where $\theta = 0$ is for a kick aligned with the NS orbital velocity vector. Panel (a) shows the case of no impact effects on the companion (blue distribution in Fig. 4.14) and panel (b) shows the case where impact effects determined from our simulations are included (red distribution in Fig. 4.14). Colours represent the magnitude of the companion star from disrupted binaries (as a fraction of the maximum runaway velocity). Grey shows cases where the NS and companion star merge. The white regions for large θ are cases where the binary remains bound and so there is no runaway companion.

duces an ejecta profile that is different from that used in previous work, which has employed an analytic function for the ejecta distribution derived from the theory of shocks travelling through a one-dimensional atmosphere. The progenitor model used here is still somewhat artificial in construction, with a constant mass loss parameter late in its evolution. As understanding of Type Ibc progenitors improves (for some recent investigations, see Kim et al. 2015), future work would benefit from a more realistic progenitor model by modelling the mass loss processes in detail.

- We have investigated the mass removed from the companion in the very close binary separations seen in Type Ibc supernovae, as well as the net change in momentum of the companion star due to the shell impact and later ablation of material. We show that an extrapolation of results from Type Ia supernova simulations do not provide a good fit to the Type Ibc scenarios considered here, and we provide updated fits to the distance-dependence of these results. In agreement with Liu et al. (2015), we find lower values of the removed mass and impact velocity of the companion compared to earlier estimates; however, we find generally larger impact velocities. Discrepancies in the results are due not only to differences in companion models but also to differences in the distribution of momentum in the ejecta.
- We investigated the morphology of the SNR shortly after the shell has passed the companion, as well as the pollution of the SNR with material stripped from the companion, which, for the case of Type Ibc supernovae, may be a detectable fraction of the total mass in the ejecta (several $10^{-2} M_{\odot}$ out of $\sim 2M_{\odot}$). The metallicity of the SNR is found to be highest in the inner regions of the SNR, and in this region the ablation of hydrogen from the outer layers of the companion star can dilute the metallicity on the side of the SNR facing the companion, resulting in a strong asymmetry in metallicity in the orbital plane.
- The companion star is additionally found to modify the morphology of the SNR in two distinct ways: as anticipated, a hole forms in the SNR on the side of the companion; also, an increase in the SNR density is seen in a ring around the hole, which may enhance the luminosity in SNR observations.
- We have also considered subsequent state of the companion after the shell impact and removal of mass during the shell impact, and have confirmed that the luminosity of the star can be orders of magnitude larger than the main-sequence luminosity during the release of thermal energy from the shock-heated outer layers.

Acknowledgements

We are grateful to Nathan de Vries for his assistance with an early version of the supernova explosion code in *AMUSE*, and to Arjen van Elteren and Inti Pelupessy for *AMUSE* code development. We also thank the two anonymous referees, whose comments helped improve this manuscript. This work was supported by the Netherlands Research Council (NWO grant numbers 612.071.305 [LGM] and 639.073.803 [VICI]), the Netherlands Research School for Astronomy (NOVA), the Interuniversity Attraction Poles Programme initiated by the Belgian Science Policy Office (IAP P7/08 CHARM), and by the European Union's Horizon 2020 Research and Innovation programme under grant agreement No. 671564.

5 A method to infer globular cluster evolution from observations of blue stragglers: the case of Hodge 11

A. Rimoldi, S. F. Portegies Zwart, E. M. Rossi
To be submitted

Blue straggler stars (BSSs) are ubiquitous in galactic globular clusters. Sitting above the main sequence turn-off, BSSs appear younger than the rest of the cluster. Two formation channels are often proposed to explain their origin: collisions between stars and binary mass transfer. The former is more likely at higher stellar densities, and therefore in particular after a cluster has undergone core collapse. We study the possible collisional origin of 24 of the innermost BSSs in the 11.7 Gyr-old Large Magellanic Cloud globular cluster Hodge 11, and use the derived collision times to estimate the time of cluster core collapse. To construct model BSSs, we adopt masses for hypothetical pairs of stars and collision times. We then use stellar evolution and collision codes in the Astrophysical Multipurpose Software Environment to evolve the two stars to the moment of collision, merge them, and then evolve the collision product to the age of the cluster. For each observed BSS, we find the best fitting collision time and the masses of the two merging stars. The results show that the distribution of mass between the two colliding stars has some degeneracy, but the time at which they collide is better defined. The formation rate of BSSs can be described well by the superposition of a constant background rate of 1.7 Gyr^{-1} and an exponentially decaying function with a peak at 3.4 Gyr (corresponding to the BSSs nearest to the turn-off) and an e -folding time of 1.4 Gyr. We attribute the background contribution to binary mass transfer and coalescence, which are not particularly sensitive to the dynamical evolution of the star cluster. The exponential rate we attribute to dynamically induced stellar collisions during the core collapse of the globular cluster. The expected moment of core collapse for Hodge 11 is then consistent with the peak of the exponential function (or somewhat earlier). The relatively long decay in the exponential curve may then be attributed to an episode of gravothermal oscillations, persisting for more than a Gyr.

5.1 Introduction

Since their discovery in the globular cluster M3, blue straggler stars (BSSs; Sandage 1953) have been a popular indicator for the dynamical evolution of stellar clusters (Stryker 1993; Bailyn 1995; Ferraro 2015). The two leading mechanisms for their origin involve collisions between stars in the cluster (Hills and Day 1976) and mass transfer (or coalescence) in binary stars (McCrea 1964). Both of these processes rejuvenate the star with respect to its surroundings, because they tend to make the star more massive, and fresh hydrogen may be mixed in the stellar interior, extending its main sequence lifetime. As a consequence, both processes lead to a population of stars that appear to be younger (born at a later epoch) than the other cluster members. It turns out to be difficult to objectively make a distinction between these two origin processes, and both are expected to contribute to the formation of BSSs (Davies 2015). Slight differences in the response to the moment at which mass is added, and subtleties in the stellar evolution, depending on how the stellar mass increases, give rise to slight differences in the observational characteristics (Ferraro et al. 2015).

We will test and study the consequences of the hypothesis that BSSs are the result of a collision between two stars, and use this to make inferences about the dynamical evolution of a globular cluster. As a template BSS population, we adopt those observed with the *Hubble Space Telescope* (HST) in the Large Magellanic Cloud cluster Hodge 11 (Li et al. 2013). The 162 BSSs in this $11.7^{+0.2}_{-0.1}$ Gyr-old star cluster appear to be composed of two distinct populations. The innermost BSSs, in the cluster core region (27 stars, at ≤ 15 arc seconds), are systematically lower in the colour-magnitude space (see Fig. 5.1) than the outermost subsample (also 27 stars, between 85 and 100 arc seconds; Li et al. 2013). This difference in color is consistent with earlier calculations on the origin of BSSs from direct stellar collisions, which tend to produce fainter BSSs that are rather close to the zero-age main sequence compared to those from a binary mass-transfer origin (Portegies Zwart et al. 1997a,b; Sills et al. 2002). This distinction is consistent with the collisional (blue) BSSs being in the densest regions where most collisions tend to occur, whereas outside the core it is suggested that binary evolution processes are dominant (Davies et al. 2004). Although stellar collisions tend to occur in the core, this collision rate increases sharply when the cluster experiences a phase of core collapse.

The ~ 40 BSSs in the globular cluster NGC 1261 show a similar bimodal distribution of red and blue BSSs. The latter population tend to be slightly more concentrated than the former, and both populations are more concentrated than the subgiants in the cluster. The blue BSS population was attributed to a core collapse in the star cluster, which, according to single stellar evolution models should have occurred about 200 Myr ago (Simunovic et al. 2014). Simunovic et al. (2014) adopted single stellar evolution models to study the BSS population in the Hertzsprung-Russell (HR) diagram, and correlate them with the moment of core collapse.

Our approach is similar in terms of using the blue BSSs to find the moment of

core collapse in Hodge 11. As we are interested in a population with the highest likelihood to have been formed from stellar collisions, we focus here on the innermost subsample of 27 BSSs in Hodge 11 (though we will also compare our results with the outermost subsample). However, instead of a more straightforward HR diagram analysis, we take the approach of simulating the collision process of the stars in order to reconstruct the histories of individual BSSs in the cluster. We approach the problem in two ways. We first create a grid of initial conditions to predict the final HST V and $V - I$ magnitudes, on which we fit the sample of BSSs by interpolation. As a second approach, the collision components for some selected BSSs are estimated by means of a Markov-Chain Monte Carlo (MCMC) method, in which the observed V and $V - I$ magnitudes of each BSS, as well as the age of the cluster, are used as goodness-of-fit parameters in the optimization algorithm. We compare the results of the two methods, providing a validation of our MCMC method by means of the gridded data.

5.2 Method

For both the MCMC and grid approaches, we employ the same method of generating a BSS. We first outline this method of creating BSS models and how the stellar properties are converted into observational predictions. We then discuss the two approaches in applying these predictions to the observed data.

5.2.1 BSS models

In order to construct each BSS model, we employ two astrophysics codes within the Astrophysical Multipurpose Software Environment (AMUSE; Portegies Zwart et al. 2009, 2013a). We start by constructing internal stellar structure models of two component stars with masses M_1 and M_2 using the Henyey code MESA (Paxton et al. 2011). The two stars are initialised with a metallicity of $Z = 0.0002$ ($[\text{Fe}/\text{H}] \approx -1.98$), representative of the low birth metallicity of the globular cluster stars (Li et al. 2013). Both of these stars are then evolved to identical ages, representing the collision time t_{col} . Agreement of the ages is achieved by constraining the final time steps applied by MESA; if the internally-determined MESA time steps are used, they are typically too coarse on the main sequence to get agreement of the final two stellar ages.

Once the stellar structure models have been constructed, we then merge the two stars using a second code in AMUSE, Make-Me-A-Massive-Star (MMAMS; Gaburov et al. 2008). MMAMS uses an entropy-sorting algorithm to determine the new equilibrium of a stellar collision, which extends a method first used for low-mass main sequence star collisions (Lombardi et al. 1996, 2002, 2003). This method of calculating the stellar structure typically takes a few minutes to produce a result, which allows us to perform a large sample of parameter space. A parameter search using full hydrodynamic simulations of such collisions would be infeasible, as the equivalent calculations can take a day or more on the same hardware (Gaburov et al. 2008). Finally, once the collision

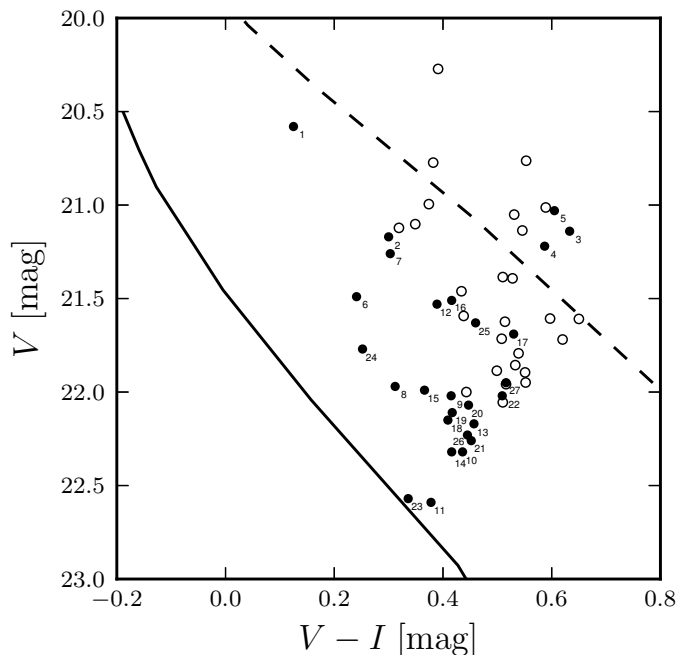


Figure 5.1: Positions on the colour-magnitude diagram for all the BSSs in Hodge 11. Bullets correspond to the inner population (≤ 15 arc seconds) of 27 BSSs (see Table 5.1), and open circles correspond to the outer population (between 85 and 100 arc seconds) of 27 BSSs. The solid black line shows the single-star zero-age main sequence as calculated in MESA with metallicity $Z = 0.0002$ and converted to V and $V - I$ space as described in Section 5.2.1. The dashed black line shows the terminal-age main sequence, as reported by AMUSE for the MESA models. The inner points are numbered corresponding to Table 5.1.

product has been generated, it is loaded back into MESA, and this BSS is then evolved until the age of the cluster.

Conversion from simulation results to observational parameters

Once we have produced a BSS model from MESA and MMAMS, we need to determine the equivalent V and I magnitudes in order to compare with observed BSSs. To do so, we have adapted a code used in Martínez-Barbosa et al. (2016), which was originally developed for predictions of *Gaia* magnitudes from simulated solar siblings in the Milky Way, and interfaced it with our blue-straggler code. We have modified this code to use the HST WFPC2 camera passbands¹ F555W and F814W (the V and I equivalent bands) that were used in the observations of Li et al. (2013).

¹The response functions were obtained at: <ftp://ftp.stsci.edu/cdbs/comp/wfpc2/>

Given a stellar structure model from MESA, we first find a best-match stellar spectrum from the BaSeL database of stellar spectra (Westera et al. 2002). We then perform a convolution of this spectrum with each filter response function in order to obtain a flux. This flux in each band is then converted to an observed magnitude by applying both a (true) distance modulus ($\mu_0 = 18.5$; Alves 2004; Li et al. 2013), as well as an extinction, where we use a colour excess of $E(B - V) = 0.09$ for Hodge 11 (Li et al. 2013) along with the $A/E(B - V)$ conversions to the two WFPC2 bands in Schlegel et al. (1998). This gives the final ‘observed’ V and I magnitudes from the simulation, which can then be directly compared with the observational HST data.

In Fig. 5.1, we overlay the single-star zero-age main sequence (ZAMS; solid line) and terminal-age main sequence (TAMS; dashed line) from $Z = 0.0002$ models in MESA, converted to V and $V - I$ using this method, on the colour-magnitude diagram (CMD) of the observed Hodge 11 BSSs. A star is flagged as having left the main sequence (therefore having reached the TAMS) if, according to MESA, the core hydrogen fraction reaches 1 per cent and the core temperature is dropping.

5.2.2 Grid approach

The grid was generated using an $8 \times 27 \times 24$ array of initial conditions over the respective intervals of $0.5 M_\odot \leq M_1 \leq 0.85 M_\odot$, $0.2 M_\odot \leq M_2 \leq 0.85 M_\odot$ and $0.1 \leq t_{\text{col}} \leq 11.7$ Gyr. The grid is immediately reduced in size along the M_2 dimension by the constraint $M_1 \leq M_2$. For the final ages of all the models in the grid, we take the accepted value of the age of the cluster, $t_{\text{H11}} = 11.7$ Gyr (Li et al. 2013).

Any stars that evolve off the main sequence before t_{H11} are terminated, and no BSS result is assigned to these initial conditions. This defines a TAMS edge to our parameter space. Although there may be some rejuvenation of the core with hydrogen during a collision, any collisions where one component is beyond the TAMS (Hertzsprung gap or later) will still have a substantial core, and the BSS is therefore expected to remain an evolved star after the collision (Portegies Zwart and Verbunt 1996; Portegies Zwart et al. 1997b). The lack of a need to explore evolution at, or beyond, the Hertzsprung gap has an advantageous side-effect of reducing the computational time, as stars start to undergo rapid structure changes at this point in their evolution and the calculations of their evolution in MESA slows down considerably.

After removing samples that produce no BSS model (for example, where the BSS leaves the main sequence before t_{H11} , or initial conditions where $M_2 > M_1$) the number of unique initial conditions that produce a BSS is 1490. Finally, to use the grid for comparison with the observed data, we convert the properties of the simulated model to V and $V - I$ magnitudes using the method in Section 5.2.1. We will describe the results of applying our grid to the observed BSS in Section 5.3.

#	F555W	σ_{F555W}	F814W	σ_{F814W}	V-I	σ_{V-I}
1	20.58	0.019	20.45	0.022	0.125	0.029
2	21.17	0.014	20.87	0.013	0.300	0.019
3	21.14	0.014	20.51	0.011	0.633	0.018
4	21.22	0.017	20.63	0.012	0.587	0.021
5	21.03	0.044	20.43	0.038	0.605	0.058
6	21.49	0.020	21.24	0.016	0.241	0.026
7	21.26	0.015	20.95	0.015	0.303	0.021
8	21.97	0.026	21.66	0.022	0.312	0.034
9	22.02	0.063	21.60	0.066	0.415	0.091
10	22.32	0.029	21.89	0.028	0.436	0.040
11	22.59	0.031	22.21	0.038	0.378	0.049
12	21.53	0.022	21.14	0.016	0.389	0.027
13	22.17	0.024	21.71	0.022	0.457	0.033
14	22.32	0.030	21.90	0.025	0.416	0.039
15	21.99	0.022	21.62	0.021	0.366	0.030
16	21.51	0.016	21.09	0.015	0.416	0.022
17	21.69	0.019	21.16	0.016	0.530	0.025
18	22.15	0.029	21.74	0.024	0.409	0.038
19	22.11	0.026	21.69	0.024	0.417	0.035
20	22.07	0.025	21.62	0.024	0.447	0.035
21	22.26	0.031	21.81	0.024	0.452	0.039
22	22.02	0.056	21.51	0.055	0.509	0.078
23	22.57	0.031	22.23	0.031	0.336	0.044
24	21.77	0.019	21.52	0.049	0.252	0.053
25	21.63	0.020	21.17	0.017	0.460	0.026
26	22.23	0.027	21.78	0.030	0.445	0.040
27	21.95	0.022	21.43	0.019	0.516	0.029

Table 5.1: Observed magnitudes in *Hubble Space Telescope* WFPC2 bands, and their errors, for the inner blue straggler stars in Hodge 11. Stars that were used in our MCMC runs are shown in bold.

5.2.3 MCMC approach

Our approach here starts by defining the end point in parameter space, which includes the observed V and I magnitudes of the BSS and the current age of the globular cluster, t_{H11} , as well as the errors on these values. We then select the masses of the two stars, M_1 and M_2 ($M_2 \leq M_1$) as well as a collision time t_{col} ($t_{\text{col}} < t_{\text{H11}}$), and create a BSS model from these initial parameters as outlined in Section 5.2.1. A goodness of fit of the final BSS model is then performed by comparing the model V , $V - I$ and age with the observed parameters, weighted by the observational error in each parameter. A Markov Chain is used to iteratively repeat this calculation, in which M_1 , M_2 and t_{col} are selected from the allotted parameter space until we have a consistent match with the observed BSS.

The MCMC analysis was performed using the python code `emcee` (Foreman-Mackey et al. 2013). Our MCMC code was constructed to also accommodate fast tests (using simple Gaussian functions rather than the full BSS simulations), in order to first confirm that the method is working as expected (that is, it can correctly reconstruct the original parameters used in the Gaussian distributions). The algorithm used in `emcee` employs an ensemble of ‘walkers’ that concurrently sample the parameter space at each step in the Markov Chain. Foreman-Mackey et al. (2013) recommend that a large number of walkers are used, although the number of walkers running in parallel is limited in practice by available computational resources. For the results presented here, we used 64 walkers, which we found gave convergence in a reasonable number of steps; the burn-in of the chain, after which the statistics should not be affected by the initial positions of the walkers, was typically only ~ 50 steps.

For the MCMC approach, the final age of the star is now taken as a fitted parameter, as in fact the age of the cluster has some error derived from isochrone fitting: $t_{\text{H11}} = 11.7^{+0.2}_{-0.1}$ Gyr. In the MCMC runs, the BSS models are run up to an age of $t_{\text{H11}} + 5\sigma_{t_{\text{H11}}}^+ = 12.7$ Gyr (provided that they have not left the main sequence by this time), and the age of the BSS is used in the goodness of fit for a track on the color-magnitude diagram between $t_{\text{H11}} \pm 5\sigma_{t_{\text{H11}}}$. If the BSS leaves the main sequence after $t_{\text{H11}} - 5\sigma_{t_{\text{H11}}}^-$ but before $t_{\text{H11}} + 5\sigma_{t_{\text{H11}}}^+$, the evolution is stopped at the moment it leaves the main sequence and the goodness of fit is performed on the track between $t_{\text{H11}} - 5\sigma_{t_{\text{H11}}}^-$ and the time it leaves the main sequence.

For the MCMC chains, we constrain the walkers within the parameter space to physically reasonable values of the initial parameters M_1 , M_2 and t_{col} . For initial conditions where any of these values are less than zero, where $M_1 < M_2$ or where $t_{\text{H11}} < t_{\text{col}}$, the log prior is set to $-\infty$. Similarly, a very conservative upper bound is placed on the initial masses to prevent walkers performing calculations in an unreasonably high set of initial masses. To obtain a rough estimate of the mass of the BSS, the mass-luminosity relation is used, based on the luminosity of the star (derived from the dereddened V -band magnitude and distance modulus) using $M_{\text{BSS,est}} = (L/L_{\odot})^{1/3.88} M_{\odot}$. If the sum $M_1 + M_2$ exceeds the conservative limit of $5 M_{\text{BSS,est}}$ in the walker initial conditions, the collision component masses are flagged as being too large, the posterior is

again automatically set to $-\infty$ and the full BSS simulation does not run for this step. For any initial conditions where a star leaves the main sequence, the evolution is also terminated (as per the reasoning in Section 5.2.2) and the log posterior is set to $-\infty$.

Finally, our code catches the rare cases where any of either of the AMUSE community codes fails; for example, in the case of not converging on a result in MMAMS, or in the case the mass becomes too low for MESA to initialise ($\lesssim 0.1 M_{\odot}$). To keep the runs fault-tolerant, such exceptions are caught and the code assigns $-\infty$ to the posterior probability, and then the next iteration is initiated.

For successful blue straggler models, the posterior required by emcee, in logarithmic form, is the sum of the log of the prior and the log of the likelihood. A naïve prior choice may be the estimated initial mass function of Hodge 11. However, the mass function in the centre of the cluster after core collapse, where it is suggested that collisions are more common, may be of a different form. Therefore, for the current work, the prior on all parameters in emcee is taken to be flat, implying a log probability of 0 in all cases.

The log likelihood is calculated from our simulation results and observational data using

$$\frac{1}{2} \sum_i \frac{(X_i - O_i)^2}{\sigma_i^2} - \ln(2\pi\sigma^2), \quad (5.1)$$

where X is the value of the parameter determined from the simulation, O is the observed value of the parameter, and σ is the error in the observed value.² The likelihood is calculated based on three final parameters compared between the simulations and observations (with errors): the V and $V - I$ magnitudes (calculated as outlined in Section 5.2.1) and the age.

We have additionally created a parallelised MCMC code using a distributed version of AMUSE (Drost et al. 2012), in order speed up the calculations, where we are able to take advantage of the parallel stretch-move capabilities of the emcee package. This enables the walkers to be assigned across not just multiple cores on one machine, or across nodes of a cluster, but on any networked resource that can run the AMUSE code.

Table 5.1 shows the inner 27 BSSs in Hodge 11, with the BSSs selected for our MCMC investigations in bold. These stars were chosen in order to test a wide region of the colour-magnitude space of the sample of BSSs. Fig. 5.1 shows the BSSs on the CMD, where the inner and outer blue stragglers are shown as bullets and open circles, respectively.

²Note that the maximisation of likelihood is found by the relative differences in the value from equation (5.1). Therefore, when comparing likelihoods, the factor of 1/2 and the second term containing only σ will cancel across trials, and so in practice this is equivalent to simply comparing $\sum_i (X_i - O_i)^2 / \sigma_i^2$.

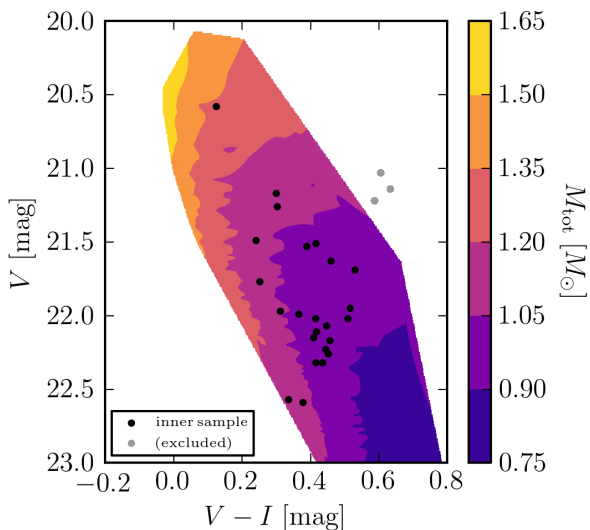


Figure 5.2: Contours of total mass $M_{\text{tot}} = M_1 + M_2$ of the two merging component stars located in the observational colour-magnitude space. The points represent the innermost 27 BSSs, where the three grey points are the stars excluded from our analysis as they sit beyond the TAMS.

5.3 Results

We begin this section by considering the results from fitting the grid of simulated BSSs to the observed BSS populations. We then consider the results from the approach of using MCMC searches for the most likely collision components of individual BSSs.

5.3.1 Grid results

Once the grid was generated and converted to observational values (using the method in 5.2.2), we performed a best-fit of the observational data to the grid results. The results from the grid were interpolated, and the best-fit was then carried out by minimising equation (5.1) using the observed and simulated values of the two parameters V and $V - I$.

Our grid results showed that the V and $V - I$ values are generally degenerate in M_1 and M_2 , implying that the division of total mass between the two colliding stars does not strongly influence the final position of the BSS on the CMD. Despite this degeneracy, we did still find a rough trend from low to high mass for each of M_1 and M_2 , from the lower right to upper left of the CMD. Reflecting the trends seen in the individual masses, the *total* mass M_{tot} has a more clearly defined result in V and $V - I$, and this is shown in Fig. 5.2.

The value of t_{col} is also well defined in V and $V - I$, and we show contours of the grid results in Fig. 5.3. Fitting the inner 24 BSSs that sit within the grid results for t_{col} (black points in Fig. 5.3) allows us to generate a cumulative distribution function (CDF) of collision times found from this method, and this is shown in Fig. 5.4. To compare with the CDFs of collision times from the grid data, we investigate two pos-

Figure 5.3: Contours of collision time t_{col} located in the observational colour-magnitude space. The points represent the innermost 27 BSSs, where the three grey points are the stars excluded from our analysis as they sit beyond the TAMS.

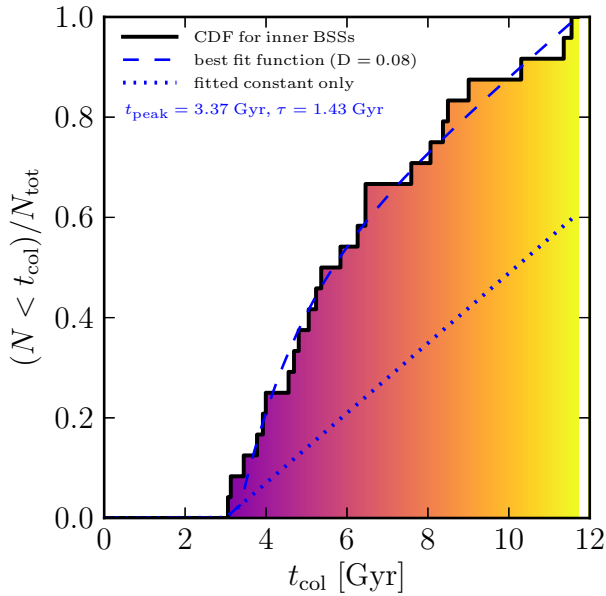
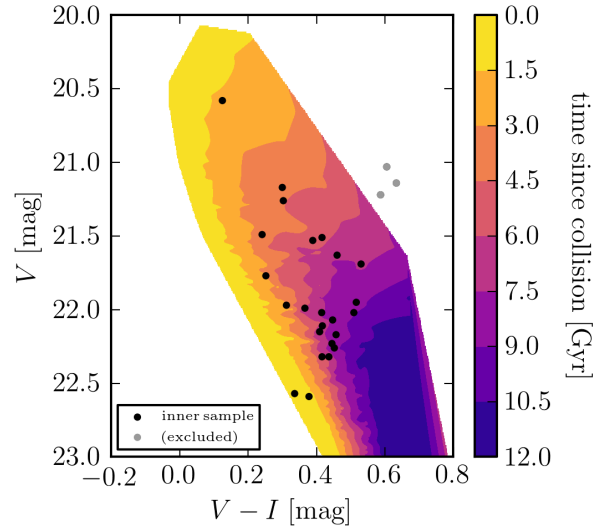


Figure 5.4: Cumulative distribution function (CDF) of t_{col} for the inner BSSs fitted from the grid data (as shown in the contours of Fig. 5.3). The colour under the CDF corresponds to the same colouring in the contours of Fig. 5.3. The solid blue line shows the best-fit exponential function (on top of a constant background) for collision probability. The dotted blue line shows the constant background to this fit alone.

sible fitting functions. In each case, we assume that BSSs formed from other channels (such as binary mass transfer) produce a signal in these results equivalent to a constant background rate for formation. Therefore, we try fitting the CDF with two components: a function representing the time-dependent formation probability via collisions, and a time-independent background probability.

For our fit, we used an exponentially decaying probability of collision, decaying from a time t_{peak} , with a decay time constant (e -folding time) τ , on top of a time-independent background probability, c . Due to the cut-off in observed BSS in our sample at ~ 3 Gyr, an additional filter is applied to the fitting functions where any BSS formation rate below this observational cut-off, t_{min} , is set to 0. The fitting function is, therefore,

$$p_{\text{col}}(t) \equiv \begin{cases} 0 & t < t_{\text{min}} \\ c & t_{\text{min}} \leq t < t_{\text{col}} \\ b \exp((t_{\text{peak}} - t)/\tau) + c & \text{otherwise} . \end{cases} \quad (5.2)$$

Note that we do not impose any constraint in any of the fitting that requires $t_{\text{col}} > t_{\text{min}}$, only that all parameters must be positive. To find the best fit to the CDFs for these functions, we use a Nelder-Mead simplex optimisation to find the minimum Kolmogorov–Smirnov (KS) statistic over the free parameters t_{peak} , τ , b and c .³

The best-fit exponential function is overlaid on the data in Fig. 5.4, as well as the constant background from this fit as a dotted line. The parameters of the best-fit exponential component are shown in the figure; the constant background corresponds to a formation rate of 1.7 Gyr^{-1} . If we can attribute the constant background to a signal from mass-transfer origins, this suggests that the majority of collisional BSSs formed between 3 and 6 Gyr, where we attribute the peak of exponential component with the core-collapse time of the cluster, $t_{\text{cc}} \approx 3.4$ Gyr. By 6 Gyr, the exponential component has contributed two-thirds of the total BSS formation. By the age of the cluster, the formation of BSSs from the constant background becomes the dominant contribution (~ 60 per cent of the total).

5.3.2 MCMC results

An example of MCMC walker positions for a specific inner BSS, number 1 in Table 5.1, is shown in Fig. 5.5. It is evident from Fig. 5.5 that the positions of the walkers (and therefore the statistics derived from them) after step ~ 70 are not affected by the

³We also considered an alternative fitting function to model a burst of BSS formation modelled by a Gaussian, centred on t_{col} with a width of σ , on top of a constant background probability, c . We found that, after optimisation, both functions can fit the data equally well; however, the best-fit Gaussian requires a large dispersion ($t_{\text{peak}} = 3.4$ Gyr, $\sigma = 1.8$ Gyr). This, therefore, implies that a narrow burst of formation does not describe these results—and, in agreement with the exponential distribution, a gradually decaying formation probability provides a better model.

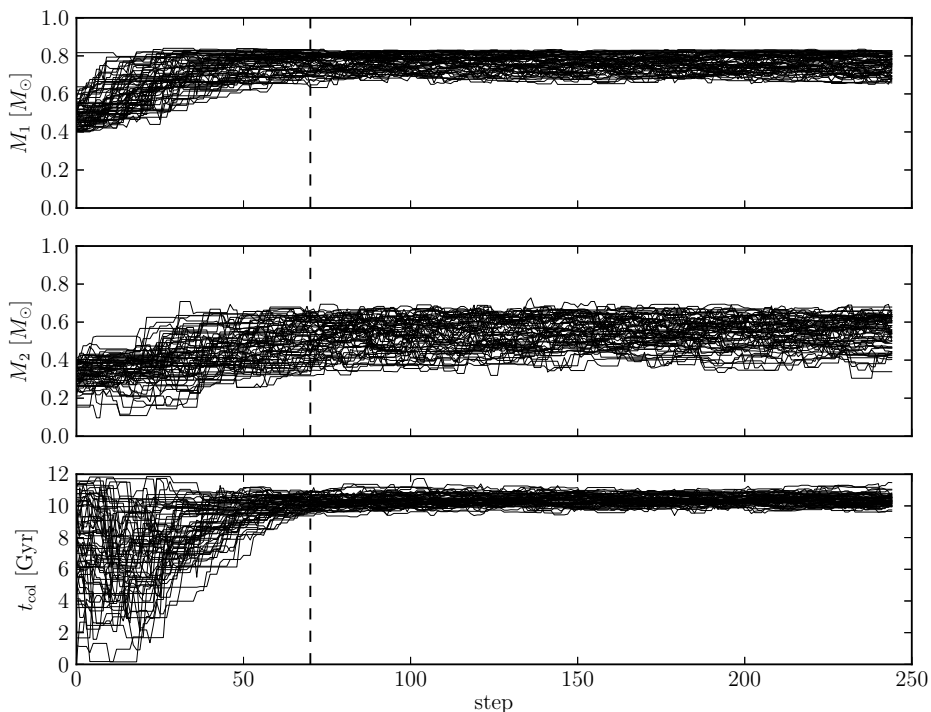


Figure 5.5: Positions of walkers used for the MCMC run for inner BSS 1. The parameters from top to bottom are: the mass of the more massive star, the mass of the less massive star, and the collision time. The black dashed line shows the cut for the chain burn-in; positions prior to this are not used for the final statistics.

initial positions of assigned to the chain. We therefore discard the first 70 steps as burn-in values for the chain, and produce results from the remaining steps. For the other MCMC runs, we use the same approach for finding a burn-in position.

A triangle plot, showing the samples for the MCMC run of the same example BSS (number 1), is presented in Fig. 5.6, to illustrate relationship between the three parameters M_1 , M_2 and t_{col} . These distributions are based on the positions of all the walkers in parameter space after removing the burn-in of 70 steps. We overlay three dashed lines on the distributions corresponding to the 16th percentile, the median and the 84th percentile of the distributions (to be compared with the parameter and σ estimates in Table 5.2).

Table 5.2 shows the results from all our MCMC runs. In general (as shown for the specific example of BSS 1), we find that the value of t_{col} is better defined than M_1 and M_2 . This is in agreement with the results from the grid, which showed that although the total mass of the merging stars was better defined, there was degeneracy in the distribution of that mass between M_1 and M_2 .

BSS #	steps	M_1	$\sigma_{M_1}^-$	$\sigma_{M_1}^+$	M_2	$\sigma_{M_2}^-$	$\sigma_{M_2}^+$	t_{col}	$\sigma_{t_{\text{col}}}^-$	$\sigma_{t_{\text{col}}}^+$	grid t_{col}
1	245	0.77	0.04	0.06	0.55	0.08	0.10	10.34	0.38	0.33	10.31
7	136	0.68	0.09	0.09	0.43	0.10	0.13	7.59	0.59	0.48	7.59
12	146	0.66	0.09	0.08	0.38	0.10	0.13	6.22	0.71	0.67	6.46
23	139	0.66	0.08	0.08	0.40	0.10	0.12	9.04 [†]	2.49	1.65	11.55
24	168	0.68	0.08	0.08	0.44	0.08	0.11	8.63	1.50	1.68	9.01
26	201	0.63	0.09	0.09	0.35	0.10	0.11	4.63 [‡]	1.99	1.46	3.99
27	155	0.59	0.10	0.08	0.36	0.09	0.13	3.25	0.79	0.73	3.13

Table 5.2: Results of MCMC search for the collision components of selected innermost BSSs. All MCMC chains used 64 walkers per step. The first column gives the BSS number corresponding to the first column of Table 5.1. Masses are in units of M_{\odot} and collision times are given in units of Gyr. The ‘steps’ column corresponds to the number of MCMC steps in the chain used in determining these results, including the burn-in values (which ranged from 40 \sim 70 steps). The final column shows the best-fit value of t_{col} from the grid results for comparison. †: shows strong bimodality in the result for t_{col} (therefore the median value should be taken with caution); ‡: shows mild bimodality in t_{col}

In Table 5.2 we also list the best-fit value of t_{col} obtained from the grid results. Comparing the results for t_{col} determined from the grid interpolation with those found in the MCMC runs shows good agreement between the two techniques (except for multi-modal solutions affecting the median value). The general agreement of the MCMC results with the grid interpolation provides confirmation of the effectiveness of our MCMC approach in finding solutions for this problem.

5.3.3 An independent estimate of the core-collapse time

For comparison with our estimate of the core-collapse time ($t_{\text{cc}} \approx 3.4$ Gyr), we consider an independent means of estimating t_{cc} described in Pijloo et al. (2015). This technique uses the observed conditions of clusters as fitting parameters for another MCMC method, which is based on a parametrised cluster evolution code (EMACSS; Alexander and Gieles 2012).

The cluster mass, galactocentric radius, velocity at this radius, and half-light radii are all used as fitting parameters for this approach. For Hodge 11, the first three of these parameters were respectively taken from Suntzeff et al. (1992), Freeman and Gascoigne (1977) and Alves and Nelson (2000). A range of possible (projected) half-light radii were considered, $2 \text{ pc} \leq r_{\text{phl}} \leq 4 \text{ pc}$, as this value is somewhat uncertain in the literature for Hodge 11.

Core-collapse was found to be around, or before, ~ 3 Gyr for simulations with $r_{\text{phl}} \lesssim 3.7$ pc (T. Pijloo, personal communication, 2015). There is then a large jump to $t_{\text{cc}} \sim 8$ Gyr found for half-mass radii only 10 per cent larger. Although there is no clear trend in t_{cc} with the (uncertain) half-light radius, the early core-collapse times that are found at small half-light radii are broadly consistent with our previous estimate. Inverting the problem, if we take our predicted core-collapse time to be true, the core-collapse times found using this independent method suggest that the half-light radius

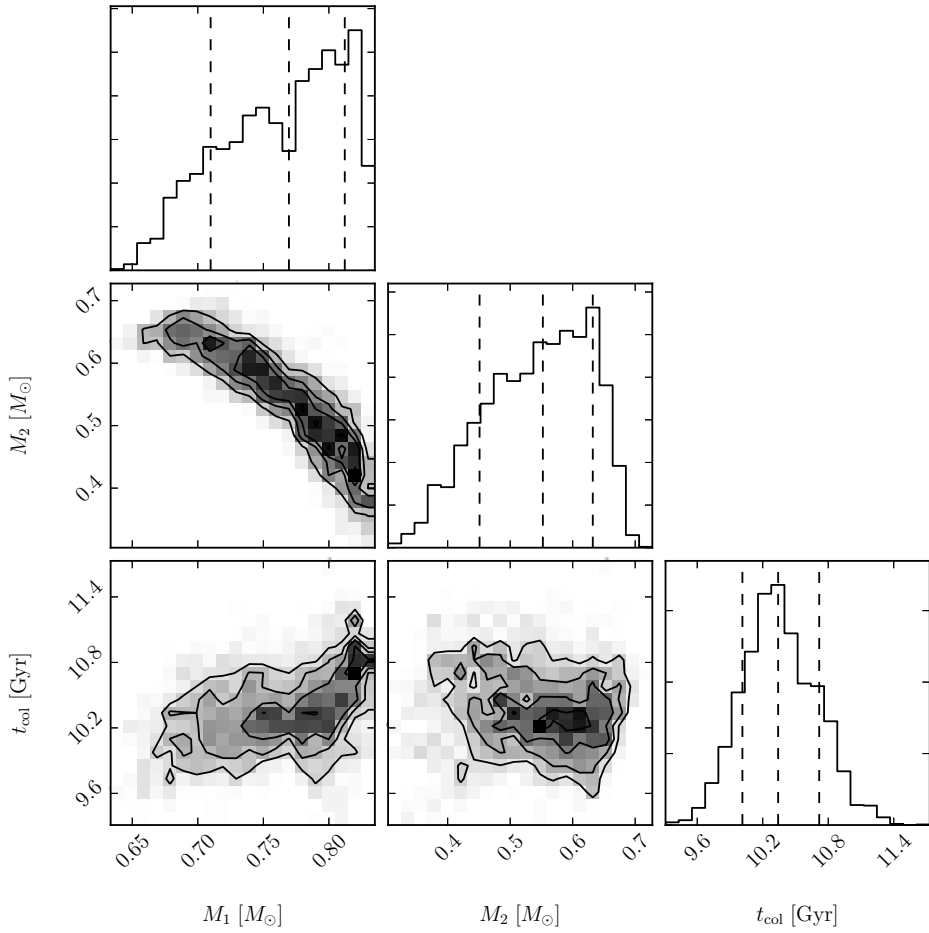


Figure 5.6: Triangle plot showing the outcome of MCMC sampling for inner BSS 1. M_1 and M_2 are the collision component masses, and t_{col} is the collision time. The vertical dashed lines show the median value, with the 16th and 84th percentiles on either side. These results were produced with 64 walkers, after removing 70 burn-in steps.

of Hodge 11 must be $r_{\text{phl}} \lesssim 3.7$ pc in order to agree with this value.

5.4 Discussion and conclusions

The 11.7 Gyr-old globular cluster Hodge 11 in the Large Magellanic Cloud has a rich population of blue stragglers. A total of 54 of these have been studied by Li et al. (2013), who separated them in equal portions of a more centrally concentrated population and a more extended population. They suggest that the inner population resulted from dynamical collisions between stars, whereas the homogeneous population could be the result of mass transfer in binary systems. Here, we examined the same BSSs in order to predict the properties of the collision that would be required to form them, as well as what this can tell us about the dynamical history of the cluster.

Beginning with the innermost BSSs, we adopt the assumption that all blue stragglers are the result of a collision between two stars which, at some moment t_{col} , merge to a single star, after which it continues to evolve to the age of the cluster. In attempting to reproduce the observed blue straggler population, we determine the best combination of primary mass, secondary mass and the moment of the collision. Following our conversion of the observed luminosity and colours, several blue stragglers turn out to have already left the main sequence. We excluded those from our analysis, leaving our fitting procedure with 24 of the innermost BSSs, which reside in a region where collisions have been argued to be more likely.

The procedure was carried out with the stellar evolution code MESA (Paxton et al. 2011) to evolve the two stars to the collision time, and we adopt the Make-Me-A-Massive-Star entropy-sorting algorithm (Gaburov et al. 2008) to carry out the stellar collisions. After the collision calculation is completed, we continue the evolution of the resulting single star using MESA. The code coupling was realised with the Astronomical Multipurpose Software Environment (Portegies Zwart et al. 2013a). A critical step of comparing our simulation results with observations is the conversion of the parameters from the stellar evolution calculations to the HST magnitudes, which is achieved by convolutions of the HST response functions with the best-fit synthetic spectra.

We have carried out the analysis in two different ways: by calculating a grid of primary masses, secondary masses and collision times, and by a Markov Chain Monte Carlo method. In the former analysis, we notice that the individual stellar masses tend to be rather unconstrained. The Markov Chain calculations indicate that this is caused by the degeneracy in the masses of the primary and secondary stars. The total stellar mass provides a better defined parameter, whereas the mass ratio can vary over a much wider range. The collision time can also be determined quite distinctly for each blue straggler, and it is in particular this quantity that we interpret.

By fitting the CDF of the collision times, we recognise two contributions to BSS formation: a constant BSS formation rate of $\sim 1.7 \text{ Gyr}^{-1}$, which we tentatively attribute to the effect of binary mass transfer and coalescence, and an exponential decay peaking at 3.4 Gyr and with an e -folding time of 1.4 Gyr, which we attribute to col-

lisions originating from the core collapse of the cluster. The decay time scale in the exponential may then be attributed to the multiple collapses in the period following the main core collapse. These gravothermal oscillations (or core oscillations, depending on the details of the gravothermodynamics) can last for time scales of \sim Gyr, which is consistent with our derived decay time scale (see, for example, Breen and Heggie 2012, and references therein).

We also performed a two-sample KS test between the CDFs obtained by fitting the individual innermost and outermost BSS subsamples to the grid independently. The KS statistic for these two distributions is $D = 0.32$; with the given sample sizes, this corresponds to a p-value of 0.16, which does not support rejecting the null hypothesis that the two samples are drawn from the same population. Alternatively, under the assumption that our best-fit distribution for the innermost BSSs represents the true formation probability, we also performed a one-sample KS test for the CDF of the outermost BSSs against this distribution.⁴ As expected, this gives a similar statistic of $D = 0.29$. With the sample size of 21 inner BSS that lie on the grid, the p-value is 0.051; this is a stronger result, though not quite significant at the 5 per cent level. Therefore, in the framework of the current analysis—that is, based on fitting to t_{col} from collisional models alone—our results cannot rule out the hypothesis that the same mechanisms (and therefore t_{col} distributions) govern the origin of the innermost and outermost BSSs.

A caveat to this approach is the cut-off used to determine the BSS star population used in Li et al. (2013). In order to be considered a BSS, a star had to be more than 3σ away from the (isochrone-fitted) ridge-line of the cluster. This likely omits some BSSs created by collisions that are within 3σ of the ridge-line, and therefore some stars that correspond to the earliest collision times (see Fig. 5.4) will be missed in the sample.

Inverting the cluster evolution, using the observed parameters, an MCMC search with a parametrised cluster evolution code can be used to provide an alternative estimation of the core-collapse time (Pijloo et al. 2015). The moment of core collapse in this reconstruction is uncertain, and is quite sensitive to the cluster half-light radius; the prediction that the cluster has indeed undergone core-collapse within its lifetime, however, is more robust. Within the limitations of this analysis, the results suggest Hodge 11 experienced core collapse $\lesssim 3$ Gyr after birth if the half-light radius is sufficiently low ($3 \sim 4$ pc).

Both of our approaches to estimating collision components of BSSs have some uncertainty due to degeneracy. In the case of the grid, although a much clearer trend was evident in t_{col} and M_{tot} than (separately) M_1 and M_2 , there was still some overlap on colour-magnitude space in some of these results, which results in some uncertainty in the interpolation. In the case of the MCMC chains, degeneracy is not only seen in M_1 and M_2 especially, but there is also evidence for bimodality in some solutions for t_{col} as shown in Fig. 5.7 (and therefore averaging should be treated with caution).

⁴That is, the parameters of the tested distribution are *not* derived from the sample data, as we are now comparing a different subsample of the BSS population.

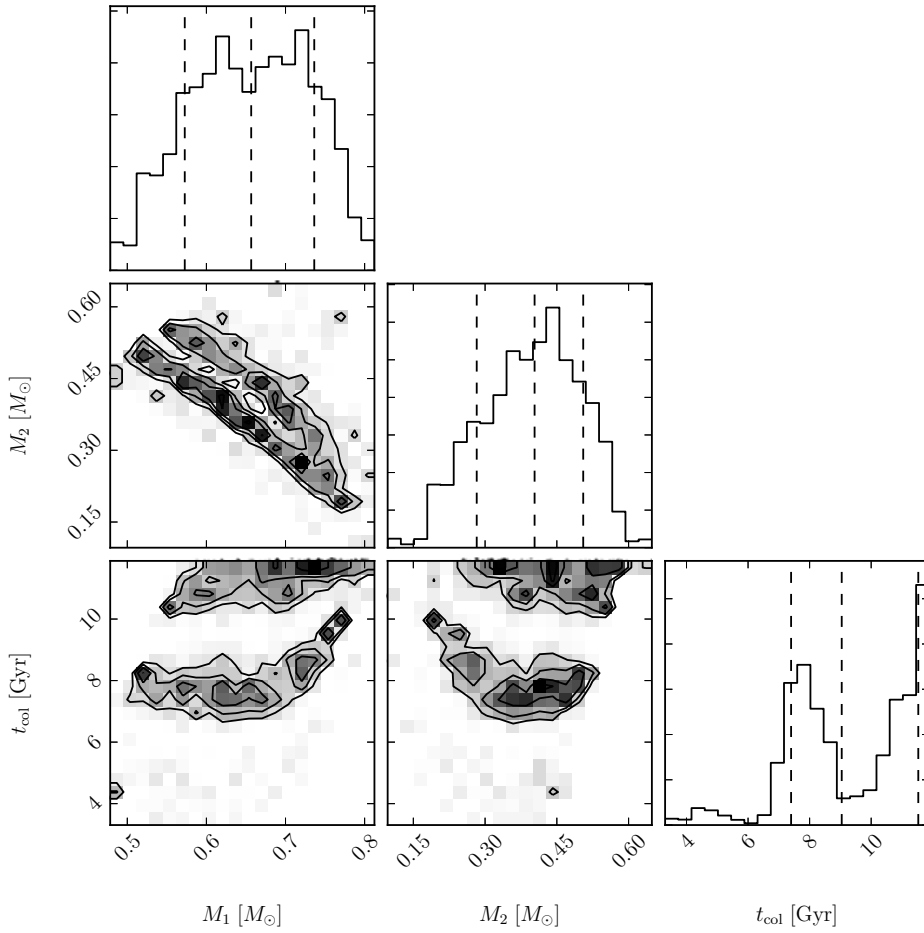


Figure 5.7: Triangle plot showing the outcome of MCMC sampling for inner BSS 23. This example has been included to show the clear bimodality in t_{col} for this result (the strongest case of bimodality out of all BSSs considered). Parameters and markers are the same as for Fig. 5.6. These results were produced with 64 walkers, after removing 50 burn-in steps.

Some multi-modality seen in the results is due to the inherent gridding in producing V and $V - I$ from the stellar models (even in the MCMC solutions) due to the finite library of stellar spectra used in the conversions from the stellar models.

A final caveat in this analysis is that the binary mass-transfer population is probably better modelled by adding mass to the stellar surface of the emerging blue straggler, rather than by applying the adopted entropy sorting algorithm, and the details of our conclusions may be affected by this. However, we do not know beforehand which blue stragglers are formed via one channel or the other, and therefore it would be somewhat complicated to invoke two formation scenarios. It would, nevertheless, in principle, be possible to conduct a primary component and optimization algorithm to the two distinct populations, taking into account the inner and the outer binary conditions. This would be a computationally intensive and rather uncertain undertaking without a guarantee that it provides a unique answer to the question of how the two populations are (or should) be divided among the individual blue stragglers. We therefore currently limit our analysis to the method described.

Our work shows that this method applied to BSS samples in other environments can be used to infer cluster dynamical evolution. This method is complementary to other techniques that use BSSs as a ‘dynamical clock’, such as inferring the current dynamical state of a cluster from the radial distribution of BSSs (Ferraro et al. 2012). As we could not rule out the hypothesis that the outermost BSSs in Hodge 11 come from the distribution that describes the innermost BSSs, a possible explanation is that collisional BSSs formed from an early core collapse may percolate to larger radii. Therefore, caution should be exercised when making a distinction of formation channels using radial positions of BSSs alone.

Acknowledgements

This work was supported by the Netherlands Research Council (NWO grant numbers 612.071.305 [LGM] and 639.073.803 [VICI]) and by the Netherlands Research School for Astronomy (NOVA). We are grateful to Carmen Martínez-Barbosa for providing us with her code for generating magnitudes from BaSeL spectra and for instructing us on its use. We also thank Tjibaria Pijloo for supplying core-collapse estimates for Hodge 11, as well as Chengyuan Li and Richard de Grijs for supplying data on the BSSs in Hodge 11.

Thesis summary

Stellar catastrophes

A star much more massive than our Sun ends its life in a spectacular fashion. Once its nuclear fuel is exhausted, the core of such a star can no longer support itself, and collapses into a compact object—either a neutron star or a black hole. Within seconds, the remaining outer layers of the star are violently expelled in a (core-collapse) *supernova* explosion.

An immense amount of energy is released in a supernova—about 100 times more than what the Sun will provide over its entire 10 billion year lifetime. Nearly all of this energy is quietly carried away by neutrinos, particles that are copiously produced during the supernova but are almost undetectable through their weak interaction with other matter. Only 0.01% of the energy is emitted as the light that so conspicuously signals the death of the star. Despite being such a small fraction of the total energy, in its earliest days the luminosity of a supernova is still enough to outshine a whole galaxy worth of stars. The remaining energy, about 1% of the total, goes into the motion of the gas that is shed from the star during the explosion. As this material, the *supernova ejecta*, expands into the surrounding medium, it sweeps up more gas, and evolves as a *supernova remnant* (Figure 5.8). Supernova remnants feature in most chapters of this thesis.

Most known supernova remnants are expanding into a relatively uniform interstellar medium that sits between the stars. However, in this thesis I investigate a more extreme medium—the environments found at the centres of massive galaxies. At the heart of nearly all large galaxies is at least one ‘supermassive’ black hole. In the case of our own Milky Way Galaxy, this black hole has about 4 million times the mass of the Sun. Despite being so massive, it is gravitationally dominant only over a region equivalent to a few times the distance between the Sun and the nearest known star.⁵ Within this *sphere of influence*, ‘winds’ of particles emitted from nearby stars are captured by the black hole, forming an *accretion flow*. Many young, massive stars (the type of star expected to undergo a supernova explosion) have been observed near

⁵Proxima Centauri—about 1 parsec, or 4 light years from the Sun

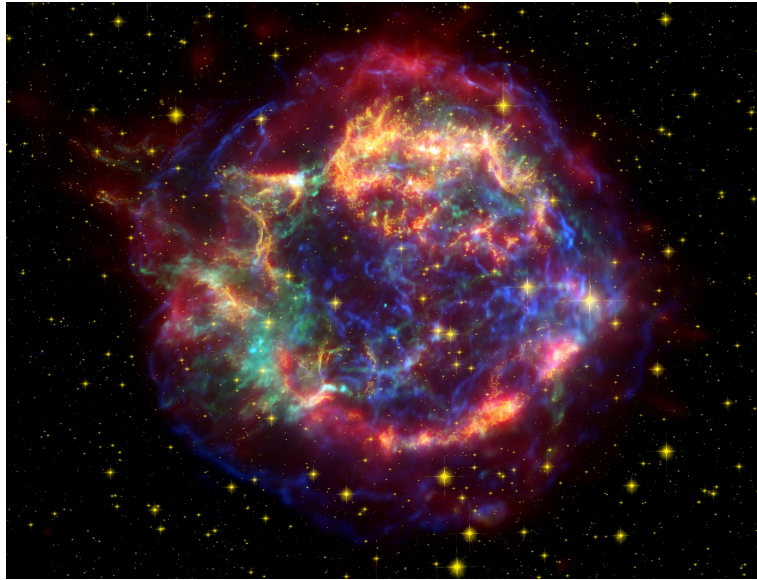


Figure 5.8: The core-collapse supernova remnant Cassiopeia A. Red represents infrared light from the *Spitzer Space Telescope*, orange is visible light seen by the *Hubble Space Telescope*, and blue and green are X-ray light from the *Chandra X-ray Observatory*. The compact object left behind from the explosion can be seen as the cyan point near the center of the shell. Credit: O. Krause, G. H. Rieke, E. Le Floch, K. D. Gordon, E. Egami, J. Biegging, E. Young, J. L. Hinz (Steward Observatory); S. M. Birkmann, S. P. Quanz (Max-Planck-Institut für Astronomie); J. P. Hughes (Rutgers University); D. C. Hines (Space Science Institute).

supermassive black holes, which has been seen most clearly in the Milky Way.

Properties of the accretion flow of the black hole, such as the variation in gas density over distance, depend on how energy and matter is transported within it. A number of different mechanisms have been proposed, leading to different possible models of the accretion flow. When a supernova explodes in such an environment, its evolution is determined by the structure of this gas around the black hole.

Supernovae can have dramatic effects on much more immediate surroundings, such as a companion star that is paired to the exploding star in a *binary* system. If the companion is close enough, the impact from the explosion will substantially distort the star, removing material from its outer layers and giving it a kick in the direction of the expanding material. In some cases, the binary may be unbound by the supernova, so that the companion escapes as a *runaway* star. Knowledge of how the companion star is affected by the supernova, and how the supernova remnant is affected by the companion, can help to inform searches for these companions. An understanding of runaway stars from unbound binaries is also important to distinguish them from other sources of stars with high velocities.

Finally, I focus on another type of catastrophic stellar event—this time, not an ex-

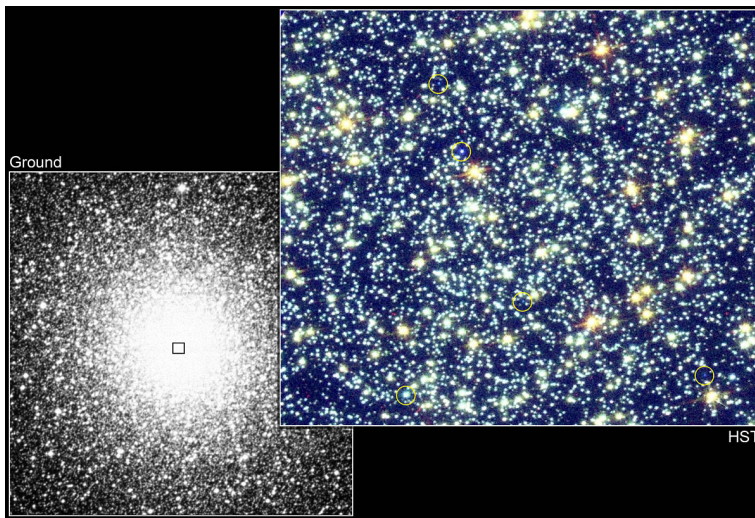


Figure 5.9: One of the most impressive globular clusters in the southern sky, 47 Tucanae. On the left is an image of the cluster from a ground-based telescope. On the right, the *Hubble Space Telescope* (HST) can resolve individual stars in the centre of the cluster, where blue straggler stars have been identified (circled). Credit: R. Saffer (Villanova University), D. Zurek (STScI) and NASA/ESA.

plosion of a star, but the collision of two stars. Although stars can collide in many possible environments, the occurrence is most commonly associated with stars deep within globular clusters (Figure 5.9). Globular clusters are ancient, dense objects whose stars formed around the same time. They are devoid of the gas required to form any more new stars. Yet, puzzlingly, short-lived blue stars have been found in all of these clusters that have been studied so far. At first blush, these stars should not be there; had they formed with the rest of the cluster, the lifetimes of these stars are too short for them to still exist. Two formation mechanisms are often considered for these *blue straggler* stars: the transfer of mass from one star to another in a binary system, or the collision between two stars. Stellar collisions, in particular, are more likely when the density of stars is very high, which is the case in the centres of globular clusters. The likelihood of a collision is further increased if the globular cluster has undergone a rapid increase in density known as *core collapse* (not to be confused with the type of supernova of the same name).

Clues from stellar catastrophes

The work presented here uses the catastrophic stellar events outlined above to investigate different aspects of their larger environment. The first part of this thesis examines what happens to supernova remnants in the innermost regions of galaxies like our own. In Chapter 2, I first develop a technique for predicting the evolution of super-

nova remnants in non-uniform density environments. This was created to investigate what happens to supernova remnants in the accretion flow near supermassive black holes, although the method is general enough to be applied to other types of environments. Different types of accretion flow will result in different shapes, sizes or lifetimes of supernova remnants. If we can predict how supernova remnants evolve in these environments, we can infer something about the medium into which they are expanding, and therefore about the surroundings of supermassive black holes.

Having established this method, in Chapter 3 I then make predictions of what could be observed from supernova remnants near supermassive black holes. Due to the vast distances to even the nearest massive galaxies, we cannot enjoy the same level of detail that can be resolved in the centre of our Milky Way Galaxy. Nevertheless, even if we are unable to observe the shape or size of supernova remnants directly, we can still measure their light, which is bright in X-rays when the supernova remnant is young. Therefore, in this chapter I estimate what contribution young supernova remnants can have to the X-ray emission from the centres of galaxies. I show that it can compete with other sources of X-rays, such as the emission from the accretion flow of the supermassive black hole itself. This is an important consideration in attempts to look for supermassive black holes in other galaxies, which in the present-day Universe tend to be relatively dormant, or *quiescent* (and are therefore more difficult to observe due to very little radiation being emitted).

In Chapter 4, I demonstrate what happens to a star that is a companion to a supernova explosion. I study a scenario that had not been well examined previously—a companion star very close to a star that has been stripped of much of its outer gas prior to its supernova explosion. These *stripped core-collapse supernovae*, categorised as Type Ib or Type Ic supernovae, have small amounts of ejecta that impact the companion star at high velocities. I use simulations with the Astrophysical Multipurpose Software Environment (AMUSE) to study the amount of mass removed from a companion star, as well as the kick in velocity it receives when it is hit by the expanding supernova ejecta. This information is helpful for predictions of the observable properties of runaway stars. Finally, I look at other effects such as the possible signature of the companion star in the expanding supernova remnant.

In Chapter 5, I use models of blue straggler stars (formed from stellar collisions) to learn about the globular cluster that contains them. I use simulations in AMUSE to evolve and collide stars at a given time to produce a blue straggler. Because the masses of the stars as well as the time at which they collide are varied, this produces a large number of possible models. The resulting models are compared with *Hubble Space Telescope* observations of blue straggler stars in a globular cluster, by determining what would be observed by this telescope for each of our model blue stragglers. By comparing the models with observations, we can estimate the formation times of the observed blue stragglers. In turn, it is possible to then make inferences about the history of the globular cluster, such as when it may have undergone core collapse.

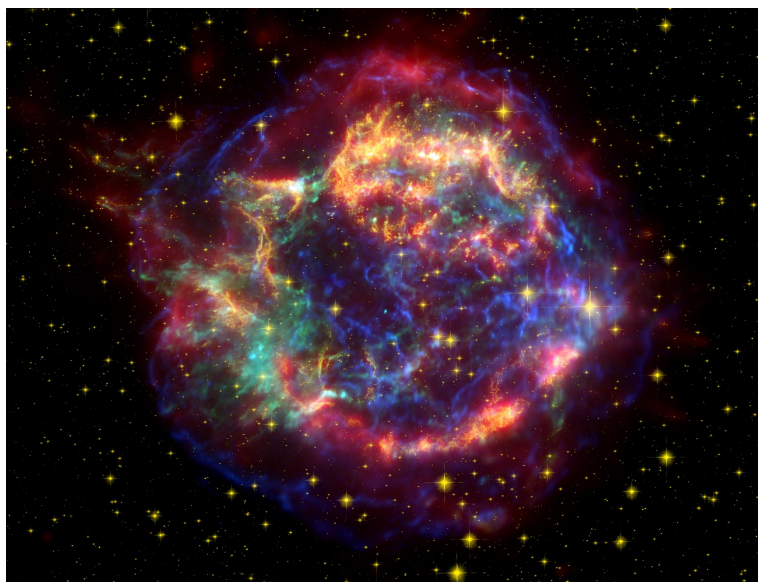
Nederlandse samenvatting

Stellaire catastrofes

Het leven van een ster, die velen malen zwaarder is dan de zon, zal op een spectaculaire manier eindigen. Als de nucleaire brandstof van de ster is uitgeput dan kan de kern van de ster zichzelf niet langer ondersteunen en zal ineenstorten tot een compact object—een neutronen ster of een zwart gat. Binnen enkele seconden na deze ineenstorting zullen vervolgens de buitenste lagen van de ster met veel geweld worden weggeblazen tijdens een (kern ineenstorting) *supernova* explosie.

Bij de supernova explosie komt er een enorme hoeveelheid energie vrij—ongeveer 100 keer meer dan wat de Zon gedurende zijn complete levenscyclus, van 10 miljard jaar, produceert. Bijna al deze energie wordt stilletjes weggevoerd door neutrino's, deeltjes die overvloedig tijdens de supernova worden geproduceerd maar die door hun zwakke interactie met andere materie bijna niet detecteerbaar zijn. Van alle energie wordt maar ongeveer 0.01% uitgestoten als licht, wat vervolgens zo opvallend de dood van de ster aangeeft. Ondanks dat licht maar zo'n klein deel van de totale supernova energie vormt, zal de lichtsterkte in de begin dagen van de supernova die van het gehele sterrenstelsel overtreffen. De overige energie, ongeveer 1% van de totale energie, zorgt voor de beweging van het gas dat, tijdens de explosie, wordt uitgestoten door de ster. Terwijl dit materiaal, de *supernova uitstoot*, uitdijt in het omliggende medium zal het meer gas in beweging zetten en zich uiteindelijk ontwikkelen tot een *supernovarest* (Figuur 5.10). In de meeste hoofdstukken van dit proefschrift zullen supernovaresten een rol spelen.

De meeste bekende supernovaresten breiden zich uit in het relatieve uniforme interstellaire medium dat zich tussen de sterren bevindt. Echter, in dit proefschrift doe ik onderzoek naar extremere situaties—namelijk de omgeving zoals die gevonden wordt in de centra van massieve sterrenstelsels. In het centrum van bijna alle grote sterrenstelsels bevindt zich minstens één zwart gat. Ook in het centrum van onze Melkweg bevindt zit zo'n zwart gat, deze heeft een massa van 4 miljoen keer de massa van de zon. Ondanks de grote massa, is het gebied waarin de zwaartekracht van dit zwarte gat dominant is maar ongeveer zo groot als een aantal keer de afstand tussen



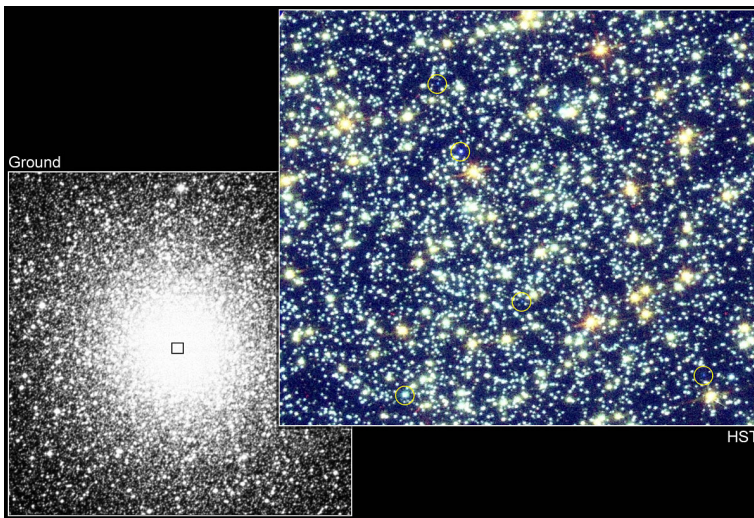
Figuur 5.10: De kern ineenstorting supernovarest Cassiopeia A. Rood representeert het infrarode licht opgevangen met de *Spitzer Space Telescope*, oranje het zichtbare licht zoals gezien door de *Hubble Space Telescope*, blauw en groen zijn de röntgenstralen zoals opgevangen door de *Chandra X-ray Observatory*. Het compacte object dat het gevolg is van de explosie kan worden gezien als het cyaan gekleurde punt in het centrum van de afbeelding. Credit: O. Krause, G. H. Rieke, E. Le Floch, K. D. Gordon, E. Egami, J. Biegging, E. Young, J. L. Hinz (Steward Observatory); S. M. Birkmann, S. P. Quanz (Max-Planck-Institut für Astronomie); J. P. Hughes (Rutgers University); D. C. Hines (Space Science Institute).

de Zon en de dichtstbijzijnde ster⁶. Binnen de *invloedsfeer* van een zwart gat zullen deeltjes, die van sterren worden weggeblazen door sterrenwinden, gevangen worden door de *accretie stromen* van het zwarte gat. Vele jonge, massieve sterren (het soort ster dat naar verwachting een supernova zal vormen) zijn waargenomen in de omgeving van super massieve zwarte gaten, deze zijn het beste zichtbaar in onze eigen Melkweg.

De eigenschappen van de accretie stromingen, zoals de variatie in gasdichtheid is afhankelijk van hoe de energie en materie wordt getransporteerd. Er zijn verschillende modellen om deze stromingen te beschrijven afhankelijk van welk onderliggend mechanisme verondersteld wordt. Maar in alle gevallen zal de structuur van het gas rondom het zwarte gat de evolutie van de supernova explosie bepalen.

Supernova's hebben een dramatisch effect op hun directe omgeving, zoals een begeleidende ster welke een paar vormt met de exploderende ster in een *dubbelster* systeem. Als de begeleidende ster dichtbij genoeg is, zal de supernova explosie de ster aanzienlijk verstoren want de buitenste gaslagen van de ster zullen worden weggeblazen in de richting van het uitdijende materiaal. In sommige gevallen kan de dubbelster

⁶Proxima Centauri—ongeveer 1 parsec, oftewel 4 lichtjaar vanaf de Zon



Figuur 5.11: Eén van de meest indrukwekkende bolvormige sterrenhopen in de zuidelijke hemel, 47-Tucanae. Links is een afbeelding van de bolhoop gemaakt door een telescoop vanaf de grond. Rechts een afbeelding die gemaakt is door de *Hubble Space Telescope* (HST) welke de individuele sterren in het centrum van de cluster kan zien, waar blauwe achterblijvers zijn geïdentificeerd (omcirkeld). Credit: R. Saffer (Villanova University), D. Zurek (STScI) and NASA/ESA.

zelfs ongebonden raken door de supernova en zal de begeleidende ster wegschieten als een *ontsnappende* ster. Kennis over hoe de supernova de begeleidende ster beïnvloed, en hoe de supernovarest wordt beïnvloed door de begeleidende ster kan helpen bij de observationele zoektocht naar dit soort begeleiders. Verstand van ontsnappende sterren uit ongebonden dubbelsterren is ook belangrijk om onderscheid te maken tussen ontsnappende sterren en andere snel bewegende sterren.

Verder richten we ons op een andere, ster gerelateerde, catastrofale gebeurtenis—deze keer geen explosie, maar een botsing tussen twee sterren. Alhoewel sterren in veel verschillende omgevingen kunnen botsen, komt deze gebeurtenis het vaakst voor diep in de centra van bolvormige sterrenhopen, bolhopen (Figuur 5.11). Een bolhoop is een oude groep sterren, ontdaan is van gas dat vereist is voor het vormen van nieuwe sterren en waarvan de sterren dicht op elkaar staan en ongeveer op hetzelfde moment ontstaan zijn. Toch zijn er, op raadselachtige wijze, in alle tot op heden bestudeerde bolhopen kort levende blauwe sterren waargenomen. Op het eerste gezicht zouden deze sterren er niet moeten zijn; hun levensduur is te kort om nog steeds aanwezig te zijn als ze tegelijk met de rest van de bolhoop gevormd waren. Twee oorzaken worden vaak als mogelijkheid gezien voor de formatie van dit soort *blauwe achterblijvers*: massatransport van de ene ster in een dubbelster systeem naar de andere ster of een botsing tussen twee sterren. Sterbotsingen in het bijzonder zijn kansrijker als de dichtheid van de sterren erg hoog is, wat in het centrum van bolhopen het geval is. De kans op een botsing wordt verder verhoogd wanneer de sterrenhoop een snelle toename van

dichtheid heeft ondergaan, een zogenaamde *kern ineenstorting* (niet te verwarren met het soort supernova met dezelfde naam).

Wat we kunnen leren van stellaire catastrofes

Het in dit proefschrift gepresenteerd werk gebruikt de hierboven geïntroduceerde catastrofale gebeurtenissen om verschillende aspecten van hun omliggende omgeving te onderzoeken. In het eerste deel onderzoek ik wat er gebeurt met supernovaresten in de binnenste regionen van sterrenstelsels zoals de Melkweg. Om te beginnen, ontwikkelen we in hoofdstuk 2, een techniek om te voorspellen hoe supernovaresten zich ontwikkelen in omgevingen met een niet-uniforme dichtheid. Dit was ontwikkeld om te onderzoeken wat er gebeurt met supernovaresten in de accretie stromen vlak bij super massieve zwarte gaten, maar de methode is algemeen genoeg om te worden toegepast op andere soorten omgevingen. Verschillende soorten accretie stromen zullen resulteren in verschillende vormen, groottes en levensduren van supernovaresten. Als we kunnen voorspellen hoe supernovaresten evolueren in deze omgevingen, dan kunnen we iets afleiden over het medium waarin ze uitdijen, en daardoor iets zeggen over de omgevingen van super massieve zwarte gaten.

Nu deze methode gedefinieerd is maak ik vervolgens in hoofdstuk 3 voorspellingen over wat er geobserveerd kan worden van supernovaresten nabij super massieve zwarte gaten. Vanwege de enorme afstanden tot zelfs de dichtstbijzijnde massieve sterrenstelsels, kunnen we niet genieten van hetzelfde detail niveau als wat kan worden bereikt in het centrum van de Melkweg. Niettemin, zelfs als we niet in staat zijn om de vorm of grootte van supernovaresten direct waar te nemen, kunnen we nog steeds hun lichtsterkte meten, welke erg helder is in röntgenstralen als de supernovarest jong is. Daarom schatten we in dit hoofdstuk wat de bijdrage van jonge supernovaresten is aan de röntgenstraling vanuit de centra van sterrenstelsels. We tonen aan dat het kan concurreren met andere bronnen van röntgenstraling, zoals de emissie die de accretie stromen van het super massieve zwarte gat zelf veroorzaken. Dit is een belangrijke overweging bij de zoektocht naar super massieve zwarte gaten in andere sterrenstelsels, die in het huidige Heelal de neiging hebben om relatief inactief te zijn, oftewel *rustig* (doordat er zeer weinig straling wordt uitgestoten zijn ze moeilijker waar te nemen).

In hoofdstuk 4 onderzoek ik wat er gebeurt met een ster die de begeleider is van een supernova explosie. We onderzoeken een tot nu toe niet uitgebreid onderzocht scenario—een begeleidende ster welke zeer dicht bij een ster staat welke, voordat hij ontploft als een supernova, is ontdaan van bijna al zijn buitenste gas lagen. Deze *gestripte kern-ineenstorting supernova*, gecategoriseerd als type Ib of type Ic supernova, hebben kleine hoeveelheden ejecta welke met hoge snelheden inslaan op de begeleidende ster. We gebruiken simulaties, gedaan met de Astrofysische Multifunctionele Software Omgeving (AMUSE), om te onderzoeken hoeveel massa van de begeleidende ster wordt verwijderd en welke schok en versnelling de ster ondergaat wanneer die geraakt wordt door de uitdijende supernova ejecta. Deze informatie is behulpzaam

om voorspellingen te doen over de observeerbare eigenschappen van dit soort ontsnappende sterren. Tot slot kijk ik naar andere effecten, zoals de mogelijke unieke handtekening van de begeleidende ster in de uitdijende supernovarest.

In hoofdstuk 5 gebruik ik modellen van, door ster botsingen gevormde, blauwe achterblijvers om meer te leren over de bolhopen waarin ze zich bevinden. We gebruiken simulaties, gemaakt met AMUSE, om sterren te evolueren en op een bepaalde tijd te laten botsen zodat ze een blauwe achterblijver vormen. Doordat ik zowel de massa als het botsingstijdstip van de sterren varieer produceer ik een grote hoeveelheid modellen. Deze zijn vervolgens vergeleken met observaties, gemaakt met de *Hubble Space Telescope*, van blauwe achterblijvers in bolhopen door voor elk model te bepalen wat er door de telescoop zou moeten zijn waargenomen. Door de modellen te vergelijken met de observaties is het mogelijk om het formatie tijdstip van deze blauwe achterblijvers te schatten. En vervolgens kunnen er conclusies getrokken worden over de formatie geschiedenis van de bolhopen, zoals wanneer deze een kern instorting hebben ondergaan.

Bibliography

- J. A. Ahumada and E. Lapasset. New catalogue of blue stragglers in open clusters. *A&A*, 463: 789–797, February 2007. doi: 10.1051/0004-6361:20054590.
- P. E. R. Alexander and M. Gieles. A prescription and fast code for the long-term evolution of star clusters. *MNRAS*, 422:3415–3432, June 2012. doi: 10.1111/j.1365-2966.2012.20867.x.
- T. Alexander. Stellar processes near the massive black hole in the Galactic center [review article]. *Phys. Rep.*, 419:65–142, November 2005. doi: 10.1016/j.physrep.2005.08.002.
- D. R. Alves. A review of the distance and structure of the Large Magellanic Cloud. *New A Rev.*, 48:659–665, July 2004. doi: 10.1016/j.newar.2004.03.001.
- D. R. Alves and C. A. Nelson. The Rotation Curve of the Large Magellanic Cloud and the Implications for Microlensing. *ApJ*, 542:789–803, October 2000. doi: 10.1086/317023.
- M. Asplund, N. Grevesse, A. J. Sauval, and P. Scott. The Chemical Composition of the Sun. *ARA&A*, 47:481–522, September 2009. doi: 10.1146/annurev.astro.46.060407.145222.
- F. K. Baganoff, Y. Maeda, M. Morris, M. W. Bautz, W. N. Brandt, W. Cui, J. P. Doty, E. D. Feigelson, G. P. Garmire, S. H. Pravdo, G. R. Ricker, and L. K. Townsley. Chandra X-Ray Spectroscopic Imaging of Sagittarius A* and the Central Parsec of the Galaxy. *ApJ*, 591: 891–915, July 2003. doi: 10.1086/375145.
- C. D. Baily. Blue Stragglers and Other Stellar Anomalies: Implications for the Dynamics of Globular Clusters. *ARA&A*, 33:133–162, 1995. doi: 10.1146/annurev.aa.33.090195.001025.
- G. H. Ball, R. Narayan, and E. Quataert. Spectral Models of Convection-dominated Accretion Flows. *ApJ*, 552:221–226, May 2001. doi: 10.1086/320465.
- E. Y. Bannikova, A. V. Karnaushenko, V. M. Kontorovich, and V. M. Shulga. A new exact solution of Kompaneets equation for a shock front. *Astronomy Reports*, 56:496–503, July 2012. doi: 10.1134/S1063772912060017.
- H. Bartko, F. Martins, T. K. Fritz, R. Genzel, Y. Levin, H. B. Perets, T. Paumard, S. Nayakshin, O. Gerhard, T. Alexander, K. Dodds-Eden, F. Eisenhauer, S. Gillessen, L. Mascetti, T. Ott, G. Perrin, O. Pfuhl, M. J. Reid, D. Rouan, A. Sternberg, and S. Trippe. Evidence for Warped Disks of Young Stars in the Galactic Center. *ApJ*, 697:1741–1763, June 2009. doi: 10.1088/0004-637X/697/2/1741.
- H. Bartko, F. Martins, S. Trippe, T. K. Fritz, R. Genzel, T. Ott, F. Eisenhauer, S. Gillessen, T. Paumard, T. Alexander, K. Dodds-Eden, O. Gerhard, Y. Levin, L. Mascetti, S. Nayakshin, H. B. Perets, G. Perrin, O. Pfuhl, M. J. Reid, D. Rouan, M. Zilka, and A. Sternberg. An Extremely Top-Heavy Initial Mass Function in the Galactic Center Stellar Disks. *ApJ*, 708:834–840, January 2010. doi: 10.1088/0004-637X/708/1/834.

- M. C. Begelman. Radiatively inefficient accretion: breezes, winds and hyperaccretion. *MNRAS*, 420:2912–2923, March 2012. doi: 10.1111/j.1365-2966.2011.20071.x.
- M. C. Bersten, O. G. Benvenuto, G. Folatelli, K. Nomoto, H. Kuncarayakti, S. Srivastav, G. C. Anupama, R. Quimby, and D. K. Sahu. iPTF13bvn: The First Evidence of a Binary Progenitor for a Type Ib Supernova. *AJ*, 148:68, October 2014. doi: 10.1088/0004-6256/148/4/68.
- G. S. Bisnovatyι-Kogan and S. A. Silich. Shock-wave propagation in the nonuniform interstellar medium. *Reviews of Modern Physics*, 67:661–712, July 1995. doi: 10.1103/RevModPhys.67.661.
- R. D. Blandford and M. C. Begelman. On the fate of gas accreting at a low rate on to a black hole. *MNRAS*, 303:L1–L5, February 1999. doi: 10.1046/j.1365-8711.1999.02358.x.
- R. D. Blandford and M. C. Begelman. Two-dimensional adiabatic flows on to a black hole - I. Fluid accretion. *MNRAS*, 349:68–86, March 2004. doi: 10.1111/j.1365-2966.2004.07425.x.
- J. M. Blondin, E. B. Wright, K. J. Borkowski, and S. P. Reynolds. Transition to the Radiative Phase in Supernova Remnants. *ApJ*, 500:342, June 1998. doi: 10.1086/305708.
- R. D. Blum, S. V. Ramírez, K. Sellgren, and K. Olsen. Really Cool Stars and the Star Formation History at the Galactic Center. *ApJ*, 597:323–346, November 2003. doi: 10.1086/378380.
- T. Böker, M. Sarzi, D. E. McLaughlin, R. P. van der Marel, H.-W. Rix, L. C. Ho, and J. C. Shields. A Hubble Space Telescope Census of Nuclear Star Clusters in Late-Type Spiral Galaxies. II. Cluster Sizes and Structural Parameter Correlations. *AJ*, 127:105–118, January 2004. doi: 10.1086/380231.
- P. G. Breen and D. C. Hoggie. Gravothermal oscillations in multicomponent models of star clusters. *MNRAS*, 425:2493–2500, October 2012. doi: 10.1111/j.1365-2966.2012.21688.x.
- S. W. Bruenn, A. Mezzacappa, W. R. Hix, E. J. Lentz, O. E. Bronson Messer, E. J. Lingerfelt, J. M. Blondin, E. Endeve, P. Marronetti, and K. N. Yakunin. Axisymmetric Ab Initio Core-collapse Supernova Simulations of 12–25 M_{Sun} Stars. *ApJ*, 767:L6, April 2013. doi: 10.1088/2041-8205/767/1/L6.
- R. M. Buchholz, R. Schödel, and A. Eckart. Composition of the galactic center star cluster. Population analysis from adaptive optics narrow band spectral energy distributions. *A&A*, 499:483–501, May 2009. doi: 10.1051/0004-6361/200811497.
- A. Burkert, M. Scharfmann, C. Alig, S. Gillessen, R. Genzel, T. K. Fritz, and F. Eisenhauer. Physics of the Galactic Center Cloud G2, on Its Way toward the Supermassive Black Hole. *ApJ*, 750:58, May 2012. doi: 10.1088/0004-637X/750/1/58.
- D. N. Burrows, J. A. Kennea, G. Ghisellini, V. Mangano, B. Zhang, K. L. Page, M. Eracleous, P. Romano, T. Sakamoto, A. D. Falcone, J. P. Osborne, S. Campana, A. P. Beardmore, A. A. Breeveld, M. M. Chester, R. Corbet, S. Covino, J. R. Cummings, P. D’Avanzo, V. D’Elia, P. Esposito, P. A. Evans, D. Fugazza, J. M. Gelbord, K. Hiroi, S. T. Holland, K. Y. Huang, M. Im, G. Israel, Y. Jeon, Y.-B. Jeon, H. D. Jun, N. Kawai, J. H. Kim, H. A. Krimm, F. E. Marshall, P. Mészáros, H. Negoro, N. Omodei, W.-K. Park, J. S. Perkins, M. Sugizaki, H.-I. Sung, G. Tagliaferri, E. Troja, Y. Ueda, Y. Urata, R. Usui, L. A. Antonelli, S. D. Barthelmy, G. Cusumano, P. Giommi, A. Melandri, M. Perri, J. L. Racusin, B. Sbarufatti, M. H. Siegel, and N. Gehrels. Relativistic jet activity from the tidal disruption of a star by a massive black hole. *Nature*, 476:421–424, August 2011. doi: 10.1038/nature10374.
- S. Campana, M. Colpi, S. Mereghetti, L. Stella, and M. Tavani. The neutron stars of Soft X-ray Transients. *A&A Rev.*, 8:279–316, 1998. doi: 10.1007/s001590050012.
- Y. Cao, S. R. Kulkarni, D. A. Howell, A. Gal-Yam, M. M. Kasliwal, S. Valenti, J. Johansson,

- R. Amanullah, A. Goobar, J. Sollerman, F. Taddia, A. Horesh, I. Sagiv, S. B. Cenko, P. E. Nugent, I. Arcavi, J. Surace, P. R. Woźniak, D. I. Moody, U. D. Rebbapragada, B. D. Bue, and N. Gehrels. A strong ultraviolet pulse from a newborn type Ia supernova. *Nature*, 521: 328–331, May 2015. doi: 10.1038/nature14440.
- R. A. Chevalier and P. C. Plait. The nature of S Andromedae (SN 1885A). *ApJ*, 331:L109–L112, August 1988. doi: 10.1086/185246.
- R. A. Chevalier and N. Soker. Asymmetric envelope expansion of supernova 1987A. *ApJ*, 341: 867–882, June 1989. doi: 10.1086/167545.
- M. H. Christopher, N. Z. Scoville, S. R. Stolovy, and M. S. Yun. HCN and HCO⁺ Observations of the Galactic Circumnuclear Disk. *ApJ*, 622:346–365, March 2005. doi: 10.1086/427911.
- R. P. Church, J. Dischler, M. B. Davies, C. A. Tout, T. Adams, and M. E. Beer. Mass transfer in eccentric binaries: the new oil-on-water smoothed particle hydrodynamics technique. *MNRAS*, 395:1127–1134, May 2009. doi: 10.1111/j.1365-2966.2009.14619.x.
- W. I. Clarkson, K. C. Sahu, J. Anderson, R. M. Rich, T. E. Smith, T. M. Brown, H. E. Bond, M. Livio, D. Minniti, A. Renzini, and M. Zoccali. The First Detection of Blue Straggler Stars in the Milky Way Bulge. *ApJ*, 735:37, July 2011. doi: 10.1088/0004-637X/735/1/37.
- S. A. Colgate. Ejection of Companion Objects by Supernovae. *Nature*, 225:247–248, January 1970. doi: 10.1038/225247a0.
- S. M. Couch and E. P. O’Connor. High-resolution Three-dimensional Simulations of Core-collapse Supernovae in Multiple Progenitors. *ApJ*, 785:123, April 2014. doi: 10.1088/0004-637X/785/2/123.
- S. M. Couch and C. D. Ott. The Role of Turbulence in Neutrino-driven Core-collapse Supernova Explosions. *ApJ*, 799:5, January 2015. doi: 10.1088/0004-637X/799/1/5.
- J. Cuadra, S. Nayakshin, V. Springel, and T. Di Matteo. Galactic Centre stellar winds and Sgr A* accretion. *MNRAS*, 366:358–372, February 2006. doi: 10.1111/j.1365-2966.2005.09837.x.
- M. B. Davies. *Formation Channels for Blue Straggler Stars*, page 203. 2015. doi: 10.1007/978-3-662-44434-4_9.
- M. B. Davies, G. Piotto, and F. de Angeli. Blue straggler production in globular clusters. *MNRAS*, 349:129–134, March 2004. doi: 10.1111/j.1365-2966.2004.07474.x.
- R. I. Davies, F. Müller Sánchez, R. Genzel, L. J. Tacconi, E. K. S. Hicks, S. Friedrich, and A. Sternberg. A Close Look at Star Formation around Active Galactic Nuclei. *ApJ*, 671: 1388–1412, December 2007. doi: 10.1086/523032.
- N. de Vries, S. Portegies Zwart, and J. Figueira. The evolution of triples with a Roche lobe filling outer star. *MNRAS*, 438:1909–1921, March 2014. doi: 10.1093/mnras/stt1688.
- N. Degenaar, J. M. Miller, J. Kennea, N. Gehrels, M. T. Reynolds, and R. Wijnands. The X-Ray Flaring Properties of Sgr A* during Six Years of Monitoring with Swift. *ApJ*, 769: 155, June 2013. doi: 10.1088/0004-637X/769/2/155.
- W. Dehnen and H. Aly. Improving convergence in smoothed particle hydrodynamics simulations without pairing instability. *MNRAS*, 425:1068–1082, 2012.
- L. Dessart, S. Blondin, D. J. Hillier, and A. Khokhlov. Constraints on the explosion mechanism and progenitors of Type Ia supernovae. *MNRAS*, 441:532–550, June 2014. doi: 10.1093/mnras/stu598.
- T. Do, A. M. Ghez, M. R. Morris, J. R. Lu, K. Matthews, S. Yelda, and J. Larkin. High

- Angular Resolution Integral-Field Spectroscopy of the Galaxy's Nuclear Cluster: A Missing Stellar Cusp? *ApJ*, 703:1323–1337, October 2009. doi: 10.1088/0004-637X/703/2/1323.
- T. Do, J. R. Lu, A. M. Ghez, M. R. Morris, S. Yelda, G. D. Martinez, S. A. Wright, and K. Matthews. Stellar Populations in the Central 0.5 pc of the Galaxy. I. A New Method for Constructing Luminosity Functions and Surface-density Profiles. *ApJ*, 764:154, February 2013a. doi: 10.1088/0004-637X/764/2/154.
- T. Do, G. D. Martinez, S. Yelda, A. Ghez, J. Bullock, M. Kaplinghat, J. R. Lu, A. H. G. Peter, and K. Phifer. Three-dimensional Stellar Kinematics at the Galactic Center: Measuring the Nuclear Star Cluster Spatial Density Profile, Black Hole Mass, and Distance. *ApJ*, 779:L6, December 2013b. doi: 10.1088/2041-8205/779/1/L6.
- N. Drost, J. Maassen, M. A. J. van Meersbergen, H. E. Bal, F. Inti Pelupessy, S. Portegies Zwart, M. Kliphuis, H. A. Dijkstra, and F. J. Seinstra. High-Performance Distributed Multi-Model / Multi-Kernel Simulations: A Case-Study in Jungle Computing. *ArXiv e-prints*, March 2012.
- A. Duquennoy and M. Mayor. Multiplicity among solar-type stars in the solar neighbourhood. II - Distribution of the orbital elements in an unbiased sample. *A&A*, 248:485–524, August 1991.
- V. V. Dwarkadas and J. Gruszko. What are published X-ray light curves telling us about young supernova expansion? *MNRAS*, 419:1515–1524, January 2012. doi: 10.1111/j.1365-2966.2011.19808.x.
- P. Eggleton. *Evolutionary Processes in Binary and Multiple Stars*. July 2006.
- P. P. Eggleton. The evolution of low mass stars. *MNRAS*, 151:351, 1971.
- P. P. Eggleton. Approximations to the radii of Roche lobes. *ApJ*, 268:368, May 1983. doi: 10.1086/160960.
- F. Eisenhauer, R. Genzel, T. Alexander, R. Abuter, T. Paumard, T. Ott, A. Gilbert, S. Gillessen, M. Horrobin, S. Trippe, H. Bonnet, C. Dumas, N. Hubin, A. Kaufer, M. Kissler-Patig, G. Monnet, S. Ströbele, T. Szeifert, A. Eckart, R. Schödel, and S. Zucker. SINFONI in the Galactic Center: Young Stars and Infrared Flares in the Central Light-Month. *ApJ*, 628: 246–259, July 2005. doi: 10.1086/430667.
- J. J. Eldridge, M. Fraser, J. R. Maund, and S. J. Smartt. Possible binary progenitors for the Type Ib supernova iPTF13bvn. *MNRAS*, 446:2689–2695, January 2015. doi: 10.1093/mnras/stu2197.
- L. Ferrarese and H. Ford. Supermassive Black Holes in Galactic Nuclei: Past, Present and Future Research. *Space Sci. Rev.*, 116:523–624, February 2005. doi: 10.1007/s11214-005-3947-6.
- L. Ferrarese and D. Merritt. A Fundamental Relation between Supermassive Black Holes and Their Host Galaxies. *ApJ*, 539:L9–L12, August 2000. doi: 10.1086/312838.
- L. Ferrarese, P. Côté, J.-C. Cuillandre, S. D. J. Gwyn, E. W. Peng, L. A. MacArthur, P.-A. Duc, A. Boselli, S. Mei, T. Erben, A. W. McConnachie, P. R. Durrell, J. C. Mihos, A. Jordán, A. Lançon, T. H. Puzia, E. Emsellem, M. L. Balogh, J. P. Blakeslee, L. van Waerbeke, R. Gavazzi, B. Vollmer, J. J. Kavelaars, D. Woods, N. M. Ball, S. Boissier, S. Courteau, E. Ferriere, G. Gavazzi, H. Hildebrandt, P. Hudelot, M. Huertas-Company, C. Liu, D. McLaughlin, Y. Mellier, M. Milkeraitis, D. Schade, C. Balkowski, F. Bournaud, R. G. Carlberg, S. C. Chapman, H. Hoekstra, C. Peng, M. Sawicki, L. Simard, J. E. Taylor, R. B. Tully, W. van Driel, C. D. Wilson, T. Burdullis, B. Mahoney, and N. Manset. The

- Next Generation Virgo Cluster Survey (NGVS). I. Introduction to the Survey. *ApJS*, 200:4, May 2012. doi: 10.1088/0067-0049/200/1/4.
- F. R. Ferraro. Exotic populations in Globular Clusters: Blue Stragglers as tracers of the internal dynamical evolution of stellar systems. *ArXiv e-prints*, February 2015.
- F. R. Ferraro, B. Lanzoni, E. Dalessandro, G. Beccari, M. Pasquato, P. Miocchi, R. T. Rood, S. Sigurdsson, A. Sills, E. Vesperini, M. Mapelli, R. Contreras, N. Sanna, and A. Mucciarelli. Dynamical age differences among coeval star clusters as revealed by blue stragglers. *Nature*, 492:393–395, December 2012. doi: 10.1038/nature11686.
- F. R. Ferraro, B. Lanzoni, E. Dalessandro, A. Mucciarelli, and L. Lovisi. *Blue Straggler Stars in Globular Clusters: A Powerful Tool to Probe the Internal Dynamical Evolution of Stellar Systems*, page 99. 2015. doi: 10.1007/978-3-662-44434-4_5.
- R. A. Fesen, C. L. Gerardy, K. M. McLin, and A. J. S. Hamilton. Hubble Space Telescope Images and Spectra of the Remnant of SN 1885 in M31. *ApJ*, 514:195–201, March 1999. doi: 10.1086/306938.
- R. A. Fesen, P. A. Höflich, A. J. S. Hamilton, M. C. Hammell, C. L. Gerardy, A. M. Khokhlov, and J. C. Wheeler. The Chemical Distribution in a Subluminous Type Ia Supernova: Hubble Space Telescope Images of the SN 1885 Remnant. *ApJ*, 658:396–409, March 2007. doi: 10.1086/510998.
- D. F. Figer. *Massive-star formation in the Galactic center.*, pages 40–59. 2009. doi: 10.1017/CBO9780511770593.004.
- Donald F. Figer, R. Michael Rich, Sungsoo S. Kim, Mark Morris, and Eugene Serabyn. An Extended Star Formation History for the Galactic Center from Hubble Space Telescope NICMOS Observations. *The Astrophysical Journal*, 601(1):319, 2004.
- D. Foreman-Mackey, D. W. Hogg, D. Lang, and J. Goodman. emcee: The MCMC Hammer. *PASP*, 125:306–312, March 2013. doi: 10.1086/670067.
- K. C. Freeman and S. C. B. Gascoigne. The LMC Cluster Hodge 11. *Proceedings of the Astronomical Society of Australia*, 3:136, September 1977.
- C. Fremling, J. Sollerman, F. Taddia, M. Ergon, S. Valenti, I. Arcavi, S. Ben-Ami, Y. Cao, S. B. Cenko, A. V. Filippenko, A. Gal-Yam, and D. A. Howell. The rise and fall of the Type Ib supernova iPTF13bvn. Not a massive Wolf-Rayet star. *A&A*, 565:A114, May 2014. doi: 10.1051/0004-6361/201423884.
- C. L. Fryer. Mass Limits For Black Hole Formation. *ApJ*, 522:413–418, September 1999. doi: 10.1086/307647.
- B. A. Fryxell and W. D. Arnett. Hydrodynamic effects of a stellar explosion on a binary companion star. *ApJ*, 243:994–1002, February 1981. doi: 10.1086/158664.
- R. F. Gabbasov, J. Klapp-Escribano, J. Suárez-Cansino, and L. Di Sigalotti. Numerical simulations of the kelvin-helmholtz instability with the gadget-2 sph code. In Jaime Klapp and Abraham Medina, editors, *Experimental and Computational Fluid Mechanics*, Environmental Science and Engineering, pages 291–298. Springer International Publishing, 2014. ISBN 978-3-319-00115-9. doi: 10.1007/978-3-319-00116-6_24.
- E. Gaburov, J. C. Lombardi, and S. Portegies Zwart. Mixing in massive stellar mergers. *MNRAS*, 383:L5–L9, January 2008. doi: 10.1111/j.1745-3933.2007.00399.x.
- D. Gaggero, M. Taoso, A. Urbano, M. Valli, and P. Ullio. Towards a realistic astrophysical interpretation of the gamma-ray Galactic center excess. *J. Cosmology Astropart. Phys.*, 12:056, December 2015. doi: 10.1088/1475-7516/2015/12/056.

- D. García-Senz, C. Badenes, and N. Serichol. Is There a Hidden Hole in Type Ia Supernova Remnants? *ApJ*, 745:75, January 2012. doi: 10.1088/0004-637X/745/1/75.
- C. Ge, Z. Li, X. Xu, Q. Gu, Q. D. Wang, S. Roberts, R. P. Kraft, C. Jones, and W. R. Forman. X-Ray Emissivity of Old Stellar Populations: A Local Group Census. *ApJ*, 812:130, October 2015. doi: 10.1088/0004-637X/812/2/130.
- K. Gebhardt, R. Bender, G. Bower, A. Dressler, S. M. Faber, A. V. Filippenko, R. Green, C. Grillmair, L. C. Ho, J. Kormendy, T. R. Lauer, J. Magorrian, J. Pinkney, D. Richstone, and S. Tremaine. A Relationship between Nuclear Black Hole Mass and Galaxy Velocity Dispersion. *ApJ*, 539:L13–L16, August 2000. doi: 10.1086/312840.
- A. Generozov, N. C. Stone, and B. D. Metzger. Circumnuclear media of quiescent supermassive black holes. *MNRAS*, 453:775–796, October 2015. doi: 10.1093/mnras/stv1607.
- R. Genzel, F. Eisenhauer, and S. Gillessen. The Galactic Center massive black hole and nuclear star cluster. *Reviews of Modern Physics*, 82:3121–3195, October 2010. doi: 10.1103/RevModPhys.82.3121.
- A. M. Ghez, G. Duchêne, K. Matthews, S. D. Hornstein, A. Tanner, J. Larkin, M. Morris, E. E. Becklin, S. Salim, T. Kremenek, D. Thompson, B. T. Soifer, G. Neugebauer, and I. McLean. The First Measurement of Spectral Lines in a Short-Period Star Bound to the Galaxy’s Central Black Hole: A Paradox of Youth. *ApJ*, 586:L127–L131, April 2003. doi: 10.1086/374804.
- A. M. Ghez, S. Salim, N. N. Weinberg, J. R. Lu, T. Do, J. K. Dunn, K. Matthews, M. R. Morris, S. Yelda, E. E. Becklin, T. Kremenek, M. Milosavljevic, and J. Naiman. Measuring distance and properties of the milky way’s central supermassive black hole with stellar orbits. *The Astrophysical Journal*, 689(2):1044, 2008.
- S. Gillessen, F. Eisenhauer, S. Trippe, T. Alexander, R. Genzel, F. Martins, and T. Ott. Monitoring Stellar Orbits Around the Massive Black Hole in the Galactic Center. *The Astrophysical Journal*, 692(2):1075, 2009.
- J. I. González Hernández, P. Ruiz-Lapuente, H. M. Taberner, D. Montes, R. Canal, J. Méndez, and L. R. Bedin. No surviving evolved companions of the progenitor of SN 1006. *Nature*, 489:533–536, September 2012. doi: 10.1038/nature11447.
- J. Goodman and J. Weare. Ensemble samplers with affine invariance. *Communications in Applied Mathematics and Computational Science*, 5(1):65–80, 2010.
- F. Hanke, B. Müller, A. Wongwathanarat, A. Marek, and H.-T. Janka. SASI Activity in Three-dimensional Neutrino-hydrodynamics Simulations of Supernova Cores. *ApJ*, 770:66, June 2013. doi: 10.1088/0004-637X/770/1/66.
- W. K. Hastings. Monte carlo sampling methods using markov chains and their applications. *Biometrika*, 57(1):97–109, 1970. doi: 10.1093/biomet/57.1.97.
- V. Heard and R. S. Warwick. XMM-Newton observations of the Galactic Centre Region - I. The distribution of low-luminosity X-ray sources. *MNRAS*, 428:3462–3477, February 2013a. doi: 10.1093/mnras/sts284.
- V. Heard and R. S. Warwick. XMM-Newton observations of the Galactic Centre Region - II. The soft-thermal emission. *MNRAS*, 434:1339–1354, September 2013b. doi: 10.1093/mnras/stt1102.
- L. G. Henyey, J. E. Forbes, and N. L. Gould. A New Method of Automatic Computation of Stellar Evolution. *ApJ*, 139:306, 1964.
- R. M. Herrnstein and P. T. P. Ho. The Nature of the Molecular Environment within 5 Parsecs

- of the Galactic Center. *ApJ*, 620:287–307, February 2005. doi: 10.1086/426047.
- J. G. Hills. The effects of sudden mass loss and a random kick velocity produced in a supernova explosion on the dynamics of a binary star of arbitrary orbital eccentricity - Applications to X-ray binaries and to the binary pulsars. *ApJ*, 267:322–333, April 1983. doi: 10.1086/160871.
- J. G. Hills. Hyper-velocity and tidal stars from binaries disrupted by a massive Galactic black hole. *Nature*, 331:687–689, February 1988. doi: 10.1038/331687a0.
- J. G. Hills and C. A. Day. Stellar Collisions in Globular Clusters. *Astrophys. Lett.*, 17:87, February 1976.
- R. Hirai, H. Sawai, and S. Yamada. The Outcome of Supernovae in Massive Binaries; Removed Mass, and its Separation Dependence. *ApJ*, 792:66, September 2014. doi: 10.1088/0004-637X/792/1/66.
- L. C. Ho. Radiatively Inefficient Accretion in Nearby Galaxies. *ApJ*, 699:626–637, July 2009. doi: 10.1088/0004-637X/699/1/626.
- J. R. Hurley, O. R. Pols, and C. A. Tout. Comprehensive analytic formulae for stellar evolution as a function of mass and metallicity. *MNRAS*, 315:543–569, July 2000. doi: 10.1046/j.1365-8711.2000.03426.x.
- S. Ichimaru. Bimodal behavior of accretion disks - Theory and application to Cygnus X-1 transitions. *ApJ*, 214:840–855, June 1977. doi: 10.1086/155314.
- J. M. Jackson, N. Geis, R. Genzel, A. I. Harris, S. Madden, A. Poglitsch, G. J. Stacey, and C. H. Townes. Neutral gas in the central 2 parsecs of the Galaxy. *ApJ*, 402:173–184, January 1993. doi: 10.1086/172120.
- H.-T. Janka. Explosion Mechanisms of Core-Collapse Supernovae. *Annual Review of Nuclear and Particle Science*, 62:407–451, November 2012. doi: 10.1146/annurev-nucl-102711-094901.
- A. Jordán, J. P. Blakeslee, P. Côté, L. Ferrarese, L. Infante, S. Mei, D. Merritt, E. W. Peng, J. L. Tonry, and M. J. West. The ACS Fornax Cluster Survey. I. Introduction to the Survey and Data Reduction Procedures. *ApJS*, 169:213–224, April 2007. doi: 10.1086/512778.
- J. Kane, R. P. Drake, and B. A. Remington. An Evaluation of the Richtmyer-Meshkov Instability in Supernova Remnant Formation. *ApJ*, 511:335–340, January 1999. doi: 10.1086/306685.
- D. Kasen. Seeing the Collision of a Supernova with Its Companion Star. *ApJ*, 708:1025–1031, January 2010. doi: 10.1088/0004-637X/708/2/1025.
- K. S. Kawabata, K. Maeda, K. Nomoto, S. Taubenberger, M. Tanaka, J. Deng, E. Pian, T. Hattori, and K. Itagaki. A massive star origin for an unusual helium-rich supernova in an elliptical galaxy. *Nature*, 465:326–328, May 2010. doi: 10.1038/nature09055.
- J. A. Kennea, D. N. Burrows, C. Kouveliotou, D. M. Palmer, E. Göğüş, Y. Kaneko, P. A. Evans, N. Degenaar, M. T. Reynolds, J. M. Miller, R. Wijnands, K. Mori, and N. Gehrels. Swift Discovery of a New Soft Gamma Repeater, SGR J1745-29, near Sagittarius A*. *ApJ*, 770:L24, June 2013. doi: 10.1088/2041-8205/770/2/L24.
- R. C. Kennicutt and N. J. Evans. Star Formation in the Milky Way and Nearby Galaxies. *ARA&A*, 50:531–608, September 2012. doi: 10.1146/annurev-astro-081811-125610.
- W. F. Kern and J. R. Bland. *Solid Mensuration with Proofs*. 1948.
- W. E. Kerzendorf, D. Yong, B. P. Schmidt, J. D. Simon, C. S. Jeffery, J. Anderson, P. Podsiadlowski, A. Gal-Yam, J. M. Silverman, A. V. Filippenko, K. Nomoto, S. J. Murphy, M. S. Bessell, K. A. Venn, and R. J. Foley. A High-resolution Spectroscopic Search

- for the Remaining Donor for Tycho's Supernova. *ApJ*, 774:99, September 2013. doi: 10.1088/0004-637X/774/2/99.
- H.-J. Kim, S.-C. Yoon, and B.-C. Koo. Observational Properties of Type Ib/c Supernova Progenitors in Binary Systems. *ApJ*, 809:131, August 2015. doi: 10.1088/0004-637X/809/2/131.
- S. Komossa. Ludwig Biermann Award Lecture: X-ray Evidence for Supermassive Black Holes at the Centers of Nearby, Non-Active Galaxies. In R. E. Schielicke, editor, *Reviews in Modern Astronomy*, volume 15 of *Reviews in Modern Astronomy*, page 27, 2002.
- A. S. Kompaneets. A Point Explosion in an Inhomogeneous Atmosphere. *Soviet Physics Doklady*, 5:46, July 1960.
- B.-C. Koo and C. F. McKee. Dynamics of adiabatic blast waves in media of finite mass. *ApJ*, 354:513–528, May 1990. doi: 10.1086/168712.
- J. Kormendy and L. C. Ho. Coevolution (Or Not) of Supermassive Black Holes and Host Galaxies. *ARA&A*, 51:511–653, August 2013. doi: 10.1146/annurev-astro-082708-101811.
- D. G. Korycansky. An off-center point explosion in a radially stratified medium - Kompaneets approximation. *ApJ*, 398:184–189, October 1992. doi: 10.1086/171847.
- H. Kuncarayakti, K. Maeda, M. C. Bersten, G. Folatelli, N. Morrell, E. Y. Hsiao, S. González-Gaitán, J. P. Anderson, M. Hamuy, T. de Jaeger, C. P. Gutiérrez, and K. S. Kawabata. Nebular phase observations of the Type-Ib supernova iPTF13bvn favour a binary progenitor. *A&A*, 579:A95, July 2015. doi: 10.1051/0004-6361/201425604.
- A. Kusenko and G. Segrè. Pulsar Velocities and Neutrino Oscillations. *Physical Review Letters*, 77:4872–4875, December 1996. doi: 10.1103/PhysRevLett.77.4872.
- D. Lai, F. A. Rasio, and S. L. Shapiro. Collisions and close encounters between massive main-sequence stars. *ApJ*, 412:593–611, August 1993. doi: 10.1086/172946.
- S. Lee, S. Pak, T. R. Geballe, S.-G. Lee, C. J. Davis, M. Choi, Y. C. Minh, R. M. Herrnstein, and P. T. P. Ho. Shock interactions between Sgr A East and its environments. *Journal of Physics Conference Series*, 54:22–28, December 2006. doi: 10.1088/1742-6596/54/1/004.
- D. C. Leonard. Constraining the Type Ia Supernova Progenitor: The Search for Hydrogen in Nebular Spectra. *ApJ*, 670:1275–1282, December 2007. doi: 10.1086/522367.
- Y. Levin and A. M. Beloborodov. Stellar Disk in the Galactic Center: A Remnant of a Dense Accretion Disk? *ApJ*, 590:L33–L36, June 2003. doi: 10.1086/376675.
- C. Li, R. de Grijs, L. Deng, and X. Liu. Blue Straggler Evolution Caught in the Act in the Large Magellanic Cloud Globular Cluster Hodge 11. *ApJ*, 770:L7, June 2013. doi: 10.1088/2041-8205/770/1/L7.
- W. Li, J. S. Bloom, P. Podsiadlowski, A. A. Miller, S. B. Cenko, S. W. Jha, M. Sullivan, D. A. Howell, P. E. Nugent, N. R. Butler, E. O. Ofek, M. M. Kasliwal, J. W. Richards, A. Stockton, H.-Y. Shih, L. Bildsten, M. M. Shara, J. Bibby, A. V. Filippenko, M. Ganeshalingam, J. M. Silverman, S. R. Kulkarni, N. M. Law, D. Poznanski, R. M. Quimby, C. McCully, B. Patel, K. Maguire, and K. J. Shen. Exclusion of a luminous red giant as a companion star to the progenitor of supernova SN 2011fe. *Nature*, 480:348–350, December 2011. doi: 10.1038/nature10646.
- H. B. Liu, P. T. P. Ho, M. C. H. Wright, Y.-N. Su, P.-Y. Hsieh, A.-L. Sun, S. S. Kim, and Y. C. Minh. Interstellar Medium Processing in the Inner 20 pc in Galactic Center. *ApJ*, 770:44, June 2013. doi: 10.1088/0004-637X/770/1/44.
- Z. W. Liu, R. Pakmor, F. K. Röpkke, P. Edelmann, B. Wang, M. Kromer, W. Hillebrandt, and

- Z. W. Han. Three-dimensional simulations of the interaction between Type Ia supernova ejecta and their main sequence companions. *A&A*, 548:A2, December 2012. doi: 10.1051/0004-6361/201219357.
- Z.-W. Liu, T. M. Tauris, F. K. Röpkke, T. J. Moriya, M. Kruckow, R. J. Stancliffe, and R. G. Izzard. The interaction of core-collapse supernova ejecta with a companion star. *A&A*, 584:A11, December 2015. doi: 10.1051/0004-6361/201526757.
- J. C. Lombardi, A. P. Thrall, J. S. Deneva, S. W. Fleming, and P. E. Grabowski. Modelling collision products of triple-star mergers. *MNRAS*, 345:762–780, November 2003. doi: 10.1046/j.1365-8711.2003.06999.x.
- J. C. Lombardi, Jr., F. A. Rasio, and S. L. Shapiro. Collisions of Main-Sequence Stars and the Formation of Blue Stragglers in Globular Clusters. *ApJ*, 468:797, September 1996. doi: 10.1086/177736.
- J. C. Lombardi, Jr., J. S. Warren, F. A. Rasio, A. Sills, and A. R. Warren. Stellar Collisions and the Interior Structure of Blue Stragglers. *ApJ*, 568:939–953, April 2002. doi: 10.1086/339060.
- K. S. Long, W. P. Blair, P. F. Winkler, R. H. Becker, T. J. Gaetz, P. Ghavamian, D. J. Helfand, J. P. Hughes, R. P. Kirshner, K. D. Kuntz, E. K. McNeil, T. G. Pannuti, P. P. Plucinsky, D. Saul, R. Tüllmann, and B. Williams. The Chandra ACIS Survey of M33: X-ray, Optical, and Radio Properties of the Supernova Remnants. *ApJS*, 187:495–559, April 2010. doi: 10.1088/0067-0049/187/2/495.
- L. A. Lopez, E. Ramirez-Ruiz, D. Castro, and S. Pearson. The Galactic Supernova Remnant W49B Likely Originates from a Jet-driven, Core-collapse Explosion. *ApJ*, 764:50, February 2013. doi: 10.1088/0004-637X/764/1/50.
- J. R. Lu, T. Do, A. M. Ghez, M. R. Morris, S. Yelda, and K. Matthews. Stellar Populations in the Central 0.5 pc of the Galaxy. II. The Initial Mass Function. *ApJ*, 764:155, February 2013. doi: 10.1088/0004-637X/764/2/155.
- P. Lundqvist, A. Nyholm, F. Taddia, J. Sollerman, J. Johansson, C. Kozma, N. Lundqvist, C. Fransson, P. M. Garnavich, M. Kromer, B. J. Shappee, and A. Goobar. No trace of a single-degenerate companion in late spectra of supernovae 2011fe and 2014J. *A&A*, 577:A39, May 2015. doi: 10.1051/0004-6361/201525719.
- N. Lützgendorf, E. v. d. Helm, F. I. Pelupessy, and S. Portegies Zwart. Stellar winds near massive black holes - the case of the S-stars. *MNRAS*, 456:3645–3654, March 2016. doi: 10.1093/mnras/stv2918.
- Y. Maeda, F. K. Baganoff, E. D. Feigelson, M. Morris, M. W. Bautz, W. N. Brandt, D. N. Burrows, J. P. Doty, G. P. Garmire, S. H. Pravdo, G. R. Ricker, and L. K. Townsley. A Chandra Study of Sagittarius A East: A Supernova Remnant Regulating the Activity of Our Galactic Center? *ApJ*, 570:671–687, May 2002. doi: 10.1086/339773.
- D. Maoz, F. Mannucci, and G. Nelemans. Observational Clues to the Progenitors of Type Ia Supernovae. *ARA&A*, 52:107–170, August 2014. doi: 10.1146/annurev-astro-082812-141031.
- E. Marietta, A. Burrows, and B. Fryxell. Type IA Supernova Explosions in Binary Systems: The Impact on the Secondary Star and Its Consequences. *ApJS*, 128:615–650, June 2000. doi: 10.1086/313392.
- S. Markoff. Revelations in our own backyard: Chandra’s unique Galactic Center discoveries. *Proceedings of the National Academy of Science*, 107:7196–7201, April 2010. doi: 10.1073/pnas.

- 0914070107.
- F. R. Marleau, D. Clancy, and M. Bianconi. The ubiquity of supermassive black holes in the Hubble sequence. *MNRAS*, September 2013. doi: 10.1093/mnras/stt1503.
- D. P. Marrone, J. M. Moran, J.-H. Zhao, and R. Rao. An Unambiguous Detection of Faraday Rotation in Sagittarius A*. *ApJ*, 654:L57–L60, January 2007. doi: 10.1086/510850.
- C. A. Martínez-Barbosa, A. G. A. Brown, T. Boekholt, S. Portegies Zwart, E. Antiche, and T. Antoja. The evolution of the Sun’s birth cluster and the search for the solar siblings with Gaia. *MNRAS*, 457:1062–1075, March 2016. doi: 10.1093/mnras/stw006.
- T. Maruyama, T. Kajino, N. Yasutake, M.-K. Cheoun, and C.-Y. Ryu. Asymmetric neutrino emission from magnetized proto-neutron star matter including hyperons in relativistic mean field theory. *Phys. Rev. D*, 83(8):081303, April 2011. doi: 10.1103/PhysRevD.83.081303.
- S. Mattila, P. Lundqvist, J. Sollerman, C. Kozma, E. Baron, C. Fransson, B. Leibundgut, and K. Nomoto. Early and late time VLT spectroscopy of SN 2001el - progenitor constraints for a type Ia supernova. *A&A*, 443:649–662, November 2005. doi: 10.1051/0004-6361:20052731.
- C. D. Matzner and C. F. McKee. The Expulsion of Stellar Envelopes in Core-Collapse Supernovae. *ApJ*, 510:379–403, January 1999. doi: 10.1086/306571.
- N. J. McConnell, C.-P. Ma, K. Gebhardt, S. A. Wright, J. D. Murphy, T. R. Lauer, J. R. Graham, and D. O. Richstone. Two ten-billion-solar-mass black holes at the centres of giant elliptical galaxies. *Nature*, 480:215–218, December 2011. doi: 10.1038/nature10636.
- W. H. McCrea. Extended main-sequence of some stellar clusters. *MNRAS*, 128:147, 1964.
- C. F. McKee and J. K. Truelove. Explosions in the interstellar medium. *Phys. Rep.*, 256:157–172, May 1995. doi: 10.1016/0370-1573(94)00106-D.
- J. C. McKinney, A. Tchekhovskoy, and R. D. Blandford. General relativistic magnetohydrodynamic simulations of magnetically choked accretion flows around black holes. *MNRAS*, 423:3083–3117, July 2012. doi: 10.1111/j.1365-2966.2012.21074.x.
- F. Melia and H. Falcke. The Supermassive Black Hole at the Galactic Center. *ARA&A*, 39:309–352, 2001. doi: 10.1146/annurev.astro.39.1.309.
- X. Meng, X. Chen, and Z. Han. The Impact of Type Ia Supernova Explosions on the Companions in a Binary System. *PASJ*, 59:835–840, August 2007. doi: 10.1093/pasj/59.4.835.
- N. Metropolis. The beginning of the monte carlo method. *Los Alamos Science*, pages 125–130, 1987.
- Nicholas Metropolis, Arianna W. Rosenbluth, Marshall N. Rosenbluth, Augusta H. Teller, and Edward Teller. Equation of state calculations by fast computing machines. *The Journal of Chemical Physics*, 21(6):1087–1092, 1953. doi: 10.1063/1.1699114.
- D. Milisavljevic, A. M. Soderberg, R. Margutti, M. R. Drout, G. Howie Marion, N. E. Sanders, E. Y. Hsiao, R. Lunnan, R. Chornock, R. A. Fesen, J. T. Parrent, E. M. Levesque, and E. Berger. SN 2012au: A Golden Link between Superluminous Supernovae and Their Lower-luminosity Counterparts. *ApJ*, 770:L38, June 2013. doi: 10.1088/2041-8205/770/2/L38.
- B. P. Miller, E. Gallo, J. E. Greene, B. C. Kelly, T. Treu, J.-H. Woo, and V. Baldassare. X-Ray Constraints on the Local Supermassive Black Hole Occupation Fraction. *ApJ*, 799:98, January 2015. doi: 10.1088/0004-637X/799/1/98.
- M. Molaro, R. Khatri, and R. A. Sunyaev. A thin diffuse component of the Galactic ridge X-ray emission and heating of the interstellar medium contributed by the radiation of Galactic

- X-ray binaries. *A&A*, 564:A107, April 2014. doi: 10.1051/0004-6361/201323332.
- L. K. Morabito and X. Dai. A Bayesian Monte Carlo Analysis of the M - σ Relation. *ApJ*, 757:172, October 2012. doi: 10.1088/0004-637X/757/2/172.
- M. Morris, F. Baganoff, M. Munro, C. Howard, Y. Maeda, E. Feigelson, M. Bautz, N. Brandt, G. Chartas, G. Garmire, and L. Townsley. Deep X-Ray Imaging of the Central 20 Parsecs of the Galaxy with Chandra. *Astronomische Nachrichten Supplement*, 324:167–172, September 2003. doi: 10.1002/asna.200385110.
- M. Morris, C. Howard, M. Munro, F. K. Baganoff, S. Park, E. Feigelson, G. Garmire, and N. Brandt. The Hot Interstellar Medium of the Galactic Center: Observations with Chandra. In S. Pfalzner, C. Kramer, C. Staubmeier, and A. Heithausen, editors, *The Dense Interstellar Medium in Galaxies*, page 281, 2004.
- M. P. Munro, F. K. Baganoff, M. W. Bautz, E. D. Feigelson, G. P. Garmire, M. R. Morris, S. Park, G. R. Ricker, and L. K. Townsley. Diffuse X-Ray Emission in a Deep Chandra Image of the Galactic Center. *ApJ*, 613:326–342, September 2004. doi: 10.1086/422865.
- M. P. Munro, E. Pfahl, F. K. Baganoff, W. N. Brandt, A. Ghez, J. Lu, and M. R. Morris. An Overabundance of Transient X-Ray Binaries within 1 Parsec of the Galactic Center. *ApJ*, 622:L113–L116, April 2005. doi: 10.1086/429721.
- R. Narayan and I. Yi. Advection-dominated accretion: A self-similar solution. *ApJ*, 428:L13–L16, June 1994. doi: 10.1086/187381.
- R. Narayan and I. Yi. Advection-dominated Accretion: Underfed Black Holes and Neutron Stars. *ApJ*, 452:710, October 1995. doi: 10.1086/176343.
- R. Narayan, I. Yi, and R. Mahadevan. Explaining the spectrum of Sagittarius A* with a model of an accreting black hole. *Nature*, 374:623–625, April 1995. doi: 10.1038/374623a0.
- N. Neumayer and C. J. Walcher. Are Nuclear Star Clusters the Precursors of Massive Black Holes? *Advances in Astronomy*, 2012:709038, 2012. doi: 10.1155/2012/709038.
- M. Nynka, C. J. Hailey, K. Mori, F. K. Baganoff, F. E. Bauer, S. E. Boggs, W. W. Craig, F. E. Christensen, E. V. Gotthelf, F. A. Harrison, J. Hong, K. M. Perez, D. Stern, S. Zhang, and W. W. Zhang. High-energy X-Rays from J174545.5-285829, the Cannonball: A Candidate Pulsar Wind Nebula Associated with Sgr A East. *ApJ*, 778:L31, December 2013. doi: 10.1088/2041-8205/778/2/L31.
- R. P. Olling, R. Mushotzky, E. J. Shaya, A. Rest, P. M. Garnavich, B. E. Tucker, D. Kasen, S. Margheim, and A. V. Filippenko. No signature of ejecta interaction with a stellar companion in three type Ia supernovae. *Nature*, 521:332–335, May 2015. doi: 10.1038/nature14455.
- T. Padmanabhan. *Theoretical Astrophysics, Volume 2: Stars and Stellar Systems*. 2001.
- R. Pakmor, F. K. Röpkke, A. Weiss, and W. Hillebrandt. The impact of type Ia supernovae on main sequence binary companions. *A&A*, 489:943–951, October 2008. doi: 10.1051/0004-6361:200810456.
- R. Pakmor, P. Edelmann, F. K. Röpkke, and W. Hillebrandt. Stellar GADGET: a smoothed particle hydrodynamics code for stellar astrophysics and its application to Type Ia supernovae from white dwarf mergers. *MNRAS*, 424:2222–2231, August 2012. doi: 10.1111/j.1365-2966.2012.21383.x.
- K.-C. Pan, P. M. Ricker, and R. E. Taam. Impact of Type Ia Supernova Ejecta on Binary Companions in the Single-degenerate Scenario. *ApJ*, 750:151, May 2012. doi: 10.1088/0004-637X/750/2/151.
- S. Park, M. P. Munro, F. K. Baganoff, Y. Maeda, M. Morris, G. Chartas, D. Sanwal, D. N.

- Burrows, and G. P. Garmire. A Candidate Neutron Star Associated with Galactic Center Supernova Remnant Sagittarius A East. *ApJ*, 631:964–975, October 2005. doi: 10.1086/432639.
- T. Paumard, R. Genzel, F. Martins, S. Nayakshin, A. M. Beloborodov, Y. Levin, S. Trippe, F. Eisenhauer, T. Ott, S. Gillessen, R. Abuter, J. Cuadra, T. Alexander, and A. Sternberg. The Two Young Star Disks in the Central Parsec of the Galaxy: Properties, Dynamics, and Formation. *ApJ*, 643:1011–1035, June 2006. doi: 10.1086/503273.
- B. Paxton, L. Bildsten, A. Dotter, F. Herwig, P. Lesaffre, and F. Timmes. Modules for Experiments in Stellar Astrophysics (MESA). *ApJS*, 192:3, January 2011. doi: 10.1088/0067-0049/192/1/3.
- P. J. E. Peebles. Star Distribution Near a Collapsed Object. *ApJ*, 178:371–376, December 1972. doi: 10.1086/151797.
- F. I. Pelupessy, A. van Elteren, N. de Vries, S. L. W. McMillan, N. Drost, and S. F. Portegies Zwart. The Astrophysical Multipurpose Software Environment. *A&A*, 557:A84, September 2013. doi: 10.1051/0004-6361/201321252.
- O. Petruk. On the Transition of the Adiabatic Supernova Remnant to the Radiative Stage in a Nonuniform Interstellar Medium. *Journal of Physical Studies*, 9:364–373, 2005.
- O. Pfuhl, T. K. Fritz, M. Zilka, H. Maness, F. Eisenhauer, R. Genzel, S. Gillessen, T. Ott, K. Dodds-Eden, and A. Sternberg. The Star Formation History of the Milky Way’s Nuclear Star Cluster. *ApJ*, 741:108, November 2011. doi: 10.1088/0004-637X/741/2/108.
- J. T. Pijloo, S. F. Portegies Zwart, P. E. R. Alexander, M. Gieles, S. S. Larsen, P. J. Groot, and B. Devecchi. The initial conditions of observed star clusters - I. Method description and validation. *MNRAS*, 453:605–637, October 2015. doi: 10.1093/mnras/stv1546.
- P. Podsiadlowski. On the Evolution and Appearance of a Surviving Companion after a Type Ia Supernova Explosion. *ArXiv e-prints*, March 2003.
- G. Ponti, M. R. Morris, R. Terrier, F. Haberl, R. Sturm, M. Clavel, S. Soldi, A. Goldwurm, P. Predehl, K. Nandra, G. Bélanger, R. S. Warwick, and V. Tatischeff. The XMM-Newton view of the central degrees of the Milky Way. *MNRAS*, 453:172–213, October 2015. doi: 10.1093/mnras/stv1331.
- S. Portegies Zwart, S. McMillan, S. Harfst, D. Groen, M. Fujii, B. Ó. Nualláin, E. Glebbeek, D. Heggie, J. Lombardi, P. Hut, V. Angelou, S. Banerjee, H. Belkus, T. Fragos, J. Fregeau, E. Gaburov, R. Izzard, M. Jurić, S. Justham, A. Sottoriva, P. Teuben, J. van Bever, O. Yaron, and M. Zemp. A multiphysics and multiscale software environment for modeling astrophysical systems. *New A*, 14:369–378, May 2009. doi: 10.1016/j.newast.2008.10.006.
- S. Portegies Zwart, S. L. W. McMillan, E. van Elteren, I. Pelupessy, and N. de Vries. Multiphysics simulations using a hierarchical interchangeable software interface. *Computer Physics Communications*, 183:456–468, March 2013a. doi: 10.1016/j.cpc.2012.09.024.
- S. Portegies Zwart, S. L. W. McMillan, E. van Elteren, I. Pelupessy, and N. de Vries. Multiphysics simulations using a hierarchical interchangeable software interface. *Computer Physics Communications*, 183:456–468, March 2013b. doi: 10.1016/j.cpc.2012.09.024.
- S. F. Portegies Zwart and F. Verbunt. Population synthesis of high-mass binaries. *A&A*, 309:179–196, May 1996.
- S. F. Portegies Zwart, P. Hut, S. L. W. McMillan, and F. Verbunt. Star cluster ecology. II. Binary evolution with single-star encounters. *A&A*, 328:143–157, December 1997a.
- S. F. Portegies Zwart, P. Hut, and F. Verbunt. Star cluster ecology. I. A cluster core with

- encounters between single stars. *A&A*, 328:130–142, December 1997b.
- E. Quataert. A Dynamical Model for Hot Gas in the Galactic Center. *ApJ*, 613:322–325, September 2004. doi: 10.1086/422973.
- E. Quataert and A. Gruzinov. Convection-dominated Accretion Flows. *ApJ*, 539:809–814, August 2000. doi: 10.1086/309267.
- P. Ramachandran and G. Varoquaux. Mayavi: 3D Visualization of Scientific Data. *Computing in Science & Engineering*, 13(2):40–51, 2011. ISSN 1521-9615.
- F. A. Rasio and J. C. Lombardi, Jr. Smoothed particle hydrodynamics calculations of stellar interactions. *Journal of Computational and Applied Mathematics*, 109:213–230, September 1999.
- D. A. Rastegaev. Multiplicity and Period Distribution of Population II Field Stars in Solar Vicinity. *AJ*, 140:2013–2024, December 2010. doi: 10.1088/0004-6256/140/6/2013.
- N. Rea, P. Esposito, J. A. Pons, R. Turolla, D. F. Torres, G. L. Israel, A. Possenti, M. Burgay, D. Viganò, A. Papitto, R. Perna, L. Stella, G. Ponti, F. K. Baganoff, D. Haggard, A. Camero-Arranz, S. Zane, A. Minter, S. Mereghetti, A. Tiengo, R. Schödel, M. Feroci, R. Mignani, and D. Götz. A Strongly Magnetized Pulsar within the Grasp of the Milky Way’s Supermassive Black Hole. *ApJ*, 775:L34, October 2013. doi: 10.1088/2041-8205/775/2/L34.
- M. J. Rees, M. C. Begelman, R. D. Blandford, and E. S. Phinney. Ion-supported tori and the origin of radio jets. *Nature*, 295:17–21, January 1982. doi: 10.1038/295017a0.
- M. Revnivtsev, S. Sazonov, M. Gilfanov, E. Churazov, and R. Sunyaev. Origin of the Galactic ridge X-ray emission. *A&A*, 452:169–178, June 2006. doi: 10.1051/0004-6361:20054268.
- M. Revnivtsev, S. Sazonov, E. Churazov, W. Forman, A. Vikhlinin, and R. Sunyaev. Discrete sources as the origin of the Galactic X-ray ridge emission. *Nature*, 458:1142–1144, April 2009. doi: 10.1038/nature07946.
- A. Rimoldi, E. M. Rossi, T. Piran, and S. Portegies Zwart. The fate of supernova remnants near quiescent supermassive black holes. *MNRAS*, 447:3096–3114, March 2015. doi: 10.1093/mnras/stu2630.
- P. Ruiz-Lapuente, F. Comeron, J. Méndez, R. Canal, S. J. Smartt, A. V. Filippenko, R. L. Kurucz, R. Chornock, R. J. Foley, V. Stanishev, and R. Ibata. The binary progenitor of Tycho Brahe’s 1572 supernova. *Nature*, 431:1069–1072, October 2004. doi: 10.1038/nature03006.
- M. Sakano, R. S. Warwick, A. Decourchelle, and P. Predehl. XMM-Newton observations of Sagittarius A East. *MNRAS*, 350:129–139, May 2004. doi: 10.1111/j.1365-2966.2004.07571.x.
- H. Sana, S. E. de Mink, A. de Koter, N. Langer, C. J. Evans, M. Gieles, E. Gosset, R. G. Izzard, J.-B. Le Bouquin, and F. R. N. Schneider. Binary Interaction Dominates the Evolution of Massive Stars. *Science*, 337:444–446, July 2012. doi: 10.1126/science.1223344.
- A. R. Sandage. The color-magnitude diagram for the globular cluster M 3. *AJ*, 58:61–75, 1953.
- M. Sarzi, H.-W. Rix, J. C. Shields, L. C. Ho, A. J. Barth, G. Rudnick, A. V. Filippenko, and W. L. W. Sargent. The Stellar Populations in the Central Parsecs of Galactic Bulges. *ApJ*, 628:169–186, July 2005. doi: 10.1086/428637.
- B. E. Schaefer and A. Pagnotta. An absence of ex-companion stars in the type Ia supernova remnant SNR 0509-67.5. *Nature*, 481:164–166, January 2012. doi: 10.1038/nature10692.
- K. Schawinski, C. M. Urry, S. Virani, P. Coppi, S. P. Bamford, E. Treister, C. J. Lintott, M. Sarzi, W. C. Keel, S. Kaviraj, C. N. Cardamone, K. L. Masters, N. P. Ross, D. An-

- dreescu, P. Murray, R. C. Nichol, M. J. Raddick, A. Slosar, A. S. Szalay, D. Thomas, and J. Vandenberg. Galaxy Zoo: The Fundamentally Different Co-Evolution of Supermassive Black Holes and Their Early- and Late-Type Host Galaxies. *ApJ*, 711:284–302, March 2010. doi: 10.1088/0004-637X/711/1/284.
- L. Scheck, T. Plewa, H.-T. Janka, K. Kifonidis, and E. Müller. Pulsar Recoil by Large-Scale Anisotropies in Supernova Explosions. *Physical Review Letters*, 92(1):011103, January 2004. doi: 10.1103/PhysRevLett.92.011103.
- L. Scheck, K. Kifonidis, H.-T. Janka, and E. Müller. Multidimensional supernova simulations with approximative neutrino transport. I. Neutron star kicks and the anisotropy of neutrino-driven explosions in two spatial dimensions. *A&A*, 457:963–986, October 2006. doi: 10.1051/0004-6361:20064855.
- D. J. Schlegel, D. P. Finkbeiner, and M. Davis. Maps of Dust Infrared Emission for Use in Estimation of Reddening and Cosmic Microwave Background Radiation Foregrounds. *ApJ*, 500:525–553, June 1998. doi: 10.1086/305772.
- R. Schödel, T. Ott, R. Genzel, R. Hofmann, M. Lehnert, A. Eckart, N. Mouawad, T. Alexander, M. J. Reid, R. Lenzen, M. Hartung, F. Lacombe, D. Rouan, E. Gendron, G. Rousset, A.-M. Lagrange, W. Brandner, N. Ageorges, C. Lidman, A. F. M. Moorwood, J. Spyromilio, N. Hubin, and K. M. Menten. A star in a 15.2-year orbit around the supermassive black hole at the centre of the Milky Way. *Nature*, 419:694–696, October 2002. doi: 10.1038/nature01121.
- R. Schödel, T. Ott, R. Genzel, A. Eckart, N. Mouawad, and T. Alexander. Stellar Dynamics in the Central Arcsecond of Our Galaxy. *ApJ*, 596:1015–1034, October 2003. doi: 10.1086/378122.
- A. Schruba, A. K. Leroy, F. Walter, F. Bigiel, E. Brinks, W. J. G. de Blok, G. Dumas, C. Kramer, E. Rosolowsky, K. Sandstrom, K. Schuster, A. Usero, A. Weiss, and H. Wiesemeyer. A Molecular Star Formation Law in the Atomic-gas-dominated Regime in Nearby Galaxies. *AJ*, 142:37, August 2011. doi: 10.1088/0004-6256/142/2/37.
- K. M. Schure, D. Kosenko, J. S. Kaastra, R. Keppens, and J. Vink. A new radiative cooling curve based on an up-to-date plasma emission code. *A&A*, 508:751–757, December 2009. doi: 10.1051/0004-6361/200912495.
- L. I. Sedov. *Similarity and Dimensional Methods in Mechanics*. 1959.
- F. Shankar, D. H. Weinberg, and J. Miralda-Escudé. Self-Consistent Models of the AGN and Black Hole Populations: Duty Cycles, Accretion Rates, and the Mean Radiative Efficiency. *ApJ*, 690:20–41, January 2009. doi: 10.1088/0004-637X/690/1/20.
- P. R. Shapiro. Relativistic blast waves in two dimensions. I - The adiabatic case. *ApJ*, 233: 831–850, November 1979. doi: 10.1086/157446.
- A. Sills, T. Adams, M. B. Davies, and M. R. Bate. High-resolution simulations of stellar collisions between equal-mass main-sequence stars in globular clusters. *MNRAS*, 332:49–54, May 2002. doi: 10.1046/j.1365-8711.2002.05266.x.
- M. Simunovic, T. H. Puzia, and A. Sills. The Blue Straggler Star Population in NGC 1261: Evidence for a Post-core-collapse Bounce State. *ApJ*, 795:L10, November 2014. doi: 10.1088/2041-8205/795/1/L10.
- S. J. Smartt. Progenitors of Core-Collapse Supernovae. *ARA&A*, 47:63–106, September 2009. doi: 10.1146/annurev-astro-082708-101737.
- V. Springel. The cosmological simulation code GADGET-2. *MNRAS*, 364:1105–1134, De-

- cember 2005a. doi: 10.1111/j.1365-2966.2005.09655.x.
- V. Springel. The cosmological simulation code GADGET-2. *MNRAS*, 364:1105–1134, 2005b.
- L. L. Stryker. Blue stragglers. *PASP*, 105:1081–1100, October 1993. doi: 10.1086/133286.
- N. B. Suntzeff, R. A. Schommer, E. W. Olszewski, and A. R. Walker. Spectroscopy of giants in LMC clusters. III - Velocities and abundances for NGC 1841 and Reticulum and the properties of the metal-poor clusters. *AJ*, 104:1743–1764, November 1992. doi: 10.1086/116356.
- R. A. Sunyaev, M. Markevitch, and M. Pavlinsky. The center of the Galaxy in the recent past - A view from GRANAT. *ApJ*, 407:606–610, April 1993. doi: 10.1086/172542.
- Y. Suwa, T. Yoshida, M. Shibata, H. Umeda, and K. Takahashi. Neutrino-driven explosions of ultra-stripped Type Ic supernovae generating binary neutron stars. *MNRAS*, 454:3073–3081, December 2015. doi: 10.1093/mnras/stv2195.
- T. M. Tauris. Maximum speed of hypervelocity stars ejected from binaries. *MNRAS*, 448: L6–L10, March 2015. doi: 10.1093/mnras/slu189.
- T. M. Tauris and R. J. Takens. Runaway velocities of stellar components originating from disrupted binaries via asymmetric supernova explosions. *A&A*, 330:1047–1059, February 1998.
- G. Taylor. The Formation of a Blast Wave by a Very Intense Explosion. I. Theoretical Discussion. *Royal Society of London Proceedings Series A*, 201:159–174, March 1950. doi: 10.1098/rspa.1950.0049.
- J. K. Truelove and C. F. McKee. Evolution of Nonradiative Supernova Remnants. *ApJS*, 120: 299–326, February 1999. doi: 10.1086/313176.
- M. Tsuboi, A. Miyazaki, and S. K. Okumura. A Galactic Center 50-km s⁻¹ Molecular Cloud with an Expanding Shell. *PASJ*, 61:29–, February 2009. doi: 10.1093/pasj/61.1.29.
- J. Vink. Supernova remnants: the X-ray perspective. *A&A Rev.*, 20:49, December 2012. doi: 10.1007/s00159-011-0049-1.
- C. J. Walcher, T. Böker, S. Charlot, L. C. Ho, H.-W. Rix, J. Rossa, J. C. Shields, and R. P. van der Marel. Stellar Populations in the Nuclei of Late-Type Spiral Galaxies. *ApJ*, 649: 692–708, October 2006. doi: 10.1086/505166.
- Q. D. Wang, M. A. Nowak, S. B. Markoff, F. K. Baganoff, S. Nayakshin, F. Yuan, J. Cuadra, J. Davis, J. Dexter, A. C. Fabian, N. Grosso, D. Haggard, J. Houck, L. Ji, Z. Li, J. Neilsen, D. Porquet, F. Ripple, and R. V. Shcherbakov. Dissecting X-ray-Emitting Gas Around the Center of Our Galaxy. *Science*, 341:981–983, August 2013. doi: 10.1126/science.1240755.
- D. C. Warren and J. M. Blondin. Three-dimensional numerical investigations of the morphology of Type Ia SNRs. *MNRAS*, 429:3099–3113, March 2013. doi: 10.1093/mnras/sts566.
- Stephen Weinberg. A bethe unit. *Physics World*, 19(2):17, 2006.
- N. Werner, J. B. R. Oonk, M. Sun, P. E. J. Nulsen, S. W. Allen, R. E. A. Canning, A. Simionescu, A. Hoffer, T. Connor, M. Donahue, A. C. Edge, A. C. Fabian, A. von der Linden, C. S. Reynolds, and M. Ruszkowski. The origin of cold gas in giant elliptical galaxies and its role in fuelling radio-mode AGN feedback. *MNRAS*, 439:2291–2306, April 2014. doi: 10.1093/mnras/stu006.
- P. Westera, T. Lejeune, R. Buser, F. Cuisinier, and G. Bruzual. A standard stellar library for evolutionary synthesis. III. Metallicity calibration. *A&A*, 381:524–538, January 2002. doi: 10.1051/0004-6361:20011493.
- J. C. Wheeler, M. Lecar, and C. F. McKee. Supernovae in binary systems. *ApJ*, 200:145–157,

- August 1975. doi: 10.1086/153771.
- A. Wongwathanarat, H.-T. Janka, and E. Müller. Three-dimensional neutrino-driven supernovae: Neutron star kicks, spins, and asymmetric ejection of nucleosynthesis products. *A&A*, 552:A126, April 2013. doi: 10.1051/0004-6361/201220636.
- S.E. Woosley and A. Heger. Nucleosynthesis and remnants in massive stars of solar metallicity. *Physics Reports*, 442(1-6):269 – 283, 2007. ISSN 0370-1573. doi: 10.1016/j.physrep.2007.02.009. The Hans Bethe Centennial Volume 1906-2006.
- Z. Xue and B. E. Schaefer. Newly Determined Explosion Center of Tycho’s Supernova and the Implications for Proposed Ex-companion Stars of the Progenitor. *ApJ*, 809:183, August 2015. doi: 10.1088/0004-637X/809/2/183.
- P. A. Young and C. L. Fryer. Uncertainties in Supernova Yields. I. One-dimensional Explosions. *ApJ*, 664:1033–1044, August 2007. doi: 10.1086/518081.
- Q. Yu and S. Tremaine. Ejection of Hypervelocity Stars by the (Binary) Black Hole in the Galactic Center. *ApJ*, 599:1129–1138, December 2003. doi: 10.1086/379546.
- F. Yuan. Advection-dominated Accretion: From Sgr A* to Other Low-luminosity AGNs. In L. C. Ho and J.-W. Wang, editors, *The Central Engine of Active Galactic Nuclei*, volume 373 of *Astronomical Society of the Pacific Conference Series*, page 95, October 2007.
- L. R. Yungelson, E. P. J. van den Heuvel, J. S. Vink, S. F. Portegies Zwart, and A. de Koter. On the evolution and fate of super-massive stars. *A&A*, 477:223–237, January 2008. doi: 10.1051/0004-6361:20078345.
- J.-P. Zahn. Tidal friction in close binary stars. *A&A*, 57:383–394, May 1977.
- Y. Zhang, Q.-S. Gu, and L. C. Ho. Stellar and dust properties of local elliptical galaxies: clues to the onset of nuclear activity. *A&A*, 487:177–183, August 2008. doi: 10.1051/0004-6361:200809660.
- J.-H. Zhao, M. R. Morris, and W. M. Goss. Radio Detection of a Candidate Neutron Star Associated with Galactic Center Supernova Remnant Sagittarius A East. *ApJ*, 777:146, November 2013. doi: 10.1088/0004-637X/777/2/146.
- K. Zubovas, G. A. Wynn, and A. Gualandris. Supernovae in the Central Parsec: A Mechanism for Producing Spatially Anisotropic Hypervelocity Stars. *ApJ*, 771:118, July 2013. doi: 10.1088/0004-637X/771/2/118.

Curriculum Vitae

I was born on July 10, 1981 in Auckland, New Zealand. From a young age, I was drawn to science, particularly fundamental physics and astronomy, and growing up I have fond memories of seeing Saturn's rings through a telescope in the back garden or reading popular books about the Universe.

After graduating from the top class at Auckland Grammar School, I enrolled in a conjoint (double) degree program to pursue interests both in physics and in other areas such as cognitive science. I graduated from the University of Auckland with both a Bachelor of Arts and a Bachelor of Science. The broad background offered in the degrees made many subjects appealing, but I ultimately stuck to my original passion for astrophysics and chose it for my master's topic at the same university.

My master's thesis, under the supervision of Dr. Graham Hill, involved developing a stellar evolution code out of static structure models. The effectiveness of my code was demonstrated by comparing the evolution results with those from other codes, and generating isochrones that were fitted to observations. I graduated from the Master of Science degree in 2010 with first-class honours and the highest possible grade.

While at the University of Auckland, I was a teaching assistant for many physics courses. I assisted with astronomy and astrophysics courses, as well as both introductory and advanced levels of physics theory and laboratory instruction. During my studies, I worked for many years at the Auckland Observatory, where I enjoyed presenting planetarium shows and talks to the public on astronomy as well as a large amount of involvement in developing that content. Additionally, in between degrees, I worked as a database administrator as well as full-time at the Auckland Observatory.

In 2011, I began my PhD programme in Leiden under the supervision of Prof. dr. Simon Portegies Zwart and Dr. Elena Maria Rossi. During this time, I have been a member of several groups: the computational astrophysics group (CAstLe, led by Prof. dr. Simon Portegies Zwart), the high-energy astrophysics group (led by Dr. Elena Maria Rossi) and the compact objects group (led by Dr. Alessandro Patruno). I have been involved in workshop organisation at Leiden Observatory, and have presented posters and talks, attended workshops and visited collaborators in a number of other locations, including Nijmegen (Netherlands), Como (Italy), Alajar (Spain) and Melbourne (Australia).

List of publications

A. Rimoldi, E. M. Rossi, T. Piran and S. F. Portegies Zwart. The fate of supernova remnants near quiescent supermassive black holes. *Monthly Notices of the Royal Astronomical Society*, 447: 3096–3114, March 2015.

doi: 10.1093/mnras/stu2630

A. Rimoldi, E. M. Rossi, E. Costantini and S. F. Portegies Zwart. The contribution of young core-collapse supernova remnants to the X-ray emission near quiescent supermassive black holes. *Monthly Notices of the Royal Astronomical Society*, 456: 2537–2549, December 2015.

doi: 10.1093/mnras/stv2799

A. Rimoldi, S. F. Portegies Zwart, E. M. Rossi. Simulations of stripped core-collapse supernovae in close binaries. *Computational Astrophysics and Cosmology*, 3: 1–19, March 2016.

doi: 10.1186/s40668-016-0015-4

A. Rimoldi, S. F. Portegies Zwart, E. M. Rossi, et al. A method to infer globular cluster evolutionary history from observations of blue stragglers: the case of Hodge 11. *To be submitted*.

Acknowledgements

Arriving for the PhD, the end seemed so far off in the future. The years have flown by far faster than I imagined, but they have been very rich, both with interesting work at the Sterrewacht and great times outside it. So, there are many people I want to thank!

First of all, thank you, Simon and Elena, for offering the opportunity of the PhD to this bloke from the opposite side of the world. I greatly appreciate all of the guidance and support you have offered me over the past several years—thank you. An important part in helping me get to the PhD was also the mentorship of my master's supervisor, Graham Hill—thanks, Graham, for your guidance back at Auckland.

Many staff at the Sterrewacht have offered assistance during my PhD. Evelijn, thanks for all your kind help with many things during my time at the Sterrewacht. Thanks also to Alexandra, Anita, Arianne, David, Debbie, Els, Erik, Jeanne, Leonardo and Liesbeth for your assistance, whether it be looking after packages from New Zealand or trying to get the 3D printer to work! Xander, thanks for your guidance during the final year (despite a full schedule of frantic PhD students to follow!).

I have enjoyed being part of a few different research groups during my time at Leiden, with a great diversity of topics that kept group meetings interesting. In Simon's CAStLe group, thank you to Adrian, Arjen, Bernadetta, Carmen, Dan, Edwin, Evghenii, Inti, Jeroen, Lucie, Michiko, Martha, Masaki, Nathan, Nora, Silvia, Steven, Thomas, Tjarda, Tjibaria and everyone else who has visited the group for many years of interesting discussions. Arjen, Inti and Nathan, thanks for your generous advice and help with using AMUSE. To the members of Elena's group over the years, Bart, Clément, James, Joshua, Mark, Tommaso, Steven, Valeriya, as well as Alessandro, Ann-Sofie, Caroline, Magdalena (and everyone who overlaps) in the compact object group, thank you for all the interesting and helpful meetings.

The size of the Sterrewacht makes for a vibrant graduate life that must be unparalleled. I'm fortunate to have met many wonderful people both inside and outside the Sterrewacht in the past several years, and so many of you have made an impact that can't be summarised in this short section. My first memories of Leiden are from before the PhD had even started, and all the prospective students were given a warm welcome by Marissa and Tiffany (also introducing some of us to the Bonte Koe, still one of my favourite spots in town!). I'm very glad to have gotten to know you both since that

first day. Thanks for being such kind and supportive friends over the years (amongst many trips away, parties, brews...). Andra, Heather, Marco, Monica—thank you for all your friendship since we started together in Leiden. Each of you has been a wonderful friend over these years. Thanks for all the memorable trips, chats, brunches and borrels (as organisers and participants!), and great times in between. Allison and Mason, I'm grateful to have been able to get to know you later in the PhD, and for more than making up for 'lost time' with your most excellent friendship and many fun times!

Dan and Jeroen, you welcomed me into the office at the very beginning, and became great friends throughout our time in room 402. Thanks for keeping it a fun place to be. Jeroen, hartstikke bedankt voor mijn samenvatting vertalen! Thanks, Sam (and Ellie and Jonas), for the great dinners and Super Bowl evenings. Bernadetta, Carmen, Daniel (H.), Daniel (R.), Emilie, Giorgia, Michiko, Rasmus, Stefania, Steven, Thibaut and Yuri, thanks for all the lunchtime company, outings and evenings of playing games or eating sushi (or, better, both at once!). Julien, Masaki, Noel, Thomas, Tjarda, thanks for the interesting chats around the office. Alan, Ali, Alex (North), Andrew, Berenice, Bram, Carl, Caroline, Clément, David, Emanuele, Gaby, Henriette, Irene, Jeroen (F.), Leah, Lucie, Marcello, Maryam, Matteo, Mattia, Mayuresh, Mike, Nicola, Sebastiaan, Silvia, Thanja, Willem, Xiaohu and the many others I've missed, thanks for the good company at lunches, borrels and outside the Sterrewacht.

While in Leiden, I have been lucky to meet a number of great friends outside of astronomy. To the 'locals'—Gorana, Mark, Mart, Olga, René, I've had a blast with you guys since some of the earliest days in Leiden, and I can't think of a better crowd to have gotten to know for life outside of the observatory! Thanks for all the great times visiting new places, and back at home—whether watching (good and bad) movies, or trying to beat Tom at poker. Alex (West), Allie, Bernard, Tom, Victor, I'm grateful to have you as good friends—and not just significant others of Sterrewachters (which goes to show astronomers can have excellent taste in partners outside the observatory!). Thanks for the many great times around Leiden and beyond. Graeme, Marlinda, Yuval and everyone else at the flats, it has been great to get to know you all over these years!

To all my friends from home—it's too long between visits, but no matter how long it's been, whenever I see you guys, thanks for being there as if we'd never left (as Jamie recently put it so well). Jamie, Martin, Peter and Simon, I'm glad to have been able to catch you all at various points during the PhD, and to have shared in some very significant moments in your lives over that time.

And, not least, to my family—thanks for keeping the home fires burning. I wouldn't be here without your support, and I've missed you all during these years at the antipodes. Dylan and Simone, thank you for all your support. It means a lot to me that you could be a part of my thesis and graduation with each of your important contributions. To my parents—thank you for showing me the Universe is so full of wonderful things. Da, I know you would be proud to see me graduate—you will be in my thoughts. Mum, your support has kept me going in too many ways to mention. Thank you for always being there for me.